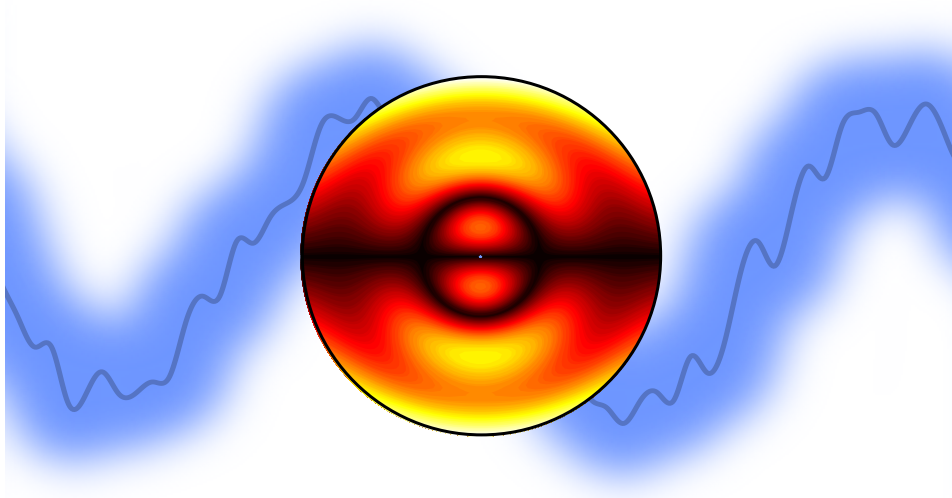


# Nonlocal Response in Metals and Semiconductors

---



Johan R. Maack

PHD THESIS

# Nonlocal Response in Metals and Semiconductors

Johan R. MAACK



Department of Photonics Engineering  
Technical University of Denmark  
September 10, 2018

Cover: Charge distribution of bulk and surface plasmons in a spherical semiconductor particle. See further discussion in chapter 5.

PhD Thesis  
*Nonlocal Response in Metals and Semiconductors*  
by Johan R. Maack

Supervisors:  
Assoc. Prof. Martijn Wubs  
Prof. N. Asger Mortensen

Structured Electromagnetic Materials group  
Department of Photonics Engineering  
Technical University of Denmark  
September 10, 2018

## Abstract (English)

In this thesis, the optical properties of the free-electron gas in metals and semiconductors are analysed theoretically using various nonlocal models. Nonlocal response is a phenomena which is not accounted for in the classical theory of the electron gas, and it is a property that will become increasingly more significant as the structures approach the nanometer scale. In particular, the collective excitations of the electrons, known as plasmons, will depend on these size-dependent, nonlocal effects.

Of particular focus in this thesis is the hydrodynamic Drude model (HDM), which may be considered the lowest-order nonlocal correction to the classical theory. We use this model to analyse the optical response of spherical metal particles, in which it predicts a size-dependent resonance shift of the localized surface plasmon (LSP) that is not found in the classical theory. We also analyse the implications of nonlocal effects for an ensemble of particles with different sizes. The combination of the size-dependent resonance shift and a distribution of particle sizes will result in an effective broadening of the resonance peak. We quantify the broadening with the HDM through numerical simulations and analytical methods.

Following the analysis of metals, the nonlocal properties of semiconductor particles are investigated. Semiconductors may for example contain a free-electron gas from doping or from the thermal distribution of electrons in intrinsic semiconductors, and we adapt the HDM to these two scenarios. We find that the relative size-dependent resonance shift of the LSP is much larger in semiconductors than in metals, which opens up for new experimental investigations in nonlocal effects. Semiconductors are furthermore promising as plasmonic materials because they offer a tunability of the optical properties that is not possible in metals. Using the HDM, we investigate the tuning of the LSP with either doping or temperature.

Finally, an extended version of the HDM is developed to properly describe semiconductors with several different kinds of charge carriers, like electrons and holes or heavy and light holes. We consider materials with two different plasmas and show how this gives rise to two longitudinal waves of acoustic and optical type, respectively. This is different from the single-fluid HDM which only predicts an optical mode. An extended version of the Mie theory is developed to account for the two longitudinal waves, and we use this to find the optical properties of semiconductor particles with two different kinds of charge carriers. We find that the two-fluid model predicts plasmon resonances that are completely absent in the single-fluid HDM.



## Resumé (Danish)

I denne afhandling er de optiske egenskaber for fri-elektrongassen i metaller og halvledere analyseret teoretisk med forskellige ikke-lokale modeller. Ikke-lokal respons er et fænomen, som den klassiske teori for elektrongassen ikke tager højde for, og det er en egenskab der bliver mere signifikant, når strukturerne nærmer sig nanometer-størrelsesordenen. Især vil de kollektive excitationer af elektronerne, bedre kendt som plasmoner, afhænge af disse størrelses-afhængige, ikke-lokale effekter.

I denne afhandling er der særligt fokus på den hydrodynamiske Drude model (HDM), der kan betragtes som den ikke-lokale korrektion af laveste orden til den klassiske teori. Vi anvender modellen til at analysere den optiske respons af sfæriske metalpartikler, hvor den forudsiger en størrelses-afhængig forskydning af resonansen for den lokaliserede overflade plasmon (LSP), der ikke er til stede i den klassiske teori. Vi undersøger desuden konsekvenserne af ikke-lokale effekter i et ensemble af partikler med forskellige størrelser. Kombinationen af den størrelses-afhængige forskydning af resonansen og fordelingen af partikelstørrelser giver anledning til en effektiv forbreddning af resonansen. Vi analyserer denne forbreddning med den HDM via numeriske simuleringer og analytiske metoder.

Efter analysen af metaller undersøger vi de ikke-lokale egenskaber for halvledere. Halvledere kan for eksempel have en fri-elektrongas fra dotering eller fra den termiske fordeling af elektroner i intrinsiske halvledere, og vi tilpasser den HDM til disse to scenarier. Vi finder en relativ størrelses-afhængig forskydning af LSP resonansen, som er meget større i halvledere end i metaller, hvilket åbner op for nye eksperimentelle undersøgelser af ikke-lokal respons. Halvledere er desuden lovende som nye plasmoniske materialer, da de har en tunabilitet af de optiske egenskaber, der ikke er mulig i metaller. Vi undersøger tunabiliteten for LSP-resonansen ved dotering og temperatur.

Til sidst udleder vi en udvidet version af den HDM for at kunne beskrive halvledere med flere forskellige typer ladningsbærere, så som elektroner og huller eller tunge og lette huller. Vi analyserer materialer med to forskellige plasmaer og viser hvordan dette giver anledning til to longitudinale bølger af hhv. akustisk og optisk type. Dette adskiller sig fra den enkelt-fluide HDM, som kun forudsiger en optisk bølge. En udvidet version af Mie-teorien udvikles med henblik på at inkludere de to longitudinale bølger, og vi anvender denne model til at finde de optiske egenskaber for halvlederpartikler med to slags ladningsbærere. Vi finder at to-fluid modellen forudsiger plasmoner, der ikke eksisterer i den enkelt-fluide HDM.



## *Acknowledgements*

I would like to thank my supervisors Asger and Martijn for their support and guidance throughout my PhD. I especially owe my thanks to Martijn who helped me with countless advices of both scientific and personal matter.

I would also like to thank professor Bill Barnes of Exeter University for giving me the opportunity to learn about collective excitations in molecules. Also Simon Horsley at the same university helped me to understand many difficult problems.

I would also like to thank former and current members of the Structured Electromagnetic Materials group for giving me an interesting place to work. And I truly appreciate the many interesting and weird conversations I had with the people in my office. Special thanks also go to Thomas Christensen and Christos Tserkezis who both answered many of my silly questions.

Finally, I would like to thank my dog, family and friends for their support during the writing of my thesis.



## List of publications

- A: C. Tserkezis, **J. R. Maack**, Z. Liu., M. Wubs, & N. A. Mortensen. *Robustness of the far-field response of nonlocal plasmonic ensembles*. *Sci. Rep.* **6**, 28441 (2016).
- B: **J. R. Maack**, N. A. Mortensen. & M. Wubs. *Size-dependent nonlocal effects in plasmonic semiconductor particles*. *EPL* **119**, 17003 (2017).
- C: **J. R. Maack**, N. A. Mortensen. & M. Wubs. *Two-fluid hydrodynamic model for semiconductors*. *Phys. Rev. B* **97**, 115415 (2018).



# Contents

<b>Abstract (English)</b>	<b>iii</b>
<b>Resumé (Danish)</b>	<b>v</b>
<b>Acknowledgements</b>	<b>vii</b>
<b>List of publications</b>	<b>ix</b>
<b>1 Introduction</b>	<b>1</b>
1.1 Outline . . . . .	2
<b>2 Fundamental theory of plasmonics</b>	<b>3</b>
2.1 Maxwell's Equations . . . . .	3
2.2 Constitutive relations . . . . .	5
2.3 The Drude model . . . . .	7
2.4 Transverse and longitudinal fields . . . . .	8
2.5 Surface plasmon polaritons . . . . .	11
2.6 Localized surface plasmons . . . . .	14
2.7 Excitation of plasmons . . . . .	15
<b>3 Nonlocal effects in metals</b>	<b>21</b>
3.1 Dielectric functions of metals . . . . .	22
3.2 Lindhard dielectric function . . . . .	24
3.3 The hydrodynamic model . . . . .	28
3.4 Nonlocal damping . . . . .	33
3.5 Mie theory . . . . .	36
3.6 Nonlocal effects in spherical nanoparticles . . . . .	38
3.7 Inhomogeneous broadening . . . . .	43
<b>4 Nonlocal effects in semiconductors</b>	<b>49</b>
4.1 Concepts of semiconductors . . . . .	50
4.2 Interband transitions, excitons, phonons and quantum size effects	56
4.3 Materials and fabrication . . . . .	57
4.4 The nonlocal parameter . . . . .	59

4.5	Blueshift of the LSP resonance . . . . .	60
4.6	Tunable plasmonics . . . . .	64
<b>5</b>	<b>Two-fluid hydrodynamic model</b>	<b>67</b>
5.1	The hydrodynamic model for two plasmas . . . . .	68
5.2	Transverse and longitudinal waves . . . . .	71
5.3	Two-fluid model and spherical particles . . . . .	73
5.4	Extinction spectra for two-fluid systems . . . . .	75
5.5	The acoustic peak . . . . .	81
<b>6</b>	<b>Conclusion and outlook</b>	<b>85</b>
<b>A</b>	<b>Longitudinal dielectric function</b>	<b>87</b>
<b>B</b>	<b>The hydrodynamic equations</b>	<b>89</b>
<b>C</b>	<b>System of linear equations for the Mie coefficients</b>	<b>95</b>
	<b>Publication A</b>	<b>97</b>
	<b>Publication B</b>	<b>111</b>
	<b>Publication C</b>	<b>123</b>
	<b>Bibliography</b>	<b>140</b>





# 1 Introduction

Plasmonics is the study of collective excitations of charged particles, and these excitations, or plasmons, are typically found in materials with a free-electron gas such as metals. In classical physics the name “plasmon” refers to the resonance, but adopting the quantum mechanical picture, plasmons can also be understood as particles in the same way photons are particles of the electromagnetic radiation.

Plasmonics has been the subject of fundamental studies for decades with the classical description by Tonks and Langmuir being one of the first contributions [1], and Pines and Bohm providing one of the earliest quantum mechanical descriptions [2]. Since then the interest has only increased with studies of the classical and quantum mechanical properties [3–6], investigations in noble metals [7–12] and other metals [13,14], different geometries [15–19] and dimensions [20–22]. The research in plasmonics has also been fueled by the many promising technological applications including sensors [23–26], cancer treatment [27], nano-electronics [28,29], field-enhancement [30–33], catalysis [34], photovoltaics [35], colour printing [36] and quantum technology [37,38].

Given the maturity of the field, it is surprising that new discoveries continue to be made in this area. While one explanation for this is the richness of the field, as indicated above, there is also another very practical reason for it: As the tools for fabrication and measurement continue to improve, the limits for how small and precise the structures can be created are pushed all the time [39,40], and this in turn leads to new research opportunities. At the same time the theoretical understanding of the physics is challenged by the new measurements and the desire to make more accurate models. Specifically, the purely classical theory for plasmons is not able to explain the properties of nanoscale structures, and more advanced theories must be applied instead.

The boundaries are also being pushed in terms of the materials used in plasmonics. While metals, and in particular noble metals, are the most widely used materials when it comes to sustaining plasmons, new possibilities are also being considered. Semiconductors constitute a group of materials that is interesting for the plasmonic community, especially because of their flexibility compared to metals [41,42], which can be used in, for example, tunable plasmonic sensors [43]. Semiconductors are also particularly suitable for biological and medical applications due to the plasmonic resonances being located in the infrared spectrum rather than the visible spectrum as for metals [44]. Another material capable of sustaining plasmons is graphene, the

two-dimensional allotrope of carbon, which is interesting both in terms of application and fundamental research [20, 45]. In the group of exotic substitutes for metals are also single molecules [46] and molecular chains known as J-aggregates [47, 48], which challenge the definition of a plasmon.

In this thesis, two current research directions of the field of plasmonics are considered. One is the development of improved theoretical models that are able to properly describe the experiments as well as provide new physical insight. The other is the exploration of semiconductors as new plasmonic materials and their advantages compared to the conventional materials. Particular focus will be on the *nonlocal* optical response of the electron plasma, where ‘nonlocal’ refers to the dependence of the material response to the external electric field. While not capturing all quantum mechanical phenomena, a nonlocal model seeks to improve upon the classical, *local* description of the optical properties, especially when it comes to modeling of nanostructures.

## 1.1 Outline

**Chapter 2** will provide the theoretical framework that goes into understanding plasmons, including the fundamentals of electromagnetic theory and the concept of optical response. The chapter will introduce the family of different plasmonic resonances, and give examples of experimental methods used to probe plasmons.

**Chapter 3** will introduce some of the nonlocal models used to study the optical response of metals with particular focus on the hydrodynamic Drude model (HDM). The electromagnetic solution for spherical geometry will be presented, and based on this, the consequences of nonlocal response in spherical metal nanoparticles will be analysed.

**Chapter 4** then considers the possibility of using semiconductors as plasmonic materials. Different types of semiconductors will be investigated, and particular focus will be on the nonlocal properties as predicted by the HDM. We will also analyse the tunability of semiconductors, which is one of the advantages they have compared to metals.

**Chapter 5** will consider an extended version of the HDM for semiconductors where several different kinds of free charge carriers are present. Semiconductors may, for example, contain both an electron and a hole plasma, and this gives rise to nonlocal effects that are absent in the traditional HDM for a single type of charge carrier.

**Chapter 6** will then provide a conclusion of the results together with an outlook on the future of plasmonics in metals and semiconductors.

## 2 Fundamental theory of plasmonics

In this chapter, the basic theory going into understanding the concept of plasmons will be presented. Although most of the content here is considered classical electrodynamics, it is the same framework that will be used when we analyze the nonlocal and semi-classical models in the following chapters. Many of the equations presented here will be used later on, and the chapter will also serve as an introduction for readers unfamiliar with the topic of plasmonics.

We will open the chapter with a brief discussion of Maxwell's Equations and the accompanying constitutive relations. Then we will introduce the Drude model which is the simplest theory for the free-electron plasma of metals. Based on this model, the different types of plasmons will then be presented including the bulk plasmon, the surface plasmon polariton and the localized surface plasmon. In the last section we will discuss the different ways plasmons can be excited and probed.

### 2.1 Maxwell's Equations

At the foundation of classical plasmonics we find Maxwell's Equations. These include Gauss's law for the electric field  $\mathbf{E}$  and the magnetic field  $\mathbf{B}$ , Faraday's Law and Ampère's Law, and they are given by [49, 50]

$$\nabla \cdot \mathbf{E} = \frac{\rho}{\varepsilon_0}, \quad (2.1a)$$

$$\nabla \cdot \mathbf{B} = 0, \quad (2.1b)$$

$$\nabla \times \mathbf{E} = -\frac{\partial \mathbf{B}}{\partial t}, \quad (2.1c)$$

$$\nabla \times \mathbf{B} = \mu_0 \mathbf{J} + \varepsilon_0 \mu_0 \frac{\partial \mathbf{E}}{\partial t}. \quad (2.1d)$$

Here  $\varepsilon_0 \approx 8.854 \cdot 10^{-12}$  F/m and  $\mu_0 = 4\pi \cdot 10^{-7}$  H/m are, respectively, the permittivity and permeability of free space. The charge density  $\rho$  is related to the current density  $\mathbf{J}$  through the continuity relation

$$\frac{\partial \rho}{\partial t} = -\nabla \cdot \mathbf{J}. \quad (2.2)$$

This is seen by applying the divergence to Eq. (2.1d), whereby we note that  $\nabla \cdot \nabla \times \mathbf{B} = 0$ , and combining it with Eq. (2.1a).

Often  $\mathbf{J}$  and  $\rho$  are split into external parts  $\mathbf{J}_{\text{ext}}$  and  $\rho_{\text{ext}}$  and induced parts

$\mathbf{J}_{\text{ind}}$  and  $\rho_{\text{ind}}$ . While  $\mathbf{J}_{\text{ext}}$  and  $\rho_{\text{ext}}$  are assumed to be controllable (or at least known beforehand), the induced parts  $\mathbf{J}_{\text{ind}}$  and  $\rho_{\text{ind}}$  depend on the material and are responses to the applied fields. Alongside this division, it will be an advantage to introduce the displacement field  $\mathbf{D}$  and the  $\mathbf{H}$ -field which are defined as [49,50]

$$\mathbf{D} = \varepsilon_0 \mathbf{E} + \mathbf{P}, \quad (2.3a)$$

$$\mathbf{H} = \frac{1}{\mu_0} \mathbf{B} - \mathbf{M}, \quad (2.3b)$$

where  $\mathbf{P}$  is the polarization and  $\mathbf{M}$  is the magnetization. These are related to the material's electric and magnetic response, respectively, and they are coupled to the induced current density by [49,50]

$$\mathbf{J}_{\text{ind}} = \nabla \times \mathbf{M} + \frac{\partial \mathbf{P}}{\partial t}. \quad (2.4)$$

In this work we will only consider non-magnetic materials which means that  $\mathbf{M} = \mathbf{0}$  and  $\mathbf{H} = \mathbf{B}/\mu_0$ . With the definitions in Eqs. (2.3), we can rewrite Eqs. (2.1a) and (2.1d) in terms of the external charges

$$\nabla \cdot \mathbf{D} = \rho_{\text{ext}}, \quad (2.5)$$

$$\nabla \times \mathbf{H} = \mathbf{J}_{\text{ext}} + \frac{\partial \mathbf{D}}{\partial t}, \quad (2.6)$$

while Eqs. (2.1b) and (2.1c) are unchanged by these definitions.

From Maxwell's Equations it is possible to derive an important equation, namely the wave equation for the electric field. Applying the curl to Eq. (2.1c), differentiation with time to Eq. (2.6) and combining those results give us

$$\nabla \times \nabla \times \mathbf{E} + \mu_0 \frac{\partial^2 \mathbf{D}}{\partial t^2} = -\mu_0 \frac{\partial \mathbf{J}_{\text{ext}}}{\partial t}. \quad (2.7)$$

From this point, it is not possible to progress further without assuming a relation between  $\mathbf{E}$  and  $\mathbf{D}$ . The simplest possible relation is a direct proportionality

$$\mathbf{D} = \varepsilon_0 \varepsilon \mathbf{E}, \quad (2.8)$$

where  $\varepsilon$  is known as the dielectric function. Equation (2.8) may be too simple, however, as we will see in next section.

## 2.2 Constitutive relations

A more general constitutive relation that connects the displacement field to the electric field is

$$\mathbf{D}(\mathbf{r}, t) = \varepsilon_0 \iint \varepsilon(\mathbf{r}, \mathbf{r}', t, t') \mathbf{E}(\mathbf{r}', t') dt' d\mathbf{r}', \quad (2.9)$$

where the  $\mathbf{D}$  now depends *nonlocally* on  $\mathbf{E}$ , i.e. the displacement field at one point in space and time potentially depends on the electrical field in all space and at all times (causality, however, ensures that  $\varepsilon = 0$  for  $t' > t$ ). Notice that in Eq. (2.9),  $\mathbf{D}$  is parallel to  $\mathbf{E}$ , which only is true in isotropic media, and depends linearly on  $\mathbf{E}$ . These are reasonable assumptions for the situations that we will consider.

Another very reasonable assumption is that time is homogeneous, which means that  $\varepsilon$  only depends on the time difference  $t - t'$  rather than on  $t$  and  $t'$  explicitly. The same assumption can be made for the spatial dependence if space is also homogeneous. Obviously, this is only true for complete vacuum, and even the simplest material will be inhomogeneous on the level of atoms. However, this *jellium model* is a reasonable approximation for many materials and one that greatly simplifies the analysis. With these assumptions, the displacement field is given by

$$\mathbf{D}(\mathbf{r}, t) = \varepsilon_0 \iint \varepsilon(\mathbf{r} - \mathbf{r}', t - t') \mathbf{E}(\mathbf{r}', t') dt' d\mathbf{r}'. \quad (2.10)$$

The advantage of this expression compared to Eq. (2.9) is that the integral constitutes a convolution in time and space. This means that the Fourier transform in time and space will be the simple product

$$\mathbf{D}(\mathbf{k}, \omega) = \varepsilon_0 \varepsilon(\mathbf{k}, \omega) \mathbf{E}(\mathbf{k}, \omega), \quad (2.11)$$

where  $\omega$  is the (angular) frequency, and  $\mathbf{k}$  is the wave vector. Since the homogeneity assumption about time always is true, and we are mainly interested in steady-state situations, we will only use the frequency-domain versions of the equations. As for the  $\mathbf{r}$ - or  $\mathbf{k}$ -dependence, we will use whichever is most suitable in the given situation.

The simple relationship between  $\mathbf{D}$  and  $\mathbf{E}$  in Eq. (2.8) can be obtained from Eq. (2.9) if the dielectric function is given by delta functions, i.e.  $\varepsilon(\mathbf{r} - \mathbf{r}', t - t') = \varepsilon \delta(\mathbf{r} - \mathbf{r}') \delta(t - t')$ . We now see that this is in fact a slightly artificial case since the delta function in time corresponds to an instantaneous response to the electric field, and we would expect this assumption to be valid only when the frequency of the field is much smaller than the characteristic frequencies

of the system. The delta function dependence in space is known as the *local response approximation* (LRA), and in the reciprocal space it is equivalent to neglecting the  $\mathbf{k}$ -dependence of the dielectric function. Much of this thesis is dedicated to analysing the implications of including or neglecting spatial nonlocality (also known as *spatial dispersion*).

Analogous to Eq. (2.9), the induced current density may also be found with a nonlocal relation to the electric field

$$\mathbf{J}_{\text{ind}}(\mathbf{r}, t) = \iint \sigma(\mathbf{r} - \mathbf{r}', t - t') \mathbf{E}(\mathbf{r}', t') dt' d\mathbf{r}', \quad (2.12)$$

where  $\sigma$  is the conductivity. Again the homogeneity of time and space are assumed, which allows us to find the Fourier transform

$$\mathbf{J}_{\text{ind}}(\mathbf{k}, \omega) = \sigma(\mathbf{k}, \omega) \mathbf{E}(\mathbf{k}, \omega). \quad (2.13)$$

The connection between  $\varepsilon$  and  $\sigma$  is found by using the relation between the current density and the polarization in Eq. (2.4) with  $\mathbf{M} = \mathbf{0}$ , which in the temporal Fourier transform (whereby  $\partial/\partial t \rightarrow -i\omega$ ) becomes

$$\mathbf{J}_{\text{ind}} = -i\omega \mathbf{P}. \quad (2.14)$$

Using this expression together with Eqs. (2.13) and (2.11) and the definition of  $\mathbf{D}$  then gives us

$$\varepsilon(\mathbf{k}, \omega) = 1 + \frac{i\sigma(\mathbf{k}, \omega)}{\omega\varepsilon_0}. \quad (2.15)$$

It is useful to split the induced current density according to  $\mathbf{J}_{\text{ind}} = \mathbf{J}_f + \mathbf{J}_b$  where  $\mathbf{J}_f$  and  $\mathbf{J}_b$  are the current densities of the free and bound charges, respectively<sup>1</sup>. Although this division is somewhat arbitrary, it does seem natural in materials like metals where  $\mathbf{J}_f$  can be associated with the (almost) free electrons of the conduction band, while  $\mathbf{J}_b$  is caused by the electrons that are more tightly bound. With this division, we also introduce the conductivities  $\sigma_f$  and  $\sigma_b$  for the free and bound charges, respectively, and this allows us to rewrite Eq. (2.15) according to

$$\varepsilon(\mathbf{k}, \omega) = 1 + \frac{i\sigma_b(\mathbf{k}, \omega)}{\omega\varepsilon_0} + \frac{i\sigma_f(\mathbf{k}, \omega)}{\omega\varepsilon_0} = \varepsilon_b(\mathbf{k}, \omega) + \frac{i\sigma_f(\mathbf{k}, \omega)}{\omega\varepsilon_0}, \quad (2.16)$$

where  $\varepsilon_b$  includes the response from the bound charges. We will consider various nonlocal relations between  $\mathbf{E}$  and  $\mathbf{J}_f$ , but in most cases we will assume that  $\varepsilon_b$  is local. This assumption allows us to rewrite the wave equation

---

<sup>1</sup>Note that this is different from the more conventional naming in Ref. [49] where  $\mathbf{J}_f$  is what we here call  $\mathbf{J}_{\text{ext}}$ .

[Eq. (2.7)] in the frequency domain as

$$\nabla \times \nabla \times \mathbf{E} - \frac{\omega^2}{c^2} \varepsilon_b(\omega) \mathbf{E} = i\mu_0\omega(\mathbf{J}_f + \mathbf{J}_{\text{ext}}), \quad (2.17)$$

where it has been used that the speed of light in vacuum is  $c = 1/\sqrt{\mu_0\varepsilon_0}$ .

## 2.3 The Drude model

A simple, local expression can be obtained for  $\varepsilon(\omega)$  by assuming the electrons to be classical, non-interacting particles. If they are subjected to an electric field  $\mathbf{E}$ , they will experience a force as found with the Lorentz Force Law  $\mathbf{F} = -e\mathbf{E}$  (where magnetic forces are ignored), and their movement is described by the differential equation

$$m \frac{\partial^2 \mathbf{r}}{\partial t^2} + m\gamma \frac{\partial \mathbf{r}}{\partial t} = -e\mathbf{E}. \quad (2.18)$$

Here  $m$  is the mass of an electron, and  $\gamma$  is a damping constant. This damping includes scattering between the electrons and the ions of the lattice, and the damping constant is related to the mean propagation time  $\tau$  by  $\gamma = 1/\tau$ . If the electric field has a harmonic time dependence, i.e.  $\mathbf{E}(t) = \mathbf{E}_0 \exp(-i\omega t)$ , the solution to the equation is of the form  $\mathbf{r}(t) = \mathbf{r}_0 \exp(-i\omega t)$  and we obtain

$$-\omega^2 m \mathbf{r}_0 - i\omega m \gamma \mathbf{r}_0 = -e\mathbf{E}_0. \quad (2.19)$$

If we further use that the current density is given by Eq. (2.13) as well as by  $\mathbf{J}_f = -ne\mathbf{u} = inew\mathbf{r}$  where  $n$  is the density of electrons and  $\mathbf{u}$  is the velocity, we obtain the following equation for the conductivity

$$\sigma_f(\omega) = \frac{i\omega ne^2}{m(\omega^2 + i\gamma\omega)}. \quad (2.20)$$

From this we can get an expression for  $\varepsilon(\omega)$  by using Eq. (2.16)

$$\varepsilon(\omega) = \varepsilon_b(\omega) - \frac{\omega_p^2}{\omega^2 + i\gamma\omega}, \quad (2.21)$$

where we have introduced the plasma frequency

$$\omega_p^2 = \frac{ne^2}{\varepsilon_0 m}. \quad (2.22)$$

Eq. (2.21) is known as the Drude dielectric function, and it is one of the most widely used models for metals. The model permits us straight away to analyze excitations in an infinite bulk of matter, which constitutes the simplest possible geometry. Consider Eq. (2.5) where the displacement field is related to  $\rho_{\text{ext}}$ . Because the Drude model is a local model, the equation can be written as

$$\varepsilon_0 \varepsilon(\omega) \nabla \cdot \mathbf{E} = \rho_{\text{ext}}. \quad (2.23)$$

The equation clearly predicts the existence of an electric field when an external charge carrier density is present, but even in the case where  $\rho_{\text{ext}} = 0$ , the equation allows for a non-zero electric field provided that  $\varepsilon(\omega) = 0$ . Physically this means that a self-sustained electric field is present in the material, something that is possible because of the collective oscillation of the electrons. This resonance of the electron plasma coupled to the electric field is known as a plasmon.

We can find the resonance frequency of this plasmon in the Drude model by solving  $\varepsilon(\omega) = 0$ . If for simplicity we assume that  $\varepsilon_b = 1$  and  $\gamma = 0$ , the resonance occurs according to Eq. (2.21) at  $\omega = \omega_p$ , and it is now clear why  $\omega_p$  is called the plasma frequency. At this frequency, the electron plasma resonates synchronously everywhere in the bulk, and for this reason, the resonance is known as a *bulk plasmon*. Naturally, no resonance can sustain itself indefinitely, and in a more realistic scenario where the loss constant  $\gamma$  is different from 0, the solution to the plasmon condition  $\varepsilon(\omega) = 0$  will be a complex frequency, which in turn corresponds to a decaying oscillation.

## 2.4 Transverse and longitudinal fields

It can be shown that the electric field can be separated into a transverse and a longitudinal part [51]. The transverse part  $\mathbf{E}^T$  is characterized by being divergence-free, i.e.  $\nabla \cdot \mathbf{E}^T = 0$ , and the polarization for transverse plane waves will be orthogonal to the direction of propagation. On the other hand, a longitudinal field  $\mathbf{E}^L$  is characterized by being rotation-free, i.e.  $\nabla \times \mathbf{E}^L = \mathbf{0}$ , and the polarization for longitudinal plane waves will be parallel to the direction of propagation. From this definition it is also clear that all magnetic fields are transverse since  $\nabla \cdot \mathbf{B} = 0$  according to Eq. (2.1b).

In reciprocal space, the division into  $\mathbf{E}^T$  and  $\mathbf{E}^L$  can be understood through projection operators  $\mathbf{T}$  and  $\mathbf{L}$  [52]. The longitudinal projection operator is given by  $\mathbf{L} = \hat{\mathbf{k}} \otimes \hat{\mathbf{k}}$  where  $\hat{\mathbf{k}} = \mathbf{k}/k$ , and the longitudinal part is then found by  $\mathbf{E}^L = \mathbf{L}\mathbf{E}$ . The transverse projection operator is defined by  $\mathbf{T} = \mathbf{I} - \mathbf{L}$  with  $\mathbf{I}$  being the identity operator which ensures that  $\mathbf{E} = \mathbf{E}^T + \mathbf{E}^L$ .

One of the reasons why it makes sense to separate the field into transverse and longitudinal parts is that these fields often interact differently with the

material. This also means that we need to consider two different dielectric functions,  $\varepsilon_T$  and  $\varepsilon_L$ , for transverse and longitudinal fields, respectively, which further implies that the total dielectric function has to be a tensor. The situation is simplified, however, by choosing the orthogonal basis  $\{\hat{\mathbf{k}}, \hat{\mathbf{e}}_1(\mathbf{k}), \hat{\mathbf{e}}_2(\mathbf{k})\}$ , where  $\hat{\mathbf{k}}$  is the direction of propagation, and  $\hat{\mathbf{e}}_1(\mathbf{k})$  and  $\hat{\mathbf{e}}_2(\mathbf{k})$  are in the remaining two transverse directions. Choosing this basis set makes the tensor dielectric function  $\varepsilon(\mathbf{k}, \omega)$  diagonal [52]

$$\varepsilon(\mathbf{k}, \omega) = \mathbf{T}\varepsilon_T(\mathbf{k}, \omega) + \mathbf{L}\varepsilon_L(\mathbf{k}, \omega) = \begin{pmatrix} \varepsilon_L(\mathbf{k}, \omega) & 0 & 0 \\ 0 & \varepsilon_T(\mathbf{k}, \omega) & 0 \\ 0 & 0 & \varepsilon_T(\mathbf{k}, \omega) \end{pmatrix}. \quad (2.24)$$

Including a tensor dielectric function in the constitutive relation for  $\mathbf{D}$  gives us

$$\begin{aligned} \mathbf{D}(\mathbf{k}, \omega) &= \varepsilon_0 \varepsilon(\mathbf{k}, \omega) \cdot \mathbf{E}(\mathbf{k}, \omega) \\ &= \varepsilon_0 [\varepsilon_T(\mathbf{k}, \omega) \mathbf{E}^T(\mathbf{k}, \omega) + \varepsilon_L(\mathbf{k}, \omega) \mathbf{E}^L(\mathbf{k}, \omega)], \end{aligned} \quad (2.25)$$

where we clearly see the separation into transverse and longitudinal response. Note that although the dielectric function now is a tensor, the material is still assumed to be isotropic.

Let us now consider the impact of separation into transverse and longitudinal fields on the definition of plasmons. To this end, we will look at the spatial Fourier transform (whereby  $\nabla \rightarrow i\mathbf{k}$ ) of Eq. (2.5)

$$i\mathbf{k} \cdot \mathbf{D}(\mathbf{k}, \omega) = ik\varepsilon_0\varepsilon_L(\mathbf{k}, \omega)E^L(\mathbf{k}, \omega) = \rho_{\text{ext}}(\mathbf{k}, \omega), \quad (2.26)$$

where we have used that  $\mathbf{k} \cdot \mathbf{E}^T = 0$  and  $\mathbf{k} \cdot \mathbf{E}^L = kE^L$ . As noted in previous section, this shows that a self-sustained oscillation of the electric field may exist if the dielectric function is zero. But now we see that this condition applies specifically to the longitudinal field and the longitudinal dielectric function, and we therefore arrive at the condition for *longitudinal plasmons*

$$\varepsilon_L(\mathbf{k}, \omega) = 0. \quad (2.27)$$

A similar analysis can be carried out for the wave equation [Eq. (2.7)], which in reciprocal space becomes

$$\mathbf{k} \times \mathbf{k} \times \mathbf{E}(\mathbf{k}, \omega) + \omega^2 \mu_0 \mathbf{D}(\mathbf{k}, \omega) = -i\omega \mu_0 \mathbf{J}_{\text{ext}}(\mathbf{k}, \omega). \quad (2.28)$$

This equation can be separated into transverse and longitudinal parts by using the continuity equation [Eq. (2.2)] for the external charges. In reciprocal space

this becomes

$$-i\mathbf{k} \cdot \mathbf{J}_{\text{ext}} = -i\omega\rho_{\text{ext}} = \omega\mathbf{k} \cdot \mathbf{D}, \quad (2.29)$$

and by using the fact that only longitudinal fields are parallel to  $\mathbf{k}$ , the equation can be rewritten as

$$-i\mathbf{k} \cdot \mathbf{J}_{\text{ext}}^{\text{L}} = -i\omega\rho_{\text{ext}} = \omega\mathbf{k} \cdot \mathbf{D}^{\text{L}}. \quad (2.30)$$

This shows that the longitudinal parts in Eq. (2.28) cancel. The equation with the remaining transverse parts is

$$-k^2\mathbf{E}^{\text{T}}(\mathbf{k}, \omega) + \frac{\omega^2}{c^2}\varepsilon_{\text{T}}(\mathbf{k}, \omega)\mathbf{E}^{\text{T}}(\mathbf{k}, \omega) = -i\omega\mu_0\mathbf{J}_{\text{ext}}^{\text{T}}(\mathbf{k}, \omega). \quad (2.31)$$

We now have an expression that relates the transverse electric field to an external, transverse current density. But the equation also allows for the existence of an electric field even if  $\mathbf{J}_{\text{ext}}^{\text{T}} = \mathbf{0}$ , and we see that the condition for transverse electric fields is

$$\frac{\omega^2}{c^2}\varepsilon_{\text{T}}(\mathbf{k}, \omega) = k^2. \quad (2.32)$$

This equation reveals something fundamental about transverse fields: Even if  $\varepsilon_{\text{T}}$  is local, i.e. has no dependence on  $\mathbf{k}$ , we can still obtain a finite value of  $k$  from Eq. (2.32) which means that the material can sustain propagating, transverse electric fields. Even in vacuum where  $\varepsilon_{\text{T}} = 1$ , such traveling waves can exist. The reason is, of course, that the electric field couples to the magnetic field (and vice versa), and this electromagnetic radiation can in principle be found in any medium.<sup>1</sup>

The situation is different for the self-sustained longitudinal fields which cannot couple to the magnetic field (since the latter is purely transverse). Instead they have to couple to the electron plasma as we saw it for the Drude model in previous section. However, the dielectric function in this simple model is local, and accordingly does not allow for propagating, longitudinal waves. To have propagating waves we need a wave equation similar to Eq. (2.7) which contains  $\mathbf{E}^{\text{L}}$  as well as its spatial derivative to second order, and this is not possible in a local model [where we have the simple relationship in Eq. (2.23)]. In chapter 3 we will analyse a nonlocal model, and there we indeed obtain a wave equation for longitudinal fields.

We will end this section by noting that in the limit  $\mathbf{k} = \mathbf{0}$  we always have  $\varepsilon_{\text{T}} = \varepsilon_{\text{L}}$  for isotropic media [51]. We will not prove it here, but it can be understood intuitively by noting that the wavelength in this limit goes to infinity.

<sup>1</sup>Although rarely considered, equation (2.32) also allows for the existence of what could be called *transverse plasmons*. Since the transverse electric field always is coupled to the magnetic field, such plasmons would inevitably be closely coupled to the electromagnetic radiation.

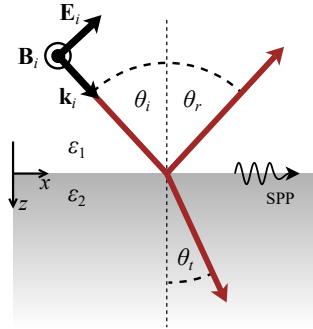


**Figure 2.1:** The incoming wave with electric field  $\mathbf{E}_i$ , magnetic field  $\mathbf{B}_i$  and wave vector  $\mathbf{k}_i$  is reflected and transmitted at the interface between materials with  $\varepsilon_1$  and  $\varepsilon_2$ . Notice that the magnetic field is pointing *out* of the paper for incident, reflected and transmitted waves.

The electric field will be in phase everywhere in space and therefore has lost its “sense” of direction. An example of this is the Drude model, where the local dielectric function is used for both transverse and longitudinal fields.

## 2.5 Surface plasmon polaritons

In this section we will explore a type of plasmons occurring at the interface between two different media, and we will see that these excitations share properties with both longitudinal and transverse fields. Consider the scenario in Fig 2.1 where an electromagnetic plane wave is incident on a interface between medium 1 and 2 located at  $z = 0$ . The two media are characterized by local dielectric functions  $\varepsilon_1$  and  $\varepsilon_2$ , and the geometry is infinite in the  $x$ - and  $y$ -directions. We will here consider a wave that is propagating in the  $xz$ -plane with the magnetic field polarized in the  $y$ -direction, something that is known as the transverse magnetic (TM) mode. At the interface the incident ( $i$ ) wave will be partially reflected ( $r$ ) and transmitted ( $t$ ), and the fields are all given by  $\mathbf{E}_j(\omega, \mathbf{r}) = \mathbf{E}_{j0} \exp(i\mathbf{k}_j \cdot \mathbf{r} - i\omega t)$  where  $j = i, r, t$  and  $\mathbf{k}_j = [k_{jx}, 0, k_{jz}]$  and  $k_{jx} = k_j \sin \theta_j$ . This problem contains several unknowns which can be found by applying the appropriate boundary conditions (BCs). Two such BCs can be obtained directly from Maxwell’s Equations by assuming nonmagnetic materials and zero external surface current [49], and they relate the parallel

components of the fields in the two media at the interface

$$\mathbf{E}_1^{\parallel} - \mathbf{E}_2^{\parallel} = \mathbf{0}, \quad (2.33a)$$

$$\mathbf{B}_1^{\parallel} - \mathbf{B}_2^{\parallel} = \mathbf{0}. \quad (2.33b)$$

Here the  $\mathbf{B}$  field can be found from Eq. (2.1c). These equations put restraints on both the amplitudes and the phases of the waves, and from either of them we find that  $k_{ix} = k_{rx} = k_{tx} = k_x$ ,  $k_{iz} = -k_{rz} = k_{1z}$  and  $k_{tz} = k_{2z}$ . The wave numbers are according to Eq. (2.32) given by  $k_n^2 = \varepsilon_n \omega^2 / c^2$  where  $n = 1, 2$ , and they must additionally fulfill the simple relation

$$k_n = (k_x^2 + k_{nz}^2)^{1/2}. \quad (2.34)$$

From these relations we find that the reflected field is related to the incoming field by the expression  $E_{r0} = r_{\text{TM}} E_{i0}$ , where

$$r_{\text{TM}} = \frac{\varepsilon_2 k_{1z} - \varepsilon_1 k_{2z}}{\varepsilon_2 k_{1z} + \varepsilon_1 k_{2z}}, \quad (2.35)$$

is known as the Fresnel reflection coefficient for the TM mode.

Analogous to the definition of bulk plasmons used in previous section, we notice that even if  $E_{i0} = 0$ , the outgoing field  $E_{r0}$  can be different from zero if simultaneously  $r_{\text{TM}}$  has a pole. This occurs when  $\varepsilon_1 k_{2z} + \varepsilon_2 k_{1z} = 0$ , and if  $k_{1z}$  and  $k_{2z}$  are positive, this condition can only be fulfilled when  $\varepsilon_1$  and  $\varepsilon_2$  have opposite signs. This can for example be accomplished if medium 1 is characterized by a positive dielectric constant  $\varepsilon_1$  (as is true for a simple dielectric), while medium 2 is a metal with a dielectric function  $\varepsilon_2(\omega)$  as the one in the Drude model with  $\omega < \omega_p / \sqrt{\varepsilon_b}$  [see Eq. (2.21)]. With these material choices, we find

$$k_x(\omega) = \frac{\omega}{c} \sqrt{\frac{\varepsilon_1 \varepsilon_2(\omega)}{\varepsilon_1 + \varepsilon_2(\omega)}}. \quad (2.36)$$

We now see that if  $k_x$  is real-valued and  $k_{nz}$  imaginary-valued, the field is a wave propagating in the  $x$ -direction while being confined in the  $z$ -direction. This mode is known as a surface plasmon polariton (SPP), and it is obtained if  $k_x > k_1$  and  $\varepsilon_1 + \varepsilon_2(\omega) < 0$ .

In Fig. 2.2a, the dispersion relation in Eq. (2.36) is plotted with  $\varepsilon_2(\omega)$  given by Eq. (2.21),  $\varepsilon_1$  and  $\varepsilon_b$  set to 1 and no damping ( $\gamma = 0$ ). Here we see a branch of the solution at low frequencies where  $k_x$  is real-valued (shown with a solid line). This is the SPP mode, and it has different characteristics for low and high values of  $k_x$ . For low wavenumbers, the mode coincides almost exactly with the dispersion relation for electromagnetic radiation  $k = \sqrt{\varepsilon_1} \omega / c$ ,

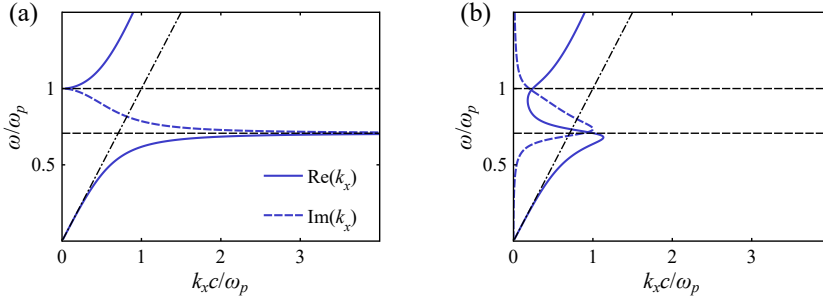


**Figure 2.2:** Dispersion relations for a SPP when (a)  $\gamma = 0$  and (b)  $\gamma = 0.1\omega_p$ . The consequence of loss in the metal is a back-bending of the SPP mode.

which is shown with the dash-dotted line, and in this region the SPP is mainly transverse. For higher values of  $k_x$ , the mode becomes more longitudinal in nature, and for  $k_x \rightarrow \infty$  we get  $\omega = \omega_{\text{SP}} = \omega_p / \sqrt{\varepsilon_2 + \varepsilon_b} = \omega_p / \sqrt{2}$ .

For frequencies above  $\omega_{\text{SP}}$ , the wave number  $k_x$  becomes imaginary-valued as indicated with the dashed line in Fig 2.2a, and this corresponds to an attenuated (non-propagating) mode. Above  $\omega_p$  we have again a mode with real values of  $k_x$  which is sometimes called the *Brewster mode*. This is not a surface plasmon, however, since both  $\varepsilon_1$  and  $\varepsilon_2$  are positive in this region, and it turns out that this mode actually is due to a zero of  $r_{\text{TM}}$  rather than a pole.

Figure 2.2b shows the effect of adding loss to the system by choosing  $\gamma = 0.1\omega_p$  (which is comparable to damping constants in real metals). Now the SPP mode no longer continues to infinity as we approach  $\omega_{\text{SP}}$ , and instead it is “bent back” and connected to the Brewster mode. We also see that the loss represented by  $\text{Im}(k_x)$  in general is nonzero for all frequencies, but finds its maximum value close to  $\omega_{\text{SP}}$ . This loss results in a finite propagation length, defined as  $1/\text{Im}(k_x)$ , which in metals is on the order of  $10^{-5}$  m [53].

One of the characteristic features of surface plasmons is the ability to confine electric fields well below the diffraction limit. This can be understood directly from  $k_{n,z}$  which, because they are complex, result in an exponential decay of the field away from the interface. Unfortunately, the confinement, which may be of technological interest, is largest at  $\omega_{\text{SP}}$  where the loss also reaches its maximum.

In this section we started out by assuming a TM-polarized field. The argument for this is that the transverse electric (TE) mode (with the  $\mathbf{E}$  field polarized parallel to the interface) does not support SPPs [54].

## 2.6 Localized surface plasmons

The geometry considered in the previous section was infinite in the  $xy$ -plane, but surface plasmons may also exist in finite structures. Due to the confinement in space, surface plasmons in finite structures are standing waves, rather than traveling ones, and are known as localized surface plasmons (LSPs). Any shape may support LSP modes, but geometries where Maxwell's Equations can be solved analytically are essentially limited to spheres [55], spheroids [56] and infinite cylinders [57] (which are only finite in two directions). Beyond these shapes, numerical tools such as finite element solvers have to be used instead (see for instance [58]). Alternatively, one can choose to solve the problem in the quasi-static approximation. By assuming that the fields are static, the electric field becomes rotation-free [see Eq. (2.1c)], which means that it is given by  $\mathbf{E} = -\nabla\phi$  where the scalar  $\phi$  is the electric potential. The problem is now reduced to solving  $\nabla^2\phi = -\rho/\varepsilon_0$  which is much simpler, and solutions to the electric potential exist for several geometries, like e.g. a wedge [59]. In the *quasi*-static approximation, the solution to the full time-dependent problem is simply assumed to be equal to the static solution modulated with  $e^{-i\omega t}$ . This is equivalent to assuming that the speed of light is infinite, and the approximation is also known as the *nonretarded* solution.

In this thesis the focus will be on spherical particles, which is one of the few geometries where the solution to Maxwell's Equations is known. However, we will content ourselves with the quasi-static approximation in this chapter and return to the full retarded solution in chapter 3.

Consider a spherical metal particle of radius  $R$  with dielectric function  $\varepsilon_2(\omega)$  surrounded by a material with dielectric constant  $\varepsilon_1$  (see Fig. 2.4a on page 17). If this particle is excited by a plane wave with a much larger wavelength than the radius, the incident field can be assumed to be homogeneous, i.e. constant in space. For an exciting field with amplitude  $E_0$  and polarization in the  $z$  direction, the field outside  $\mathbf{E}_1$  and inside  $\mathbf{E}_2$  the particle are given by [53]

$$\mathbf{E}_1 = E_0(\cos\theta\hat{\mathbf{r}} - \sin\theta\hat{\boldsymbol{\theta}}) + E_0\frac{\varepsilon_2(\omega) - \varepsilon_1}{\varepsilon_2(\omega) + 2\varepsilon_1}\frac{R^3}{r^3}(2\cos\theta\hat{\mathbf{r}} + \sin\theta\hat{\boldsymbol{\theta}}), \quad (2.37)$$

$$\mathbf{E}_2 = E_0\frac{3\varepsilon_1}{\varepsilon_2(\omega) + 2\varepsilon_1}(\cos\theta\hat{\mathbf{r}} - \sin\theta\hat{\boldsymbol{\theta}}). \quad (2.38)$$

The fields are here represented in spherical coordinates  $r$ ,  $\theta$  and  $\phi$ , and the "hats" indicate unit vectors. Notice that the second term of  $\mathbf{E}_1$  goes to zero for  $r \rightarrow \infty$  leaving us with  $\mathbf{E}_1 = E_0(\cos\theta\hat{\mathbf{r}} - \sin\theta\hat{\boldsymbol{\theta}}) = E_0\hat{\mathbf{z}}$  as expected.

Following the same argument as for SPPs and bulk plasmons, we see that  $\mathbf{E}_1$  can be different from 0 even if  $E_0 = 0$ . This corresponds to the excitation

of a dipole LSP, and it occurs when

$$\varepsilon_2(\omega) + 2\varepsilon_1 = 0, \quad (2.39)$$

which is known as the *Fröhlich condition*. If we assume that the metal is described by the Drude dielectric function [Eq. (2.21)] and that  $\varepsilon_b$  is independent of  $\omega$ , we find the resonance frequency to be

$$\omega_{\text{LSP}} = \frac{\omega_p}{\sqrt{\varepsilon_b + 2\varepsilon_1}}, \quad (2.40)$$

which becomes  $\omega_{\text{LSP}} = \omega_p/\sqrt{3}$  if  $\varepsilon_b = \varepsilon_1 = 1$ . We notice that the frequency is independent of the size of the particle, and this is a consequence of using the local, quasi-static approximation. In chapter 3 we will present the full solution to Maxwell's Equations which reveals a size dependence of the resonance as well as the existence of LSPs of higher order than the dipole.

## 2.7 Excitation of plasmons

The ability to excite and measure plasmons is crucial to experimental investigations, and there are several ways to accomplish this, depending on the type of plasmon and what property we are interested in.

### Excitation of SPPs

Let us first consider the excitation of surface plasmon polaritons at the interface between a metal and a dielectric. The SPPs were introduced in section 2.5 as the poles of the reflection coefficient  $r_{\text{TM}}$  for planar electromagnetic waves. But because  $k_{1z}$  has to be imaginary-valued (otherwise it would not be a surface plasmon), the exciting field cannot simply be a traveling wave in medium 1. This can also be understood from Fig. 2.2 where the light-line (which is the dispersion of a traveling wave) never crosses the SPP dispersion: the traveling wave will not have sufficiently high  $k_x$  to couple to the SPP.

One remedy is to let the wave propagate towards the interface and then, very close to the metal surface, switch to a medium of a different dielectric constant, such that the  $z$ -component of the wave vector becomes imaginary. This setup is shown in Fig. 2.3a where a prism of dielectric constant  $\varepsilon_p$  is positioned above the interface with a small gap of medium 1 in between. If  $\varepsilon_p > \varepsilon_1$ , the incoming wave will experience total internal reflection at the prism-dielectric interface for angles above  $\theta_c = \arcsin(\sqrt{\varepsilon_1/\varepsilon_p})$ . An evanescent wave will then reach the metal-dielectric interface and excite the SPP.

The excitation method shown in Fig. 2.3a is known as the Otto configuration [60]. An alternative setup is the Kretschmann configuration [61] shown in

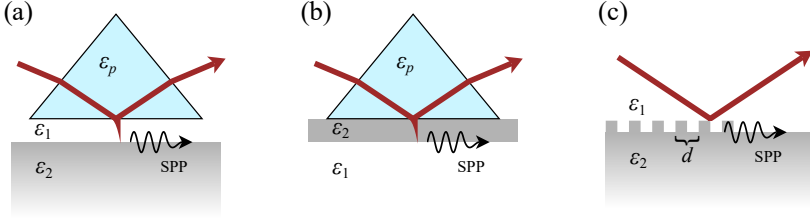


**Figure 2.3:** Various methods for exciting SPPs. (a) Otto configuration, (b) Kretschmann configuration and (c) grating coupling.

Fig. 2.3b, where the SPP on one side of a metal film is excited by an incident wave on the other side. In Fig. 2.3c a third configuration is shown where a grating is used to excite the SPP. By modulating the surface with a pattern of periodicity  $d$ , a multiple of the wavenumber  $\Lambda = 2\pi/d$  is added to  $k_x$  of the incoming wave which makes coupling to the SPP possible.

### Excitation of LSPs

The excitation of LSPs on finite structures is in a way simpler than than exciting SPPs on the semi-infinite interface. The reason is that the finite structures “add” the necessary  $k$  component to make it possible for light to couple with the surface plasmons (similar to the grating in Fig. 2.3c). In section 2.6 we considered a spherical particle that was excited by a plane wave with a wavelength  $\lambda$  much larger than  $R$ , resulting in a field outside the particle given by Eq. (2.38). Comparing this expression with the field from an ideal dipole with dipole moment  $\mathbf{p} = p\hat{\mathbf{z}}$  [53]

$$\mathbf{E} = \frac{p}{4\pi\epsilon_0\epsilon_1 r^3} \left( 2 \cos\theta \hat{\mathbf{r}} + \sin\theta \hat{\boldsymbol{\theta}} \right), \quad (2.41)$$

we see that the field from the sphere is equal to that from a dipole if  $p = \epsilon_2 \alpha E_0$  where

$$\alpha = 4\pi\epsilon_0 \frac{\epsilon_2(\omega) - \epsilon_1}{\epsilon_2(\omega) + 2\epsilon_1} R^3. \quad (2.42)$$

This quantity is known as the polarizability of the sphere, and it quantifies the particle’s tendency to be polarized by the field. Introducing  $\alpha$  has the advantage that it allows us to calculate the energy absorption rate with  $\mathcal{P}_{\text{abs}} = (\omega\epsilon_2 E_0^2/2)\text{Im}(\alpha)$  [62]. If we furthermore divide this value with the incident

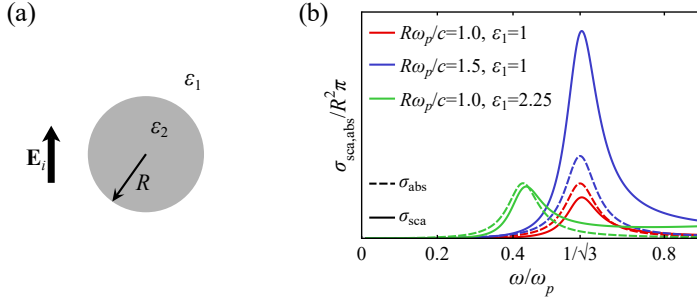


**Figure 2.4:** (a) A spherical particle with radius  $R$  and dielectric function  $\varepsilon_2$  surrounded by a medium with  $\varepsilon_1$ . (b) Absorption cross sections (dashed lines) and scattering cross sections (solid lines) as found with Eqs. (2.43) and (2.44) for three different scenarios:  $R\omega_p/c = 1$  and  $\varepsilon_1 = 1$  (red lines),  $R\omega_p/c = 1.5$  and  $\varepsilon_1 = 1$  (blue lines), and  $R\omega_p/c = 1$  and  $\varepsilon_1 = 2.25$  (green lines). The Drude model with  $\gamma = 0.1\omega_p$  and  $\varepsilon_b = 1$  is used for the particle.

energy flow  $\mathcal{I}_{\text{inc}} = E_0^2 \sqrt{\varepsilon_0 \varepsilon_1 / \mu_0} / 2$ , then we find the *absorption cross section*

$$\sigma_{\text{abs}} = \frac{k_1}{\varepsilon_0} \text{Im}(\alpha), \quad (2.43)$$

where  $k_1 = \sqrt{\varepsilon_1} \omega / c$ . The polarizability also allows us to find the *scattering cross section* [62]

$$\sigma_{\text{sca}} = \frac{k_1^4}{6\pi\varepsilon_0^2} |\alpha|^2, \quad (2.44)$$

which is the scattered fraction of the energy. Notice how the absorption cross section depends on  $R^3$ , while the scattering cross section depends on  $R^6$ . This means that absorption dominates for small particles, while scattering is important for larger particles.

The absorption and scattering cross sections are shown in Fig. 2.4b for a metal particle in different scenarios. The dielectric function of the metal is given by Eq. (2.21) with  $\varepsilon_b = 1$  and  $\gamma = 0.1\omega_p$ , and the cross sections were found with Eqs. (2.43) and (2.44). We notice that all the curves have a single peak which is the dipole LSP resonance also found with Eq. (2.40). The red and blue lines show the spectra for two different particle sizes, and we see how the absorption cross section (dashed lines) is larger than the scattering cross section (solid lines) for the small particle, while the situation is reversed for the large particle. The spectral position of the LSP, however, is the same for

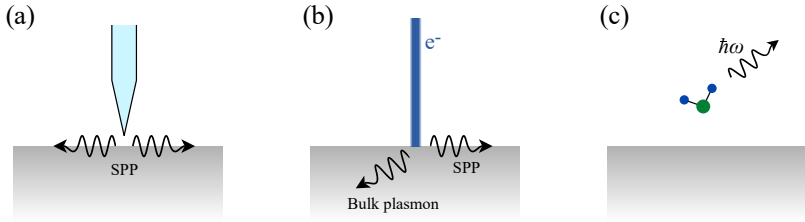


**Figure 2.5:** Various near-field measurements: (a) SNOM using a tapered fiber, (b) EELS using an electron beam and (c) LDOS affecting the decay rate of an emitter such as a molecule.

the two particle sizes, which reflects the fact that the local, quasi-static model does not predict any size-dependence of the LSP peak. Also shown in the figure with green lines are the cross sections for  $\epsilon_1 = 2.25$ , and we see how changing the surrounding medium can move the LSP peak in agreement with Eq. (2.40).

In this thesis we will also use the *extinction cross section*, which is defined as  $\sigma_{\text{ext}} = \sigma_{\text{abs}} + \sigma_{\text{sca}}$  and describes the total energy extracted from the incoming wave. In the quasi-static approximation, however, the extinction is identical to the absorption for a point dipole because radiation effects are not included. A remedy may be to define a radiation-corrected polarizability [63], but the full solution to Maxwell's Equations used in next chapter does not have this problem.

## Near-field measurements

The methods mentioned so far in this section are all far-field measurements i.e. the exciting field is a plane wave. A different type of probing methods used in plasmonics is near-field measurements including scanning near-field optical microscopy (SNOM), electron energy loss spectroscopy (EELS) and the coupling of emitters to the local density of states (LDOS). These methods have two advantages over far-field measurements: they can probe plasmons that do not couple to plane waves, and they allow for very high spatial resolution. Although near-field measurements will not be used in this thesis, a very brief overview of the methods is given in this section.

In a SNOM experiment (see Fig. 2.5a) a tapered fiber tip is used to excite plasmons as well as to pick up the response [64–66]. The thin tip provides a high spatial resolution as well as the extra  $k$ -value needed to couple to SPPs. Typically the optical measurement is combined with vibrations of the tip to

provide information of the topology akin to the atomic force microscopy.

EELS can be considered the by-product of transmission electron microscopy (TEM) where electrons are sent through a sample to obtain Ångstrom resolution (see Fig. 2.5b). By simultaneously recording the energy lost to excitations in the sample, it is possible to construct a detailed picture of plasmons and other resonances [67, 68]. By using EELS it is possible to obtain more detailed information about higher-order modes and bulk plasmons than far-field measurements allow [69].

In the third example of a near-field measurement, an emitter is positioned close to the metal surface (see Fig. 2.5c). The presence of the surface and especially the surface plasmon will alter the LDOS or  $\rho(\omega, \mathbf{r})$ , which in turn changes the decay rate  $\Gamma$  of the emitter according to  $\Gamma \propto \rho(\omega, \mathbf{r})$  [53, 70]. Examples of such emitters are atoms, molecules and quantum dots.



### 3 Nonlocal effects in metals

The Drude model introduced in previous chapter is widely used and has, despite its simplicity, proven its accuracy many times over. But as the sizes of the structures diminish, the Drude model loses its predictive power. It therefore becomes necessary to seek out a different or an augmented model when studying the optical response of nanoscale structures.

For very small geometries, the idea of continuous states no longer holds, and the electronic structure is rather described by discrete energy levels than bands. It is clear that the assumption of a free electron plasma loses its validity for such systems, and instead more microscopic models such as cluster theories or density functional theory should be applied [71–73]. The splitting of continuous bands into discrete levels is loosely known as *quantum size effects*, and for metals it typically sets in for structures smaller than 1 nm [71]. We will not consider this regime here, and instead we will limit ourselves to slightly larger geometries where the assumption of continuous bands is expected to be valid. For semiconductors, which are considered in next chapter, this lower size limit may need readjustment.

Even if we stay out of the regime of quantum size effects, the Drude model may still fail to describe some of the properties that are important for small structures. In particular, the Drude model is derived in the local response approximation (LRA) where the polarization at one point only depends on the electric field at exactly that point. This is a reasonable assumption for macroscopic structures, but when the geometries become comparable to the internal length scale of the electron gas, a nonlocal description has to be adopted instead.

In this chapter, we will briefly consider the Lindhard model, which implicitly includes nonlocality through its quantum mechanical derivation. We will then switch our attention to the semi-classical hydrodynamic Drude model (HDM), where a nonlocal relation between  $\mathbf{J}$  and  $\mathbf{E}$  is derived from the Boltzmann Equation. We will see how the Lindhard model and the HDM are similar on some points and different on others. The HDM will be used to obtain the optical properties of metal nanoparticles, and we will see how the predictions of the model differ from those in the LRA. While the simple description in section 2.6 predicted a LSP resonance that was independent of the particle size, we will now see how application of the HDM leads to a blueshifted resonance for smaller particles. Additionally, the full solution of Maxwell's Equations used here also gives rise to a size-dependence that was not present in the quasi-static model considered in previous chapter.

The situation may be further complicated by the presence of an ensemble of particles of different sizes. In any experiment, the sample will be described by a distribution of particles sizes, and together with the size-dependent LSP frequency, the actual measured spectrum will have a different appearance than a simple one-size model would predict. This will be the subject of the last section, which is also directly related to Publication A.

While the HDM captures important nonlocal effects such as the blueshift, its semi-classical origin means that it omits phenomena related to the single-particle properties. Especially single-particle excitations, which are known to cause size-dependent loss and therefore are important to structures on the nanoscale, are absent in the HDM. A remedy for this is the generalized nonlocal optical response (GNOR) model which also will be presented in this chapter. Being a free-electron model, the HDM also fails to include interband transitions, which are inevitable in real metals. The next section therefore presents a simple approach to account for these resonances.

### 3.1 Dielectric functions of metals

The Drude model only includes the response of the free electron gas, and especially for higher frequencies, the interband transitions have to be accounted for as well. Interband transitions include excitations of electrons from lower-lying bands to the conduction band or higher bands, and this can be modeled as bound particles in a harmonic oscillator. In this simple description, known as the Lorentz model, each interband transition is associated with a natural frequency  $\omega_j$ , an oscillator strength  $f_j$  and a damping constant  $\gamma_j$ , and the dielectric function is given by [49]

$$\varepsilon(\omega) = 1 + \sum_{j=1}^N \frac{f_j \tilde{\omega}_p^2}{\omega_j^2 - \omega^2 - i\gamma_j \omega}, \quad (3.1)$$

where  $\tilde{\omega}_p$  has an expression similar to the plasma frequency in the Drude model. In Fig. 3.1 the real and imaginary parts of a dielectric function in the Lorentz model with  $N = 3$  are shown. We here see that the imaginary part  $\varepsilon''(\omega)$  has a peak for every resonance corresponding to increased loss in the proximity of  $\omega_j$ . The real part  $\varepsilon'(\omega)$ , on the other hand, displays a staircase-like pattern where the level following a resonance is lower than before. For very high frequencies,  $\varepsilon'(\omega)$  will always go to 1, as the material is unable to respond to such fast changes in the field and therefore will behave as vacuum.

To describe real metals, the Lorentz model can be combined with the Drude model from the previous chapter such that the dielectric function will contain a term from the free-electron response plus a term from the interband

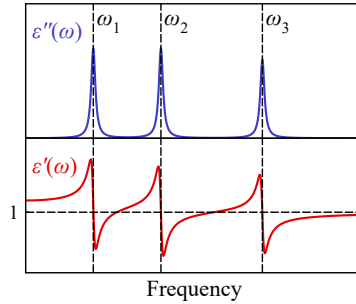


**Figure 3.1:** The Lorentz model [Eq. (3.1)] for the dielectric function with three oscillators. The blue line is the imaginary part  $\varepsilon''(\omega)$ , and the red line is the real part  $\varepsilon'(\omega)$ .

transitions. And now we see that the background dielectric function  $\varepsilon_b(\omega)$  in Eq. (2.21) actually contains the interband transitions (together with the ever-present “1”). Sometimes the background dielectric function is given the symbol  $\varepsilon_\infty$ , where ‘ $\infty$ ’ only indicates that the frequency is high enough to ignore the free-electron response (and not that the frequency actually approaches infinity).

In some cases, the background dielectric function due to interband transitions may be assumed to be constant. We see from Fig. 3.1 that this is the case for frequencies well below the first interband transition where  $\varepsilon''(\omega) \approx 0$ , and  $\varepsilon'(\omega)$  settles on a constant value. To test this hypothesis, let us consider the experimental values for the dielectric functions of gold and silver shown in Fig. 3.2. Also shown in the figures with black lines are the dielectric functions as found with the Drude model [Eq. (2.21)], where  $\varepsilon_b$  for gold and silver is set to 10 and 3.3, respectively. We see that the Drude model captures the free-electron response of the low-frequency region quite well, as expected, while the predictions for higher frequencies are less accurate. The interband transitions will give rise to absorption in the high-frequency region, and this also explains the yellow colour of gold.

To properly model the dielectric function in both the low- and high-frequency regions, one can choose to combine the Drude model (or another free-electron model) with the Lorentz model for interband transitions, but in this chapter we will use a different procedure. Because the main interest is the response of the free electrons, the interband transitions will simply be modeled by using the experimental values for the dielectric function  $\varepsilon_{\text{exp}}(\omega)$ . With this

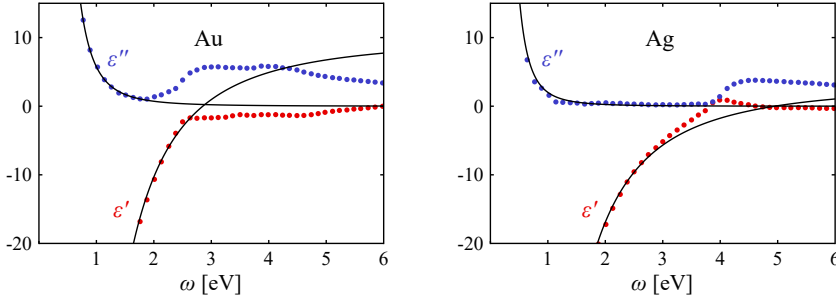


**Figure 3.2:** Dielectric functions for gold (left) and silver (right) where the real parts are shown with red dots, and the imaginary parts are shown with blue dots. The data is from Johnson and Christy [74]. The Drude dielectric function is shown with a black line. The parameters in the Drude model are  $\hbar\omega_p = 9.02$  eV,  $\hbar\gamma = 0.071$  eV and  $\varepsilon_b = 10$  for the gold and  $\hbar\omega_p = 8.99$  eV,  $\hbar\gamma = 0.025$  eV and  $\varepsilon_b = 3.3$  for silver.

method, which was also used in Ref. [75],  $\varepsilon_b(\omega)$  is given by

$$\varepsilon_b(\omega) = \varepsilon_{\text{exp}}(\omega) + \frac{\omega_p^2}{\omega^2 + i\gamma\omega}, \quad (3.2)$$

which assumes that  $\varepsilon_b$  is left when the free-electron contribution is removed from  $\varepsilon_{\text{exp}}$ . It seems like nothing is accomplished by this, since the full dielectric function as found with the Drude model will be identical to  $\varepsilon_{\text{exp}}$ . However, for the nonlocal models presented in the next sections, the free-electron response will be different from what is predicted by the Drude model. The interband part of the dielectric function for metals will thus be extracted from experimental values like those in Fig. 3.2. This also means that only the free-electron response will be treated nonlocally, while the interband transitions will be modeled with a local dielectric function.

### 3.2 Lindhard dielectric function

We will now consider a quantum mechanical model for the dielectric function of an electron gas known as the random phase approximation (RPA) or the Lindhard model [76]. The starting point is the Hamiltonian for the electron gas, but with the significant simplification that electron-electron interactions are neglected, whereby the system can be described by a sum of single-particle

Hamiltonians of the form

$$H_0 = -\frac{\hbar^2}{2m}\nabla^2 + V(\mathbf{r}). \quad (3.3)$$

The solutions to the eigenvalue problem  $H_0\psi_\alpha = E_\alpha\psi_\alpha$  are the single-particle wavefunctions  $\psi_\alpha$  with the corresponding energies  $E_\alpha$ . We will not consider any spin interaction here, and the spin degeneracy can be included simply by multiplying by 2 whenever we are counting states.

Let us now look at the situation where the electrons are influenced by an external electric field  $\mathbf{E}(\mathbf{r}, t)$ . If the field is longitudinal, it can be related to an electric potential by  $\mathbf{E} = -\nabla\phi$ , which in turn gives us the potential energy by  $U = -e\phi$ . Without loss of generality, we can assume that the dependence in time and space is harmonic (since we can always combine the fields linearly), whereby the potential energy can be written as

$$U(\mathbf{r}, t) = U_0 e^{i\mathbf{k}\cdot\mathbf{r} - i\omega t} + \text{c.c.} \quad (3.4)$$

Here 'c.c.' indicates the complex conjugate, and  $U_0 = -ieE_0/k$  (the amplitude of the electric field  $E_0$  should not be confused with the energy). Given the perturbation  $U(\mathbf{r}, t)$  to the system  $H_0$ , one can calculate the transition probability between two states  $\psi_\alpha$  and  $\psi_\beta$  using Fermi's Golden Rule and the assumption of linear response. And as shown in Appendix A, this can be used to find the longitudinal dielectric function

$$\varepsilon_L(\mathbf{k}, \omega) = 1 + \frac{2e^2}{\varepsilon_0 k^2} \frac{1}{V} \sum_{\alpha\beta} \frac{|\langle\psi_\beta|e^{i\mathbf{k}\cdot\mathbf{r}}|\psi_\alpha\rangle|^2}{E_\beta - E_\alpha - \hbar\omega - i\eta} [f(E_\alpha) - f(E_\beta)], \quad (3.5)$$

where  $V$  is the volume, and  $\eta$  is a positive infinitesimal quantity. The function  $f$  is the distribution function, or occupancy probability, and for electrons this will be equal to the Fermi-Dirac distribution. Apart from the assumptions of the non-interacting electrons and the linear dependence of the response, this is a quite general expression, and no restraints have been put on the form of the wavefunctions. We will now make the assumption that the electrons are free particles, whereby the wavefunctions become plane waves given by  $\psi_{\mathbf{k}'}(\mathbf{r}) = 1/\sqrt{V} \exp(i\mathbf{k}' \cdot \mathbf{r})$ . The consequence is that the matrix element in  $\varepsilon_L$  will be equal to unity when the excitation occurs from  $\mathbf{k}'$  to  $\mathbf{k}' + \mathbf{k}$  and zero otherwise, and we arrive at the Lindhard dielectric function

$$\varepsilon_L(\mathbf{k}, \omega) = \varepsilon_b(\omega) + \frac{2e^2}{\varepsilon_0 k^2} \frac{1}{V} \sum_{\mathbf{k}'} \frac{[f(\mathbf{k}') - f(\mathbf{k}' + \mathbf{k})]}{E(\mathbf{k}' + \mathbf{k}) - E(\mathbf{k}') - \hbar\omega - i\eta}. \quad (3.6)$$

Notice that we have allowed for the inclusion of interband transitions through

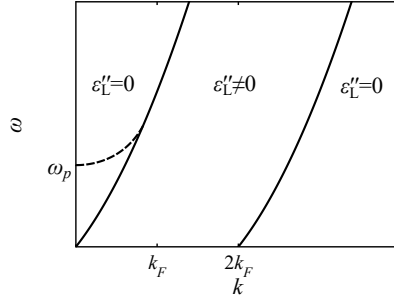


**Figure 3.3:** The Lindhard model predicts two regions in the  $k\omega$ -diagram where  $\varepsilon_L'' = 0$  separated by a region where  $\varepsilon_L'' \neq 0$ . The dispersion of the bulk plasmon is shown with a dashed line, and we see that the line crosses into the region of Landau damping.

$\varepsilon_b(\omega)$ , which is set to 1 in the typical derivation of the Lindhard dielectric function.

It is possible to evaluate an approximate expression for  $\varepsilon_L$  under the assumption that  $E(\mathbf{k}' + \mathbf{k}) - E(\mathbf{k}') \ll \hbar\omega + i\eta$ , which is fulfilled for small values of  $\mathbf{k}$ . Additionally, we will approximate the distribution function  $f$  by a step function, which is equivalent to assuming zero temperature in the Fermi-Dirac distribution. In the Supporting Information to publication B, it is shown how these assumptions allow us to derive an expression for  $\varepsilon_L$  by using a geometric series expansion. And although publication B is not in focus in this chapter, the derivation is quite general. The result is

$$\varepsilon_L(k, \omega) = \varepsilon_b(\omega) - \frac{\omega_p^2}{\omega^2 + i\gamma\omega} - \frac{\omega_p^2}{(\omega^2 + i\gamma\omega)^2} \frac{3}{5} v_F^2 k^2 - \frac{\omega_p^2}{(\omega^2 + i\gamma\omega)^2} \frac{\hbar^2}{4m^2} k^4 - \frac{\omega_p^2}{(\omega^2 + i\gamma\omega)^3} \frac{3}{7} v_F^4 k^4 - \dots, \quad (3.7)$$

where  $\omega_p$  is the plasma frequency defined in Eq. (2.22), and  $v_F$  is the Fermi velocity defined by

$$v_F = \frac{\hbar k_F}{m}, \quad (3.8)$$

with the electron mass  $m$  and the Fermi wavenumber  $k_F$ . Now we see that in the limit  $k \rightarrow 0$ , the expression for  $\varepsilon_L$  reduces to the dielectric function in the Drude model [Eq. (2.21)]. But in general, the Lindhard dielectric function is a function of the wavenumber, and this in turn means that the bulk plasmon frequency found with the condition  $\varepsilon_L(k, \omega) = 0$  will depend on  $k$ .

Although the series expansion in Eq. (3.7) will be of greatest interest here, it is possible to derive an exact, analytical expression for  $\varepsilon_L$ . Assuming zero temperature and taking the limit  $\eta \rightarrow 0$ , the evaluation of the sum in Eq. (3.6) results in [76,77]

$$\varepsilon'_L(k, \omega) = 1 + \frac{k_{\text{TF}}^2}{2k^2} + \frac{k_{\text{TF}}^2 k_F}{4k^3} \left[ (1 - x_1^2) \ln \left| \frac{x_1 + 1}{x_1 - 1} \right| + (1 - x_2^2) \ln \left| \frac{x_2 + 1}{x_2 - 1} \right| \right], \quad (3.9a)$$

$$\varepsilon''_L(k, \omega) = \frac{k_{\text{TF}}^2 k_F \pi}{4k^3} [(1 - x_1^2) \Theta(1 - x_1^2) - (1 - x_2^2) \Theta(1 - x_2^2)], \quad (3.9b)$$

where  $\varepsilon_L$  is split into real and imaginary parts and it has been assumed that  $\varepsilon_b(\omega) = 1$ . Here  $\Theta$  is the step function, and we have used the definitions

$$k_{\text{TF}}^2 = \frac{m e^2 k_F}{\varepsilon_0 \pi^2 \hbar^2}, \quad x_1 = \frac{k}{2k_F} - \frac{m\omega}{\hbar k k_F}, \quad x_2 = \frac{k}{2k_F} + \frac{m\omega}{\hbar k k_F},$$

where  $k_{\text{TF}}$  is the Thomas-Fermi screening wavenumber. In Eqs. (3.9) we have taken the limit  $\eta \rightarrow 0$ , and yet we obtain an imaginary part that is different from zero. The loss represented by  $\varepsilon''_L$  is known as Landau damping, and it is caused by dissipation of energy into single-particle excitations. Clearly this is only possible when both  $k$  and  $\omega$  are such that particles in the parabolic band can be excited from below the Fermi level to the unoccupied states above the Fermi level. This also explains the step functions in the expression for  $\varepsilon''_L$ , and we see that we must have

$$\frac{\hbar^2}{2m} (k^2 - 2kk_F) < \hbar\omega < \frac{\hbar^2}{2m} (k^2 + 2kk_F) \quad (3.10)$$

for single-particle excitations to occur. This is shown in the dispersion diagram for the dielectric function in Fig. 3.3, where two solid lines mark the boundaries for single-particle excitations and, thereby, Landau damping. Also shown in the figure, with a dashed line, is the dispersion relation for the bulk plasmon as found by solving  $\varepsilon'_L(k, \omega) = 0$ . The line has been cut off at the boundary to the  $\varepsilon''_L \neq 0$  region to indicate that the plasmon will be strongly suppressed by Landau damping there.

The Lindhard model is very simple in the sense that the electrons are assumed to be free particles modeled as plane waves, but it captures two important nonlocal, i.e.  $k$ -dependent, features that are absent in the Drude dielectric function: dispersion of the bulk plasmon resonance and nonlocal damping in the form of Landau damping. These nonlocal effects will be analysed further in the next sections. It should be mentioned that the dielectric function in

Eq. (3.7) includes classical, ohmic loss through  $\omega \rightarrow \omega + i\gamma$ , which does not fulfill particle conservation. Although we will not consider it here, this defect can be repaired by including the Mermin correction to the dielectric function [78].

### 3.3 The hydrodynamic model

The Lindhard model is (within the given assumptions) exact, but it is only valid for the infinite medium. We are therefore interested in a more practical model that allows us to find the optical response of finite structures like, for instance, spherical particles. The hydrodynamic Drude model (HDM), or simply the hydrodynamic model, is an example of such a model, and it can be thought of as either an extension of the classical Drude model or a simplification of the Lindhard model. In this section, we will consider the derivation of the HDM from the Boltzmann Equation which is the most common procedure.

#### The HDM from the Boltzmann Equation

Consider an ensemble of electrons described by the one-particle distribution function  $f(\mathbf{r}, \mathbf{p}, t)$  where  $\mathbf{r}$  is the position and  $\mathbf{p}$  is the momentum. The evolution of this function in time  $t$  is given by the Boltzmann Equation [79,80]

$$\frac{\partial f}{\partial t} + \nabla_{\mathbf{r}} f \cdot \mathbf{v} + \nabla_{\mathbf{p}} f \cdot \mathbf{F} = I_{\text{coll}}[f], \quad (3.11)$$

where  $\nabla_{\mathbf{r}}$  and  $\nabla_{\mathbf{p}}$  are the gradients in the  $\mathbf{r}$  and  $\mathbf{p}$  spaces, respectively. The particle velocity is given by  $\mathbf{v}$ , and for parabolic bands, we have the relation  $\mathbf{p} = m\mathbf{v}$  where  $m$  is the mass of the electron. The influence of the electric field on the electrons is given by  $\mathbf{F} = -e\mathbf{E}$  where  $\mathbf{F}$  is the force. On the right-hand side of Eq. (3.11) we have the collision operator  $I_{\text{coll}}$  describing the scattering of the electrons per unit of time. Often this operator is very complex and poses a serious challenge when seeking solutions to the equation. The difficulty of this operator can, however, be eliminated by invoking particle and momentum conservation.

In Appendix B it is shown how the hydrodynamic equations can be derived from Eq. (3.11) by using the following assumptions:

1. Particle and momentum are, as mentioned, conserved. While the particle conservation is trivial, the momentum conservation requires parabolic bands.
2. Magnetic forces are ignored, which is why the Lorentz force equation reduces to  $\mathbf{F} = -e\mathbf{E}$ . This is a reasonable approximation for our purposes where magnetic forces are much weaker than the electric ones.

3. The pressure tensor of the electron plasma is diagonal and given by

$$\mathbf{P} = \mathbf{I} \cdot \frac{\hbar^2(3\pi)^{2/3}}{5m} n^{5/3}, \quad (3.12)$$

where  $n$  is the electron density. More details are given Appendix B.

4. The electron density is given by  $n = n_0 + n_1$  where the induced density  $n_1$  is small compared to the equilibrium density  $n_0$ . This means that the current density can be approximated by  $\mathbf{J}_f = -en\mathbf{u} \approx -en_0\mathbf{u}$  where  $\mathbf{u}$  is the microscopically averaged value of  $\mathbf{v}$ . This average velocity is also assumed to be small such that second-order terms like  $\mathbf{u} \otimes \mathbf{u}$  can be ignored. These assumptions result in linearized versions of the hydrodynamic equations which are significantly easier to work with. For the sake of notational simplicity, we will also leave out the  $f$  indicating that we are considering free particles whereby  $\mathbf{J}_f \rightarrow \mathbf{J}$  and  $\rho_f \rightarrow \rho$ .

Under these assumptions, the linearized hydrodynamic equations are found to be

$$\frac{\partial \rho}{\partial t} = -\nabla \cdot \mathbf{J}, \quad (3.13a)$$

$$\frac{\partial^2 \mathbf{J}}{\partial t^2} = \beta^2 \nabla(\nabla \cdot \mathbf{J}) + \frac{\partial \mathbf{E}}{\partial t} \omega_p^2 \varepsilon_0, \quad (3.13b)$$

where  $\nabla \equiv \nabla_r$ . Here we immediately recognize Eq. (3.13a) as the continuity equation, which was also derived in section 2.1 directly from Maxwell's Equations. Equation (3.13b) is sometimes called the *equation of motion*, and we see that besides the plasma frequency, it also contains the parameter  $\beta$  which in Appendix B is found to be

$$\beta^2 = \frac{1}{3} v_F^2. \quad (3.14)$$

Since we will mostly be working with in the frequency domain, let us apply the temporal Fourier transform to the Eqs. (3.13) to obtain

$$i\omega \rho = \nabla \cdot \mathbf{J}, \quad (3.15a)$$

$$\frac{\beta^2}{\omega^2 + i\gamma\omega} \nabla(\nabla \cdot \mathbf{J}) + \mathbf{J} = \frac{i\omega \omega_p^2 \varepsilon_0}{\omega^2 + i\gamma\omega} \mathbf{E}, \quad (3.15b)$$

where the phenomenological damping constant  $\gamma$  also has been introduced. We have also rearranged Eq. (3.15b) a little, and now it is clear that if  $\beta = 0$ , the equation reduces to the simple relationship  $\mathbf{J} = \sigma_{\text{Drude}} \mathbf{E}$  found in the local Drude model [see Eq. (2.20)]. As we will see later, the degree of nonlocality is determined by  $\beta$ , and for this reason we will call it the *nonlocal parameter*.

### Transverse and longitudinal fields in the HDM

Equation (3.15b) provides a relation between  $\mathbf{E}$  and  $\mathbf{J}$ , but these quantities must additionally obey the wave equation derived from Maxwell's Equations. The wave equation in Eq. (2.17) in the absence of an external current density ( $\mathbf{J}_{\text{ext}} = \mathbf{0}$ ) is

$$\nabla \times \nabla \times \mathbf{E} - \frac{\omega^2}{c^2} \varepsilon_b(\omega) \mathbf{E} = i\mu_0 \omega \mathbf{J}, \quad (3.16)$$

where it has been assumed that  $\varepsilon_b$  is local. Equations (3.15b) and (3.16) can in their present state be used to find solutions for  $\mathbf{E}$  and  $\mathbf{J}$ , but in some cases it is an advantage to rewrite them a bit. Referring to section 2.4, the electric field can be separated into a transverse part  $\mathbf{E}^{\text{T}}$  and a longitudinal part  $\mathbf{E}^{\text{L}}$  which are divergence- and rotation-free, respectively. For the transverse electric field and current density, equations (3.15b) and (3.16) take the forms

$$\mathbf{J}^{\text{T}} = \frac{i\omega\omega_p^2\varepsilon_0}{\omega^2 + i\gamma\omega} \mathbf{E}^{\text{T}}, \quad (3.17a)$$

$$\nabla \times \nabla \times \mathbf{E}^{\text{T}} - \frac{\omega^2}{c^2} \varepsilon_b(\omega) \mathbf{E}^{\text{T}} = i\mu_0 \omega \mathbf{J}^{\text{T}}, \quad (3.17b)$$

where it has been used that  $\nabla \cdot \mathbf{J}^{\text{T}} = 0$ . Combining these equations to eliminate  $\mathbf{J}^{\text{T}}$  and using the general relation  $\nabla \times \nabla \times = \nabla(\nabla \cdot) - \nabla^2$  gives us

$$\nabla^2 \mathbf{E}^{\text{T}} + k_{\text{T}}^2 \mathbf{E}^{\text{T}} = \mathbf{0}, \quad (3.18)$$

where  $k_{\text{T}}$  is the transverse wavenumber given by

$$k_{\text{T}}^2 = \frac{\omega^2}{c^2} \left( \varepsilon_b(\omega) - \frac{\omega_p^2}{\omega^2 + i\gamma\omega} \right). \quad (3.19)$$

Equation (3.18) is the vector wave equation for  $\mathbf{E}^{\text{T}}$  in the HDM, and it describes the propagation of transverse electric fields with wavenumber  $k_{\text{T}}$ . The equation for  $k_{\text{T}}$  is recognized as the dispersion relation for transverse fields from Eq. (2.32) with  $\varepsilon_{\text{T}}$  being equal to the Drude dielectric function. In other words, the HDM predicts the same propagation of transverse fields as the local Drude model would.

Considering longitudinal fields, equations (3.15b) and (3.16) become

$$\frac{\beta^2}{\omega^2 + i\gamma\omega} \nabla(\nabla \cdot \mathbf{J}^{\text{L}}) + \mathbf{J}^{\text{L}} = \frac{i\omega\omega_p^2\varepsilon_0}{\omega^2 + i\gamma\omega} \mathbf{E}^{\text{L}}, \quad (3.20a)$$

$$-\frac{\omega^2}{c^2} \varepsilon_b(\omega) \mathbf{E}^{\text{L}} = i\mu_0 \omega \mathbf{J}^{\text{L}}, \quad (3.20b)$$

where it is used that  $\nabla \times \mathbf{E}^L = \mathbf{0}$ . Combining these gives us

$$\nabla^2 \mathbf{E}^L + k_L^2 \mathbf{E}^L = \mathbf{0}, \quad (3.21)$$

where  $k_L$  is the longitudinal wavenumber given by

$$k_L^2 = \frac{1}{\beta^2} \left( \omega^2 + i\gamma\omega - \frac{\omega_p^2}{\varepsilon_b(\omega)} \right). \quad (3.22)$$

Equation (3.21) describes the propagation of longitudinal fields in the HDM with wavenumber  $k_L$ . This is very different from the LRA which does not predict any propagating longitudinal waves. In the HDM it is the interaction between the electric field and the inhomogeneity of the charge carrier density that results in propagating longitudinal waves. In the “language” of the Boltzmann Equation, the inhomogeneity of  $\rho$  is caused by the pressure tensor of the electron gas given in Eq. (3.12).

### Additional boundary condition

To find the electric field, equations (3.18) and (3.21) must be supplied with the appropriate boundary conditions (BCs). As already mentioned in section 2.5, Maxwell’s Equations require that the parallel components of  $\mathbf{E}$  and  $\mathbf{B}$  are continuous across a boundary, and this is still true for the HDM. But now propagating longitudinal waves are also present, and therefore the HDM requires an additional boundary condition (ABC). Based on earlier discussions on the form of this extra condition [81–84], we will use the generally accepted ABC for a metal-dielectric interface

$$\mathbf{J}^\perp = \mathbf{0}. \quad (3.23)$$

That is, the component of the current density normal to the interface is zero, which implies that the charge cannot escape the surface of the metal. With this ABC, the equilibrium electron density  $n_0$  is assumed be a step function at the interface, which also means that *spill-out* of electrons is ignored. While this is considered a good approximation for noble metals, the correct modeling of other metals may require the inclusion of this effect [85,86].

### Dielectric functions in the HDM

The dielectric functions in the HDM can be found by transforming Eq. (3.15b) to the reciprocal space which gives us

$$-\frac{\beta^2}{\omega^2 + i\gamma\omega} \mathbf{k}(\mathbf{k} \cdot \mathbf{J}) + \mathbf{J} = \frac{i\omega\omega_p^2\varepsilon_0}{\omega^2 + i\gamma\omega} \mathbf{E}. \quad (3.24)$$

Now we can find relations between  $\mathbf{E}^T$  and  $\mathbf{J}^T$  and between  $\mathbf{E}^L$  and  $\mathbf{J}^L$  which gives us expressions for  $\sigma_T(\mathbf{k}, \omega)$  and  $\sigma_L(\mathbf{k}, \omega)$ , respectively. These can be inserted into Eq. (2.16), and we find the dielectric functions for transverse and longitudinal fields to be

$$\varepsilon_T(\omega) = \varepsilon_b(\omega) - \frac{\omega_p^2}{\omega^2 + i\gamma\omega}, \quad (3.25)$$

$$\varepsilon_L(k, \omega) = \varepsilon_b(\omega) - \frac{\omega_p^2}{\omega^2 + i\gamma\omega - \beta^2 k^2}. \quad (3.26)$$

We here notice that the longitudinal dielectric function is nonlocal, i.e. depends on  $k$ , while the transverse dielectric function is local.

### Comparison to the Lindhard model

The two models for the free electrons presented in this chapter, the Lindhard model and the HDM, both resulted in nonlocal longitudinal dielectric functions, and it therefore seems reasonable to compare them one to one. This can be done if we assume that  $\omega^2 + i\gamma\omega \gg \beta^2 k^2$  whereby  $\varepsilon_L$  in Eq. (3.26) can be expanded as a geometric series

$$\varepsilon_L(k, \omega) = \varepsilon_b(\omega) - \frac{\omega_p^2}{\omega^2 + i\gamma\omega} - \frac{\omega_p^2}{(\omega^2 + i\gamma\omega)^2} \beta^2 k^2 - \frac{\omega_p^2}{(\omega^2 + i\gamma\omega)^3} \beta^4 k^4 - \dots \quad (3.27)$$

If this equation is compared with Eq. (3.7), we see that the two expressions agree up to the third term, *provided* the nonlocal parameter  $\beta$  is given by

$$\beta^2 = \frac{3}{5} v_F^2. \quad (3.28)$$

This value is different from one in Eq. (3.14) which was derived from the expression for the pressure tensor in Eq. (3.12). It turns out that Eq. (3.14) is valid for low frequencies when  $\omega \ll \gamma$ , while Eq. (3.28) is valid for  $\omega \gg \gamma$  [87]. Halevi has furthermore derived an expression for  $\beta$  which is valid over a broader range of frequencies [88]

$$\beta^2(\omega) = \frac{\frac{3}{5}\omega + \frac{1}{3}i\gamma}{\omega + i\gamma} v_F^2, \quad (3.29)$$

where  $\beta$  is now complex-valued. For plasmonics, however, it is mainly the  $\omega \gg \gamma$  region that is of interest, and we will therefore only use the high-frequency limit for  $\beta$  given in Eq. (3.28).

### 3.4 Nonlocal damping

The comparison of Eqs. (3.27) and (3.7) shows that the HDM can be thought of as the lowest-order approximation to the Lindhard model that still includes nonlocality. However, the HDM fails to capture nonlocal damping in the form of Landau damping, which was “lost” when the expansion in Eq. (3.7) was performed. To introduce nonlocal damping into the HDM, a model has been developed which allows for a complex  $\beta$ . The model has been coined the generalized nonlocal optical response (GNOR) model, and it considers the incorporation of diffusion into the continuity equation [89]. The equation obtained is the (linearized) convection-diffusion equation

$$-\frac{\partial \rho}{\partial t} = D \nabla^2 \rho + \nabla \cdot (en_0 \mathbf{u}) = -\nabla \cdot \mathbf{J}, \quad (3.30)$$

where  $D$  is the diffusion constant. Using this expression, the hydrodynamic equation of motion becomes [89]

$$\left( \frac{\beta^2}{\omega^2 + i\gamma\omega} + \frac{D}{i\omega} \right) \nabla(\nabla \cdot \mathbf{J}) + \mathbf{J} = \frac{i\omega\omega_p^2\varepsilon_0}{\omega^2 + i\gamma\omega} \mathbf{E}, \quad (3.31)$$

and we see that it has exactly the same form as Eq. (3.15b), provided the nonlocal parameter  $\beta$  is replaced by

$$\eta^2 = \beta^2 + D(\gamma - i\omega). \quad (3.32)$$

Because the GNOR model only differs from the HDM in the value of the nonlocal parameter, it is a simple matter to include nonlocal damping in the calculations if the HDM is already implemented. However, the problem of finding a value for  $D$  still remains. In this thesis where the focus is on spherical particles, we will deduce the value by comparing the GNOR model with data from experiments, where it has been found that the damping depends on the size of the particle [90–92]. To include this effect for spherical particles, it was proposed by Kreibig and co-workers that a size-dependent term should be added to the damping constant [93]

$$\gamma' = \gamma + A \frac{v_F}{R}, \quad (3.33)$$

where  $v_F$  is the Fermi velocity, and  $R$  is the radius. The model, which is called the Kreibig model or the size-dependent damping (SDD) model, relates the damping to scattering of electrons on the surface of the particle, and the parameter  $A$  is a measure of the degree of this scattering. Such a size-dependent

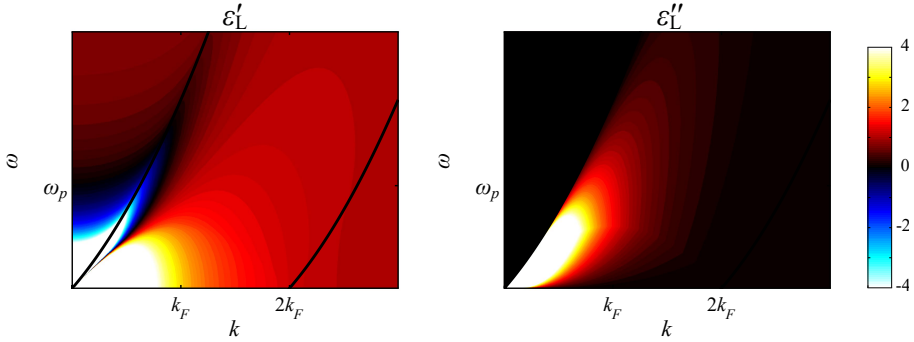


**Figure 3.4:** The dielectric function in the Lindhard model as found with Eqs. (3.9a) and (3.9b). The values  $\hbar\omega_p = 9$  eV and  $\varepsilon_b = 1$  where used. The thick black lines mark the boundaries to the region with Landau damping and are given by Eq. (3.10).

damping is also predicted by the GNOR model, where it emerges as a non-local effect: the “smallness” of the particle gives the additional  $k$ -component, and because of the complex parameter  $\eta$ , this shows up as damping. By comparing the two models, the following relation is found between  $D$  and  $A$  [94]

$$D = \frac{6}{\sqrt{10}} \frac{v_F^2}{\omega_p} A. \quad (3.34)$$

Even though it seems like the difficulty of obtaining  $D$  only has been shifted to another parameter, the advantage of Eq. (3.34) is that information on the value of  $A$  has already been made available through experimental measurements and theoretical calculations [90,95,96]. In general these studies predict a value in the order of unity, and for simplicity we will therefore use  $A = 1$  in the rest of the chapter. Apart from providing more physical insight, the GNOR model also has the advantage that it can be applied to any geometry, while the Kreibig model is limited to spherical particles. Moreover, the GNOR model includes  $k$ -dependent dispersion of the bulk plasmon which is absent in the local Kreibig model.

The nonlocal damping in the form of diffusion in the GNOR model is conceptually different from the Landau damping predicted by the Lindhard model. Yet the two models may give the same predictions for certain situations. As an example, let us consider the simple case of an infinite bulk material, which is a geometry where both models are applicable. Starting with the Lindhard

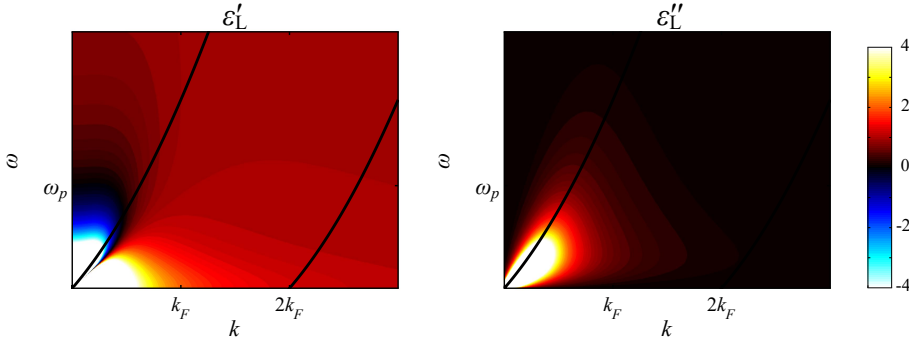


**Figure 3.5:** The dielectric function in the GNOR model as found with Eqs. (3.26), (3.28), (3.32) and (3.34). The values  $\hbar\omega_p = 9 \text{ eV}$ ,  $\gamma = 0.001\omega_p$ ,  $\varepsilon_b = 1$  and  $A = 1$  where used.

model, we will use Eqs. (3.9a) and (3.9b) to plot the real and imaginary part, respectively, of the dielectric function as contours in the momentum-frequency space. These contours are shown in Fig. 3.4, where we used  $\hbar\omega_p = 9 \text{ eV}$ ,  $\varepsilon_b = 1$  and  $k_F^3 = 3\pi^2 n$ . Here we see in the left figure that the real part  $\varepsilon'_L$  is zero (indicated with black) exactly at the plasmon dispersion which is consistent with the  $\varepsilon_L = 0$  definition of longitudinal excitations (the dispersion was also shown in Fig. 3.3). Upon entering the region with Landau damping, the plasmon dispersion is cut off, and this corresponds well with the imaginary part  $\varepsilon''_L$  (in the right figure) being different from zero in this very region.

Consider now the same contour plots for the GNOR model shown in Fig. 3.5. Here the real and imaginary parts were found with Eq. (3.26) where  $\beta$  was replaced by  $\eta$  from Eq. (3.32), and the values  $\gamma = 0.001\omega_p$  and  $A = 1$  were used together with Eqs.(3.34) and (3.28). We here see roughly the same tendencies: the dispersion of the plasmon is cut off upon entering the region with damping, and  $\varepsilon''_L$  is different from zero in only a restricted region of the momentum-frequency space. The primary difference from the Lindhard model is that the contours in the GNOR model are more “smeared out”, which is expected as the model does not directly include the single-particle excitations. As mentioned, the loss mechanisms in the two models are fundamentally different, but Figs. 3.4 and 3.5 indicate that the models predict losses of approximately same magnitude. The GNOR model, furthermore, has the advantage of being applicable for finite geometries such as the spherical particles considered in the next sections.

### 3.5 Mie theory

One of the few finite structures that Maxwell's Equations can be solved for analytically is a spherical particle. This was originally done by Mie [55], and the formalism used here is similar to the one in Ref. [97]. The goal is to find solutions to the vector wave equations in Eqs. (3.18) and (3.21), which both have the form

$$\nabla^2 \mathbf{E} + k^2 \mathbf{E} = \mathbf{0}, \quad (3.35)$$

where  $k$  is the wavenumber. First step is to solve the simpler scalar wave equation

$$\nabla^2 \psi + k^2 \psi = 0, \quad (3.36)$$

which can be solved in spherical coordinates by the method of separation of variables.<sup>1</sup> The solution is [50,97]

$$\psi_{e_{ml}}(\mathbf{r}, t) = \frac{\cos(m\phi)}{\sin(m\phi)} P_l^m(\cos\theta) z_l(kr) e^{-i\omega t}, \quad (3.37)$$

where  $r$ ,  $\theta$  and  $\phi$  are coordinates in spherical geometry, 'e' and 'o' are shorthand notation for even and odd, and  $l$  and  $m$  are integers which fulfill  $l \geq m$ . The function  $P_l^m$  is the associated Legendre polynomial, and  $z_l$  is the spherical Bessel function. A harmonic time dependence has been included in Eq. (3.37), but it is clear that this will cancel out when inserted into Eq. (3.36).

It can now be shown that the solutions to Eq. (3.35) are given by [97]

$$\mathbf{L} = \nabla \psi, \quad \mathbf{M} = \nabla \times (\mathbf{r}\psi), \quad \mathbf{N} = \frac{1}{k} \nabla \times \mathbf{M}, \quad (3.38)$$

which are known as vector wave functions. The function  $\mathbf{L}$  is purely longitudinal (since it is a gradient of a scalar function), while  $\mathbf{M}$  and  $\mathbf{N}$  are purely transverse. This also means that the solutions to the longitudinal wave function [Eq. (3.21)] will only include functions of the form  $\mathbf{L}$ , and the solutions to the transverse wave function [Eq. (3.18)] only contain  $\mathbf{M}$  and  $\mathbf{N}$  functions.

In the following we will use the notation  $\mathbf{L} = \mathbf{l}e^{-i\omega t}$  (and the same for  $\mathbf{M}$  and  $\mathbf{N}$ ) where the lowercase versions are the wave functions without time dependence. The  $\mathbf{l}_{e_{ml}}$ ,  $\mathbf{m}_{e_{ml}}$  and  $\mathbf{n}_{e_{ml}}$  functions constitute a complete basis, which means that any field can be written as a superposition of these [97]. Let us consider the case of a plane wave that is traveling in a dielectric medium without spatial dispersion whereby the field will be purely transverse. If the wave is propagating in the  $z$ -direction with the electric field polarized in the

<sup>1</sup>Note that the operator  $\nabla^2$  has two different meanings in the scalar and vector wave equation. In the scalar equation it is the usual Laplacian defined as the divergence of the gradient. In the vector equation it is rather defined as  $\nabla^2 = \nabla(\nabla \cdot) - \nabla \times \nabla \times$ . For Cartesian coordinates, however, the vector Laplacian is simply the scalar Laplacian multiplied with the identity matrix.

$x$ -direction, then it can be expanded in spherical vector wave functions according to [97]

$$\begin{aligned} \mathbf{E}_i(\mathbf{r}, t) &= E_0 e^{ik_D z - i\omega t} \hat{\mathbf{x}} \\ &= E_0 e^{-i\omega t} \sum_{l=1}^{\infty} i^l \frac{2l+1}{l(l+1)} \left( \mathbf{m}_{o1l}^{(1)}(k_D, \mathbf{r}) - i\mathbf{n}_{e1l}^{(1)}(k_D, \mathbf{r}) \right), \end{aligned} \quad (3.39)$$

where  $k_D = \sqrt{\varepsilon_D} \omega / c$  is the wavenumber of the dielectric medium. Notice that the expansion only contains functions of the form  $\mathbf{m}_{o1l}$  and  $\mathbf{n}_{e1l}$ , which is a result of the symmetry of the problem. The superscript '(1)' indicates that contained spherical Bessel functions are of the first kind  $j_l$ . Note that the magnetic field can easily be found by using Ampere's Law [Eq. (2.1c)].

The scenario which is of primary interest in this thesis is the one where the incident wave  $\mathbf{E}_i$  is scattered by a spherical particle located at  $\mathbf{r} = \mathbf{0}$  resulting in a reflected field  $\mathbf{E}_r$  and a transmitted field  $\mathbf{E}_t$  (i.e. transmitted into the particle). The reflected field will have the same overall form as  $\mathbf{E}_i$

$$\mathbf{E}_r(\mathbf{r}, t) = E_0 e^{-i\omega t} \sum_{l=1}^{\infty} i^l \frac{2l+1}{l(l+1)} \left( a_l^r \mathbf{m}_{o1l}^{(3)}(k_D, \mathbf{r}) - i b_l^r \mathbf{n}_{e1l}^{(3)}(k_D, \mathbf{r}) \right), \quad (3.40)$$

where  $a_l^r$  and  $b_l^r$  are reflection coefficients, and the superscript '(3)' indicates that the contained spherical Bessel functions are Hankel functions of the first kind  $h_l^{(1)}$ . Now, if the material of the particle had been without spatial dispersion, then the transmitted field would be given by an expression similar to Eq. (3.39). This was originally considered by Mie [55], and later Ruppin added the longitudinal component needed to describe a spatially dispersive material [98, 99]. Including the longitudinal field in the expansion, the transmitted field becomes

$$\begin{aligned} \mathbf{E}_t(\mathbf{r}, t) &= E_0 e^{-i\omega t} \sum_{l=1}^{\infty} i^l \frac{2l+1}{l(l+1)} \left( a_l^t \mathbf{m}_{o1l}^{(1)}(k_T, \mathbf{r}) \right. \\ &\quad \left. - i b_l^t \mathbf{n}_{e1l}^{(1)}(k_T, \mathbf{r}) + c_l^t \mathbf{l}_{e1l}^{(1)}(k_L, \mathbf{r}) \right), \end{aligned} \quad (3.41)$$

where  $a_l^t$ ,  $b_l^t$  and  $c_l^t$  are the transmission coefficients. The wavenumbers  $k_T$  and  $k_L$  are in the HDM given by Eqs. (3.19) and (3.22), respectively.

The task is now to determine the expansion coefficients, which is done by matching the fields at the radius  $R$  of the particle according to the boundary conditions (BCs). Apart from the standard BCs in Eqs. (2.33), we also need an additional boundary condition (ABC), which is particularly obvious from Eq. (3.41): because the longitudinal fields add an extra set of unknowns  $c_l^t$ , we also need an extra BC. Based on the discussion in section 3.3, we will use

the condition  $\mathbf{J}^\perp = \mathbf{0}$  (which is different from the ABC used by Ruppin [99]). By application of the BCs we obtain the system of equations in Appendix C from which the coefficients are easily found. Of primary interest are  $a_l^r$  and  $b_l^r$  known as the *Mie coefficients*, and they are given by

$$a_l^r = \frac{-j_l(x_D)[x_T j_l(x_T)]' + j_l(x_T)[x_D j_l(x_D)]'}{h_l^{(1)}(x_D)[x_T j_l(x_T)]' - j_l(x_T)[x_D h_l^{(1)}(x_D)]'}, \quad (3.42a)$$

$$b_l^r = \frac{-\varepsilon_D j_l(x_D) (\Delta_l + [x_T j_l(x_T)]') + \varepsilon_T j_l(x_T) [x_D j_l(x_D)]'}{\varepsilon_D h_l^{(1)}(x_D) (\Delta_l + [x_T j_l(x_T)]') - \varepsilon_T j_l(x_T) [x_D h_l^{(1)}(x_D)]'}, \quad (3.42b)$$

where  $x_D = Rk_D$  and  $x_T = Rk_T$ . The differentiation (denoted with the prime) is with respect to the argument. The  $a_l^r$  coefficients are related to oscillations of the magnetic type, while the  $b_l^r$  coefficients are related to oscillations of the electric type. The parameter  $\Delta_l$  is given by

$$\Delta_l = \frac{j_l(x_T) j_l(x_L) l(l+1)}{x_L j_l'(x_L)} \left( \frac{\varepsilon_T}{\varepsilon_\infty} - 1 \right), \quad (3.43)$$

and this contains the nonlocal response. In particular, if  $\Delta_l = 0$  then equation (3.42b) for the  $b_l^r$  coefficients reduces to the expression found in the classical Mie solution without spatial dispersion [97]. Meanwhile, the  $a_l^r$  coefficients are given by the classical solution regardless of  $\Delta_l$ , which reflects the fact that oscillations of the magnetic type do not couple to longitudinal waves.

The Mie-coefficients are of practical significance because they can be used to find the absorption, scattering and extinction cross sections directly. The scattering and extinction cross sections are given by [97]

$$\sigma_{\text{sca}} = \frac{2\pi}{k_D^2} \sum_{l=1} (2l+1) (|a_l^r|^2 + |b_l^r|^2), \quad (3.44a)$$

$$\sigma_{\text{ext}} = -\frac{2\pi}{k_D^2} \sum_{l=1} (2l+1) \text{Re}(a_l^r + b_l^r), \quad (3.44b)$$

and the absorption cross section can be found with  $\sigma_{\text{abs}} = \sigma_{\text{ext}} - \sigma_{\text{sca}}$ . Often the cross sections will be normalized with the geometric cross section  $\sigma_{\text{geom}} = \pi R^2$  to obtain a dimensionless quantity.

### 3.6 Nonlocal effects in spherical nanoparticles

When the Mie-coefficients have been determined, we can find  $\sigma_{\text{abs}}$ ,  $\sigma_{\text{ext}}$ , and  $\sigma_{\text{sca}}$  from Eqs. (3.44). In this section, we will consider some of the characteristic features in the spectra of nanoparticles, and we will see the impact

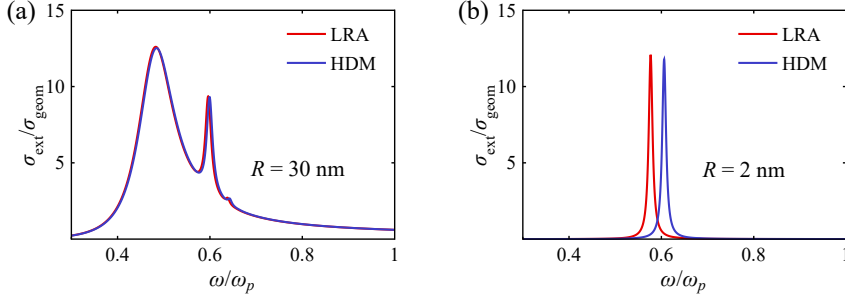


**Figure 3.6:** Extinction spectra for a spherical nanoparticle as found with the LRA model (red line) and the HDM (blue line). The radius of the particle is (a) 30 nm and (b) 2 nm.

of including nonlocality in the model. It should be mentioned that the spectra for spherical particles as found with the HDM already have been analysed in several papers using Mie theory [69, 100] or the simpler quasi-static model [101, 102]. However, the spectra demonstrate some important optical features of the HDM which will be analysed further in section 3.7 where the results of Publication A are presented. The spectra will also serve as precursors to the results of the next chapters.

### Ideal metal particles

Let us consider a material with the parameters  $\hbar\omega_p = 9 \text{ eV}$ ,  $\gamma = 0.01\omega_p$ ,  $v_F = 1.39 \times 10^6 \text{ m/s}$  and  $\varepsilon_b = 1$ . If we now have a spherical particle of this material with  $R = 30 \text{ nm}$  surrounded by vacuum ( $\varepsilon_D = 1$ ), we can find the Mie-coefficients with Eqs. (3.42) and (3.43) and the extinction cross section with Eq. (3.44b). The result is shown in Fig. 3.6a, where  $\sigma_{\text{ext}}$  has been normalized with  $\sigma_{\text{geom}}$ . Here the blue line is the spectrum predicted by the HDM, while the red line is the result in the LRA (the Drude model) obtained by setting  $\Delta_l = 0$  in Eq. (3.42b). The two models predict almost exactly the same result: a large, wide peak to the left followed by two narrower and smaller ones. The large peak is the dipole LSP resonance, which is also predicted by the quasi-static model [see Fig. 2.4b]. The next two peaks are the quadrupole and the octupole LSP resonances, respectively, and they are not present in the simple quasi-static model where the external field is completely homogeneous (they are, however, present in an extended multipolar quasi-static model [103]). Although we only see the quadrupole and octupole modes in Fig. 3.6a, an infinite series of higher-order modes exists as given by the sum in Eq. (3.44b)

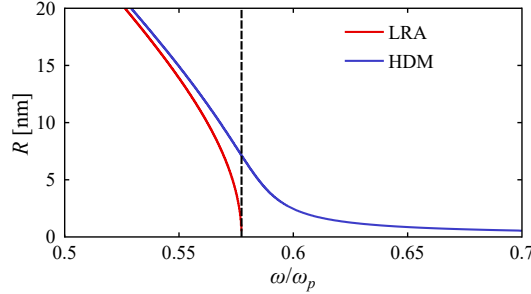


**Figure 3.7:** The spectral position of the dipole LSP resonance as a function of particle radius. The red line is the Drude model, and the blue line is the HDM. The dashed black line is the position predicted by the local, quasi-static model where there is no size-dependence of the resonance.

(the calculation here includes orders up to  $l = 16$ ). These higher-order modes become more visible by considering larger particles or, alternatively, by using a near-field measurement as described in Ref. [69].

In Fig. 3.6b are the extinction spectra shown for a particle of the same material, but with  $R = 2$  nm. One of the most apparent differences here compared to Fig. 3.6a is the absence of any visible higher-order modes, which is a consequence of the particle being much smaller than the wavelength of the field. Another striking difference is the shift of the dipole peak in the HDM compared to the LRA. This blueshift is a characteristic nonlocal effect, and it has been analysed in several papers [69, 75, 100, 101] and measured experimentally [4, 102, 104, 105]. It is caused by the surface plasmon penetrating into the bulk of particle, which will have larger relative impact as the size is reduced. Although we will not study it here, nonlocal response will also affect the optical properties of nanometer gaps between plasmonic structures such as dimers [19, 106, 107].

Apart from the nonlocal blueshift of the dipole peak in the HDM, the peaks for both models in Fig. 3.6b are located at higher frequencies compared to Fig. 3.6a. This is known as a retardation effect, whereby the finite speed of light causes a delay in the electromagnetic interaction between different parts of the particle. As the size of the particle is increased, this effect becomes more important, resulting in a redshift as a function of particle size. To analyse the combined effect of retardation and nonlocal blueshift, the spectral position of the dipole LSP is plotted as a function of radius in Fig. 3.7. Here we see that the HDM predicts a strongly blueshifted peak position as the particle size is

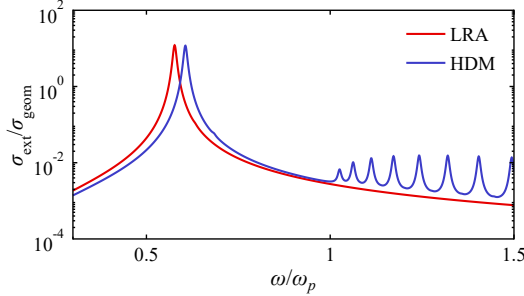


**Figure 3.8:** Extinction spectrum for a particle with  $R = 2$  nm in a semi-logarithmic coordinate system. The red line is the LRA, and the blue line is the HDM.

reduced. The LRA, on the other hand, predicts a peak position that converges towards the local, quasi-static limit  $\omega_p/\sqrt{3}$  (shown in the figure with a dashed, black line). For large particles, we see how the retardation effect results in a redshift for both the LRA and HDM.

Another characteristic nonlocal feature in the HDM is seen in Fig. 3.8 where the extinction spectrum for the 2 nm particle is plotted with logarithmic  $y$ -axis. Here additional peaks have appeared above  $\omega_p$  which are absent in the LRA. These are confined bulk plasmons, and they are a result of the fact that the HDM allows for the existence of propagating longitudinal waves which become standing waves in a confined structure. The confined bulk plasmons have been analysed theoretically [69,101,108] as well as measured experimentally [7,13,109–111].

## Realistic metal particles

Bulk plasmons are an interesting nonlocal phenomenon and certainly one that deserves more experimental investigation. However, the model from which the spectrum in Fig. 3.8 is derived includes neither the interband transitions described in section 3.1 nor the nonlocal damping described in section 3.4. Both of these effects are expected to be present in real metals, and they will result a significant damping of the bulk plasmons and the LSP.

To investigate this, let us first consider the inclusion of interband transitions with the aid of experimentally measured dielectric functions, as described in section 3.1. We will consider a gold particle of radius  $R = 2$  nm with the material parameters  $\hbar\omega_p = 9.02$  eV,  $\hbar\gamma = 0.071$  eV and  $v_F = 1.39 \times 10^6$  m/s and the experimental dielectric function  $\varepsilon_{\text{exp}}$  from Ref. [74]. From these parameters we obtain the extinction spectra in Fig. 3.9a, and we here see the huge impact

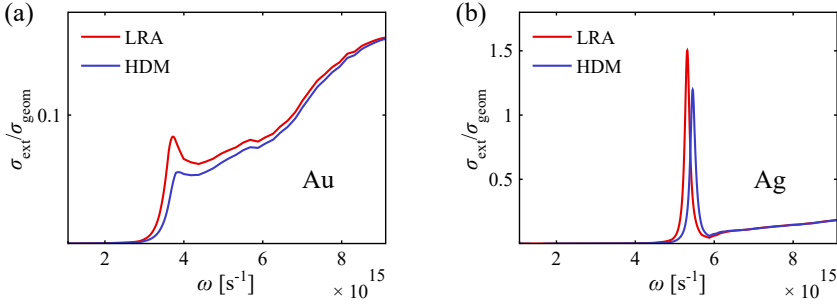


**Figure 3.9:** Extinction spectra for a spherical nanoparticle with  $R = 2$  nm as found with the Drude model (red line) and the HDM (blue line) for (a) gold and (b) silver.

that interband transitions have on the optical response. The high-frequency region of the spectrum is completely dominated by interband effects, and the dipole LSP peak has experienced strong damping. From the spectrum it is also clear that bulk plasmon resonances are unlikely to be measured in gold nanoparticles. The situation looks slightly better for the spectrum of a silver nanoparticle ( $\hbar\omega_p = 8.99$  eV,  $\hbar\gamma = 0.025$  eV and  $v_F = 1.39 \times 10^6$  m/s) shown in Fig. 3.9b, where the interband transitions are less interfering.

Let us now look at the effect of nonlocal damping on plasmon resonances (while leaving interband transitions out for clarity). In Fig. 3.10, the extinction spectrum is shown for a particle with the same parameters as in Fig. 3.6b. Together with the LRA and HDM are also the spectra predicted by the SDD and GNOR models, where  $A = 1$  is used, and  $D$  is found by Eq. (3.34). Here it is clear how the size-dependent damping results in broader peaks of less amplitude. The SDD model predicts a broadening of the peak, but because it is a local model, the spectral position is (almost) the same as in the LRA. The GNOR model, on the other hand, includes both the size-dependent broadening as well as the nonlocal blueshift from the HDM. The figure focuses on the region around the dipole LSP, but it is clear that the nonlocal damping will significantly weaken the bulk plasmons (if there is anything left from the interband loss).

The combined effect of nonlocal blueshift and damping, owing to real and imaginary parts of the nonlocal parameter, has been investigated for the dipole LSP in Ref. [89]. The authors found that the complex solution  $\omega' + i\omega''$  to

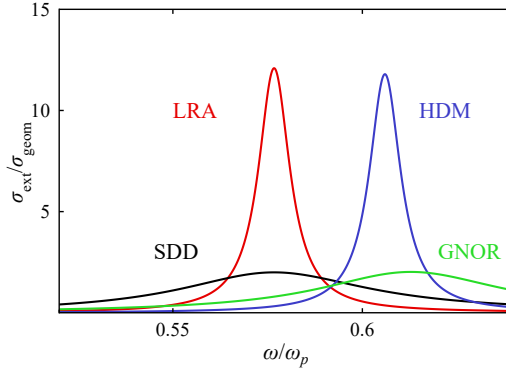


**Figure 3.10:** The extinction spectra of the LRA, SDD model, HDM and GNOR model. The parameters are  $\hbar\omega_p = 9 \text{ eV}$ ,  $\gamma = 0.01\omega_p$ ,  $v_F = 1.39 \times 10^6 \text{ m/s}$ ,  $\varepsilon_b = 1$ ,  $A = 1$  and  $R = 2 \text{ nm}$ .

the Fröhlich condition (see section 2.6) to first order in  $1/R$  is given by

$$\omega' = \frac{\omega_p}{\sqrt{3}} + \frac{\beta}{\sqrt{2}R}, \quad (3.45a)$$

$$\omega'' = -\frac{\gamma}{2} - \frac{D\omega_p}{4\sqrt{6}\beta R}, \quad (3.45b)$$

where it has been assumed that  $\varepsilon_D = \varepsilon_b = 1$ . From the real part we see how the blueshift to first order in  $1/R$  is proportional to  $\beta$ , while the imaginary part, which is related to the linewidth, has a size-dependent term proportional to  $D$ . Notice also that for the HDM where  $D = 0$ , the damping is independent of size as expected.

### 3.7 Inhomogeneous broadening

The ohmic loss included phenomenologically in the Drude model with  $\gamma$  and the size-dependent damping described by the Kreibig and GNOR model are both *homogeneous* broadening mechanisms, i.e. they depend on intrinsic properties of the materials. In this section we will investigate an *inhomogeneous* broadening mechanism which is the result of a distribution of particle sizes in an ensemble together with a size-dependent resonance frequency. The different spectral positions of the resonance peaks will effectively show up as a broadening of the peak when measuring on the ensemble. Inhomogeneous broadening will obviously be relevant for experimentalists since the spectrum

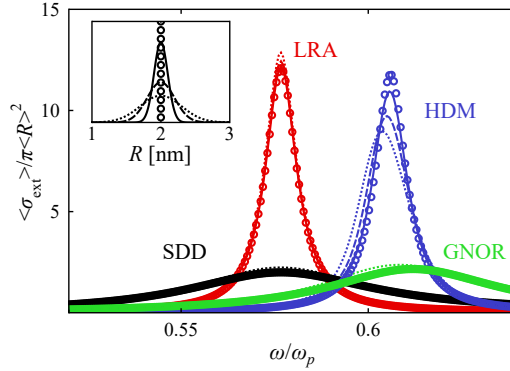


**Figure 3.11:** Averaged extinction spectra for the LRA (red), HDM (blue), SDD model (black) and GNOR model (green). The spectra were found with a delta-function distribution as well as Gaussian distributions with standard deviations of 0.1 nm, 0.2 nm and 0.3 nm (see distributions in inset). The average particle radius is in all cases  $\langle R \rangle = 2$  nm.

from a distribution of particle sizes may look very different from what they would expect from a model with only a single particle size.

To investigate the effect of inhomogeneous broadening, let us consider an ensemble of metal nanoparticles with the same parameters as in Fig. 3.10. The particles will have different radii, and we will assume that the distribution is described by a Gaussian distribution

$$f(R) = \frac{1}{\sqrt{2\pi\sigma^2}} \exp\left(-\frac{(R - \langle R \rangle)^2}{2\sigma^2}\right), \quad (3.46)$$

where  $\langle R \rangle$  is the average radius, and  $\sigma$  is the standard deviation (not to be confused with the cross section).<sup>1</sup> We will use an average radius of  $\langle R \rangle = 2$  nm and consider three different standard deviations of 0.1 nm, 0.2 nm and 0.3 nm. The extinction spectra for the different radii in the distribution are then weighted with the function  $f(R)$  and added together to obtain an averaged spectrum. The spectra will be normalized with  $\pi \langle R \rangle^2$  instead of the individual radii to avoid distortions of the averaged spectrum.

<sup>1</sup>Note that the normalization factor  $1/\sqrt{2\pi\sigma^2}$  is derived for a distribution extending from  $-\infty$  to  $\infty$ . Obviously, we will not consider particles with negative radii which means that the actual distribution is truncated at  $R = 0$ . If the distribution is sufficiently narrow, however, the normalization in Eq. (3.46) will be a good approximation

In Fig. 3.11, the averaged spectra for the LRA, HDM, SDD model and GNOR model are shown for the three standard deviations (the distributions are also shown in the inset). The homogeneous case (corresponding to a delta-function distribution) is also shown with open circles. Here we see the effect of inhomogeneous broadening most clearly for the HDM where the peak becomes broader and loses amplitude as the distribution becomes wider. We also see a small redshift of the peak which is caused by the fact that the biggest particles in the distribution at the same time have a less blueshifted resonance and a larger extinction cross section. For the LRA there is almost no inhomogeneous broadening, although this potentially could exist as a result of the included retardation effects (see also Refs. [112, 113]). In fact we see that the peak is increasing very slightly as the distribution becomes wider. This is a result of including bigger particles with a larger  $\sigma_{\text{ext}}$  while still normalizing with the average radius.

The HDM spectra in Fig. 3.11 suggest that inhomogeneous effects will be important for ensembles of metal particles. The redshift of the peak will also be relevant for a very specific type of experiment: if one wishes to investigate the nonlocal blueshift of nanoparticles, the redshift of the resonance peak would give rise to an incorrect interpretation of the results if inhomogeneous broadening is not accounted for.

The situation looks quite different, however, when size-dependent damping is included in the model. This is seen from the SDD and GNOR models in Fig. 3.11, where the homogeneous broadening completely overshadows any effect of the ensemble average. Since size-dependent damping and inhomogeneous broadening are expected to be relevant for the same group of particles, i.e. small particles, the conclusion is that for the parameters considered here, inhomogeneous broadening can be ignored when analysing spectra from an ensemble of particles.

In addition to size-dependent damping, real metals will also contain interband transitions which will further reduce the significance of inhomogeneous broadening. This is analysed in Fig. 3 in Publication A, where the average extinction spectra for the LRA, HDM and GNOR model are shown for silver nanoparticles. The dielectric function was derived in the same way as in Fig. 3.9b in the previous section and using same data from Ref. [74]. From this we see that homogeneous broadening completely dominates the optical response for all three models, and the spectra for the distribution of particles are indistinguishable from the homogeneous ones (shown with open circles). Note that Fig. 3 in Publication A uses an average radius of 2.15 nm deduced from an actual experimental particle distribution (shown in the inset).

Although inhomogeneous broadening has been shown to have negligible

impact on the far-field response, it can still be of interest to look at the problem analytically. In particular we will be interested in finding an expression for the part of the width caused by inhomogeneous broadening,  $\Delta\omega_{\text{inhom}}$ . To make the derivation simple, we will neglect homogeneous broadening, which is the same as assuming that the spectrum is a delta function

$$F(\omega, R) = \delta(\omega - \omega_{\text{LSP}}(R)), \quad (3.47)$$

where  $\omega_{\text{LSP}}(R)$  is the size-dependent peak position. Given the discussions in this section, this is clearly a crude approximation, but the result can still be useful for situations where inhomogeneous, and not homogeneous, broadening dominates.

Define now the inhomogeneous broadening as  $\Delta\omega_{\text{inhom}} = \sqrt{\langle\omega^2\rangle - \langle\omega\rangle^2}$ , where the moments are given by

$$\begin{aligned} \langle\omega^n\rangle &= \int d\omega \omega^n \langle F(\omega) \rangle = \int d\omega \omega^n \int dR F(\omega, R) P(R) \\ &= \int dR (\omega - \omega_{\text{LSP}}(R))^n P(R), \end{aligned} \quad (3.48)$$

where  $P(R)$  is the distribution function. As an approximate expression for  $\omega_{\text{LSP}}(R)$ , we can use the one given in Eq. (3.45a). In publication A and the accompanying Supplementary Information, it is shown how this results in

$$\Delta\omega_{\text{inhom}} = \beta \sqrt{\langle R^{-2} \rangle - \langle R^{-1} \rangle^2}. \quad (3.49)$$

As examples, let us consider the Gaussian distribution given by Eq. (3.46) as well as a triangular and a uniform distribution (see Fig. 3.12). Using Eq. (3.49) we find the following approximate results for  $\Delta\omega_{\text{inhom}}$  (see Supplementary Information for Publication A)

$$\text{Gaussian: } \Delta\omega_{\text{inhom}} \approx \frac{\beta\sigma}{R_0^2}, \quad (3.50a)$$

$$\text{Triangular: } \Delta\omega_{\text{inhom}} \approx \frac{\beta\delta R}{\sqrt{24}R_0^2}, \quad (3.50b)$$

$$\text{Uniform: } \Delta\omega_{\text{inhom}} \approx \frac{\beta\delta R}{\sqrt{12}R_0^2}, \quad (3.50c)$$

where  $R_0 = \langle R \rangle$  is the center of the distribution, and  $\delta R$  is the width of the triangular and uniform distributions.

To test these expressions, the averaged extinction spectrum is simulated for the three distributions for various values of  $\sigma$  and  $\delta R$  using the HDM (which

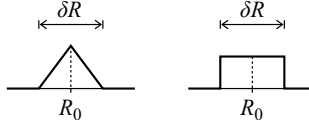


**Figure 3.12:** Sketches of the triangular and uniform distributions.

was the only model that predicted any significant inhomogeneous broadening). The full width at half maximum (FWHM) is then calculated and plotted against  $\Delta\omega_{\text{inhom}}$  as found with Eqs. (3.50). This is shown in Fig. 5 in Publication A, and for all three distributions there is a nearly linear relation between  $\Delta\omega_{\text{inhom}}$  and the FWHM. This shows the usefulness of Eq. (3.49) despite the approximations leading to the expression.

The conclusion for this section is that the nonlocal blueshift together with a distribution of particle sizes indeed result in inhomogeneous broadening of the LSP peak in the averaged spectrum. For the materials considered here, however, this broadening is completely insignificant when nonlocal damping and interband transitions are included in the model. The experimentalist can, in other words, safely analyse the extinction spectrum based on the average particle size alone. For a different material with less loss and another value for  $\beta$ , the impact of inhomogeneous broadening may have to be reconsidered.



## 4 Nonlocal effects in semiconductors

In previous chapter, we analyzed the optical response of metal particles. And due to their large density of free electrons, metals are by far the most common plasmonic materials. But other kinds of materials may also contain a free-electron plasma capable of sustaining collective excitations, and in this chapter we will analyse the plasmonic properties of semiconductors.

The free-electron plasma in semiconductors may originate from doping or from excitation of valence band electrons to the conduction band. Doping is the process by which impurities are added to the semiconductor creating either a partially filled conduction band or a partially filled valence band, and doped semiconductors can obtain densities of free charges up to  $10^{21} \text{ cm}^{-3}$  [114]. Intrinsic semiconductors without doping will also have a naturally occurring density of charge carriers originating from the thermal excitation of electrons from the valence band to the conduction band. This density will typically be very small, except for semiconductors with very narrow band gaps, where we may see densities in the order of  $10^{16} \text{ cm}^{-3}$ . Alternatively, external sources such as laser pulses can be used to excite electrons from the valence band to the conduction band, which is a process that can be applied to semiconductors with wide gaps as well.

In any case, the density of free charge carriers is expected to be smaller than in metals where typical values are in the order of  $10^{22} \text{ cm}^{-3}$ . As a consequence of this, the plasma frequency will also be smaller, since  $\omega_p \propto n^{1/2}$ , and this will in turn shift all the spectral features from the visible to the infrared (IR) spectrum. Plasmonic resonances in the IR may have technological advantages on its own [41, 44, 115], but it may also be a path to new experiments in nonlocal phenomena [116]: as the characteristic wavelength of the system increases, so does the size of the structures, which will make fabrication easier.

Another advantage of using semiconductors in plasmonics instead of metals is the tunability. While metals have a fixed electron density, semiconductors can be doped to a very wide range of electron and hole densities [41, 114]. Furthermore, semiconductors allow for dynamic tuning of the optical properties through temperature control [117, 118], external bias [119–121] or laser excitation [122].

In this chapter we will analyse the plasmonic properties of semiconductor particles, and in particular we will be interested in the nonlocal effects. Since the models presented in previous chapter were developed for a general free-electron plasma, we would expect them to be applicable to semiconductors with a few modifications. We will consider various semiconductor materials

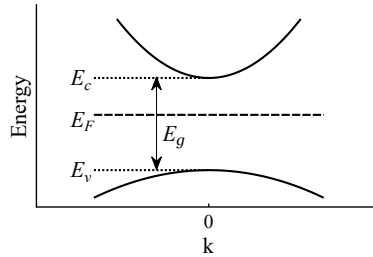


**Figure 4.1:** A simplified model of the band structure in semiconductors.

as well as different methods for obtaining the necessary density of free charge carriers, and we will see how this affects the optical response and the nonlocal effects. The discussions in this chapter are related to Publication B, with sections 4.4-4.6 presenting the results of the paper.

One of the primary complications of semiconductors compared to metals is the possible existence of several different kinds of charge carriers. While the only free charge carriers in metals are electrons, semiconductors may contain electrons and holes or light and heavy holes. We will in this chapter assume that effectively only one type of charge carrier is present and return to the difficulty of including multiple plasmas in next chapter. In this chapter, we will also leave out interband transitions and excitons (a special type of excitation characteristic for semiconductors) and focus on the optical response of the free charge carriers. The legitimacy of these omissions will be given in section 4.2, while the next section will present the fundamental concepts of semiconductors.

## 4.1 Concepts of semiconductors

Semiconductor physics is a broad and comprehensive field, which cannot be covered here (see instead Refs. [123–125] for some excellent guides in the field). However, a brief overview of the concepts of semiconductors seems in place, and this will also allow us to introduce some of the parameters used in this chapter.

### The band structure

The difference between metals and semiconductors is found in the band structure which is sketched in Fig. 4.1. In this simplified picture, we have only two bands of allowed states, the valence band and conduction band, which are

separated by the band gap  $E_g$  of forbidden energies. The bands are assumed to be perfectly parabolic and isotropic, and this allow us to write the dispersions as

$$\text{Conduction band: } E(k) = E_c + \frac{\hbar^2 k^2}{2m_e^*}, \quad (4.1a)$$

$$\text{Valence band: } E(k) = E_v - \frac{\hbar^2 k^2}{2m_h^*}, \quad (4.1b)$$

where  $E_c$  is the conduction band minimum, and  $E_v$  is valence band maximum. The effective masses of electrons and holes are given by  $m_e^*$  and  $m_h^*$ , respectively, and they are related to the curvature of the band through  $m^* = \hbar^2(\partial^2 E/\partial k^2)^{-1}$ .

The Fermi energy  $E_F$ , which marks the highest occupied level at 0 K, is located inside conduction band for metals, and this results in a free electron plasma even at low temperature. For semiconductors,  $E_F$  is situated inside the band gap resulting in an empty conduction band and a fully occupied valence band at 0 K, and this is the cause of the poor electrical conductivity of pure semiconductors.

The assumption of perfectly parabolic and isotropic bands described by a scalar  $m^*$  is of course artificial, and in real semiconductors the situation is more complex. This is clear from the band structures for gallium arsenide (GaAs) and indium antimonide (InSb) shown in Fig. 4.2. For both materials, the conduction band minimum and the valence band maximum are located at the  $\Gamma$  point (see the Brillouin zone Fig. 4.2), and we see that the bands only are truly parabolic at the extrema. We also see that they are anisotropic, i.e. the curvature and the effective mass depend on the direction in the reciprocal space.

To model the anisotropy, the scalar effective mass can be replaced by a tensor, but we will use a simpler approach where an average effective mass is derived. The average effective mass, however, is different for calculations of the density of states and calculations of the transport properties. The density-of-states effective mass and conductivity effective mass are given by [123]

$$m_{\text{dens}}^* \equiv m^* = (m_1^* m_2^* m_3^*)^{\frac{1}{3}}, \quad (4.2a)$$

$$m_{\text{cond}}^* = 3 \left( \frac{1}{m_1^*} + \frac{1}{m_2^*} + \frac{1}{m_3^*} \right)^{-1}, \quad (4.2b)$$

where  $m_1^*$ ,  $m_2^*$  and  $m_3^*$  are the effective masses along the principle axes of the geometry.

In the band structures in Fig. 4.2, we see that the valence band actually is

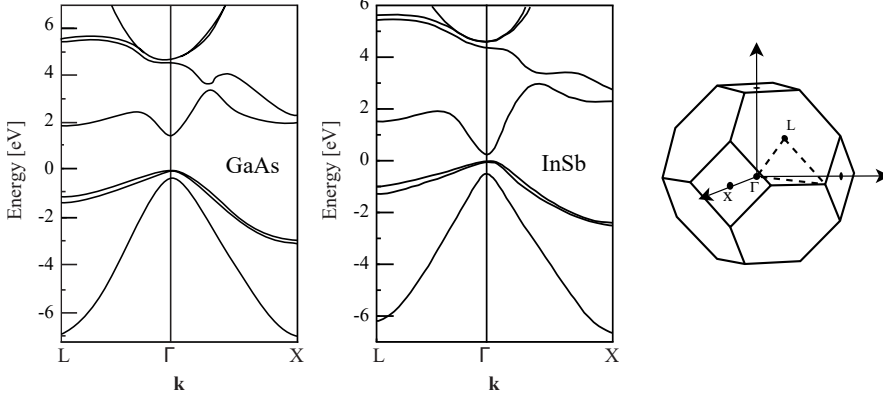


**Figure 4.2:** The band structures for GaAs and InSb with data from Ref. [126]. Also shown is the Brillouin zone for the face-centered cubic lattice, which is the geometry for GaAs and InSb.

comprised of two bands corresponding to heavy and light holes, where the light hole band has a sharper curvature (the bands are very close together). We also see the split-off band located about 0.3 eV further below, but we will not consider this band here. The light and heavy hole bands are degenerate at  $\Gamma$ , but can have very different curvatures or, equivalently, different masses  $m_{lh}^*$  and  $m_{hh}^*$ . Similar to what is done in the case of anisotropy, we can calculate average effective masses for the valence band. The density-of-states and conductivity effective masses for holes are given by [123, 127]

$$m_h^* = \left( m_{lh}^{*\frac{3}{2}} + m_{hh}^{*\frac{3}{2}} \right)^{\frac{2}{3}}, \quad (4.3a)$$

$$m_{h,\text{cond}}^* = \frac{m_{lh}^{*\frac{3}{2}} + m_{hh}^{*\frac{3}{2}}}{m_{lh}^{*\frac{1}{2}} + m_{hh}^{*\frac{1}{2}}}. \quad (4.3b)$$

Note that the simple equations for the dispersions in Eqs. (4.1) use the density-of-states effective masses.

The non-parabolic shape of the bands will give rise to an effective mass that depends on doping and temperature. And although there are models that account for non-parabolic bands [128], other effects will have impact on the

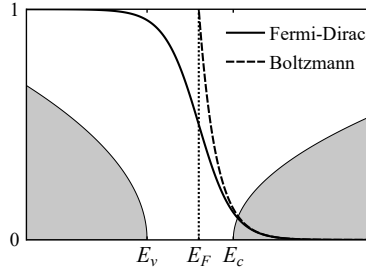


**Figure 4.3:** The Fermi-Dirac distribution (solid line) coincides with the Boltzmann distribution (dashed line) for energies above  $E_c$ . Also shown in the figure is the Fermi energy (dotted line) and sketches of the density of states for the valence and conduction band (grey areas).

effective masses such as temperature dilation of the lattice and increased impurity scattering. We will not try to model all of these complications, and instead we will simply use the best and most suitable experimental or numerical data for  $m^*$  and  $m_{\text{cond}}^*$ , if necessary calculated with Eqs. (4.2) and (4.3).

### Intrinsic semiconductors

For intrinsic semiconductors, the density of free charge carriers originates from thermal excitation of electrons across the band gap. The distribution of the electrons in the bands is given by the Fermi-Dirac function

$$f(E) = \frac{1}{e^{\frac{E-E_F}{k_B T}} + 1}, \quad (4.4)$$

where  $k_B$  is the Boltzmann constant, and  $T$  is the temperature. The distribution is shown in Fig. 4.3. To find the density of electrons in the conduction band  $n_e$ , the occupation probability  $f(E)$  is combined with the density of states of the conduction band [123]

$$g_c(E) = \frac{(2m_e^*)^{\frac{3}{2}}}{2\pi^2\hbar^3} \sqrt{E - E_c}, \quad (4.5)$$

where  $m_e^*$  is the density-of-states effective mass. The expression is derived from the parabolic band structure given in Eq. (4.1a) together with the fact that the volume in reciprocal space taken up by a single state is  $(2\pi)^3/V$ , where  $V$  is total volume in real space. The density  $n_e$  can then be found with

$$n_e = \int_{E_c}^{\infty} g_c(E) f(E) dE. \quad (4.6)$$

Although choosing infinity as the upper bound is artificial, the distribution  $f(E)$  will in practice cut off the integration at low energies. In the simple band structure in Fig. 4.1, the situation is completely symmetric for the conduction and valence bands. This means that the density of holes in the valence band can be found with a similar equation, except that now the distribution  $[1 - f(E)]$  is used instead of  $f(E)$ .

If we are in the conduction band ( $E > E_c$ ), and the temperature is sufficiently low, we can assume that  $E - E_F \gg k_B T$ . In this case, the Fermi-Dirac distribution in Eq. (4.4) can be approximated by the Boltzmann distribution

$$f(E) \approx e^{-\frac{E-E_F}{k_B T}}, \quad (4.7)$$

which is also sketched in Fig. 4.3. A similar argument can be made for the valence band. With this approximation it is possible to evaluate the integrals for  $n_e$  and  $n_h$ , and by invoking charge neutrality,  $n_e = n_h$ , one finds the following expression for the charge carrier densities [123]

$$n_e = n_h = 2 \left( \frac{2\pi k_B T}{h^2} \right)^{\frac{3}{2}} m_e^{*\frac{3}{4}} m_h^{*\frac{3}{4}} \exp\left(\frac{-E_g}{2k_B T}\right). \quad (4.8)$$

## Doped semiconductors

while the electron and hole densities in intrinsic semiconductors typically will be relatively low, doped semiconductors allow for controllable high densities. By adding donor or acceptor atoms to the host semiconductor, discrete energy levels develop inside the band gap. For  $n$ -doping, the donor energy level is located close to the conduction band, and thermal energy allows electrons to be excited to the conduction band to form a density of free electrons  $n_e$  (see Fig. 4.4). In a similar way,  $p$ -doping gives rise to a density of holes  $n_h$  in the valence band.

The position of the donor and acceptor levels in the band gap depends in a complex manner on the impurity atoms and the host semiconductor [129]. For room temperature, however, it is often reasonable to assume that the acceptor and donor atoms have been completely ionized. We will assume that this is the case for our calculations, which means that the majority carrier densities are given by  $n_e = N_d$  for donor concentrations  $N_d$  and  $n_h = N_a$  for acceptor concentrations  $N_a$ . For both  $n$ - and  $p$ -doped materials, the minority carrier concentration in thermal equilibrium can be found by the simple relation  $n_{\text{int}}^2 = n_e n_h$ , where  $n_{\text{int}}$  is the charge carrier density for the intrinsic material [123]

While doping allows us to reach electron and hole concentrations that are much larger than in intrinsic semiconductors, the densities are still limited by

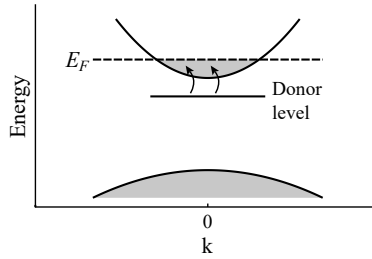


**Figure 4.4:** For  $n$ -doped semiconductors, donor atoms will give rise to a density of electrons in the conduction band. The Fermi level is located inside the conduction band for  $n$ -doped materials.

several factors. One mechanism is doping compensation whereby impurity atoms start behaving as both  $p$ -type and  $n$ -type dopants, and further doping will effectively result in a lower charge carrier density [130]. For very high doping concentrations, the solid solubility of the dopants will also be an upper limit [131].

### Transport properties

When an electric field is applied to the semiconductor, the electrons will experience a force equal to  $-e\mathbf{E}$ . The electrons will not increase their speed indefinitely, but will eventually collide with the atoms whereby they lose their energy. If the average time between collisions is  $\tau$ , one can find the average drift velocity of the electrons to be

$$\mathbf{u}_e = -\frac{1}{m_{e,\text{cond}}^*} \tau e \mathbf{E} = -\mu_e \mathbf{E}, \quad (4.9)$$

where  $m_{e,\text{cond}}^*$  is the conductivity effective mass, and  $\mu_e$  is known as the mobility of the electrons. The drift velocity for holes is given by a similar equation.

The mean propagation time  $\tau$  is primarily affected by two different scattering mechanisms. *Lattice scattering* is caused by thermal vibration of the lattice atoms, and this will lead to reduction of  $\tau$  in any semiconductor above absolute zero. The effect obviously becomes more significant as the temperature is increased, and it has been found that the dependence of the mobility on temperature roughly is  $T^{-3/2}$  [123]. *Impurity scattering* is the result of the ionized dopant atoms affecting the electrons and holes through the Coulomb force, and this process becomes more prominent as the doping concentration is increased. On the other hand is the effect reduced for higher temperatures, where the thermal energy of the charge carriers allows them to escape the

Coulomb attraction of the impurity atoms.

Because the damping constant is related to the propagation time by  $\gamma = 1/\tau$ , equation (4.9) allows us to write [132]

$$\gamma_i = \frac{e}{\mu_i m_{i,\text{cond}}^*}, \quad (4.10)$$

where  $i = e, h$ . The advantage of this equation is that  $\gamma_i$  can be used directly in the Drude model or the HDM from previous chapters, while  $\mu_i$  usually can be found in semiconductor data tables. As a result of lattice and impurity scattering, we naturally expect  $\mu_i$  to depend on temperature and doping [133]. But often will  $m_{i,\text{cond}}^*$  also depend on doping, which is partially explained the non-parabolic bands giving a different curvature as the Fermi level changes [134,135]. The effective mass may also depend on temperature due to dilation of the lattice [136].

## 4.2 Interband transitions, excitons, phonons and quantum size effects

While interband transitions can have a serious impact on the plasmonic resonances in metal particles (as we saw in previous chapter), the situation is expected to be different for semiconductors. The shift of the spectral features to lower frequencies also moves the plasmonic resonances away from interband transitions. This means that as long as the energies considered are less than  $E_g$ , it is safe to assume that interband transitions can be captured by a frequency independent  $\varepsilon_b$ . This constant can typically be found in data tables.

Another type of excitation which is characteristic of semiconductors is *excitons*, which are caused by electron-hole pairs bound to each other by the Coulomb force. Because they are more tightly bound than free electrons and holes in the conduction and valence bands, respectively, the energy level of the exciton is lower than  $E_c$  by the binding energy  $E_{\text{bind}}$ . Excitons can be described by a hydrogen model where the hole plays the role of the nucleus, and this model is able to predict the discrete levels inside the band gap [137]. In the model, one has to account for the electric screening of the hole and electron caused by the dielectric background which weakens the binding energy. Especially semiconductors with narrow band gaps have larger screening, and excitons can therefore be ignored for these materials. Also doped semiconductors will have a significant screening effect due to the high density of free charge carriers. Since the focus in this chapter will be on these two groups of semiconductors, it is reasonable to ignore excitons for our purposes.

Semiconductors may also support phonons, and especially non-elemental

materials may contain optical phonons that can interact with the electromagnetic radiation. The phonon resonances are typically located in the infrared spectrum [138], and because of this, they may interact with the plasmons [139–142]. For simplicity we will not include phonons in the calculations here, but they can be included in the dielectric function with a Lorentz oscillator model as is done in, for example, reference 140.

When considering the optical response of nanoscale semiconductor particles, quantum size effects (QSE) such as those that are found in quantum dots are expected to be relevant. The degree of discretization can be estimated from a particle-in-a-box model where the distance between the energy levels can be found as the inverse of the average density of states without spin [71]:  $\Delta E = 2\hbar^2\pi^2/(m^*V)/(3\pi^2n)^{1/3}$ . QSE become significant when  $\Delta E$  is comparable to the thermal energy  $k_B T$ , which for a metal particle at room temperature with  $V = 4\pi R^3/3$  happens for  $R \approx 1$  nm. For semiconductors, where  $n$  and  $m^*$  typically are smaller than for metals, these effects start to occur at  $R \approx 10$  nm (and at cryogenic temperature, for even larger particles [143]). To stay out of the QSE regime, semiconductors are therefore more restrictive than metals.

Since we intend to use a plasma model for the semiconductors (the LRA or HDM), we also have to ensure that the particle contains sufficient free charge carriers to be considered a plasma. Although there is no clear boundary, it seems obvious that a semiconductor particle containing less than 1 electron on average is poorly modeled with a plasma model. We will therefore choose a lower limit for our model of 50 free charge carriers per particle.

### 4.3 Materials and fabrication

Due to its application in microchips and electrical circuits, silicon (Si) is one the most widely used semiconductors. It can be  $n$ -doped with group V elements like phosphorous and arsenic and  $p$ -doped with group III elements such as boron and gallium. It allows for doping concentrations as high as  $10^{21}$  cm $^{-3}$  before it is limited by the solid solubility [149], and plasmonics in Si has been shown for both  $n$ - and  $p$ -doping [150–154]. Plasmonic devices based on Si also have the advantage of being compatible with existing CMOS technology [155]. However, the mobility of Si is relatively low (see Table 4.1), and this will result in higher loss and smearing out of spectral features.

Based on the mobility, GaAs seems to be a better choice for plasmonics. GaAs can be  $n$ -doped with Si to concentrations of  $10^{19}$  cm $^{-3}$  where doping compensation starts being a limitation [156]. It can also be  $p$ -doped with carbon (C) or beryllium (Be) to concentrations of  $10^{21}$  cm $^{-3}$  [157]. Bulk plasmons have been observed in both  $n$ -doped [158–160] and  $p$ -doped [161, 162] GaAs

**Table 4.1:** The material parameters for various semiconductors. The mass  $m_e^*$  for Si is from Ref. [144]. The masses  $m_e^*$  and  $m_{hh}^*$  for InSb are taken from Refs. [136] and [145], respectively. For GaAs,  $m_e^*$  and  $m_{e,\text{cond}}^*$  (which depends on the doping level  $N_d$ ) are from Ref. [135], and  $m_{ih}^*$  and  $m_{hh}^*$  are from Ref. [146].  $E_g$  for InSb is taken from Ref. [147], and  $\mu_e$  and  $\mu_h$  for GaAs are from Ref. [133]. The rest of the data are taken from Ref. [148]. Note that for InSb and ZnO, the value of  $m_{e,\text{cond}}^*$  is assumed to be identical to  $m_e^*$ . All values are for 300 K except the last column and values marked with \*.

	Si	GaAs	ZnO	InSb (300 K)	InSb (400 K)
$\varepsilon_\infty$	11.97	10.86	3.72	15.68	15.68
$E_g$ (eV)	1.124	1.424	3.44*	0.174	0.146
$\mu_e$ (cm <sup>2</sup> V <sup>-1</sup> s <sup>-1</sup> )	1450	7000 <sup>a</sup> 2900 <sup>c</sup>	20 <sup>d</sup>	77000	48000
$\mu_h$ (cm <sup>2</sup> V <sup>-1</sup> s <sup>-1</sup> )	370	400 <sup>a</sup> 190 <sup>c</sup>	—	850	480
$m_e^*/m_0$	1.18	0.0636	0.275 <sup>b*</sup>	0.0115	0.0100
$m_{e,\text{cond}}^*/m_0$	0.43	0.0636 <sup>a</sup> 0.0695 <sup>c</sup>	0.275 <sup>b*</sup>	0.0115	0.0100
$m_{ih}^*/m_0$	0.153*	0.093	—	0.016*	0.016*
$m_{hh}^*/m_0$	0.59*	0.50	0.59*	0.37	0.40

<sup>a</sup>  $N_d = 0$  cm<sup>-3</sup>      <sup>c</sup>  $N_d = 10^{18}$  cm<sup>-3</sup>      \*  $T \approx 4$  K

<sup>b</sup>  $N_d = 10^{17}$  cm<sup>-3</sup>      <sup>d</sup>  $N_d = 5 \cdot 10^{19}$  cm<sup>-3</sup>

using EELS. Plasmon resonances have also been observed in other III-V semiconductors [163–165].

Another group of semiconductors suitable for plasmonics is transparent conducting oxides (TCOs). This group includes indium tin oxide (ITO), aluminum-doped zinc oxide (AZO) and indium-doped cadmium oxide (In:CdO), and one of the advantages of these materials is the possibility to obtain very high doping levels [41, 166]. Plasmons have been observed in ITO [120, 121, 167–170], AZO [171–173] and In:CdO [122, 174] as well as other TCOs [175–180].

Plasmonics has also been studied for transition metal chalcogenides such as copper sulfide (Cu<sub>2-x</sub>S) [181, 182]. These materials are not doped by adding impurities, but instead obtain intrinsic doping through the stoichiometric composition. Other semiconductors in this group like Cu<sub>2-x</sub>Se and Cu<sub>2-x</sub>Te have also been shown to support plasmons [42, 183, 184].

While doped semiconductors are the most obvious choice for plasmonic materials, intrinsic semiconductors may also contain a relatively large density of

thermally excited charge carriers if the band gap is narrow enough. An example of such a material is InSb which has a band gap of  $E_g \approx 0.17$  eV (the band structure is shown in Fig. 4.2). Plasmonic resonances have already been observed in intrinsic InSb [116, 118, 185–187].

The fabrication methods for doped and intrinsic semiconductors, either thin film or particles, are diverse and numerous. Doped semiconductors can, for instance, be fabricated by diffusion [188], ion-implantation [152, 189] or molecular beam epitaxy [165, 190]. TCO films are typically grown by laser ablation, sputtering or chemical vapor deposition [41, 191], while nanoparticles can be synthesized by e.g. flame spray pyrolysis [192]. Various liquid phase chemical methods can be used to synthesize copper chalcogenide nanoparticles [181, 183, 184, 193] and InSb nanoparticles [194]. Nanoparticles of various semiconductor materials can also be fabricated by laser ablation [195, 196].

## 4.4 The nonlocal parameter

The models presented in chapter 2 and 3 are valid for a general free-particle plasma. This means that once values for the parameters  $\omega_p$ ,  $\gamma$  and  $\beta$  have been determined, the expressions derived for the Mie-coefficients and the extinction cross section can be applied directly to semiconductors. In this section we will therefore present expressions for these parameters. The results in this section and the next two are directly related to Publication B.

The damping constant  $\gamma$  is given by Eq. (4.10), where  $\mu$  and  $m_{\text{cond}}^*$  are found in data tables. The plasma frequency is given by exactly the same equation as for metals, except that the free electron mass is replaced by the density-of-states effective mass to account for the curvature of the band

$$\omega_p^2 = \frac{e^2 n}{\varepsilon_0 m^*}. \quad (4.11)$$

The charge carrier density  $n$  is assumed to be identical to  $N_d$  or  $N_a$  for doped semiconductors, while it is given by Eq. (4.8) for intrinsic semiconductors. For intrinsic semiconductors there will always be a density of holes identical to the electron density (due to charge conservation), but in this chapter we will only include the electron density in the calculation of the optical response of intrinsic semiconductors. The argument is that  $m_h^*$  typically is larger than  $m_e^*$ , which results in a smaller plasma frequency for the holes compared to the electrons. The consequence of this is that electrons dominate the optical properties, and the holes, as a reasonable approximation, can be neglected. In the next chapter, we will analyse the effect of including both electrons and holes in the optical response.

The expression for  $\beta$  in doped semiconductors will, apart from the effective mass, be identical to the one for metals

$$\beta^2 = \frac{3}{5} \frac{\hbar^2 k_F^2}{m^{*2}}, \quad (\text{Doped}) \quad (4.12)$$

where  $k_F^3 = 3\pi^2 n$  (see e.g. Eq. (S7) in the Supporting Information to Publication B). This expression assumes, similar to the case of metals, that the distribution function of the electrons is a step function.

For intrinsic semiconductors with thermally excited electrons, the equation for  $\beta$  is different. It is possible to derive a simple expression if the temperature is low enough for the Boltzmann distribution to be used instead of the Fermi-Dirac distribution, and in the Supporting Information to Publication B, the expression is found to be

$$\beta^2 = \frac{3k_B T}{m^*}. \quad (\text{Intrinsic}) \quad (4.13)$$

For temperatures where the Boltzmann distribution is a poor approximation, the value of  $\beta$  can still be found numerically.

## 4.5 Blueshift of the LSP resonance

With the parameters at hand we are ready to calculate the optical properties of semiconductors. We will choose to focus on spherical particles which allows us to use Eqs. (3.42) and (3.43) for the Mie-coefficients and Eq. (3.44b) for the extinction cross section from previous chapter.

The first material we will consider is GaAs doped with a donor concentration of  $N_d = 10^{18} \text{ cm}^{-3}$ . Using the material parameters given in Table 4.1 together with Eqs. (4.10)-(4.12) we find  $\omega_p = 2.24 \times 10^{14} \text{ s}^{-1}$ ,  $\beta = 4.36 \times 10^5 \text{ m/s}$  and  $\gamma = 8.72 \times 10^{12} \text{ s}^{-1}$ . From the plasma frequency we already see that the plasmon resonances will be found in the infrared ( $\lambda_p = 8.41 \mu\text{m}$ ), which is different from metal particles studied in previous chapter where the LSP resonance occurred in the visible spectrum.

If the radius of the GaAs particle is  $R = 40 \text{ nm}$ , and it is surrounded by vacuum ( $\varepsilon_D = 1$ ), we get the extinction spectra in Fig. 4.5a. The figure shows the spectra for both the LRA and the HDM, where the local result (dashed, red line) is obtained by setting  $\Delta_l = 0$  in Eq. (3.42b). As we saw for metals, the dipole LSP resonance is blueshifted in the HDM compared to the LRA. But if we compare with, for example, the extinction spectra for a 2 nm silver particle in Fig. 3.9b, we see that the relative blueshift is larger for the GaAs particle. This is a surprising result given the much larger radius of the GaAs particle and the inverse relationship between the nonlocal blueshift and  $R$  [see

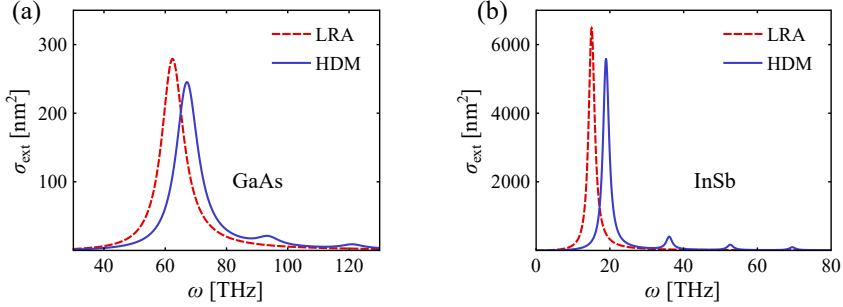


**Figure 4.5:** (a) The extinction spectra for an  $n$ -doped GaAs particle with  $N_d = 10^{18} \text{ cm}^{-3}$ ,  $R = 40 \text{ nm}$  and  $\varepsilon_D = 1$ . (b) The extinction spectra for an intrinsic InSb particle at 300 K with  $R = 200 \text{ nm}$  and  $\varepsilon_D = 1$ . The large peaks are the dipole LSP (for both the LRA and the HDM), and the small peaks are confined bulk plasmons (only for the HDM).

Eq. (3.45a)]. Also the confined bulk plasmon resonances above the LSP peak are clearly visible in Fig. 4.5a, while a semi-logarithmic plot had to be used to reveal them in metals [see Fig. 3.8].

The primary explanation for the larger nonlocal blueshift in GaAs is the lower charge carrier density. According to Eq. (3.45a), the blueshift in the HDM is proportional to  $\beta$  which in turn depends on  $n^{1/3}$  [see Eq. (4.12)]. At the same time, the plasma frequency is according to Eq. (4.11) proportional to  $n^{1/2}$ . This means that although the absolute blueshift  $\Delta\omega$  will depend on  $n^{1/3}$ , the relative blueshift defined as  $\Delta\omega/\omega_p$  will be proportional to  $n^{-1/6}$ . Another reason for the increased blueshift in GaAs is the effective mass. From Eqs. (4.11) and (4.12) one finds that  $\Delta\omega/\omega_p$  is proportional to  $m^{*-1/2}$ . The smaller electron effective mass typically found in semiconductors therefore also contributes to the relative blueshift.

The strong nonlocal effects are also found in other types of semiconductors. In Fig. 4.5b are the extinction spectra shown for an intrinsic InSb particle with thermally excited charge carriers. As mentioned before, only the electrons are included in the calculation. The temperature is set to 300 K, and despite a radius of 200 nm, the blueshift of the LSP peak is even more pronounced than for the GaAs particle. This is caused by a smaller effective mass in InSb (see Table 4.1) as well as a different expression for  $\beta$  [see Eq. (4.13)]. The bulk plasmon peaks are also clearer which is a result of a higher mobility of the electrons in InSb compared to GaAs.

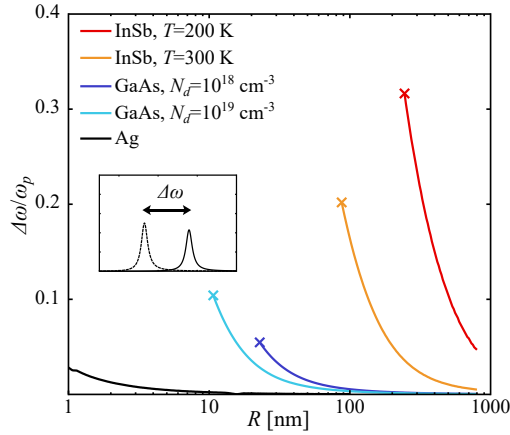


**Figure 4.6:** The relative blueshift of the LSP resonance for  $n$ -doped GaAs, intrinsic InSb and silver. The  $x$ 's at the end of the lines mark the size where the total number of free charge carriers in the particle is 50 (which was the chosen lower limit). This point occurs for silver at a radius smaller than 1 nm.

To investigate the blueshift in semiconductors further, the relative value  $\Delta\omega/\omega_p$  is plotted as a function of radius in Fig. 4.6 for different materials. The blue lines show the blueshift for GaAs particles with two different doping concentrations. The relative blueshift increases for smaller particles, which is expected from the  $1/R$  dependence in Eq. (3.45a). We also see that for particles of equal size, the blueshift is larger for lower doping. The largest relative blueshifts in the figure are obtained by the intrinsic InSb particles, and especially by the particles at 200 K. However, if one wishes to measure the blueshift experimentally, the amplitude also play a role. And while lower temperature in intrinsic semiconductors and lower dopant concentration in doped semiconductors give stronger blueshift, the amplitude will also be reduced.

Also shown in the figure with a black line is the blueshift in silver particles. This calculation uses the same parameters as Fig. 3.9b in previous chapter. Here we clearly see how the relative blueshift is much smaller for silver and occurs for very small particles. Keep in mind, though, that the *absolute* blueshift is still larger in silver particles.

The discovery that nonlocal blueshifts occur in larger particles for semiconductors than for metals can be used specifically in experimental investigations of nonlocal effects. Larger particles will simplify the fabrication process, and

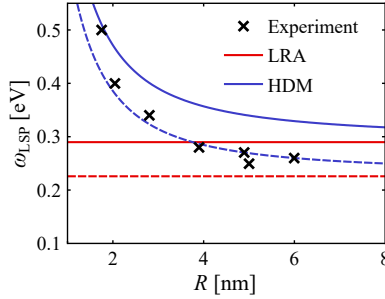


**Figure 4.7:** The spectral position for the dipole LSP resonance in  $n$ -doped ZnO nanoparticles as a function of radius. The experimental data is from Schimpf *et al.* [178]. The solid lines use the electron density  $n = 1.4 \times 10^{20} \text{ cm}^{-3}$  from [178], while the dashed lines use  $n = 0.85 \times 10^{20} \text{ cm}^{-3}$ .

a more pronounced blueshift will give clearer measurements.

The large amount of experimental data available from the literature allows us to compare the predictions of the HDM with actual measurements of semiconductor nanoparticles. One set of data relevant for our discussions here was published by Schimpf *et al.* [178] who measured the absorbance of doped zinc oxide (ZnO) particles with radii in the range 1.75 to 6 nm. The ZnO particles were photodoped, a process whereby UV radiation creates charge carriers in an otherwise intrinsic semiconductor.

In Fig. 4.7 is the measured peak position of the dipole LSP shown as a function of radius, and we see a clear blueshift for smaller particles. Also shown in the figure is the peak position as found with the LRA and the HDM (solid red and blue line, respectively). These curves were found using the data for ZnO in Table 4.1 together with an electron density of  $n = 1.4 \times 10^{20} \text{ cm}^{-3}$  that Schimpf *et al.* obtained experimentally. From Eqs. (4.10)-(4.12) we then obtain  $\omega_p = 1.26 \times 10^{15} \text{ s}^{-1}$ ,  $\beta = 5.15 \times 10^5 \text{ m/s}$  and  $\gamma = 3.20 \times 10^{14} \text{ s}^{-1}$ , and with  $\varepsilon_D = 2.25$  for toluene, we find the absorption cross section with Eq. (3.44). We see in the figure that the HDM follows the same trend as the experimental results, while the LRA does not show any size-dependence (as expected). We also see that the experimental results indicate that the electron density actually is lower than the measured value, since the LSP resonance should approach the LRA value for large radii. Therefore it is also worth while to calculate the peak position for a lower value of  $n$ . If we choose the value  $n = 0.85 \times 10^{20} \text{ cm}^{-3}$ , we instead obtain the dashed curves in the figure, and we now see that the HDM not only follows the same trend, but also agrees

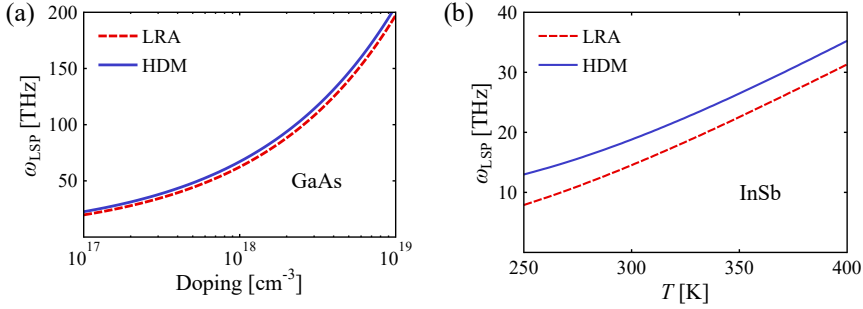


**Figure 4.8:** (a) The peak position as a function of doping for an GaAs particle with  $R = 40$  nm and  $\varepsilon_D = 1$ . (b) The peak position as a function of temperature for an intrinsic InSb particle with  $R = 200$  nm and  $\varepsilon_D = 1$ .

quantitatively with the experimental results.

Schimpf *et al.* explain the blueshift as a quantum size effect and model the discrete levels with Lorentz oscillators. The quantum confinement gives rise to higher energy of the levels, and this produces a blueshift of the LSP which matches the experimental values qualitatively. In this section it has been shown that the blueshift also can be explained as a nonlocal effect of the free electron plasma, a mechanism that is expected to be present. It should be mentioned, however, that the number of free charge carriers in the smallest particles is less than 10, which makes the application of a plasma model questionable. The nature for the blueshift observed by Schimpf *et al.* is therefore still open for explanations.

## 4.6 Tunable plasmonics

One the biggest advantages of using semiconductors in plasmonics instead of metals is the possibility of tuning the optical response, either statically through doping or dynamically through temperature or external energy sources. In this section we will consider the tunability of plasmons in semiconductors when nonlocal effects are accounted for.

The most obvious mean for altering the density of charge carriers is doping. Tuning of the plasmonic properties through doping has already been investigated by countless articles (see section 4.3 for a few references) and allows for charge carrier densities between 10<sup>16</sup> and 10<sup>21</sup> cm<sup>-3</sup> [114]. Analysing the effect of doping is straight forward as the impurity concentration can be used

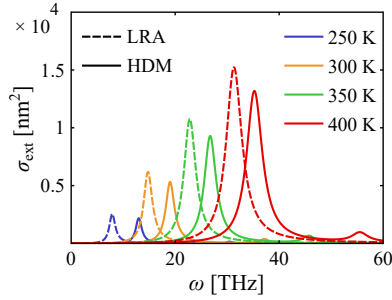


**Figure 4.9:** Extinction spectra for a 200 nm particle of intrinsic InSb at different temperatures. The solid lines are for the HDM, and the dashed lines are for the LRA.

to find  $\omega_p$  and  $\beta$  directly from Eqs. (4.11) and (4.12). This is done for a 40 nm  $n$ -doped GaAs particle in Fig. 4.8a, where the LSP peak is shown as a function of doping level for the LRA and the HDM. We see that the resonance frequency goes up with doping, as expected, and this is the case for both models.

Another method for tuning the LSP resonance is by controlling the temperature of intrinsic semiconductors. Especially a narrow band gap material like InSb with a high charge carrier density is suitable for temperature controlled plasmonics as already shown in experiments [117, 118]. The charge carrier densities depend on temperature as given by Eq. (4.8), but if high temperatures are considered, the Boltzmann distribution may not accurately describe the electron distribution, and  $n_e$  has to be found numerically. The temperature will also affect  $\beta$  through Eq. (4.13) and as well as other material parameters (see Table 4.1). Taking this into account, the temperature dependence of the LSP frequency in an InSb particle with  $R = 200$  nm is shown in Fig. 4.8b. We here see that the resonance frequency is increasing with temperature as a result of an larger electron density. In Fig. 4.9 are the extinction cross sections for the same InSb particle shown for four selected temperatures. Here we see that both the peak position *and* amplitude depend on temperature. The amplitude will naturally be of importance if the plasmon is to be measured experimentally.

It is clear that the ability to control the plasmonic properties in semiconductors is a feature with many possibilities. But as seen in Figs. 4.6 and 4.8b, nonlocal effects are expected to play a large role for semiconductor particles, even for sizes well above 100 nm. This means that an accurate prediction of the plasmonic properties of semiconductors requires inclusion of nonlocal response, for example with the HDM as was done in this chapter.



## 5 Two-fluid hydrodynamic model

In previous chapter we analysed the properties of free charge carriers in semiconductors with the HDM. Because the model was developed for a general plasma of charged particles, it was possible to transfer many of the results from metals directly to semiconductors. In doing so, however, we also neglected the possibility that several different kinds charge carriers may be present in semiconductors, such as electrons and heavy and light holes. In this chapter, we will present an extended version of the HDM that includes two plasmas of free charge carriers, and we will see that new nonlocal phenomena appear that are absent in the traditional HDM. We will call the model the *two-fluid model* to distinguish it from the typical single-fluid HDM.

There are several cases where the inclusion of only *one* kind of charge carrier is expected to be a good approximation. For *n*-doped semiconductors, the density of holes will typically be much smaller than the electron density, as is seen from the general relation  $n_h = n_{\text{int}}^2/n_e$  where  $n_{\text{int}}$  is the charge carrier density in the intrinsic semiconductor. For example, if we have  $n_e = 10^{18} \text{ cm}^{-3}$ , which can be obtained with modest doping, and  $n_{\text{int}} = 10^{15} \text{ cm}^{-3}$ , we get  $n_h = 10^{12} \text{ cm}^{-3}$ , and the semiconductor will effectively only contain electrons as free charge carriers.

Even if the densities of electrons and holes are the same (as in intrinsic semiconductors), the smaller effective mass of electrons compared to holes means that electrons will dominate the optical properties, and this justifies the application of the HDM to intrinsic InSb in previous chapter. However, it is possible that this treatment has left out interesting details, and therefore we will consider InSb again in this chapter, now including both electrons and holes.

Other intrinsic materials than InSb may also be interesting two-fluid systems. Although the intrinsic charge carrier densities will be small for semiconductors with large band gaps, external energy sources can be used to excite electrons to the conduction band creating levels of  $n_e$  and  $n_h$  that are significant. The external source may be a laser pulse as investigated experimentally in Ref. [197], and we will also consider this scenario here.

Another type of material that may host different kinds of charge carriers is *p*-doped semiconductors with light and heavy holes, and we will also analyse this situation with the two-fluid model. Although we will not consider it here, yet another kind of material with two different types of charge carriers is transition metals with *s* and *d* electrons of different effective masses [198].

In the first part of this chapter, the theoretical foundation of the two-fluid model will be presented. We will see how the model predicts the existence

of two longitudinal waves which can be identified as *optical* and *acoustic*, respectively. This is different from the single-fluid HDM which only predicts an optical longitudinal wave. To analyse the two-fluid model for spherical semiconductor particles, an extended version of the Mie theory is developed. From this we will be able to find the extinction spectra for two-fluid systems, and we will see how these contain new plasmonic resonances. The results presented in this chapter are related to Publication C.

Apart from the addition of an extra hydrodynamic fluid, the modeling of semiconductors is the same here as in previous chapter. This means that we will neglect interband transitions, excitons and phonons (see section 4.2). We will also limit ourselves to particles large enough to neglect quantum size effects and only consider charge carrier numbers high enough for a plasma model to be valid (as in last chapter we will choose the lower limit of 50 free charge carriers per semiconductor particle).

## 5.1 The hydrodynamic model for two plasmas

### The hydrodynamic equations

At the heart of the two-fluid model is the idea that each charge carrier is described by a hydrodynamic equation of motion similar to the one in Eq. (3.15b). Additionally, the wave equation from Maxwell's Equations must also have an extra current density added. If we name the two charge carriers  $a$  and  $b$ , the equations of the two-fluid model will be

$$\frac{\beta_a^2}{\omega^2 + i\gamma_a\omega} \nabla (\nabla \cdot \mathbf{J}_a) + \mathbf{J}_a = \frac{i\omega\varepsilon_0\omega_a^2}{\omega^2 + i\gamma_a\omega} \mathbf{E}, \quad (5.1a)$$

$$\frac{\beta_b^2}{\omega^2 + i\gamma_b\omega} \nabla (\nabla \cdot \mathbf{J}_b) + \mathbf{J}_b = \frac{i\omega\varepsilon_0\omega_b^2}{\omega^2 + i\gamma_b\omega} \mathbf{E}, \quad (5.1b)$$

$$-\nabla \times \nabla \times \mathbf{E} + \frac{\omega^2}{c^2} \varepsilon_\infty \mathbf{E} = -i\mu_0\omega (\mathbf{J}_a + \mathbf{J}_b), \quad (5.1c)$$

where  $\varepsilon_\infty$  is the background dielectric function (using the notation  $\varepsilon_b$  would be confusing in equations with charge carrier  $b$ ). Here we see that both charge carriers have a plasma frequency  $\omega_i$ , a damping constant  $\gamma_i$  and a nonlocal parameter  $\beta_i$ . Although we only consider two different kinds of charge carriers here, we see that the model potentially could be extended to  $n$  types of charge carriers.

Similar to what was done in chapter 3 for the HDM, we can obtain expressions for the transverse and longitudinal dielectric functions by considering

the equations in the reciprocal space. Performing the spatial Fourier transform on Eqs. (5.1) gives us

$$-\frac{\beta_a^2}{\omega^2 + i\gamma_a\omega} \mathbf{k}(\mathbf{k} \cdot \mathbf{J}_a) + \mathbf{J}_a = \frac{i\omega\varepsilon_0\omega_a^2}{\omega^2 + i\gamma_a\omega} \mathbf{E}, \quad (5.2a)$$

$$-\frac{\beta_b^2}{\omega^2 + i\gamma_b\omega} \mathbf{k}(\mathbf{k} \cdot \mathbf{J}_b) + \mathbf{J}_b = \frac{i\omega\varepsilon_0\omega_b^2}{\omega^2 + i\gamma_b\omega} \mathbf{E}, \quad (5.2b)$$

$$\mathbf{k} \times \mathbf{k} \times \mathbf{E} + \frac{\omega^2}{c^2} \varepsilon_\infty \mathbf{E} = -i\mu_0\omega (\mathbf{J}_a + \mathbf{J}_b), \quad (5.2c)$$

where we have used  $\nabla \rightarrow i\mathbf{k}$  as before. Using the definitions of transverse and longitudinal fields in section 2.4, we can obtain relations between  $\mathbf{J}^T$  and  $\mathbf{E}^T$  and between  $\mathbf{J}^L$  and  $\mathbf{E}^L$ . These relations corresponds to expressions for the conductivities  $\sigma_T$  and  $\sigma_L$ , and using Eq. (2.16) we obtain the dielectric functions

$$\varepsilon_T(\omega) = \varepsilon_\infty - \frac{\omega_a^2}{\omega^2 + i\gamma_a\omega} - \frac{\omega_b^2}{\omega^2 + i\gamma_b\omega}, \quad (5.3)$$

$$\varepsilon_L(k, \omega) = \varepsilon_\infty - \frac{\omega_a^2}{\omega^2 + i\gamma_a\omega - \beta_a^2 k^2} - \frac{\omega_b^2}{\omega^2 + i\gamma_b\omega - \beta_b^2 k^2}. \quad (5.4)$$

We here see that the transverse dielectric function in Eq. (5.3) is local, i.e. without  $k$ -dependence, which also is the case for  $\varepsilon_T$  in the HDM. Conversely, the longitudinal dielectric function depends on  $k$ , which is also similar to the HDM. Further resemblance to the HDM is seen if we consider the scenario where  $\beta_a = \beta_b$  and  $\gamma_a = \gamma_b$ . Then the two last terms in Eqs. (5.3) and (5.4) can be combined to one if we also introduce an effective plasma frequency  $\omega_{\text{eff}}^2 = \omega_a^2 + \omega_b^2$ . With this, equations (5.3) and (5.4) become identical to the expressions for  $\varepsilon_T$  and  $\varepsilon_L$  in the HDM given by Eqs. (3.25) and (3.26), respectively. In other words, the two-fluid model reduces to the single-fluid HDM when both the  $\beta$ 's and  $\gamma$ 's are identical.

## Parameters in the two-fluid model

Besides being intuitive, the idea of extending the HDM to two plasmas can also be supported by a two-band Lindhard model similar to what was done in section 3.2. In Appendix A of Publication C it is shown how the assumption of non-interacting particles in two perfectly parabolic and isotropic bands will lead us to an expression for  $\varepsilon_L$  that can be compared to Eq. (5.4). In this

derivation, the plasma frequencies and damping constants are found to be

$$\omega_i^2 = \frac{e^2 n_i}{\varepsilon_0 m_i^*}, \quad (5.5)$$

$$\gamma_i = \frac{e}{m_{i,\text{cond}}^* \mu_i}, \quad (5.6)$$

where  $i = a, b$ . The nonlocal parameter will depend on the nature of the free charge carriers. For intrinsic semiconductors we will consider electrons excited across the band gap with thermal energy or an external energy source like a laser pulse. The third scenario we will consider is  $p$ -doped materials with light and heavy holes. In Appendix A of Publication C, the nonlocal parameters in these three cases are found to be

$$\beta_i^2 = \frac{3k_B T}{m_i^*}, \quad (\text{Thermally excited}) \quad (5.7)$$

$$\beta_i^2 = \frac{3}{5} \frac{\hbar^2 k_{Fi}^2}{m_i^{*2}}. \quad (\text{Laser excited or } p\text{-doped}) \quad (5.8)$$

Equation (5.7) assumes that the Boltzmann distribution can be used as an approximation to the Fermi-Dirac distribution, which is reasonable at low temperatures. To obtain the carrier densities for intrinsic semiconductors, the expression in Eq. (4.8) from previous chapter can be used.

Equation (5.8) for laser excited charge carriers assumes that quasi-equilibria are formed in the two bands such that the step function can be used as particle distribution. The Fermi wavenumbers  $k_{Fi}$  therefore refer to the Fermi levels formed in each band. The particle densities can be found from the energy density in the laser pulse  $u_{\text{pulse}}$  together with Eq. (B6) in Appendix B of Publication C or simply by  $n_e = n_h \approx u_{\text{pulse}}/E_g$ . For both thermally excited and laser excited charge carriers, the holes are treated as a single plasma, although they actually are composed of heavy and light holes. To do this, we will use the equations for the density-of-states and conductivity effective masses of holes in Eqs. (4.3) from previous chapter.

For  $p$ -doped semiconductors we will assume complete ionization, which means that the hole density is equal to the acceptor concentration, i.e.  $N_a = n_{lh} + n_{hh}$ . This allows us to find  $k_{Flh}$  and  $k_{Fhh}$  with Eq. (B2) in Appendix B of Publication C, which in turn gives us the charge carrier densities through  $k_{Fi}^3 = 3\pi^2 n_i$ .

## 5.2 Transverse and longitudinal waves

To obtain results for the two-fluid model in finite systems, it will be an advantage to put Eqs. (5.1) in the form of vector wave equations for the transverse and longitudinal fields, respectively. This was also done for the HDM in section 3.3, and the motivation is that general solutions to the vector wave equations are known for several geometries, including the spherical.

### Vector wave equations

The transverse vector wave equation can be obtained directly from Eqs. (5.1) by using the fact that  $\nabla \cdot \mathbf{E}^T = 0$ ,  $\nabla \cdot \mathbf{J}_i^T = 0$  and  $\nabla \times \nabla \times \mathbf{E}^T = -\nabla^2 \mathbf{E}^T$ . This gives us

$$\nabla^2 \mathbf{E}^T + k_T^2 \mathbf{E}^T = \mathbf{0}, \quad (5.9)$$

where the transverse wavenumber is given by

$$k_T^2 = \frac{\omega^2}{c^2} \left( \varepsilon_\infty - \frac{\omega_a^2}{\omega^2 + i\gamma_a \omega} - \frac{\omega_b^2}{\omega^2 + i\gamma_b \omega} \right). \quad (5.10)$$

This shows that the two-fluid model predicts propagating transverse waves with wavenumber  $k_T = \sqrt{\varepsilon_T} \omega / c$  where  $\varepsilon_T$  is given by Eq. (5.3).

The wave equation for the longitudinal component is less straightforward to find because of the presence of the divergence of the current densities in Eqs. (5.1a) and (5.1b). We will here use a procedure for obtaining the longitudinal wave equation that relies on finding homogeneous equations for the current densities. The first step is to introduce  $\mathbf{J}_1$  and  $\mathbf{J}_2$  which are hybridized versions of the current densities  $\mathbf{J}_a$  and  $\mathbf{J}_b$ . They are connected with the following linear relations

$$\mathbf{J}_a^z = a_1^z \mathbf{J}_1^z + a_2^z \mathbf{J}_2^z, \quad (5.11a)$$

$$\mathbf{J}_b^z = b_1^z \mathbf{J}_1^z + b_2^z \mathbf{J}_2^z, \quad (5.11b)$$

where  $z = L, T$ . Inserting these expressions into the hydrodynamic equations (5.1) does not change anything on its own, but if we furthermore *require* that  $\mathbf{J}_1$  and  $\mathbf{J}_2$  are independent, we obtain homogeneous equations for both the transverse and longitudinal current densities. This is shown in Publication C where it is found that

$$(\nabla^2 + k_{L,j}^2) \nabla \cdot \mathbf{J}_j^L = 0, \quad (5.12)$$

where  $j = 1, 2$ . The wavenumbers  $k_{L,j}$  are found to be

$$k_{L,1,2}^2 = \frac{1}{2} \left( k_a^2 + k_b^2 \pm \sqrt{(k_a^2 - k_b^2)^2 + \frac{4\omega_a^2 \omega_b^2}{\beta_a^2 \beta_b^2 \varepsilon_\infty^2}} \right), \quad (5.13)$$

where

$$k_i^2 = \left( \omega(\omega + i\gamma_i) - \frac{\omega_i^2}{\varepsilon_\infty} \right) \frac{1}{\beta_i^2} \quad i = a, b. \quad (5.14)$$

To obtain the final state of the longitudinal vector wave equation, we will apply the divergence to Eq. (5.1c) which gives us

$$\frac{\omega^2}{c^2} \varepsilon_\infty \nabla \cdot \mathbf{E}^L = -i\mu_0 \omega \nabla \cdot [(a_1^L + b_1^L) \mathbf{J}_1^L + (a_2^L + b_2^L) \mathbf{J}_2^L], \quad (5.15)$$

where the linear relations for  $\mathbf{J}_a^L$  and  $\mathbf{J}_b^L$  have been inserted. Lets us now divide the  $\mathbf{E}$ -field into  $\mathbf{E}_1$  and  $\mathbf{E}_2$  which will depend on  $\mathbf{J}_1$  and  $\mathbf{J}_2$ , respectively. This will give us

$$\frac{\omega^2}{c^2} \varepsilon_\infty \nabla \cdot \mathbf{E}_j^L = -i\mu_0 \omega (a_j^L + b_j^L) \nabla \cdot \mathbf{J}_j^L, \quad (5.16)$$

which shows that  $\nabla \cdot \mathbf{E}_j^L$  can take the place of  $\nabla \cdot \mathbf{J}_j^L$  in Eq. (5.12). If we additionally make the following observation

$$(\nabla^2 + k_{L,j}^2) \nabla \cdot \mathbf{E}_j^L = \nabla \cdot (\nabla^2 \mathbf{E}_j^L + k_{L,j}^2 \mathbf{E}_j^L) = 0, \quad (5.17)$$

we see that because the divergence of a longitudinal field in general is non-zero, the equation is fulfilled only if

$$\nabla^2 \mathbf{E}_j^L + k_{L,j}^2 \mathbf{E}_j^L = \mathbf{0}. \quad (5.18)$$

This is the longitudinal vector wave equation, and it shows that the model predicts propagating longitudinal waves in the same way the HDM did. But differently from the HDM, the two-fluid model predicts the existence of *two* longitudinal waves with wave numbers  $k_{L,1}$  and  $k_{L,2}$ , respectively.

## Dispersion relations

To analyse the two different longitudinal waves further, the dispersion relations in Eq. (5.13) are plotted in Fig. 5.1a. The relative parameters chosen for this figure are  $\omega_b/\omega_a = 2$ ,  $\beta_b/\beta_a = 4$ ,  $\varepsilon_\infty = 1$  and  $\gamma_a = \gamma_b = 0.01\omega_a$ , and we see that the two solutions for  $k_{L,j}$  have very different appearances. The dispersion for  $k_{L,1}$  follows nearly a straight line, while  $k_{L,2}$  primarily is real above the dashed, black line given by  $\omega_{\text{eff}}/(\omega_a \sqrt{\varepsilon_\infty})$  and imaginary below. Because the frequency is non-zero for  $k_{L,2} \approx 0$ , this mode will be able to couple to electromagnetic radiation where the momentum is close to zero, and we will therefore call it the *optical mode*. Analogously we will call  $k_{L,1}$  the *acoustic mode*, and light cannot couple to this unless some method of momentum matching is used. The dispersion relations are also shown in Fig. 5.1b with

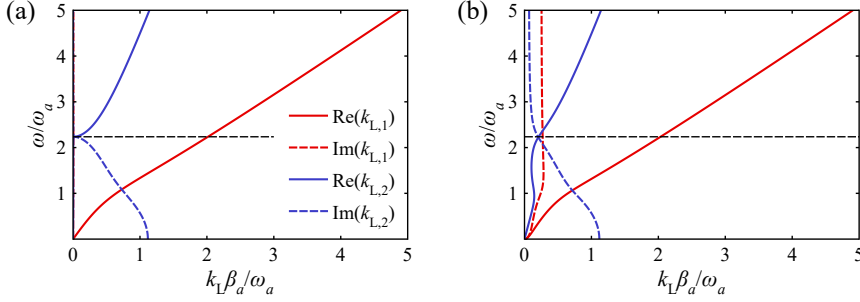


**Figure 5.1:** The dispersion relations of the optical mode (blue lines) and the acoustic mode (red lines). The full and dashed lines show the real and imaginary components, respectively, of  $k_{L,j}$ . The parameters are  $\omega_b/\omega_a = 2$ ,  $\beta_b/\beta_a = 4$ , and  $\varepsilon_\infty = 1$ . The damping constants are (a)  $\gamma_a = \gamma_b = 0.01\omega_a$  and (b)  $\gamma_a = \gamma_b = 0.5\omega_a$ . The horizontal dashed, black line is  $\omega_{\text{eff}}/(\omega_a\sqrt{\varepsilon_\infty})$ .

$\gamma_a = \gamma_b = 0.5\omega_a$ , and although the extra loss alters the curves a bit, the overall shapes remain the same.

The formation of an optical and an acoustic branch can be understood as the result of the hybridization of the two plasmas. This has been analysed before with various microscopic models [198–204], and in Ref. [202] a two-fluid hydrodynamic model was also briefly considered. The authors also arrived at the dispersion relation in Eq. (5.13), but they restricted themselves to the infinite medium. In the next sections, we will consider the two-fluid model of finite structures as well.

It should be mentioned that the single-fluid HDM only predicts an optical mode given by Eq. (3.22). From this equation we see that  $k_L$  primarily will be imaginary for  $\omega < \omega_p/\sqrt{\varepsilon_\infty}$  corresponding to an attenuated wave, and because of this, the HDM does not allow bulk plasmons to exist in this low-frequency region [108]. Similarly, the optical mode in the two-fluid model will have imaginary wave number in the region  $\omega < \omega_{\text{eff}}/\sqrt{\varepsilon_\infty}$ , which can be seen from Eq. (5.13). The acoustic mode, however, will be real also in the low-frequency region and therefore allow bulk plasmons to exist there.

### 5.3 Two-fluid model and spherical particles

In this section, we will present the solutions to the vector wave equation in spherical geometry for the two-fluid model. Although the problem is different

from the one encountered in chapters 3 and 4 due the presence of two kinds of charge carriers, we will still be able to reuse many of the previous results.

In section 3.5 we presented the solutions to the wave equation in spherical geometry, the  $\mathbf{L}$ ,  $\mathbf{M}$  and  $\mathbf{N}$  functions, and they will also be the solutions for Eqs. (5.9) and (5.18). In fact, for the region outside the particle, which we assume to be without spatial dispersion, the expressions for the fields will be identical to the ones in section 3.5. As in that section, we will here consider an incoming plane wave  $\mathbf{E}_i$  moving in the  $z$ -direction and polarized in the  $x$ -direction. The field will scatter on a spherical particle at the center of the coordinate system resulting in a reflected field  $\mathbf{E}_r$ . As in section 3.5, these fields have the expressions

$$\mathbf{E}_i(\mathbf{r}, t) = E_0 e^{-i\omega t} \sum_{l=1} i^l \frac{2l+1}{l(l+1)} \left( \mathbf{m}_{o1l}^{(1)}(k_D, \mathbf{r}) - i \mathbf{n}_{e1l}^{(1)}(k_D, \mathbf{r}) \right), \quad (5.19)$$

$$\mathbf{E}_r(\mathbf{r}, t) = E_0 e^{-i\omega t} \sum_{l=1} i^l \frac{2l+1}{l(l+1)} \left( a_l^r \mathbf{m}_{o1l}^{(3)}(k_D, \mathbf{r}) - i b_l^r \mathbf{n}_{e1l}^{(3)}(k_D, \mathbf{r}) \right), \quad (5.20)$$

where  $k_D = \sqrt{\varepsilon_D} \omega / c$  as before. The novelty compared to the HDM is found inside the particle where two longitudinal waves are present instead of one. The field transmitted into the particle is therefore given by

$$\begin{aligned} \mathbf{E}_t(\mathbf{r}, t) = E_0 e^{-i\omega t} \sum_{l=1} i^l \frac{2l+1}{l(l+1)} & \left( a_l^t \mathbf{m}_{o1l}^{(1)}(k_T, \mathbf{r}) \right. \\ & \left. - i b_l^t \mathbf{n}_{e1l}^{(1)}(k_T, \mathbf{r}) + c_{1l}^t \mathbf{l}_{e1l}^{(1)}(k_{L,1}, \mathbf{r}) + c_{2l}^t \mathbf{l}_{e1l}^{(1)}(k_{L,2}, \mathbf{r}) \right), \end{aligned} \quad (5.21)$$

where  $k_T$  is given by Eq. (5.10), and  $k_{L,j}$  are given by Eq. (5.13).

In section 3.5 we saw how the HDM required an additional boundary condition (ABC) because of the presence of a longitudinal field. Now we have two longitudinal waves with different wavenumber, and we therefore need *two* ABCs to fully determine the fields. As for the HDM, it seems reasonable to require that charge cannot escape the surface of the material (this also implies that spill-out is ignored). The ABC ensuring this is  $\mathbf{J}_a^\perp + \mathbf{J}_b^\perp = \mathbf{0}$  where the total current density perpendicular to the surface is zero. The choice for the other ABC is less straightforward, but for the calculations here we will use  $\mathbf{J}_a^\perp - \mathbf{J}_b^\perp = \mathbf{0}$ , which together with the first ABC results in  $\mathbf{J}_a^\perp = \mathbf{0}$  and  $\mathbf{J}_b^\perp = \mathbf{0}$ . This choice also means that the charge carriers cannot recombine at the interface (as might be expected by electrons and holes), and that particles of one kind cannot scatter into the other kind (as could be expected by light and heavy holes). In a model that includes these surface effects, the choice of boundary conditions will be different.

Applying the chosen ABCs together with the traditional boundary conditions  $\Delta \mathbf{E}^{\parallel} = \mathbf{0}$  and  $\Delta \mathbf{B}^{\parallel} = \mathbf{0}$  to the fields in Eqs. (5.19)-(5.21) at the  $r = R$  boundary results in a system of linear equations which are given in Appendix D of Publication C. From this, the following Mie coefficients can be derived

$$a_l^r = \frac{-j_l(x_D)[x_T j_l(x_T)]' + j_l(x_T)[x_D j_l(x_D)]'}{h_l^{(1)}(x_D)[x_T j_l(x_T)]' - j_l(x_T)[x_D h_l^{(1)}(x_D)]'}, \quad (5.22a)$$

$$b_l^r = \frac{-\varepsilon_D j_l(x_D) (\Delta_l + [x_T j_l(x_T)]') + \varepsilon_T j_l(x_T) [x_D j_l(x_D)]'}{\varepsilon_D h_l^{(1)}(x_D) (\Delta_l + [x_T j_l(x_T)]') - \varepsilon_T j_l(x_T) [x_D h_l^{(1)}(x_D)]'}, \quad (5.22b)$$

where  $x_D = Rk_D$  and  $x_T = Rk_T$ . The differentiation (denoted with the prime) is with respect to the argument. The expressions for  $a_l^r$  and  $b_l^r$  are identical to the ones found in the HDM in section 3.5, but the parameter  $\Delta_l$  is now given by

$$\Delta_l = \frac{j_l(x_T)l(l+1)}{A} \left( \frac{j_l(x_1)C_2}{x_1 j_l'(x_1)} - \frac{j_l(x_2)C_1}{x_2 j_l'(x_2)} \right), \quad (5.22c)$$

where  $x_j = Rk_{L,j}$ , and

$$C_j = \frac{\omega_a^2 \varepsilon_{\infty} k_{L,j}^2}{\beta_a^2 \left(1 + \frac{1}{\alpha_j^L}\right)} - \frac{\omega_b^2 \varepsilon_{\infty} k_{L,j}^2}{\beta_b^2 (1 + \alpha_j^L)}, \quad (5.22d)$$

$$A = \frac{(\omega^2 + i\gamma_a \omega) (\omega^2 + i\gamma_b \omega) (\alpha_1^L - \alpha_2^L) \varepsilon_{\infty}^2}{\beta_a^2 \beta_b^2 (1 + \alpha_1^L) (1 + \alpha_2^L)}, \quad (5.22e)$$

$$\alpha_j^L = \frac{b_j^L}{a_j^L} = \frac{\beta_a^2 \varepsilon_{\infty}}{\omega_a^2} (k_a^2 - k_{L,j}^2), \quad (5.22f)$$

with  $k_a$  and  $k_b$  defined in Eq. (5.14). Note that the expansion coefficients  $a_j^L$  and  $b_j^L$  should not be confused with the Mie coefficients.

As for the HDM, we see that the  $a_l^r$  coefficients are identical to the classical, local solution, while the  $b_l^r$  coefficients differ from the local solution by the inclusion of  $\Delta_l$ . Like before, the local result can be obtained by setting  $\Delta_l = 0$ .

## 5.4 Extinction spectra for two-fluid systems

In this section, the extinction spectra of spherical semiconductor particles with two kinds of charge carriers will be presented. With the Mie coefficients found in previous section, we can straight away find  $\sigma_{\text{ext}}$  with Eq. (3.44b) from chapter 3. We will first consider an idealized material that will help us understand the features of the two-fluid model, and thereafter the spectra of more realistic semiconductors will be analysed.

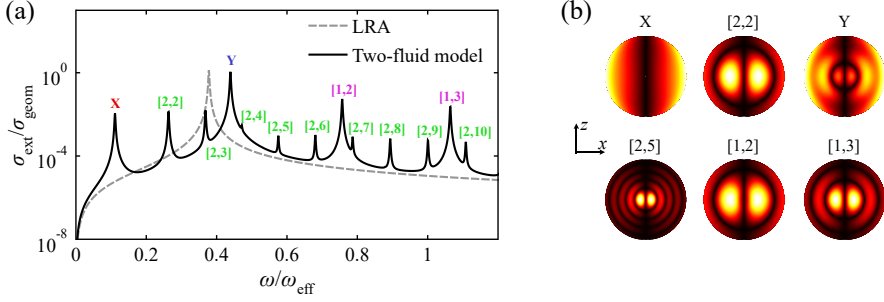


**Figure 5.2:** (a) The extinction spectra of a 10 nm particle of semiconductor A (see parameters in main text) in vacuum ( $\epsilon_D = 1$ ) as found with the two-fluid model (solid line) and the LRA (dashed line). The spectra have been normalized with  $\sigma_{\text{geom}} = \pi R^2$ , and the frequency has been normalized with  $\omega_{\text{eff}}^2 = \omega_a^2 + \omega_b^2$ . (b) The charge distribution in the  $xz$ -plane at selected frequencies. The damping constants have been set to  $\gamma_a = \gamma_b = 1.0 \times 10^{11} \text{ s}^{-1}$  to make the features more clear.

### Ideal two-fluid system

We will here study an ideal material, which we will call ‘semiconductor A’, with the parameters  $\omega_a = 3.6 \times 10^{14} \text{ s}^{-1}$ ,  $\omega_b = 1.8 \times 10^{14} \text{ s}^{-1}$ ,  $\gamma_a = \gamma_b = 1.0 \times 10^{12} \text{ s}^{-1}$ ,  $\beta_a = 4.3 \times 10^5 \text{ m/s}$ ,  $\beta_b = 1.4 \times 10^5 \text{ m/s}$  and  $\epsilon_\infty = 5$ . We will consider a spherical particle with radius  $R = 10 \text{ nm}$  and a surrounding medium with  $\epsilon_D = 1$ . Using Eqs. (3.42) and Eq. (3.44b) we find the extinction spectrum shown with the solid line in Fig. 5.2a. The spectrum is shown in a semi-logarithmic plot, and we see that a large number of peaks are present. The highest peak (marked with a ‘Y’) is the dipole LSP resonance which is also present in the LRA (shown with a dashed line). The solution in the LRA was found by setting  $\Delta_l = 0$  in Eq. (5.22b). We notice that the nonlocal two-fluid model predicts a blueshifted LSP peak similar to what we saw for the single-fluid HDM in chapters 3 and 4.

The other peaks, however, are absent in the LRA and require further investigation. The nature of them can be understood by finding poles of the  $b_l^i$  Mie coefficients in Eq. (5.22b), and these occur whenever the denominator of  $\Delta_l$  is zero. In Publication C it is shown how these poles can be found by using the

fact that  $k_a^2, k_b^2 \gg 2\omega_a\omega_b/\beta_a\beta_b\varepsilon_\infty$  at high frequencies, which gives the approximate location of the resonances

$$\omega^2 = \begin{cases} \frac{\pi^2 n^2 \beta_a^2}{R^2} + \frac{\omega_a^2}{\varepsilon_\infty} & (j = 1) \\ \frac{\pi^2 n^2 \beta_b^2}{R^2} + \frac{\omega_b^2}{\varepsilon_\infty} & (j = 2) \end{cases}, \quad (5.23)$$

where  $n = 1, 2, 3, \dots$ . We here see that the peak positions are determined by properties of either charge carrier  $a$  or  $b$ . This shows that although the acoustic and optical branches are hybridizations of the two plasmas, the charge carriers will at high frequencies decouple again and behave as independent plasmas. In Fig. 5.2a are the peaks labeled with the numbers  $[j, n]$ , and we see that the large peaks ( $j = 1$ ) above the LSP resonance are associated with charge carrier  $a$ , while the small peaks ( $j = 2$ ) are associated with charge carrier  $b$ .

To gain further understanding of the peaks, the charge distributions for selected peaks are plotted in Fig. 5.2b. The contours show the total charge density in the  $xz$ -plane when the wave is propagating in the  $z$ -direction, and the electric field is polarized in the  $x$ -direction. We here see that the first peak of the spectrum (the one marked with 'X' in Fig. 5.2a) has the characteristic of a surface plasmon with a high density of charge near the surface. The next peak in the spectrum (labeled  $[2, 2]$ ) is instead a confined bulk plasmon with the charge density closer to the center. The charge distribution is also shown for the  $[1, 2]$  resonance, and we see that it is almost identical to the distribution of the  $[2, 2]$  mode. The  $[1, 2]$  and  $[2, 2]$  modes have the same order, and they are according to Eq. (5.23) related to charge carriers  $a$  and  $b$ , respectively. The contours are also shown for the peaks labeled  $[2, 5]$  and  $[1, 3]$ , which have the patterns of higher order modes.

Finally, the charge distribution is also shown for the dipole LSP (labeled with 'Y'), and even though it has a high density of charge near the surface, as expected, it also displays the pattern of a confined bulk plasmon. The explanation is that the LSP hybridize with the confined bulk plasmon labeled  $[2, 4]$ , resulting in a resonance with features from both types of plasmons. This will not occur in the single-fluid HDM, where the bulk plasmons are clearly separated from the LSP peak (see e.g. Fig. 3.8).

In Fig. 5.2a we also see another phenomena that would not occur in the HDM, namely plasmon resonances in the frequency region below the dipole LSP resonance. For the single-fluid HDM, the optical branch will in this region be imaginary and therefore attenuated. The two-fluid model, on the other hand, also has an acoustic branch, and this permits peaks to exist in the low-frequency region.

To convince ourselves that the peaks below the LSP indeed are caused by the acoustic branch  $k_{L,1}$ , we can plot the extinction spectrum where only one

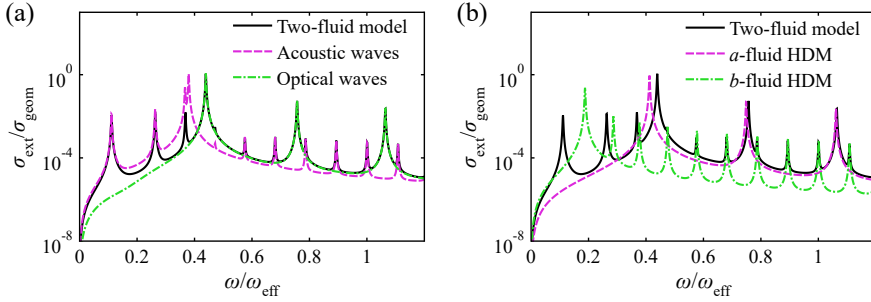


**Figure 5.3:** (a) The extinction spectrum for semiconductor A as found with the two-fluid model (solid, black line). Also shown are the spectra when only the acoustic longitudinal waves are included (dashed, magenta line) and when only the optical longitudinal waves are included (dash-dotted, green line). (b) The extinction spectra of semiconductor A in the two-fluid model (solid, black line), in the HDM with only charge carrier  $a$  (dashed, magenta line) and in the HDM with only charge carrier  $b$  (dash-dotted, green line).

of the longitudinal waves is included. Although this is a bit artificial when the Mie coefficients were derived by assuming that both longitudinal waves were present, it does give some understanding of the spectrum. In practice it is done by setting either  $C_1$  or  $C_2$  equal to zero in Eq. (5.22d). In Fig. 5.3a the extinction spectra are shown for  $C_1 = 0$  where only the acoustic branch is included (dashed, magenta line) and for  $C_2 = 0$  where only the optical branch is included (dash-dotted, green line). Here we see that the acoustic branch indeed accounts for the resonances below the LSP peak, and we will therefore call these peaks for *acoustic peaks*. We also see that the LSP resonance (largest peak) is present in both spectra, which reflects the fact that this resonance is not associated with poles of  $\Delta_l$ , but rather poles of the *entire*  $b_l^r$  coefficient.

Of particular interest is the first acoustic peak (labeled with ‘X’). Being a surface plasmon, this is different from the other acoustic peaks in the spectrum, and we will analyse this peak further in section 5.5.

## Comparison to the HDM

The two-fluid model is related to the single-fluid HDM, and we will here analyse the connection between the models. The HDM can be used to find the extinction spectrum of semiconductor A if only one of the charge carriers is included. This is done by setting  $\omega_p = \omega_i$ ,  $\beta = \beta_i$  and  $\gamma = \gamma_i$ , and then using

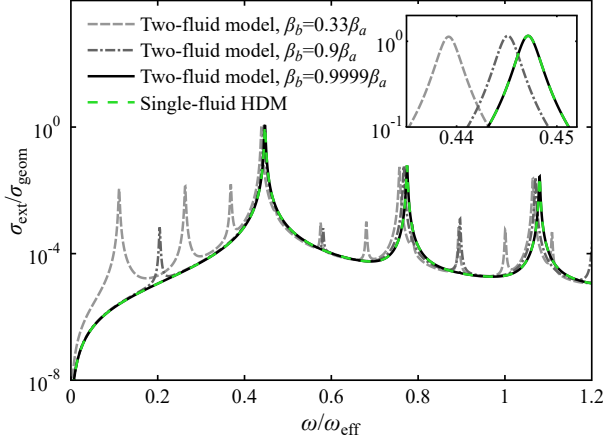


**Figure 5.4:** The extinction spectrum for semiconductor A in the two-fluid model with different values of  $\beta_b$ :  $\beta_b = 0.33\beta_a$ ,  $\beta_b = 0.9\beta_a$  and  $\beta_b = 0.9999\beta_a$ . The spectrum in the HDM with  $\beta = \beta_a$ ,  $\omega_p^2 = \omega_a^2 + \omega_b^2$  and  $\gamma = \gamma_a = \gamma_b$  is shown with a dashed, green line.

Eqs. (3.42) from chapter 3 to find the Mie coefficients.

Figure 5.3b shows the extinction spectrum found with the two-fluid model together with the spectra found with the HDM where either the  $a$ -fluid or the  $b$ -fluid is included. The dashed, magenta line shows spectra when the  $a$ -fluid is included, and we see that the bulk peaks predicted by the HDM correspond well with the bulk plasmons in two-fluid model that are related to charge carrier  $a$  ( $j = 1$ ). This is explained by the decoupling of the charge carriers at high frequencies described by Eq. (5.23), which means that the single-fluid HDM is able to predict the resonances in the high-frequency region. Similarly, if we include the  $b$ -fluid in the HDM (dash-dotted, green line), we find that the bulk plasmon peaks matches well with the bulk plasmons in the two-fluid model related to charge carrier  $b$ .

In Fig. 5.3b the dipole LSP resonance in the two-fluid model is also reproduced reasonably well by the HDM with the  $a$ -fluid. But the first acoustic peak is not reproduced by any of the single-fluid spectra, and this emphasizes the uniqueness of this resonance.

It was mentioned in section 5.1 that the two-fluid model reduces to the HDM when both the  $\beta$ 's and the  $\gamma$ 's are the same. This is shown in Fig. 5.4 where the extinction spectrum in the two-fluid model is plotted for increasingly similar  $\beta$ 's. Also shown in the figure with a dashed, green line is the spectrum in

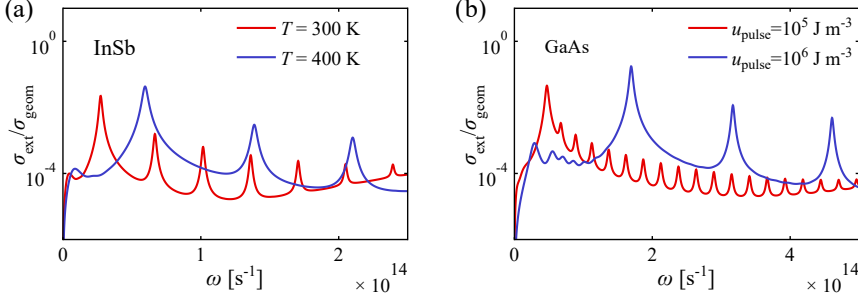


**Figure 5.5:** (a) Spectra for an InSb particle at 300 K with  $R = 100 \text{ nm}$  (red line) and at 400 K with  $R = 60 \text{ nm}$  (blue line). (b) Spectra for a GaAs particle with  $u_{\text{pulse}} = 10^5 \text{ J m}^{-3}$  and  $R = 40 \text{ nm}$  (red line) and  $u_{\text{pulse}} = 10^6 \text{ J m}^{-3}$  and  $R = 15 \text{ nm}$  (blue line).

HDM with the parameters  $\beta = \beta_a$ ,  $\omega_p^2 = \omega_a^2 + \omega_b^2$  and  $\gamma = \gamma_a = \gamma_b$ , and we see that this line coincides almost completely with the  $\beta_b = 0.9999\beta_a$  case. It should be mentioned that the LRA where  $\beta_a = \beta_b = 0$  is a special case of identical  $\beta$ 's, and this shows that none of the features of the two-fluid model will be present in the local approximation.

Another situation where the two-fluid system can be described by the single-fluid HDM is when one of the plasma frequencies is significantly smaller than the other. This also justifies the use of the HDM for intrinsic semiconductors in previous chapter, as the plasma frequency for electrons typically will be larger than that for holes. In Publication C, this argument is supported by Fig. 6, where it is shown how the spectrum in the single-fluid model with  $\omega_p = \omega_a$  is almost identical to the one predicted by the two-fluid model when  $\omega_a \gg \omega_b$ .

## Realistic semiconductors

The parameters for semiconductor A were chosen to obtain clear features in the extinction spectra. Now we will consider more realistic semiconductors with  $\omega_i$ ,  $\beta_i$  and  $\gamma_i$  given by Eqs.(5.5)-(5.8) and the charge carriers originating from either thermal excitation, laser excitation or doping. While the material parameters used here are for realistic semiconductors, we will still neglect excitations not captured by the free-electron model such as interband transitions, excitons and phonons.

The first material we will consider is intrinsic InSb with electrons excited to the conduction band by thermal energy. The material parameters for InSb at

300 K are given in Table 4.1 in chapter 4, and using Eqs. (5.5)-(5.7) we obtain the values  $\omega_e = 6.33 \times 10^{13} \text{ s}^{-1}$ ,  $\omega_h = 1.11 \times 10^{13} \text{ s}^{-1}$ ,  $\gamma_e = 1.99 \times 10^{12} \text{ s}^{-1}$ ,  $\gamma_h = 6.67 \times 10^{12} \text{ s}^{-1}$ ,  $\beta_e = 1.09 \times 10^6 \text{ m/s}$  and  $\beta_h = 1.92 \times 10^5 \text{ m/s}$ . As mentioned in the introduction of this chapter, the validity of a plasma model depends on the number of electrons  $N_e$  and holes  $N_h$  in the particle (we chose 50 charge carriers as the lower limit). We will therefore consider an InSb particle with radius  $R = 100 \text{ nm}$ , which gives us  $N_e = N_h = 60$ . The spectrum for this particle in vacuum ( $\epsilon_D = 1$ ) is shown in Fig. 5.5a with a red line, and we here recognize largest peak as the dipole LSP resonance, while the following peaks are confined bulk plasmons of the electron fluid. The bulk plasmon peaks for the hole fluid are not visible due to the low mobility of holes, but the first acoustic resonance can be seen as a small peak in the left side of the spectrum. Also shown in the figure with a blue line is the spectrum for an InSb particle at 400 K with  $R = 60 \text{ nm}$ , and we see how the increased density of charge carriers and smaller radius move the peaks to the right.

The next material we will analyse is intrinsic GaAs with electrons excited to the conduction band by a pulse of laser. If the energy density of the pulse is  $u_{\text{pulse}} = 10^5 \text{ J m}^{-3}$  and  $n_e = n_h \approx u_{\text{pulse}}/E_g$ , we can use Eqs. (5.5), (5.6) and (5.8) together with data from Table 4.1 to find  $\omega_e = 1.48 \times 10^{14} \text{ s}^{-1}$ ,  $\omega_h = 5.13 \times 10^{13} \text{ s}^{-1}$ ,  $\gamma_e = 3.95 \times 10^{12} \text{ s}^{-1}$ ,  $\gamma_h = 1.16 \times 10^{13} \text{ s}^{-1}$ ,  $\beta_e = 3.31 \times 10^5 \text{ m/s}$  and  $\beta_h = 3.98 \times 10^4 \text{ m/s}$ . Considering a particle with  $R = 40 \text{ nm}$  gives us  $N_e = N_h = 117$  and the spectrum shown in Fig. 5.5b with the red line. We here see the dipole LSP followed by electron bulk plasmons, while there are no visible hole bulk plasmons or acoustic peaks. Considering a GaAs particle with  $u_{\text{pulse}} = 10^6 \text{ J m}^{-3}$  and  $R = 15 \text{ nm}$ , however, reveals the acoustic peaks as shown with the blue line in Fig. 5.5b.

In Fig. 7 of Publication C is also shown the spectrum of a *p*-doped GaAs particle, where light and heavy holes constitute the charge carriers. However, the low mobility of the holes results in an almost featureless spectrum, and here we will not consider this particular scenario further.

## 5.5 The acoustic peak

The real novelty of the two-fluid model compared to the HDM is the presence of acoustic peaks below the LSP, and especially the first acoustic peak (labeled 'X' in Fig. 5.2a) is unique because of its surface plasmon quality. Experimental observation of this resonance could also be used for verification of the two-fluid model, and we will therefore use this section to analyse the properties of the first acoustic peak.

In Fig. 5.6(a) is the spectral position of the first acoustic peak in a GaAs particle shown as a function of radius. The charge carrier densities were created

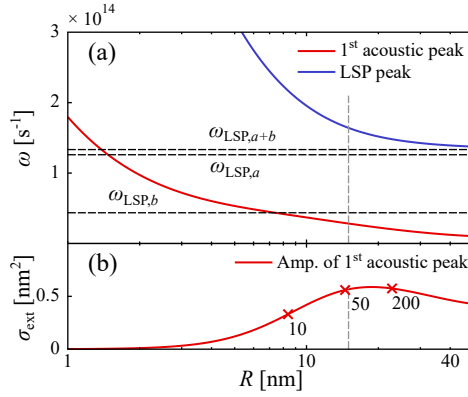


**Figure 5.6:** (a) The spectral positions of the first acoustic peak and the dipole LSP peak as functions of radius for a GaAs particle. The electrons were excited to the conduction band by a laser pulse with  $u_{\text{pulse}} = 10^6 \text{ J m}^{-3}$ . The vertical dashed line is for  $R = 15$  nm, which was used for the blue line in Fig. 5.5b. (b) The amplitude of the first acoustic peak as a function of radius. The number of electrons in the particle is shown for three particle sizes.

with a laser pulse of  $u_{\text{pulse}} = 10^6 \text{ J m}^{-3}$ . We here see that the first acoustic peak (red line) blueshifts as the particle size is reduced, a trend that is also followed by the LSP peak shown in the figure with a blue line. This size-dependent blueshift of the LSP resonance was also analysed in chapters 3 and 4 using the HDM. Also shown in the figure with dashed, black lines is the position of LSP peak in the local response approximation as given by  $\omega_{\text{LSP},a+b} = (\omega_a^2 + \omega_b^2)^{1/2} / (\epsilon_\infty + 2\epsilon_D)^{1/2}$  (including both kinds of charge carriers) and  $\omega_{\text{LSP},i} = \omega_i / (\epsilon_\infty + 2\epsilon_D)^{1/2}$  (including charge carrier  $a$  or  $b$ ).

If the acoustic plasmon is to be measured in experiments, the amplitude of the peak will play an important role. The amplitude is therefore plotted in Fig. 5.6(b) as a function of radius, and quite interestingly we see that the peak reaches a maximum at a finite particle size. To remind ourselves that we should stay in the regime of a plasma model, the number of electrons  $N_e$  is also shown in the figure for three different sizes. The maximum of the amplitude, however, occurs above the mark for 50 electrons, which was our chosen lower limit for the model.

When estimating the amplitude of the acoustic peak, it has to be taken into account that Landau damping will result in attenuation of the resonance (see section 3.4). In fact, it is expected that Landau damping will be more severe for the acoustic peak than for the regular LSP, because the almost linear dispersion of the acoustic branch places it inside the region of single particle excitations

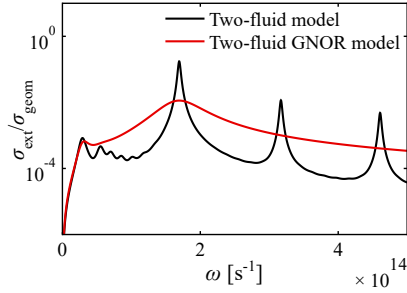


**Figure 5.7:** The extinction spectrum of a GaAs particle with  $u_{\text{pulse}} = 10^6 \text{ J m}^{-3}$  and  $R = 15 \text{ nm}$ , where nonlocal damping has been included (red line) or left out (black line).

for the infinite medium [199,205].

The two-fluid model does not account for Landau damping in its current state, but as indicated in section 3.4, the GNOR model is able to provide a reasonable estimate for the Landau damping in certain situations. The GNOR model is easily implemented for single-fluid systems, where the nonlocal parameter  $\beta$  simply is replaced by a complex version called  $\eta$ . This suggests that also the two-fluid model can be modified to account for nonlocal damping by a similar replacement. Inspired by section 3.4, it is therefore proposed that the complex nonlocal parameters in the two-fluid model are given by

$$\eta_i^2 = \beta_i^2 + D_i(\gamma_i - i\omega), \quad (5.24)$$

where  $i = a, b$ , and  $D_i$  may be found with

$$D_i = \frac{6}{\sqrt{10}} \frac{v_{Fi}^2}{\omega_i} A_i. \quad (5.25)$$

As in the case for metals, this leaves us with the difficulty of determining  $A_i$ . We will here make the simple assumption that  $A_a = A_b = 1$ , which will allow us to calculate  $\eta_a$  and  $\eta_b$  straight away. Let us consider the impact of nonlocal damping on the extinction spectrum for a GaAs particle with charge carriers excited by a laser pulse with  $u_{\text{pulse}} = 10^6 \text{ J m}^{-3}$  and a radius of  $R = 15 \text{ nm}$  (same setup as for the blue line in Fig. 5.5b). This is shown in Fig. 5.7 where the red and black lines are the spectra predicted by the two-fluid model with and without nonlocal damping, respectively. We here that the nonlocal damping results in smearing out of all the electron bulk plasmons. The first acoustic peak still remains, however, which makes experimental verification

of this peak look realistic. There is furthermore a chance that the nonlocal damping has been overestimated here, since new experiments indicate that size-dependent damping is smaller in semiconductors than in metals [174].

The first acoustic peak analysed in this section can be used to test the validity of the two-fluid model since it is a resonance that is absent in the HDM (and the LRA as well). The application of the two-fluid model to InSb and GaAs particles furthermore indicates that the acoustic peak also will be observable in realistic semiconductors, even if nonlocal damping is taken into account.

## 6 Conclusion and outlook

The classical local response approximation (LRA), where the response of the free-electron gas only depends on the electric field at the same location, is not expected to be accurate for structures on the nanometer scale. For these sizes, a different or augmented theoretical model has to be applied instead, and in this thesis, the hydrodynamic Drude model (HDM) and its extensions were investigated for metals and semiconductors.

We have first considered the optical response of metals, where the HDM provides a nonlocal relation between the electric field and the current density. We have shown how the model can be related to the quantum mechanical Lindhard model, and how this can be used to derive the nonlocal parameter  $\beta$ . The HDM predicts propagating longitudinal waves, and by adding those to the solution of Maxwell's Equations in spherical geometry, we obtained the nonlocal optical response of metal nanoparticles. We saw that the HDM predicted two phenomena absent in the LRA: A size-dependence of the localized surface plasmon (LSP) resonance, and the existence of confined bulk plasmons above the plasma frequency.

For an ensemble of nanoparticles, another secondary mechanism will start to show: The size-dependence of the LSP resonance combined with a distribution of particle sizes results in an effective broadening of the plasmon peak in the extinction spectrum. This effect will be necessary to account for when interpreting experimental spectra. However, it was found that this inhomogeneous broadening becomes negligible when other broadening mechanisms are taken into account. In particular, nonlocal damping as modeled by the generalized nonlocal optical response (GNOR) model was found to completely dominate the broadening of the LSP peak.

We also analysed the nonlocal response of semiconductor particles by taking advantage of the fact that the HDM is derived for a general electron gas. We considered semiconductors with an intrinsic density of charge carriers as well as doped materials, and in both cases was an expression for the nonlocal parameter  $\beta$  derived. From the HDM, we were able to find the extinction spectra of various semiconductor materials, and in general we found that the relative size-dependent blueshift of the LSP is much larger than in metals. This property can be used directly in experimental research of nonlocal effects since a larger resonance shift will be easier to detect.

We also derived an extended version of the HDM to account for the fact that semiconductors may contain several different kinds of charge carriers. The model included two different hydrodynamic plasmas, and we found that

these two plasmas would hybridize to form an acoustic and an optical mode. This is different from the traditional HDM, which only predicts an optical mode. By accounting for the two longitudinal waves, solutions to Maxwell's Equations in spherical symmetry were found, and using those, we were able to find the extinction spectra of semiconductor particles with two different plasmas. Here we saw the appearance of new resonances that are absent in the HDM. These resonance peaks were traced back to the acoustic mode, and because the peaks are absent in the single-fluid description, they can be used to experimentally verify the two-fluid model.

The pursuit of new plasmonic materials has led researchers to semiconductors, which are much more flexible than the traditional metals. Proper description of these materials on the nanoscale requires improved theoretical models such as the HDM presented in this thesis, but several problems and research opportunities still remain. For example, this thesis focused on spherical particles, but other geometries of semiconductors will also be interesting to analyse in a nonlocal model. In particular, it may be advantageous to consider planar systems, because these will be better suited for fabrication for certain semiconductors. The connection to experiments is important because it is measurements that eventually will verify the theoretical predictions. The experimental observation of the various nonlocal phenomena discussed in this thesis will not only add confidence to the theoretical models but also give us new knowledge of nonlocal response.

As the sizes of the semiconductor structures are further reduced, new phenomena besides the nonlocal response will start to appear. Especially quantum size effects are expected to play a role for semiconductors on the nanometer scale, as indeed is the case for quantum dots and wells. How this affects the plasmonic properties and which modeling tools to choose are questions that require more investigation.

Finally, the idea of collective excitations in the electron gas is not limited to bulk materials like metals and semiconductors. For example, the molecular chains known as J-aggregates can also support excitations similar to plasmons, and the role of nonlocal response for these materials is not yet determined.

## A Longitudinal dielectric function

In this Appendix, we will present a derivation of the longitudinal dielectric function from Fermi's Golden rule. A more detailed derivation is found in [77]. The starting point is the Hamiltonian

$$H_0 = -\frac{\hbar^2}{2m}\nabla^2 + V(\mathbf{r}), \quad (\text{A.1})$$

which is subject to the perturbation

$$U(\mathbf{r}, t) = U_0 e^{i\mathbf{k}\cdot\mathbf{r} - i\omega t} + \text{c.c.}, \quad (\text{A.2})$$

where 'c.c.' indicates the complex conjugate, and  $U_0 = -ieE_0/k$  with  $E_0$  being the amplitude of the electric field. Given the perturbation  $U(\mathbf{r}, t)$  to the system  $H_0$ , the probability that a particle will be excited from a state  $\psi_\alpha$  to a state  $\psi_\beta$  is to linear order given by Fermi's Golden Rule [206]

$$P_{\alpha\rightarrow\beta} = \frac{2\pi}{\hbar} |\langle\psi_\beta|U_0 e^{i\mathbf{k}\cdot\mathbf{r}}|\psi_\alpha\rangle|^2 \delta(E_\beta - E_\alpha - \hbar\omega), \quad (\text{A.3})$$

where the delta function ensures energy conservation. A similar probability exists for the transition the other way. Combining this with the occupation number  $f$ , which for electrons is the Fermi-Dirac distribution, we can find the total transition rate between all states

$$W(\mathbf{k}, \omega) = \frac{2\pi}{\hbar} 2 \sum_{\alpha\beta} |\langle\psi_\beta|U_0 e^{i\mathbf{k}\cdot\mathbf{r}}|\psi_\alpha\rangle|^2 \delta(E_\beta - E_\alpha - \hbar\omega) [f(E_\alpha) - f(E_\beta)]. \quad (\text{A.4})$$

The double sum is over all initial states  $\psi_\alpha$  and final states  $\psi_\beta$ . From the transition rate it is a simple matter to calculate the power dissipation from the expression  $\mathcal{P}(\mathbf{k}, \omega) = \hbar\omega W(\mathbf{k}, \omega)$ . But this can also be found classically with the integration [49]

$$\mathcal{P}(\mathbf{k}, \omega) = \int \mathbf{E} \cdot \mathbf{J} d\mathbf{r} = 2\sigma'(\mathbf{k}, \omega) \frac{k^2 |U_0|^2 V}{e^2}, \quad (\text{A.5})$$

where  $V$  is the integration volume. The current density  $\mathbf{J}$  is given by Eq. (2.12), and  $\sigma'$  is the real part of the conductivity. Furthermore, equation (2.15) provides the relation between the dielectric function and the conductivity, and we

find the imaginary part of the dielectric function to be

$$\varepsilon_L''(\mathbf{k}, \omega) = \frac{2e^2\pi}{\varepsilon_0 k^2} \frac{1}{V} \sum_{\alpha\beta} |\langle \psi_\beta | e^{i\mathbf{k}\cdot\mathbf{r}} | \psi_\alpha \rangle|^2 \delta(E_\beta - E_\alpha - \hbar\omega) [f(E_\alpha) - f(E_\beta)]. \quad (\text{A.6})$$

Due to the causality of the dielectric function, the real part will be connected to the imaginary part by the Kramers-Kronig relation, and we find  $\varepsilon_L'$  to be

$$\varepsilon_L'(\mathbf{k}, \omega) = 1 + \frac{2e^2}{\varepsilon_0 k^2} \frac{1}{V} \sum_{\alpha\beta} \frac{|\langle \psi_\beta | e^{i\mathbf{k}\cdot\mathbf{r}} | \psi_\alpha \rangle|^2}{E_\beta - E_\alpha - \hbar\omega} [f(E_\alpha) - f(E_\beta)]. \quad (\text{A.7})$$

The total dielectric function can be put together using the Dirac-identity

$$\lim_{\eta \rightarrow 0^+} \frac{1}{x - i\eta} = \text{p.v.} \frac{1}{x} + i\pi\delta(x), \quad (\text{A.8})$$

where 'p.v.' stands for principle value, and we finally arrive at

$$\varepsilon_L(\mathbf{k}, \omega) = 1 + \frac{2e^2}{\varepsilon_0 k^2} \frac{1}{V} \sum_{\alpha\beta} \frac{|\langle \psi_\beta | e^{i\mathbf{k}\cdot\mathbf{r}} | \psi_\alpha \rangle|^2}{E_\beta - E_\alpha - \hbar\omega - i\eta} [f(E_\alpha) - f(E_\beta)], \quad (\text{A.9})$$

where the limit  $\eta \rightarrow 0^+$  is assumed.

## B The hydrodynamic equations

In this Appendix, the linearized hydrodynamic equations are derived from the Boltzmann Equation. Consider an ensemble of free electrons described by the one-particle distribution function  $f(\mathbf{r}, \mathbf{p}, t)$  which is governed by the Boltzmann Equation [79]

$$\frac{\partial f}{\partial t} + \nabla_{\mathbf{r}} f \cdot \mathbf{v} + \nabla_{\mathbf{p}} f \cdot \mathbf{F} = I_{\text{coll}} [f]. \quad (\text{B.1})$$

The particle velocity  $\mathbf{v}$  fulfills the relation  $\mathbf{p} = m\mathbf{v}$  where  $m$  is the mass of the electron, and the force  $\mathbf{F}$  is in our case caused by an electric field  $\mathbf{E}$  and is given by  $\mathbf{F} = -e\mathbf{E}$  (we ignore magnetic forces). The collision operator  $I_{\text{coll}}$  may be very complex, but because we have particle conservation, we obtain a very simple result when integrating over momentum space

$$\int I_{\text{coll}} [f] d\mathbf{p} = 0. \quad (\text{B.2})$$

Similarly, we will assume that

$$\int \mathbf{p} I_{\text{coll}} [f] d\mathbf{p} = 0, \quad (\text{B.3})$$

which is a consequence of momentum conservation in the collisions.

We will derive the hydrodynamic equations through the *moments* of the distribution function given by

$$\langle M \rangle = \int M f d\mathbf{p}, \quad (\text{B.4})$$

where  $M$  is a weight function which may be set to 1,  $\mathbf{p}$ ,  $p^2$  etc. depending on the order of the moment.

If we start with  $M = 1$ , which is the zeroth moment, we find

$$\langle 1 \rangle = \int f d\mathbf{p} \equiv n(\mathbf{r}, t), \quad (\text{B.5})$$

where  $n(\mathbf{r}, t)$  is the particle density (notice that if we also integrated over  $\mathbf{r}$  space, we would obtain the total particle number  $N$ ). By taking the time

derivative of this equation, we can couple it to the Boltzmann Equation

$$\frac{\partial n}{\partial t} = \int \frac{\partial f}{\partial t} d\mathbf{p} = \int (I_{\text{coll}}[f] - \nabla_{\mathbf{r}} f \cdot \mathbf{v} - \nabla_{\mathbf{p}} f \cdot \mathbf{F}) d\mathbf{p}. \quad (\text{B.6})$$

The first term on the right-hand side disappears according to Eq. (B.2). The second term can be rewritten as

$$\nabla_{\mathbf{r}} f \cdot \mathbf{v} = \nabla_{\mathbf{r}} \cdot (f\mathbf{v}) - f(\nabla_{\mathbf{r}} \cdot \mathbf{v}), \quad (\text{B.7})$$

where we also have that

$$\nabla_{\mathbf{r}} \cdot \mathbf{v} = \frac{\partial^2 x}{\partial x \partial t} + \frac{\partial^2 y}{\partial y \partial t} + \frac{\partial^2 z}{\partial z \partial t} = \frac{\partial}{\partial t} (1 + 1 + 1) = 0. \quad (\text{B.8})$$

The third term in Eq. (B.6) describes a flow in  $\mathbf{p}$  space, and due to particle conservation, this term will be zero when integrated over momentum space. The zeroth moment therefore becomes

$$\frac{\partial n}{\partial t} = - \int \nabla_{\mathbf{r}} \cdot (f\mathbf{v}) d\mathbf{p} = - \nabla_{\mathbf{r}} \cdot \int (f\mathbf{v}) d\mathbf{p} = - \nabla_{\mathbf{r}} \cdot (n\mathbf{u}), \quad (\text{B.9})$$

where  $\mathbf{u}$  is the average velocity of the particles. We immediately recognize this as the continuity equation, which relates the change in particle density to the flow into the region.

Continuing with the first moment where  $M = \mathbf{p}$ , we find

$$\langle \mathbf{p} \rangle = \int \mathbf{p} f d\mathbf{p} \equiv mn(\mathbf{r}, t)\mathbf{u}(\mathbf{r}, t), \quad (\text{B.10})$$

and we see that we implicitly already have used this moment in the derivation of Eq. (B.9). Taking the time derivative, inserting the Boltzmann Equation and using Eq. (B.3), we find

$$m \frac{\partial(n\mathbf{u})}{\partial t} = \int \mathbf{p} (-\nabla_{\mathbf{r}} f \cdot \mathbf{v} - \nabla_{\mathbf{p}} f \cdot \mathbf{F}) d\mathbf{p}. \quad (\text{B.11})$$

The first term on the right-hand side is found to be

$$\int \mathbf{p} (\nabla_{\mathbf{r}} f \cdot \mathbf{v}) d\mathbf{p} = \nabla_{\mathbf{r}} \cdot \int \begin{pmatrix} v_x v_x & v_x v_y & v_x v_z \\ v_y v_x & v_y v_y & v_y v_z \\ v_z v_x & v_z v_y & v_z v_z \end{pmatrix} m f d\mathbf{p} = \nabla_{\mathbf{r}} \cdot \int \mathbf{v} \otimes \mathbf{v} m f d\mathbf{p}, \quad (\text{B.12})$$

where  $\nabla_{\mathbf{r}} \cdot$  operates row-wise on  $\mathbf{v} \otimes \mathbf{v}$ . We will now introduce the pressure tensor  $\mathbf{P}$

$$\begin{aligned}
 \mathbf{P} &= \int (\mathbf{v} - \mathbf{u}) \otimes (\mathbf{v} - \mathbf{u}) m f d\mathbf{p} \\
 &= \int (\mathbf{v} \otimes \mathbf{v}) m f d\mathbf{p} - \int (\mathbf{v} \otimes \mathbf{u}) m f d\mathbf{p} \\
 &\quad - \int (\mathbf{u} \otimes \mathbf{v}) m f d\mathbf{p} + \int (\mathbf{u} \otimes \mathbf{u}) m f d\mathbf{p} \\
 &= \int (\mathbf{v} \otimes \mathbf{v}) m f d\mathbf{p} - \mathbf{u} \otimes \mathbf{u} n m
 \end{aligned} \tag{B.13}$$

whereby Eq. (B.12) can be written as

$$\int \mathbf{p} (\nabla_{\mathbf{r}} f \cdot \mathbf{v}) d\mathbf{p} = \nabla_{\mathbf{r}} \cdot \mathbf{P} + \nabla_{\mathbf{r}} \cdot (\mathbf{u} \otimes \mathbf{u} n m). \tag{B.14}$$

The pressure tensor is in fact a second order moment, and it describes the pressure exerted on the electrons by the electrons themselves through thermal fluctuations and degeneracy pressure. The second term on the right-hand side of Eq. (B.11) is found to be

$$\int \mathbf{p} (\nabla_{\mathbf{p}} f \cdot \mathbf{F}) d\mathbf{p} = \int \mathbf{p} (\nabla_{\mathbf{p}} \cdot (f \mathbf{F})) d\mathbf{p} = - \int f \mathbf{F} d\mathbf{p}, \tag{B.15}$$

where  $\nabla_{\mathbf{p}} \cdot \mathbf{F} = 0$  has been used in the first step. Integration by parts was used in the second step together with the fact that  $f(p_j = \pm\infty) = 0$  for  $j = x, y, z$ . Furthermore, if we neglect magnetic forces,  $\mathbf{F}$  will be independent of  $\mathbf{p}$  and can be taken outside integral which, in turn, simply becomes the zeroth moment. With this, the first moment becomes

$$m \frac{\partial(n\mathbf{u})}{\partial t} = -\nabla_{\mathbf{r}} \cdot \mathbf{P} - \nabla_{\mathbf{r}} \cdot (\mathbf{u} \otimes \mathbf{u} n m) + \mathbf{F} \frac{n}{m}. \tag{B.16}$$

We see from Eq. (B.9) how the zeroth moment  $n$  is coupled to the first moment  $\mathbf{u}$ . Similarly, the first moment is coupled to the second moment  $\mathbf{P}$  in Eq. (B.16), and if we continued to evaluate the second moment, we would see that it would be connected to the third moment, and so on. We would therefore never arrive at a set of self-contained equations, something that is known as the *closure problem*. A work-around for this is typically to phenomenologically choose a value for the highest (and undetermined) moment in the equations which, in our case, is the pressure tensor  $\mathbf{P}$ . To make things simple, we will assume that it is diagonal which is reasonable for nearly homogeneous gasses. Furthermore, we only include the degeneracy pressure, which has a

well-known result for a Fermi gas (see e.g. chapter 5 of Ref. [207]). The pressure tensor hereby becomes

$$\mathbf{P} = \mathbf{I} \cdot \frac{\hbar^2(3\pi)^{2/3}}{5m} n^{5/3}, \quad (\text{B.17})$$

where  $\mathbf{I}$  is the identity matrix. With this choice for the pressure tensor, equation (B.16) has effectively been decoupled from higher order moments and together with Eq. (B.9) it fully describes  $n$  and  $\mathbf{u}$ .

Although we have obtained what we set out to find, we will add a final approximation to the equations. We see that Eq. (B.16) contains a nonlinear term  $\mathbf{u} \otimes \mathbf{u}$ , which complicates the situation slightly. We will therefore consider the situation where the electric field only perturbs the electron density a small amount  $n_1$  from the equilibrium density  $n_0$ . At the same time, we will assume that the average velocity  $\mathbf{u}$  itself is a small perturbation of the equilibrium situation. In this approximation we get  $n \approx n_0$  and  $n\mathbf{u} \approx n_0\mathbf{u}$ , while the term  $\mathbf{u} \otimes \mathbf{u}$  in Eq. (B.16) simply is neglected. For the pressure we find

$$\begin{aligned} \nabla_{\mathbf{r}} \cdot \mathbf{P} &= \frac{\hbar^2(3\pi)^{2/3}}{5m} \nabla_{\mathbf{r}} (n_0 + n_1)^{5/3} \\ &\approx \frac{1}{3} \frac{\hbar^2(3\pi)^{2/3}}{m} n_0^{2/3} \nabla_{\mathbf{r}} n_1 \\ &= \frac{1}{3} v_F^2 m \nabla_{\mathbf{r}} n_1, \end{aligned} \quad (\text{B.18})$$

where we have used that  $k_F^3 = 3\pi^2 n$  for a parabolic band, and  $v_F = \hbar k_F / m$  is the Fermi velocity. Equation (B.16) therefore becomes

$$\frac{\partial(n_0\mathbf{u})}{\partial t} = -\frac{1}{3} v_F^2 \nabla_{\mathbf{r}} n_1 + \mathbf{F} \frac{n_0}{m}, \quad (\text{B.19})$$

which is linear as required.

The continuity equation in the linear approximation becomes

$$\frac{\partial n_1}{\partial t} = -\nabla_{\mathbf{r}} \cdot (n_0\mathbf{u}), \quad (\text{B.20})$$

and this equation together with Eq. (B.19) constitutes the linearized hydrodynamic equations. The equations can with some advantage be combined by taking the time derivative of Eq. (B.19) and inserting Eq. (B.20)

$$\frac{\partial^2(n_0\mathbf{u})}{\partial t^2} = \frac{1}{3} v_F^2 \nabla_{\mathbf{r}} (\nabla_{\mathbf{r}} \cdot (n_0\mathbf{u})) + \frac{\partial \mathbf{F}}{\partial t} \frac{n_0}{m}. \quad (\text{B.21})$$

Finally, we will make the replacements  $\mathbf{J}_f = -en\mathbf{u} \approx -en_0\mathbf{u}$  and  $\rho_f = -en_1$  and use that the force is given by  $\mathbf{F} = -e\mathbf{E}$ , whereby we obtain

$$\frac{\partial \rho_f}{\partial t} = -\nabla_{\mathbf{r}} \cdot \mathbf{J}_f, \quad (\text{B.22a})$$

$$\frac{\partial^2 \mathbf{J}_f}{\partial t^2} = \frac{1}{3}v_F^2 \nabla_{\mathbf{r}} (\nabla_{\mathbf{r}} \cdot \mathbf{J}_f) + \frac{\partial \mathbf{E}}{\partial t} \frac{e^2 n_0}{m}. \quad (\text{B.22b})$$

This is the form of the hydrodynamic equations that are used in the main text.



## C System of linear equations for the Mie coefficients

When applying the boundary conditions  $\Delta \mathbf{E}^{\parallel} = \mathbf{0}$ ,  $\Delta \mathbf{B}^{\parallel} = \mathbf{0}$  and  $\mathbf{J}^{\perp} = \mathbf{0}$  to the electric fields in Eqs. (3.39), (3.40) and (3.41), the following system of linear equations is obtained

$$-a_i^r h_i^{(1)}(x_D) + a_i^t j_i(x_T) = j_i(x_D), \quad (\text{C.1a})$$

$$-a_i^r [x_D h_i^{(1)}(x_D)]' + a_i^t [x_T j_i(x_T)]' = [x_D j_i(x_D)]', \quad (\text{C.1b})$$

$$-b_i^r \frac{[x_D h_i^{(1)}(x_D)]'}{k_D} + b_i^t \frac{[x_T j_i(x_T)]'}{k_T} + i c_i^t j_i(x_L) = \frac{[x_D j_i(x_D)]'}{k_D}, \quad (\text{C.1c})$$

$$-b_i^r x_D h_i^{(1)}(x_D) + b_i^t x_T j_i(x_T) = x_D j_i(x_D), \quad (\text{C.1d})$$

$$-i b_i^t \frac{l(l+1)}{x_T} j_i(x_T) + c_i^t j_i'(x_L) k_L \varepsilon_b \frac{\omega^2 + i\gamma\omega}{\omega_p^2} = 0, \quad (\text{C.1e})$$

where  $x_j = k_j R$  and  $k_D = \sqrt{\varepsilon_D} \omega / c$ . The wavenumbers  $k_T$  and  $k_L$  are given by Eqs. (3.19) and (3.22), respectively.



## **Publication A**

C. Tserkezis, J. R. Maack, Z. Liu., M. Wubs & N. A. Mortensen

**Robustness of the far-field response of nonlocal plasmonic ensembles**

Sci. Rep. **6**, 28441 (2016)

# SCIENTIFIC REPORTS

OPEN

## Robustness of the far-field response of nonlocal plasmonic ensembles

Christos Tserkezis<sup>1</sup>, Johan R. Maack<sup>1</sup>, Zhaowei Liu<sup>2</sup>, Martijn Wubs<sup>1,3</sup> & N. Asger Mortensen<sup>1,3</sup>

Received: 09 March 2016

Accepted: 03 June 2016

Published: 22 June 2016

Contrary to classical predictions, the optical response of few-nm plasmonic particles depends on particle size due to effects such as nonlocality and electron spill-out. Ensembles of such nanoparticles are therefore expected to exhibit a nonclassical inhomogeneous spectral broadening due to size distribution. For a normal distribution of free-electron nanoparticles, and within the simple nonlocal hydrodynamic Drude model, both the nonlocal blueshift and the plasmon linewidth are shown to be considerably affected by ensemble averaging. Size-variance effects tend however to conceal nonlocality to a lesser extent when the homogeneous size-dependent broadening of individual nanoparticles is taken into account, either through a local size-dependent damping model or through the Generalized Nonlocal Optical Response theory. The role of ensemble averaging is further explored in realistic distributions of isolated or weakly-interacting noble-metal nanoparticles, as encountered in experiments, while an analytical expression to evaluate the importance of inhomogeneous broadening through measurable quantities is developed. Our findings are independent of the specific nonclassical theory used, thus providing important insight into a large range of experiments on nanoscale and quantum plasmonics.

Plasmonics lies among the most prominent research fields in modern nanotechnology<sup>1–3</sup>, promising exciting applications and unravelling new phenomena as the length scale reduces<sup>4–6</sup>. Traditionally, noble metals constitute the material basis for novel plasmonic devices operating in the visible<sup>7</sup>, although many recent efforts are devoted to extensions towards the ultraviolet, infrared and THz parts of the spectrum<sup>8</sup>. A key issue in noble-metal plasmonics is its association with pronounced homogeneous broadening due to Ohmic losses in the metal<sup>9</sup> and enhanced Landau damping near the surface<sup>10,11</sup>. Within classical electrodynamics, and in the quasistatic regime, radiation losses are small and the limited quality factor of plasmon resonances reflects material losses<sup>12</sup>. In other words, homogeneous broadening is important. Furthermore, the commonly employed local-response approximation (LRA) of classical electrodynamics predicts size-independent resonances for the nowadays experimentally accessible small nanoparticles (NPs) in the quasistatic regime<sup>13</sup>. As a consequence, despite the increasing impact of plasmonics and the promotion of single-particle spectroscopy<sup>14</sup>, little, if any, emphasis has been placed on the role of inhomogeneous broadening due to size distribution — even in experiments on NP ensembles with a noticeable size variation.

The observation of size-dependent resonance shifts not anticipated from classical electrodynamics has recently renewed interest in plasmons in the sub-10-nm regime<sup>15–17</sup>. State-of-the-art experiments range from single-particle spectroscopy with the aid of tightly focused electron beams<sup>15–18</sup>, to optical far-field measurements sampling the response of NP ensembles<sup>19–23</sup>. In the latter case, nonlocal effects<sup>17,24</sup> and the concomitant inhomogeneous broadening can prove important for the interpretation of ensemble measurements. Ensemble averaging effects have been theoretically explored for exciton systems<sup>25</sup>, and for large-NP plasmonic collections dominated by retardation-driven redshifts<sup>26</sup>, but related studies in nonlocal plasmonics are still missing. The unambiguous observation of size-dependent resonance shifts in single-particle spectroscopy<sup>15,17,27</sup> encourages therefore to explore broadening phenomena related to size distribution: *What is the robustness of plasmonic nonlocal effects when subject to ensemble averaging?*

The influence of ensemble spectral averaging on the far-field response of nonlocal plasmonic NP collections is studied here theoretically, starting with the ideal case of a normal distribution of free-electron, Drude-like nanospheres. Complexity is subsequently increased by considering more realistic distributions, resembling experimental histograms<sup>28</sup>, of noble-metal NPs, for which additional loss mechanisms like interband transitions and

<sup>1</sup>Technical University of Denmark, Department of Photonics Engineering, Kgs. Lyngby, 2800, Denmark. <sup>2</sup>University of California, San Diego, Department of Electrical and Computer Engineering, La Jolla, CA 92093-0407, USA. <sup>3</sup>Technical University of Denmark, Center for Nanostructured Graphene, Kgs. Lyngby, 2800, Denmark. Correspondence and requests for materials should be addressed to C.T. (email: ctse@fotonik.dtu.dk) or N.A.M. (email: asger@mailaps.org)

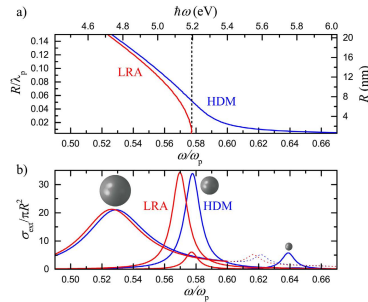


**Figure 1.** (a) Normalised frequency ( $\omega/\omega_p$ ) position of the dipolar plasmonic peak of a spherical NP described by the Drude model of equation (1), in air, as a function of its normalised radius  $R/\lambda_p$ , obtained within the LRA (red line) and HDM (blue line) models. The black dashed line displays the prediction of the quasistatic approximation,  $\omega_p/\sqrt{3}$ . The corresponding energy in eV and radius in nm are given at the top and right axis respectively, assuming a plasmon energy  $\hbar\omega_p = 9$  eV. (b) Extinction cross section ( $\sigma_{\text{ext}}$ ) spectra (normalised to the geometrical cross section  $\pi R^2$ ) for the NP of (a), for three radii,  $R/\lambda_p = 0.145$ ,  $R/\lambda_p = 0.051$ , and  $R/\lambda_p = 0.007$  (from left to right) within the LRA (red lines) and HDM (blue lines) models. For  $\hbar\omega_p = 9$  eV these radii correspond to 20, 7, and 1 nm, respectively. The quadrupolar mode of the largest NP is depicted by thin dotted lines.

electron quantum confinement are important (the latter affects Drude NPs as well). Through detailed simulations within the framework of Mie theory and its appropriate extensions<sup>13,24,29,30</sup>, we show that ensemble averaging can have significant implications in more ideal cases, but becomes practically negligible when all mechanisms related to homogeneous broadening are taken into account in noble-metal plasmonics, a behaviour preserved even when weak interparticle interactions are taken into account. Our findings are therefore expected to provide additional flexibility to the design and analysis of experiments on the nanoscale: On the one hand, analysing the far-field response of a NP collection on the basis of the ensemble mean size is proven sufficient for the purposes of most experimental studies. On the other hand, nonlocal effects are not concealed by single-NP losses in large ensembles, thus allowing to connect with single-particle electron-energy-loss studies<sup>15,17</sup>.

## Results and Discussion

**Nonlocality-induced plasmon blueshifts.** We first revisit the optical response of a small metallic nanosphere, embedded in air for simplicity. Our study is based on Mie theory<sup>13</sup> and its appropriate extension for nonlocal effects (see the Methods section for more details)<sup>31–33</sup>. The metal is described as a free-electron plasma with transverse ( $\varepsilon_t$ ) and longitudinal ( $\varepsilon_l$ ) dielectric function components given by the frequency- ( $\omega$ ) and wave vector- ( $\mathbf{k}$ ) dependent Drude<sup>13</sup> and hydrodynamic<sup>34,35</sup> models, respectively

$$\varepsilon_t(\omega) = \varepsilon_\infty - \frac{\omega_p^2}{\omega(\omega + i\gamma)}, \quad \varepsilon_l(\omega, \mathbf{k}) = \varepsilon_\infty - \frac{\omega_p^2}{\omega(\omega + i\gamma) - \beta^2 k^2}, \quad (1)$$

where  $\omega_p$  is the plasma frequency of the metal,  $\varepsilon_\infty$  is the background contribution of bound electrons and ions,  $\gamma$  is the damping rate,  $\beta$  the hydrodynamic parameter, and  $k_l$  the longitudinal wave number<sup>35</sup>. We take  $\varepsilon_\infty = 1$  and  $\gamma = 0.01 \omega_p$  to focus on the role of free electrons and ensure low loss (associated with homogeneous broadening). We further assume  $\beta = \sqrt{3/5} v_F$  as obtained within the Thomas–Fermi theory<sup>35</sup>, where  $v_F$  (taken equal to  $1.39 \times 10^6$  m s<sup>-1</sup> in the rest of the paper) is the Fermi velocity of the metal.

The size dependence of the frequency of the first (dipolar) plasmonic mode sustained by such a metallic nanosphere of radius  $R$  is plotted in Fig. 1a as obtained within LRA ( $\omega_{\text{LRA}}$ , red line) and the hydrodynamic Drude model (HDM) ( $\omega_{\text{HDM}}$ , blue line). To make our results scalable for different materials,  $\omega$  and  $R$  are normalised to the plasma frequency and wavelength,  $\omega_p$  and  $\lambda_p = 2\pi c/\omega_p$ , respectively. For a better illustration of the sizes and energies usually encountered, the corresponding plasmon energy (NP radius) is provided at the top (right) axis, assuming a typical value  $\hbar\omega_p = 9$  eV<sup>35</sup>. For very small NP sizes, LRA reproduces the quasistatic result,  $\omega_{\text{LRA}} = \omega_p/\sqrt{3}$  (vertical dashed line in Fig. 1a). For larger sizes, retardation causes the modes to drastically redshift and become wider, as also observed in the normalised extinction cross section ( $\sigma_{\text{ext}}$ ) spectra of Fig. 1b (red lines corresponding to different NP sizes within LRA). Higher-order modes will not concern us here, and the quadrupolar plasmon peak of the largest sphere in Fig. 1b is only shown by thin dotted lines. The small-size modal frequency saturation predicted by LRA gives place to a continuous blueshift when the metal nonlocal response is taken into account. Comparison between LRA and HDM (blue lines in Fig. 1b) immediately shows that the frequency shifts become larger as the NP size decreases, but no additional resonance broadening due to nonlocality is observed.

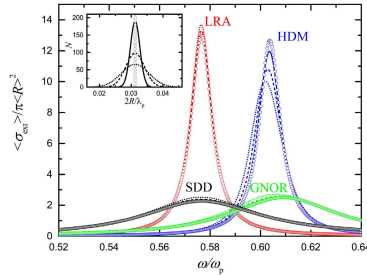


**Figure 2.** Averaged normalised extinction ( $\langle \sigma_{\text{ext}} \rangle$ ) spectra calculated for  $N = 1000$  NPs described by the dielectric function of equation (1) within the LRA (red lines), HDM (blue lines), GNOR (green lines) and SDD (black lines) models, for the size distributions shown in the inset. The average NP diameter is  $2(R)/\lambda_p = 0.031$ , which for  $\hbar\omega_p = 9$  eV corresponds to 4.3 nm, and the standard deviation of the normal distribution function is 0.2 (solid lines), 0.4 (dashed lines), and 0.6 (dotted lines). Open circles denote the corresponding spectra for the single mean-size NP, corresponding to the  $\delta$ -function distribution (open circles) of the inset.

A significantly different behaviour is expected in a statistical ensemble of small particles, where the strongly blueshifting modes of single NPs will overlap in a sequential manner, leading to important line broadening possibly even for narrow size distributions, in analogy to the effect of retardation on large NPs<sup>26</sup>. At this point we should also note that for the type of Drude metal described here, more detailed theories based on atomistic *ab initio* calculations predict frequency redshifts, instead of blueshifts, of similar magnitude, due to electron spill-out<sup>10,36–38</sup>. Indeed redshifts are measured for simple metals such as sodium<sup>38</sup>. Yet in noble metals such as silver and gold, the spill-out is less extended and the measured size-dependent blueshifts are well reproduced by HDM. An exact description of a specific material is beyond the scope of this paper, and simple nonlocal models should suffice for the study of ensemble averaging, regardless of the direction and origin of modal shifts.

**Inhomogeneous broadening in Drude-metal ensembles.** Ensemble spectral averaging is at a first step investigated by considering a collection of  $N = 1000$  of the NPs described above, with a mean diameter  $2(R)/\lambda_p = 0.031$  (corresponding to 4.3 nm for  $\hbar\omega_p = 9$  eV). The NP size follows normal distributions around this mean value as shown in the inset of Fig. 2, with standard deviations ranging from 0.2 (narrowest distribution, solid line) to 0.4 (dashed line) and 0.6 (widest distribution, dotted line). The extreme case of a  $\delta$ -function distribution, i.e., all NP diameters corresponding precisely to the mean value, is depicted by open dots. This kind of  $\delta$ -function distribution is exactly what one assumes in practice when disregarding ensemble averaging. We also note that, while the distributions of Fig. 2 are continuous functions, discrete size steps are taken in the simulations, small enough to achieve convergence of the averaged spectra. Apart from the LRA and HDM models, we also discuss calculations based on the commonly employed local size-dependent damping (SDD) model<sup>39</sup> and the Generalized Nonlocal Optical Response (GNOR) theory<sup>24</sup>. Within SDD, the damping parameter  $\gamma$  becomes size dependent,  $\gamma \rightarrow \gamma + A v_F / R$ , to effectively take into account the experimentally observed single-NP damping<sup>30</sup>. The constant  $A$ , usually taken equal to 1 (as we do here) although a large range of values can be found in literature, is introduced to phenomenologically describe the reduction of the free-electron path length and to account to some extent for quantum-size corrections in very small NPs<sup>19,39–42</sup>. On the other hand, GNOR reproduces size-dependent damping in a more physical way, by incorporating electron diffusion as a measure of a variety of electron-scattering effects, including Landau damping due to generation of electron-hole pairs<sup>43</sup>. In practice, one needs merely to replace  $\beta^2$  in equation (1) with  $\beta^2 + D(\gamma - i\omega)$ , where  $D$  is the diffusion constant of the metal. A thorough discussion on the determination of  $D$  can be found in a recent review by Raza *et al.*<sup>35</sup>; in general, it has to be chosen so as to reproduce the experimentally observed, and successfully reproduced by SDD models, plasmon damping. For the Drude-like NPs studied in this section, we find that the simple relation  $D \simeq v_F^2 / \gamma^{24}$  provides an excellent correspondence between the two models. However, it has been shown that more strict calculations are required in the case of noble metals<sup>44</sup>. While, in this respect, GNOR remains a phenomenological model, its strength is that, for arbitrarily shaped plasmonic NPs, it reproduces both the size-dependent blueshifts and the damping of plasmon modes by a simple correction in the dynamics of the free-electron fluid of HDM, whereas SDD models only capture the damping effects.

With these models at hand, we study in Fig. 2 how spectral averaging compares to single-NP response. Clearly, for the local models (LRA and SDD, red and black lines respectively), averaging does not practically affect the spectra. For all size distributions, the average extinction  $\langle \sigma_{\text{ext}} \rangle$ , normalised to the geometrical cross section of the mean-size NP,  $\pi(R)^2$  (which is known in experiments), reproduces almost perfectly the spectrum of the individual mean-size NP, without frequency shifts or line broadening. Comparison with Fig. 1 shows that, in the size range of interest, local theories have already reached the quasistatic limit and the plasmon frequencies do not shift

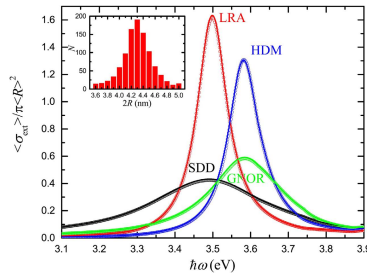


**Figure 3.** Averaged normalised extinction spectra calculated for  $N = 1000$  silver NPs described by the experimental dielectric function of Johnson and Christy<sup>45</sup> within the LRA (red line), HDM (blue line), GNOR (green line), and SDD (black line) models, for the size distribution shown by the histogram of the inset. The mean NP diameter is  $2\langle R \rangle = 4.3$  nm. Open circles denote the corresponding spectra for the single mean-size NP.

further, thus explaining the behaviour of the calculated spectra. The case becomes much different however when the spectra are size-dependent because of nonlocality, as is particularly pronounced by the HDM results. The incomplete spectral overlap for NPs of different sizes leads to an obvious broadening of the plasmon peaks, larger as the size distribution becomes wider. In addition, since larger NPs are characterised by larger extinction values, the overlap between large and small particles leads to a decrease of  $\langle \sigma_{ext} \rangle$ , and to a gradual redshift of the ensemble resonance comparing with the single nonlocal mean-size NP. One may therefore conclude that statistical averaging can lead to significant deviations in experimental far-field measurements on ensembles of plasmonic NPs with wide size distributions. Nevertheless, since HDM disregards size-dependent damping mechanisms, it is crucial to take such effects into account. In view of the previous discussion, this is straightforward within GNOR (green spectra in Fig. 2). The differences between single-NP and ensemble response are now smoothed, leading to smaller additional modal shifts and almost negligible line broadening due to size inhomogeneity: the spectral width is mainly due to single-particle nonlocal broadening.

**Inhomogeneous broadening in noble-metal ensembles.** The important result of negligible effect of spectral averaging when single-NP size-dependent damping is taken into account may be appealing, but its validity was displayed only for ideal Drude metals and for normal size distributions. In order to connect with more practical, experimentally feasible situations, it is therefore important to carry out similar statistical studies for more realistic distributions in noble metals. We consider a collection of  $N = 1000$  silver NPs, described by the experimental dielectric function ( $\epsilon_{exp}$ ) of Johnson and Christy<sup>45</sup>, following the size distribution shown by the histogram of the inset of Fig. 3. In order to apply the HDM, SDD and GNOR models, we obtain  $\epsilon_{\infty}$  in equation (1) from the experimental values by subtracting the Drude part:  $\epsilon_{\infty} = \epsilon_{exp} + \omega_p^2/[\omega(\omega + i\gamma)]$ , taking  $\hbar\omega_p = 8.99$  eV and  $\hbar\gamma = 0.025$  eV, values which describe bulk silver excellently. For SDD and GNOR we further assume  $A = 1$  and  $D = 3\sqrt{10}Av_p^2/(5\omega_p)$ , respectively<sup>35</sup>. The calculated spectra of Fig. 3 display now an almost negligible difference between single-NP and averaged spectra, even for the more pronounced in Fig. 2 HDM case. Homogeneous line broadening dominates the ensemble optical response, especially when single-NP size-dependent damping is taken into account within the more complete GNOR theory. This observation further strengthens our conclusion that inhomogeneous line broadening is not pronounced in most realistic NP ensembles (despite the non-negligible nonlocal response). Far-field optical experiments on small-NP ensembles can indeed be conducted for the observation of nonlocal frequency shifts, and their interpretation can be performed on the basis of the properties of the mean-size NP in the collection.

In addition to the study of isolated NPs, and the displayed robustness of their far-field optical response, an aspect that we have so far disregarded is the interaction between NPs in the ensemble. It is widely known that once plasmonic NPs are brought close to each other their interaction leads to significant modal redshifts, increasing as the interparticle gap is reduced<sup>46</sup>. A modified optical response is therefore expected for an ensemble of interacting small NPs, where two competing mechanisms, those of size-dependent blueshifts and interaction-induced redshifts are simultaneously present. The importance of this interplay is explored here, assuming that the average NP distance does not become smaller than  $R$ , thus preventing the particles from entering the nearly-touching regime, where purely quantum effects such as tunnelling become relevant<sup>47,48</sup>. Such distance control can be achieved nowadays with unprecedented precision, in dilute solutions with DNA- or ligand-functionalised NPs<sup>30,49–51</sup>. We assume  $N_p = 1000$  dimers of identical, 4.3-nm silver NPs, separated by a gap of width  $d$ , as shown schematically in the inset of Fig. 4. The interparticle gap width follows a normal distribution around its mean value,  $\langle d \rangle = 3.2$  nm, ranging from 4.3 nm (a full NP width separating the two spheres) to 2.1 nm, as shown by the histogram of the inset. Comparison between Figs 3 and 4 shows that NP interaction can lead to a small plasmon redshift, of about 3–4 nm, both for the local case (only LRA is shown in Fig. 4 as the effect of SDD is well reproduced by its nonlocal

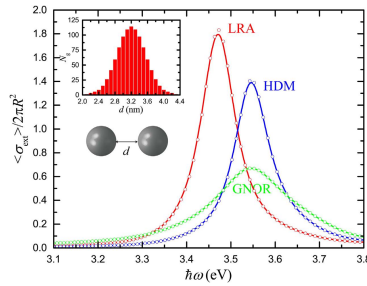


**Figure 4.** Averaged normalised extinction ( $\langle \sigma_{\text{ext}} \rangle / 2\pi R^2$  here, since the geometrical cross section corresponds to the area occupied by two NPs) spectra calculated for  $N_s = 1000$  silver NP dimers (both NPs have a diameter of 4.3 nm, separated by a gap of width  $d$ , as shown schematically in the inset, within the LRA (red line), HDM (blue line), and GNOR (green line) models. The gap width follows the normal distribution of the histogram of the inset, with a mean value  $\langle d \rangle = 3.2$  nm. Open circles denote the corresponding spectra for the single mean-gap dimer.

counterpart, GNOR) and the nonlocal models. These relatively weak interactions owe their reduced strength to the small NP size and become important, according to our simulations, only for interparticle distances smaller than the NP radius. More importantly, the additional line broadening caused by such interactions is practically negligible, as it is immediately clear through comparison between Figs 3 and 4, and in any case it does not originate from the nonlocal optical response. It is therefore adequate, in most cases of practical interest, to disregard interactions and assume isolated NPs instead. Nevertheless, for a more strict description, it is still sufficient to take interactions into account through the average NP distance in the ensemble, as can be verified by the open dots in Fig. 4, which reproduce almost perfectly the gap-averaged spectra.

**Analytical evaluation of the importance of inhomogeneous broadening.** Having considered situations where inhomogeneous broadening can be either strong or negligible, a simple way to decide on its importance without resorting to detailed simulations is desirable. To this end, we develop an analytical model which describes inhomogeneous broadening in terms of just the first two negative-order (or, with some further approximations, positive-order) moments of any NP-size distribution function. In practice, with a simple experimental size histogram at hand, one should be immediately able to tell whether the spectra are affected by inhomogeneous broadening. We begin by considering the dipole resonance in a single metallic NP, neglecting homogeneous broadening for the moment. Such a resonance can then be described by a spectral function  $F(\omega, R) \simeq \delta(\omega - \omega_{\text{LRA}} - \eta/R)$ , where  $\eta$  ( $\propto \beta$  in our case) gives the strength of the leading-order  $1/R$  correction associated with nonlocal response<sup>33</sup>. In an ensemble of non-interacting particles characterised by a size distribution  $P(R)$ , the ensemble-averaged spectral function will be  $\langle F(\omega) \rangle = \int dR F(\omega, R) P(R)$ . Our aim is to express the ensemble-averaged optical properties, such as the resonance frequency  $\langle \omega \rangle$ , with the aid of the  $n$ th-order statistical moments of the particle ensemble, i.e.  $\langle R^n \rangle = \int_0^\infty dR R^n P(R)$ . The homogeneous delta-function line shape allows to express the  $n$ th-order spectral moment  $\langle \omega^n \rangle = \int d\omega \omega^n \langle F(\omega) \rangle$  directly in terms of moments of the particle-size distribution,

$$\langle \omega^n \rangle = \int dR (\omega_{\text{LRA}} + \eta/R)^n P(R) = \langle (\omega_{\text{LRA}} + \eta/R)^n \rangle. \quad (2)$$

It is then straightforward to derive expressions for  $\langle \omega \rangle$  and the inhomogeneous broadening width,  $\Delta\omega_{\text{inhom}} = \sqrt{\langle \omega^2 \rangle - \langle \omega \rangle^2}$ , through the statistical moments of the particle-size distribution. As a key result, which allows to estimate the inhomogeneous broadening only in terms of the first two statistical moments of  $P(R)$  and the nonlocal blueshift  $\delta\omega_{\text{LRA-NL}} = \langle \omega \rangle - \omega_{\text{LRA}} = \eta \langle R^{-1} \rangle$  ( $\simeq \eta / \langle R \rangle$  in a more crude approximation), it is shown that (see the related Discussion in the Supplementary Information)

$$\frac{\Delta\omega_{\text{inhom}}}{\delta\omega_{\text{LRA-NL}}} = \sqrt{\frac{\langle R^{-2} \rangle - \langle R^{-1} \rangle^2}{\langle R^{-1} \rangle^2}} \simeq \sqrt{\frac{\langle R^2 \rangle - \langle R \rangle^2}{\langle R \rangle^2}}. \quad (3)$$

The first equality relates to the first and second negative-order moments of  $P(R)$ , which are quite unusual ways of characterising a particle-size distribution – in most other contexts the positive-order moments (such as the mean value and variance) are the ones of interest. In the Discussion of the Supplementary Information we demonstrate the link between negative- and positive-order moments to obtain the second approximate identity in equation (3), which links directly to the relative particle-size fluctuation  $\Delta R / \langle R \rangle$ . This result holds for any description beyond classical electrodynamics that gives a  $1/R$  leading-order blueshift of the LRA resonance

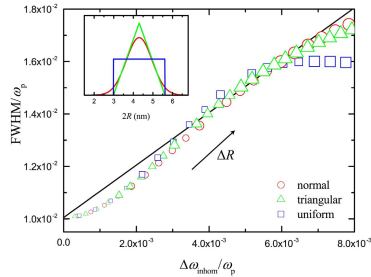


**Figure 5.** Parametric plot (open symbols) of  $\Delta\omega_{\text{inhom}}$  calculated from equation (3) versus FWHM obtained from simulations for a Drude-like NP within HDM ( $\beta = \sqrt{3/5} v_F$ ,  $\gamma = 0.01\omega_p$  in equation (1), for the size distributions shown in the inset. The average NP diameter is fixed at  $2\langle R \rangle/\lambda_p = 0.0312$  (corresponding to 4.3 nm when  $\hbar\omega_p = 9$  eV). Three different size distributions are plotted: uniform (blue line), triangular (green line) and (truncated) normal (red line). For the uniform (blue squares) and triangular (green triangles) cases, the distribution width increases from  $0.13 \cdot 10^{-2}$  to  $2.80 \cdot 10^{-2}$  (0.18 nm to 3.86 nm), while the standard deviation of the normal distribution (red circles) increases from  $0.32 \cdot 10^{-3}$  to  $7.00 \cdot 10^{-3}$  (0.044 nm to 0.965 nm). Increasing point size schematically depicts increasing distribution width. The black line denotes  $\text{FWHM} = \Delta\omega_{\text{inhom}} + \text{FWHM}_0$ .

frequency. Most importantly, it does not change if we replace  $\eta$  with  $-\eta$  to describe a corresponding  $1/R$  redshift, so that our findings can be easily generalised to include other nonclassical effects, as anticipated above.

To test the validity of equation (3), we use it to evaluate  $\Delta\omega_{\text{inhom}}$  for certain distribution shapes and widths, assuming for simplicity  $\eta = \beta$ . The result is then compared to the full-width-half-maximum (FWHM) of the (averaged) plasmon peak calculated in each case by simulations performed for an ideal free-electron metal within HDM, with  $\beta = \sqrt{3/5} v_F$  and  $\gamma = 0.01\omega_p$ . As long as equation (3) holds, for different widths of the distribution,  $\Delta\omega_{\text{inhom}}$  is expected to follow a linear relation with FWHM. In Fig. 5 this is done for the three distributions shown in the inset: uniform, triangular and (truncated) normal. These examples are rather extreme situations, but in all cases an almost linear relation between  $\Delta\omega_{\text{inhom}}$  and FWHM, following the line  $\text{FWHM} = \Delta\omega_{\text{inhom}} + \text{FWHM}_0$  (black line in Fig. 5), where  $\text{FWHM}_0$  is the FWHM of the single mean-size NP, is indeed observed. For most distribution widths, all three examples give results that lie close to this line, indicating that the simple formula of equation (3) not only gives a good estimate of inhomogeneous broadening, regardless of the shape of the distribution, but can also be used to estimate the FWHM. It is worth noting that, for the uniform distribution, which is one of the most extreme situations to encounter in practice, larger deviations from the predictions of equation (3) are calculated as the distribution width becomes wider. This is due to the fact that, for wider distributions, a significant number of larger NPs is present in the ensemble. The extinction cross section of these NPs, which scales with  $R^3$ , dominates the optical response, leading to a shifting of the averaged far-field response towards longer wavelengths. This effect is efficiently masked in more realistic situations, like the triangular and normal distributions of Fig. 5, for which larger NPs form just the tail of the distribution function, but cannot be neglected in a wide uniform distribution. Finally, it should also be stressed that, while the average NP size considered in Fig. 5 corresponds to 4.3 nm, the small-NP tails of the distribution functions are allowed to enter the sub-nm region, where classical or nonlocal electrodynamics are expected to fail, and approaches based either on quantum-corrected models<sup>15,52</sup> or fully quantum-mechanical calculations<sup>36,37,53</sup> should be employed. Nevertheless, such NP sizes, for which plasmonic effects are negligible and cluster fluorescence dominates instead<sup>54</sup>, concern only the tails of the widest distribution functions in Fig. 5, for which small deviations already start to appear. Consequently, calculating the corresponding spectra within HDM or GNOR will not practically affect our conclusions.

## Conclusion

In summary, the effect of inhomogeneous broadening of plasmon resonances due to nonlocal response in ensembles of small plasmonic NPs was explored through detailed simulations and analytical modelling. While inhomogeneous broadening is negligible in the LRA, it can be an important issue for Drude-like metals, especially within the standard HDM approach which neglects size-dependent damping in individual NPs. Crucially, however, ensemble averaging is shown to produce almost negligible deviations in most situations of practical interest, as illustrated for realistic size distributions of noble-metal NPs, and within the more accurate GNOR model. Nanoscale experiments involving large numbers of NPs can thus be designed and analysed in terms of the response of the mean-size NP in the ensemble, while far-field spectra of large NP collections are still expected to display the fingerprints of nonlocality, as in single-particle spectroscopies. We derived a simple equation to directly identify whether inhomogeneous broadening becomes important, simply through knowledge of the size distribution function in an ensemble. Our work provides therefore a valuable, general tool for the analysis of far-field optical spectra in modern experiments on plasmonics.

## Methods

**Nonlocal Mie theory.** Here we summarise the fully-retarded Mie theory for a spherical plasmonic particle treated within HDM (and GNOR through a simple substitution of the hydrodynamic  $\beta$  parameter). The multipolar response of a sphere including nonlocal effects was determined by Ruppin<sup>29,31</sup> by extending Mie theory<sup>13</sup> to take into account the excitation of longitudinal waves. In the framework of Mie theory, the extinction cross section of a sphere of radius  $R$  embedded in a homogeneous host medium is given by<sup>13</sup>

$$\sigma_{\text{ext}} = -\frac{2\pi}{k_h^2} \sum_{\ell=1}^{+\infty} (2\ell + 1) \text{Re}(t_\ell^{\text{TE}} + t_\ell^{\text{TM}}), \quad (4)$$

where  $\ell$  denotes the angular momentum and  $k_h$  is the wave number in the host medium, which is described by a dielectric function  $\varepsilon_h$ . Assuming that the magnetic permeabilities, both in the sphere and in the host medium are equal to 1, the nonlocal scattering coefficients are<sup>29,31–33</sup>

$$t_\ell^{\text{TE}} = \frac{-j_\ell(x_i)[x_h j_\ell(x_h)]' + j_\ell(x_h)[x_i j_\ell(x_i)]'}{j_\ell(x_i)[x_h h_\ell^+(x_h)]' - h_\ell^+(x_h)[x_i j_\ell(x_i)]'}, \quad (5)$$

$$t_\ell^{\text{TM}} = \frac{-\varepsilon_j j_\ell(x_i)[x_h j_\ell(x_h)]' + \varepsilon_h j_\ell(x_h)[x_i j_\ell(x_i)]' + \Delta_\ell}{\varepsilon_j j_\ell(x_i)[x_h h_\ell^+(x_h)]' - \varepsilon_h h_\ell^+(x_h)[x_i j_\ell(x_i)]' + \Delta_\ell}, \quad (6)$$

where  $j_\ell(x)$  and  $h_\ell^+(x)$  are the spherical Bessel and first-type Hankel functions, respectively, while  $x_h = k_h R$  and  $x_i = k_i R$ . Here  $k_i$  is the (transverse) wave number inside a sphere described by a transverse dielectric function  $\varepsilon_i$ . The nonlocal correction  $\Delta_\ell$  to the Mie coefficients is given as

$$\Delta_\ell = \ell(\ell + 1) j_\ell(x_i) \frac{\varepsilon_i - \varepsilon_\infty}{\varepsilon_\infty} \frac{j_\ell(x_i)}{x_i j_\ell'(x_i)}, \quad (7)$$

where  $x_i = k_i R$  and  $k_i$  is the longitudinal wave number in the sphere, associated with the longitudinal dielectric function  $\varepsilon_i$ , which is frequency- and wave vector-dependent. The dispersion of longitudinal waves is given by  $\varepsilon_i(\omega, \mathbf{k}) = 0$ . In the limiting case where  $\Delta_\ell = 0$  we retrieve the local result of standard Mie theory. All numerical results for isolated NPs have been obtained from numerical evaluations of equation (4). The corresponding results for NP dimers were obtained by use of a commercial finite-element method solver (COMSOL Multiphysics 5.0, RF module), using the appropriate extension to include nonlocal effects<sup>55,56</sup>.

## References

- Maier, S. A. *Plasmonics: Fundamentals and Applications* (Springer, 2007).
- Brongersma, M. L. Introductory lecture: nanoplasmonics. *Faraday Discuss.* **178**, 9–36 (2015).
- Baev, A., Prasad, P. N., Agren, H., Samoc, M. & Wegener, M. Metaphotonics: An emerging field with opportunities and challenges. *Phys. Rep.* **594**, 1–60 (2015).
- Editorial. Focusing in on applications. *Nature Nanotechnology* **10**, 1 (2015).
- Brongersma, M. L., Halas, N. J. & Nordlander, P. Plasmon-induced hot carrier science and technology. *Nature Nanotechnology* **10**, 25–34 (2015).
- Koenderink, A. F., Ali, A. & Polman, A. Nanophotonics: shrinking light-based technology. *Science* **348**, 516–521 (2015).
- Murray, W. A. & Barnes, W. L. Plasmonic materials. *Adv. Mater.* **19**, 3771–3782 (2007).
- Naik, G. V., Shalae, V. M. & Boltasseva, A. Alternative plasmonic materials: beyond gold and silver. *Adv. Mater.* **25**, 3264–3294 (2013).
- Khurging, J. B. How to deal with the loss in plasmonics and metamaterials. *Nature Nanotechnology* **10**, 2–6 (2015).
- Yan, W., Wubs, M. & Mortensen, N. A. Projected dipole model for quantum plasmonics. *Phys. Rev. Lett.* **115**, 137403 (2015).
- Jin, D. *et al.* Quantum-spillover-enhanced surface-plasmonic absorption at the interface of silver and high-index dielectrics. *Phys. Rev. Lett.* **115**, 193901 (2015).
- Wang, F. & Shen, Y. R. General properties of local plasmons in metal nanostructures. *Phys. Rev. Lett.* **97**, 206806 (2006).
- Bohren, C. F. & Huffman, D. R. *Absorption and Scattering of Light by Small Particles* (Wiley, 1983).
- Olson, J. *et al.* Optical characterization of single plasmonic nanoparticles. *Chem. Soc. Rev.* **44**, 40–57 (2015).
- Scholl, J. A., Koh, A. L. & Dionne, J. A. Quantum plasmon resonances of individual metallic nanoparticles. *Nature* **483**, 421–427 (2012).
- Raza, S. *et al.* Blueshift of the surface plasmon resonance in silver nanoparticles studied with EELS. *Nanophotonics* **2**, 131–138 (2013).
- Raza, S. *et al.* Multipole plasmons and their disappearance in few-nanometre silver nanoparticles. *Nature Communications* **6**, 8788 (2015).
- Wiener, A. *et al.* Electron-energy loss study of nonlocal effects in connected plasmonic nanoprisms. *ACS Nano* **7**, 6287–6296 (2013).
- Baida, H. *et al.* Quantitative determination of the size dependence of surface plasmon resonance damping in single Ag@SiO<sub>2</sub> nanoparticles. *Nano Lett.* **9**, 3463–3469 (2009).
- Taylor, R. W. *et al.* Precise subnanometer plasmonic junctions for SERS within gold nanoparticle assemblies using cucurbit[*n*]uril “glue”. *ACS Nano* **5**, 3878–3887 (2011).
- Grammatikopoulos, S. *et al.* Self-assembled Au nanoparticles on heated Corning glass by dc magnetron sputtering: size-dependent surface plasmon resonance tuning. *J. Nanopart. Res.* **15**, 1446 (2013).
- Ferry, V. E., Smith, I. M. & Alivisatos, A. P. Symmetry breaking in tetrahedral chiral plasmonic nanoparticle assemblies. *ACS Photon.* **1**, 1189–1196 (2014).
- Tserkezis, C. *et al.* Optical response of metallic nanoparticle heteroaggregates with subnanometric gaps. *Part. Part. Syst. Charact.* **31**, 152–160 (2014).
- Mortensen, N. A., Raza, S., Wubs, M., Søndergaard, T. & Bozhevolnyi, S. I. A generalized non-local optical response theory for plasmonic nanostructures. *Nature Communications* **5**, 3809 (2014).
- Ruppin, R. Optical absorption by excitons in microcrystals. *J. Phys. Chem. Solids* **50**, 877–882 (1989).

26. Pelton, M. & Bryant, G. W. *Introduction to Metal-Nanoparticle Plasmonics* (Wiley, 2013).
27. Ouyang, F., Batson, P. E. & Isaacson, M. Quantum size effects in the surface-plasmon excitation of small metallic particles by electron-energy-loss spectroscopy. *Phys. Rev. B* **46**, 15421–15425 (1992).
28. Nallathamby, P. D., Huang, T. & Xu, X.-H. N. Design and characterization of optical nanorulers of single nanoparticles using optical microscopy and spectroscopy. *Nanoscale* **2**, 1715–1722 (2010).
29. Ruppin, R. Optical properties of small metal spheres. *Phys. Rev. B* **11**, 2871–2876 (1975).
30. Kreibig, U. & Genzel, L. Optical absorption of small metallic particles. *Surf. Sci.* **156**, 678–700 (1985).
31. Ruppin, R. Optical properties of a plasma sphere. *Phys. Rev. Lett.* **31**, 1434–1437 (1973).
32. David, C. & García de Abajo, F. J. Spatial nonlocality in the optical response of metal nanoparticles. *J. Phys. Chem. C* **115**, 19470–19475 (2011).
33. Christensen, T. *et al.* Nonlocal response of metallic nanospheres probed by light, electrons, and atoms. *ACS Nano* **8**, 1745–1758 (2014).
34. McMahon, J. M., Gray, S. K. & Schatz, G. C. Nonlocal optical response of metal nanostructures with arbitrary shape. *Phys. Rev. Lett.* **103**, 097403 (2009).
35. Raza, S., Bozhevolnyi, S. I., Wubs, M. & Mortensen, N. A. Nonlocal optical response in metallic nanostructures. *J. Phys. Condens. Matter* **27**, 183204 (2015).
36. Stella, L., Zhang, P., García-Vidal, F. J., Rubio, A. & García-González, P. Performance of nonlocal optics when applied to plasmonic nanostructures. *J. Phys. Chem. C* **117**, 8941–8949 (2013).
37. Teperik, T. V., Nordlander, P., Aizpurua, J. & Borisov, A. G. Robust subnanometric plasmon ruler by rescaling of the nonlocal optical response. *Phys. Rev. Lett.* **110**, 263901 (2013).
38. Toscano, G. *et al.* Resonance shifts and spill-out effects in self-consistent hydrodynamic nanoplasmonics. *Nature Communications* **6**, 7132 (2015).
39. Kreibig, U. & v. Fragstein, C. The limitation of electron mean free path in small silver particles. *Z. Physik* **224**, 307–323 (1969).
40. Kawabata, A. & Kubo, R. Electronic properties of fine metallic particles. II. Plasma resonance absorption. *J. Phys. Soc. Jpn.* **21**, 255–284 (1966).
41. Kraus, W. A. & Schatz, G. C. Plasmon resonance broadening in small metal particles. *J. Chem. Phys.* **79**, 6130–6139 (1983).
42. Del Fatti, N., Vallée, F., Flytzanis, C., Hamaoka, Y. & Nakamura, A. Electron dynamics and surface plasmon resonance nonlinearities in metal nanoparticles. *Chem. Phys.* **251**, 215–226 (2000).
43. Li, X., Xiao, D. & Zhang, Z. Landau damping of quantum plasmons in metal nanostructures. *New. J. Phys.* **15**, 023011 (2013).
44. Raza, S., Wubs, M., Bozhevolnyi, S. I. & Mortensen, N. A. Nonlocal study of ultimate plasmon hybridization. *Opt. Lett.* **40**, 839–842 (2015).
45. Johnson, P. B. & Christy, R. W. Optical constants of the noble metals. *Phys. Rev. B* **6**, 4370–4379 (1972).
46. Romero, I., Aizpurua, J., Bryant, G. W. & García de Abajo, F. J. Plasmons in nearly touching metallic nanoparticles: singular response in the limit of touching dimers. *Opt. Express* **14**, 9988–9999 (2006).
47. Savage, K. J. *et al.* Revealing the quantum regime in tunnelling plasmonics. *Nature* **491**, 574–577 (2012).
48. Scholl, J. A., García-Etxarri, A., Koh, A. L. & Dionne, J. A. Observation of quantum tunneling between two plasmonic nanoparticles. *Nano Lett.* **13**, 564–569 (2013).
49. Aslan, K., Luhrs, C. C. & Pérez-Luna, V. H. Controlled and reversible aggregation of biotinylated gold nanoparticles with straptalavidin. *J. Phys. Chem. B* **108**, 15631–15639 (2004).
50. Hofman, A., Schmiel, P., Stein, B. & Graf, C. Controlled formation of gold nanoparticle dimers using multivalent thiol ligands. *Langmuir* **27**, 15165–15175 (2011).
51. Fan, J. A. *et al.* DNA-enabled self-assembly of plasmonic nanoclusters. *Nano Lett.* **11**, 4859–4864 (2011).
52. Esteban, R., Borisov, A. G., Nordlander, P. & Aizpurua, J. Bridging quantum and classical plasmonics with a quantum-corrected model. *Nature Communications* **3**, 825 (2012).
53. Barbry, M. *et al.* Atomistic near-field nanoplasmonics: reaching atomic-scale resolution in nanooptics. *Nano Lett.* **15**, 3410–3419 (2015).
54. Wei, J. *et al.* Lysozyme-stabilized gold fluorescent cluster: Synthesis and application as Hg<sup>2+</sup> sensor. *Analyst* **135**, 1406–1410 (2010).
55. Toscano, G., Raza, S., Jaou, A.-P., Mortensen, N. A. & Wubs, M. Modified field enhancement and extinction by plasmonic nanowire dimers due to nonlocal response. *Opt. Express* **20**, 4176–4188 (2012).
56. Nanoplasmonics Lab, www.nanopl.org.

## Acknowledgements

Stimulating discussions with Wei Yan, and help by Søren Raza with the COMSOL nonlocal extension, are gratefully acknowledged. C.T. was supported by funding from the People Programme (Marie Curie Actions) of the European Union's Seventh Framework Programme (FP7/2007–2013) under REA grant agreement number 609405 (COFUNDPostdocDTU). We gratefully acknowledge support from the Villum Foundation via the VKR Centre of Excellence NATEC-II and from the Danish Council for Independent Research (FNU 1323-00087). The Center for Nanostructured Graphene is sponsored by the Danish National Research Foundation, Project DNRF103.

## Author Contributions

All authors contributed to the conception of the project and writing of the manuscript. C.T. and J.R.M. performed the simulations, C.T., J.R.M., M.W. and N.A.M. analysed the results.

## Additional Information

**Supplementary information** accompanies this paper at <http://www.nature.com/srep>

**Competing financial interests:** The authors declare no competing financial interests.

**How to cite this article:** Tserkezis, C. *et al.* Robustness of the far-field response of nonlocal plasmonic ensembles. *Sci. Rep.* **6**, 28441; doi: 10.1038/srep28441 (2016).



This work is licensed under a Creative Commons Attribution 4.0 International License. The images or other third party material in this article are included in the article's Creative Commons license, unless indicated otherwise in the credit line; if the material is not included under the Creative Commons license, users will need to obtain permission from the license holder to reproduce the material. To view a copy of this license, visit <http://creativecommons.org/licenses/by/4.0/>

# Robustness of the far-field response of nonlocal plasmonic ensembles: Supplementary Information

Christos Tserkezis<sup>1,\*</sup>, Johan R. Maack<sup>1</sup>, Zhaowei Liu<sup>2</sup>, Martijn Wubs<sup>1,3</sup>, and N. Asger Mortensen<sup>1,3,\*</sup>

<sup>1</sup>Technical University of Denmark, Department of Photonics Engineering, Kgs. Lyngby, 2800, Denmark

<sup>2</sup>University of California, San Diego, Department of Electrical and Computer Engineering, La Jolla, CA 92093-0407, USA

<sup>3</sup>Technical University of Denmark, Center for Nanostructured Graphene, Kgs. Lyngby, 2800, Denmark  
[ctse@fotonik.dtu.dk](mailto:ctse@fotonik.dtu.dk); [asger@mailaps.org](mailto:asger@mailaps.org)

## Supplementary Discussion

### Derivation of equation (3) of the main text

In the main text we have defined the inhomogeneous broadening width as

$$\Delta\omega_{\text{inhom}} = \sqrt{\langle\omega^2\rangle - \langle\omega\rangle^2} \quad (\text{S1})$$

From equation (2) of the main text, the first- and second-order moments of  $\omega$  are

$$\langle\omega\rangle = \langle(\omega_{\text{LRA}} + \eta/R)\rangle \quad (\text{S2})$$

and

$$\langle\omega^2\rangle = \langle(\omega_{\text{LRA}} + \eta/R)^2\rangle, \quad (\text{S3})$$

respectively. Then

$$\Delta\omega_{\text{inhom}} = \sqrt{\langle(\omega_{\text{LRA}} + \frac{\eta}{R})^2\rangle - \langle(\omega_{\text{LRA}} + \frac{\eta}{R})\rangle^2} = \sqrt{\langle\omega_{\text{LRA}}^2 + \frac{2\omega_{\text{LRA}}\eta}{R} + \frac{\eta^2}{R^2}\rangle - \eta^2} = \eta\sqrt{\langle\frac{1}{R^2}\rangle - \langle\frac{1}{R}\rangle^2}. \quad (\text{S4})$$

In the above we have taken into account that (naturally)  $\langle\omega_{\text{LRA}}\rangle = \omega_{\text{LRA}}$  and  $\langle\eta\rangle = \eta$ . Using  $\delta\omega_{\text{LRA}\rightarrow\text{NL}} = \eta\langle R^{-1}\rangle$ , it is then straightforward to derive equation (3) of the main text.

### Statistical moments: relating negative to positive moments

For a narrow distribution function  $P(R)$ , without significant small- and large-particle tails, the negative-order moments appearing in the first equality of equation (3) of the main text can be expressed in terms of the more common positive-order moments, to give the approximate result on the right-hand side of equation (3) of the main text. This challenge is illustrated in Supplementary Fig. 1.

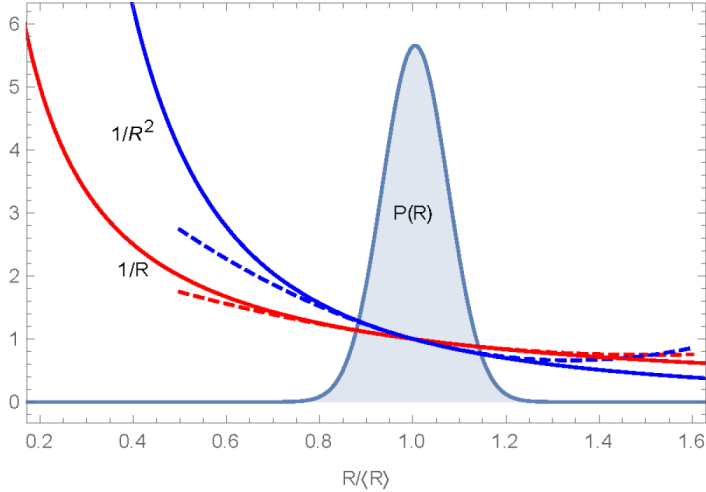
For the first negative-order moment,  $R^{-1}$  can be expressed as a Taylor series expanded around the average of the distribution,  $R_0 = \langle R\rangle$ ,

$$\frac{1}{R} = \sum_{n=0}^{+\infty} \frac{1}{R_0^{n+1}} (R_0 - R)^n = \frac{1}{R_0} - \frac{1}{R_0^2} (R - R_0) + \frac{2}{2R_0^3} (R - R_0)^2 \dots, \quad (\text{S5})$$

and then the moment  $\langle R^{-1} \rangle$  can be calculated with

$$\langle R^{-1} \rangle = \int_{-\infty}^{+\infty} R^{-1} P(R) dR = \int_{-\infty}^{+\infty} \sum_{n=0}^{+\infty} \frac{1}{R_0^{n+1}} (R_0 - R)^n P(R) dR. \quad (\text{S6})$$

In this expression,  $R^{-1}$  and the Taylor expansion go to infinity when  $R = 0$ , which may cause the integral to diverge. It must be therefore required that  $P(R) = 0$  for  $R \leq 0$ , which occurs of course for any realistic function  $P(R)$ . Furthermore, the summation is performed over infinite terms, and there is no immediate reason to truncate it. In fact, if  $R > 2R_0$  each subsequent  $n + 1$  term in the sum will be larger in absolute value than the previous,  $n$ , and of opposite sign. To be able to truncate this series, we must ensure that each  $n + 1$  term is smaller than the previous one, and this is done by requiring that  $P(R) = 0$  for  $R \geq 2R_0$ .



**Supplementary Figure 1:** Taylor series approximation of negative-order moments for a narrow distribution function. The dashed lines illustrate Taylor series approximations to the first and second negative-order moments, see equations (S7) and (S10).

We can now derive an approximate result for  $\langle R^{-1} \rangle$ . By including the first three terms of the series we get

$$\frac{1}{R} \simeq \frac{1}{R_0} - \frac{R - R_0}{R_0^2} + \frac{(R - R_0)^2}{R_0^3}, \quad (\text{S7})$$

which implies that

$$\left\langle \frac{1}{R} \right\rangle \simeq \frac{1}{R_0} + \frac{\langle (R - R_0)^2 \rangle}{R_0^3}, \quad (\text{S8})$$

and consequently (neglecting high-order terms)

$$\left\langle \frac{1}{R} \right\rangle^2 \simeq \frac{1}{R_0^2} + \frac{2\langle (R - R_0)^2 \rangle}{R_0^4}. \quad (\text{S9})$$

Likewise, for the second negative-order moment we Taylor expand  $1/R^2$  around  $R_0$  to get

$$\frac{1}{R^2} \simeq \frac{1}{R_0^2} - \frac{2(R-R_0)}{R_0^3} + \frac{3(R-R_0)^2}{R_0^4}, \quad (\text{S10})$$

which in turn implies that

$$\left\langle \frac{1}{R^2} \right\rangle \simeq \frac{1}{R_0^2} + \frac{3\langle (R-R_0)^2 \rangle}{R_0^4}. \quad (\text{S11})$$

Then, for the size fluctuations we have

$$\left\langle \frac{1}{R^2} \right\rangle - \left( \frac{1}{R} \right)^2 \simeq \frac{\langle (R-R_0)^2 \rangle}{R_0^4}, \quad (\text{S12})$$

and thus

$$\sqrt{\left\langle \frac{1}{R^2} \right\rangle - \left( \frac{1}{R} \right)^2} \simeq \frac{1}{R_0} \frac{\sqrt{\langle (R-R_0)^2 \rangle}}{R_0} = \frac{1}{\langle R \rangle} \frac{\sqrt{\langle R^2 \rangle - \langle R \rangle^2}}{\langle R \rangle}. \quad (\text{S13})$$

### Uniform distribution

As a particular example that can be treated analytically, we consider a uniform distribution function

$$P(R) = \frac{1}{\delta R} \theta(R - R_0 + \delta R/2) \theta(-R + R_0 + \delta R/2), \quad (\text{S14})$$

where  $\theta(x)$  is the Heaviside function. By construction,  $P(R)$  is normalised and with a mean value of  $\langle R \rangle = R_0$ , while  $\langle (R - R_0)^2 \rangle = \frac{1}{12} (\delta R)^2$ . The requirement that all radii in the distribution are positive gives a bound on its parameters, namely that  $R_0 \geq \delta R/2$ . For the first negative-order moment we get

$$\langle R^{-1} \rangle = \frac{1}{\delta R} \int_{R_0 - \delta R/2}^{R_0 + \delta R/2} dR R^{-1} = \langle R \rangle^{-1} g_1\left(\frac{\delta R}{\langle R \rangle}\right), \quad (\text{S15})$$

with

$$g_1(x) = x^{-1} \ln\left(\frac{2+x}{2-x}\right) = 1 + \frac{1}{12} x^2 + \mathcal{O}(x^4). \quad (\text{S16})$$

Similarly, for the second negative-order moment we get

$$\langle R^{-2} \rangle = \frac{1}{\delta R} \int_{R_0 - \delta R/2}^{R_0 + \delta R/2} dR R^{-2} = \langle R \rangle^{-2} g_2\left(\frac{\delta R}{\langle R \rangle}\right), \quad (\text{S17})$$

with

$$g_2(x) = \frac{4}{4-x^2} = 1 + \frac{1}{4} x^2 + \mathcal{O}(x^4). \quad (\text{S18})$$

In this way we can directly calculate

$$\sqrt{\left\langle \frac{1}{R^2} \right\rangle - \left( \frac{1}{R} \right)^2} \simeq \frac{1}{\sqrt{12}} \frac{\delta R}{R_0}. \quad (\text{S19})$$

Returning to Supplementary equation (S13) we indeed find the same result. In a similar way, for the case of the triangular and normal distribution that concern us in the main text, the result is

$$\text{Triangular: } \sqrt{\langle \frac{1}{R^2} \rangle - \langle \frac{1}{R} \rangle^2} \simeq \frac{1}{\sqrt{24}} \frac{\delta R}{R_0^2} \quad (\text{S20})$$

$$\text{Normal: } \sqrt{\langle \frac{1}{R^2} \rangle - \langle \frac{1}{R} \rangle^2} \simeq \frac{\sigma}{R_0^2}, \quad (\text{S21})$$

where  $\sigma$  is the standard deviation of the normal distribution. Note that the normal distribution is truncated, limited in the region  $R = 0 - 2R_0$ .



## **Publication B**

J. R. Maack, N. A. Mortensen & M. Wubs

**Size-dependent nonlocal effects in plasmonic semiconductor particles**

EPL **119**, 17003 (2017)

## Size-dependent nonlocal effects in plasmonic semiconductor particles

J. R. MAACK<sup>1</sup>, N. A. MORTENSEN<sup>2,3</sup> and M. WUBS<sup>1,3</sup>

<sup>1</sup> Department of Photonics Engineering, Technical University of Denmark - Ørsted's Plads 343, DK-2800 Kongens Lyngby, Denmark

<sup>2</sup> Center for Nano Optics & Danish Institute for Advanced Study, University of Southern Denmark - Campusvej 55, DK-5230 Odense M, Denmark

<sup>3</sup> Center for Nanostructured Graphene, Technical University of Denmark - Ørsted's Plads 343, DK-2800 Kongens Lyngby, Denmark

received 12 June 2017; accepted 16 August 2017

published online 11 September 2017

PACS 78.20.Bh – Theory, models, and numerical simulation

PACS 73.20.Mf – Collective excitations (including excitons, polarons, plasmons and other charge-density excitations)

PACS 78.30.Fs – III-V and II-VI semiconductors

**Abstract** – Localized surface plasmons (LSP) in semiconductor particles are expected to exhibit spatial nonlocal response effects as the geometry enters the nanometer scale. To investigate these nonlocal effects, we apply the hydrodynamic model to nanospheres of two different semiconductor materials: intrinsic InSb and  $n$ -doped GaAs. Our results show that the semiconductors indeed display nonlocal effects, and that these effects are even more pronounced than in metals. In a 150 nm InSb particle at 300 K, the LSP frequency is blueshifted 35%, which is orders of magnitude larger than the blueshift in a metal particle of the same size. This property, together with their tunability, makes semiconductors a promising platform for experiments in nonlocal effects.

Copyright © EPLA, 2017

**Introduction.** – It has been known for a while that the Drude model for metals is only applicable when the geometry is sufficiently large compared to intrinsic length scales of the electron gas. When analyzing nanoscale structures, the model becomes less accurate and a different or augmented model becomes necessary. A model which has successfully described metal structures on the nanoscale is the hydrodynamic Drude model (HDM) [1–5], where wave vector dependence is added to the Drude dielectric function. Due to this, the model has been able to explain observable nonlocal effects, such as longitudinal waves inside the metal and a size-dependent shift of the resonance frequency of localized surface plasmons (LSP) [6].

However, the HDM is not necessarily restricted to metals, but could be relevant for other nanoscale structures with a free-electron-like plasma as well. In this paper, we consider the application of the HDM to semiconductors, where the charge carriers are electrons and/or holes. This leads to new predictions, different from the well-known insights obtained by application of the usual Drude model to semiconductors [7]. Among the most notable differences between metals and semiconductors are the densities

and the effective masses of the charge carriers. Metals have large free-carrier concentrations and effective masses roughly equal to that of the free electron. Semiconductors on the other hand mostly have lower charge carrier densities, and these furthermore depend strongly on doping level and temperature. The effective masses will vary from material to material, and usually the effective masses of holes and electrons are different.

As briefly mentioned by Hanham *et al.* [8], these characteristics can be exploited to investigate nonlocal effects in ways that are not immediately possible in metals. By using semiconductors, the frequency of operation shifts from the optical spectrum to the infrared or THz bands because the plasma frequency, which depends on the charge carrier density, is lower than in metals. As we predict here, the size-dependent nonlocal effects will simultaneously manifest themselves in larger structures than in metals, which is good news for both fabrication and observation.

The optical properties of semiconductors have already been described by many semiclassical and quantum-mechanical models (see for example [9]). In particular, semiconductors are known to exhibit quantum

confinement when the size of the structure is on the nanometer scale, such as in quantum wells and dots [10]. But in some cases, the plasma description is more suitable. An example is InSb which is characterized by an extremely small band gap ( $E_g \sim 0.17$  eV) and a high charge carrier density at room temperature. This material was used by Hanham *et al.*, as well as in earlier papers on plasmonics [11–13], and in all cases the charge carriers were treated as a plasma. Another example is doped semiconductors where additional charge carriers have been supplied by the donors or acceptors. Plasmonics in doped semiconductors has additional advantages such as tunability [14], and plasmonic experiments with both *n*- and *p*-doping have been conducted [15–21].

In the region between semiconductors described by a plasma model (such as the Drude model) and quantum dots is a transition zone, where neither macroscopic nor microscopic theories are ideal. This region, which is defined by the size of the structures as well as the number of charge carriers, has been the subject of both experimental [22–27] and theoretical [28–32] studies. In this paper we will investigate semiconductor particles that are large enough to contain sufficient charge carriers to be described by a plasma model, yet small enough to display nonlocal effects (implying that the Drude model becomes inaccurate). We will focus on spherical particles of intrinsic InSb and *n*-doped GaAs and use the HDM to calculate the optical properties. To set a lower limit of our model, we use the results from Zhang *et al.* [29] who estimated the onset of quantum confinement effects in semiconductors using first-principles calculations. Although they find no hard transition, their results show that for a nanoparticle with a radius of 2.5 nm and only a few charge carriers, the plasma model is able to reproduce the DFT calculations reasonably well. But to make sure we are in the plasma regime, we will only consider particles containing more than 50 charge carriers (and, as seen in the results section, radii much larger than 2.5 nm).

We will mainly look at intraband transitions, as these affect the properties of the plasma directly, while interband transitions for simplicity are ignored. This is a reasonable assumption as long as the energies considered are smaller than the band gap. Another kind of excitations characteristic of semiconductors is excitons, which give rise to energy levels inside the band gap and modifications to the conduction band edge. However, for materials with a very narrow band gap, like InSb, the excitons are bound so weakly that they usually can be neglected [9]. Similarly for doped semiconductors, the screening effect of the high charge carrier density weakens the excitonic bond. For the materials that we study here, it is therefore a reasonable approximation to ignore exciton effects.

Given the assumptions above, the hydrodynamic equations of motion can be rederived for charge carriers in semiconductors, and in the next section, the key expressions in the model will be presented. These expressions will then be applied to spherical nanoparticles, and

finally the results of the numerical simulations will be discussed.

### The model. –

**Dielectric functions.** The hydrodynamic Drude model is characterized by a nonlocal longitudinal dielectric function [33,34]

$$\epsilon_L(k, \omega) = \epsilon_\infty - \frac{\omega_p^2}{\omega^2 + i\gamma\omega - \beta^2 k^2}, \quad (1)$$

where  $\omega_p$  is the plasma frequency,  $\gamma$  is the damping rate,  $\epsilon_\infty$  is the background dielectric constant, and  $\beta$  is a parameter that describes the strength of nonlocality. In this paper,  $\epsilon_\infty$  is chosen to be constant in  $\omega$ , which is a good approximation for energies smaller than the band gap.

For the degenerate electron gas in metals,  $\beta$  is directly related to the Fermi velocity  $v_F$  (see refs. [5,6]), but for semiconductors, the parameter depends on several conditions. The most obvious complication in semiconductors compared to metals is the presence of more than one kind of moving charge carrier, including electrons and heavy and light holes. The electrons, however, have a much smaller effective mass than the holes for a typical semiconductor, and therefore they will determine the optical properties almost entirely. This means that the holes can be ignored as a first approximation whenever electrons are present as majority charge carriers, as they are in this paper. Semiconductors also differ from metals in the sense that changes in charge carrier densities can be created by different means. If the electrons are thermally excited to the conduction band, and the bands are assumed to be parabolic, one can derive the expression for the dielectric function using a simple quantum-mechanical model similar to the Lindhard model (see the Supporting Information [Supplementarymaterial.pdf](#)). In this derivation,  $\beta$  is given by

$$\beta^2 = \frac{3k_B T}{m_e^*}, \quad (2)$$

where  $m_e^*$  is the effective mass of the electron,  $T$  is the temperature, and  $k_B$  is the Boltzmann constant. This expression is only valid for low temperatures where the Fermi-Dirac distribution can be approximated with the Boltzmann distribution. If this is not the case, the value of  $\beta$  can be found with numerical methods.

If the semiconductor instead is *n*-doped (and we neglect electrons thermally excited from the valence band to the conduction band), then  $\beta$  is given by

$$\beta^2 = \frac{3}{5} v_F^2 = \frac{3}{5} \frac{\hbar^2}{m_e^*} (3\pi^2 n)^{\frac{2}{3}}, \quad (3)$$

where  $n$  is the electron density. Equation (3) can also be used if the charge carriers are created by an external energy source, *e.g.* a laser pulse that can excite carriers across the band gap. This situation would of course be complicated by the relaxation of the charge carriers over time, and assumptions about a quasi-equilibrium would

have to be made (and we will not consider this here). Note, that the two expressions for  $\beta$  also can be found in [12].

The equations for the plasma frequency  $\omega_p$  and the damping rate  $\gamma$ , however, are independent of the excitation method and in all cases are given by

$$\omega_p^2 = \frac{n e^2}{\epsilon_0 m_e^*}, \quad (4)$$

$$\gamma = \frac{e}{m_{e,cond}^* \mu_e}, \quad (5)$$

where  $\mu_e$  is the mobility of the electron. Here  $m_{e,cond}^*$  is the conductivity effective mass of the electron, and this is in general different from  $m_e^*$  (which is called the density-of-states effective mass). Only for isotropic and perfectly parabolic bands are they identical [35].

For doped semiconductors,  $n$  is equal to the doping concentration  $N_D$  if the donors are completely ionized (which is a good approximation at room temperature). For thermally excited electrons in intrinsic semiconductors,  $n$  is given by [35]

$$n = 2 \left( \frac{2\pi k_B T}{h^2} \right)^{\frac{3}{2}} m_e^{*\frac{3}{4}} m_h^{*\frac{3}{4}} \exp\left(-\frac{E_g}{2k_B T}\right), \quad (6)$$

where  $m_h^*$  is the density-of-states effective mass of the holes. The equations is valid when the Boltzmann distribution is accurate, but numerical methods can be used to find  $n$  if this is not the case.

While the longitudinal dielectric function in eq. (1) is nonlocal in the HDM, the transversal dielectric function is local [33,34], *i.e.*

$$\epsilon_T(\omega) = \epsilon_\infty - \frac{\omega_p^2}{\omega^2 + i\gamma\omega}. \quad (7)$$

*The hydrodynamic equations.* The two dielectric functions together with Maxwell's equations produce the following equations in real space [6,36,37]:

$$-\nabla \times \nabla \times \mathbf{E} + \frac{\omega^2}{c^2} \epsilon_\infty \mathbf{E} = -i\mu_0 \omega \mathbf{J}, \quad (8a)$$

$$\frac{\beta^2}{\omega^2 + i\gamma\omega} \nabla(\nabla \cdot \mathbf{J}) + \mathbf{J} = \frac{i\omega \epsilon_0 \omega_p^2}{\omega^2 + i\gamma\omega} \mathbf{E}, \quad (8b)$$

where the first is the classical wave equation, and the second is the linearized nonlocal hydrodynamic equation. These equations provide a relation between the electrical field  $\mathbf{E}$  and the induced current density  $\mathbf{J}$ . In a local approximation ( $\beta \approx 0$ ), eq. (8b) would reduce to Ohm's law, *i.e.*  $\mathbf{J} \propto \mathbf{E}$  with the constant of proportionality given by the usual Drude conductivity  $\sigma_D = i\omega \epsilon_0 \omega_p^2 / (\omega^2 + i\gamma\omega)$ . The relation between these equation and  $\epsilon_L(k, \omega)$  and  $\epsilon_T(\omega)$  is easily seen for an infinite medium by using a Fourier transform [6,33].

Equations (8a) and (8b) can be solved for various geometries when provided with the necessary boundary conditions, using either analytical approaches or numerical

methods [5,34,37–40]. The continuities of  $\mathbf{E}_\parallel$  and  $\mathbf{B}_\parallel$  across the boundary are the natural first two boundary conditions. However, an additional third boundary condition is needed in the case of the HDM. Under the assumption of an infinite work function, the boundary condition is  $\mathbf{J}_\perp = \mathbf{0}$ , *i.e.* the charge carriers cannot escape the material (see [6] for a discussion). This choice implies that the spill-out of electrons at the interface is ignored [4].

*The Mie coefficients.* Given the boundary conditions, the solutions for  $\mathbf{E}$  and  $\mathbf{J}$  are found for spherical symmetry. This was originally done by Mie for transversal waves [41], and then later Ruppini added the longitudinal component which is present for the HDM [42]. The final result is contained in two transversal coefficients denoted by  $a_n^j$  and  $b_n^j$  and one longitudinal coefficient denoted by  $c_n^j$ . Here  $n$  is an integer, and  $j$  indicates whether the field is reflected from the sphere ( $j = r$ ) or transmitted into the sphere ( $j = t$ ). The coefficient  $c_n^r$  is zero as the surrounding medium is assumed to be a dielectric and unable to support longitudinal waves.

However, because our additional boundary condition is different from Ruppini's, we will instead of his results use the solution from David *et al.* [38] where the reflection coefficients are given by

$$a_n = \frac{-j_n(x_D)[x_T j_n(x_T)]' + j_n(x_T)[x_D j_n(x_D)]'}{h_n^{(1)}(x_D)[x_T j_n(x_T)]' - j_n(x_T)[x_D h_n^{(1)}(x_D)]'}, \quad (9a)$$

$$b_n^r = \frac{-\epsilon_D j_n(x_D)(\Delta_n + [x_T j_n(x_T)]') + \epsilon_T j_n(x_T)[x_D j_n(x_D)]'}{\epsilon_D h_n^{(1)}(x_D)(\Delta_n + [x_T j_n(x_T)]') - \epsilon_T j_n(x_T)[x_D h_n^{(1)}(x_D)]'}. \quad (9b)$$

Here,  $x_D = Rk_D = \sqrt{\epsilon_D} R\omega/c$  and  $x_T = Rk_T = \sqrt{\epsilon_T} R\omega/c$ . The parameter  $\epsilon_D$  is the dielectric constant of the surrounding dielectric and  $\epsilon_T$  is given by eq. (7). The function  $j_n$  is the spherical Bessel function of the first kind, and  $h_n^{(1)}$  is the spherical Hankel function of the first kind. The differentiation (denoted with the prime) is with respect to the argument. The nonlocal parameter  $\Delta_n$  is given by [38]

$$\Delta_n = \frac{j_n(x_T)j_n(x_L)n(n+1)}{x_L j_n'(x_L)} \left( \frac{\epsilon_T}{\epsilon_\infty} - 1 \right), \quad (10)$$

where  $x_L = Rk_L$  and the longitudinal wave vector is [38]

$$k_L = \frac{1}{\beta} \sqrt{\omega^2 + i\gamma\omega - \frac{\omega_p^2}{\epsilon_\infty}}. \quad (11)$$

The coefficients  $a_n$  and  $b_n$  are related to oscillations of the magnetic and electric type, respectively. Note that the expression for  $a_n$  is identical to the classical local solution, while the expression for  $b_n$  is not [43]. Setting  $\Delta_n = 0$ , however, reduces the  $b_n$  coefficients to their classical local-response counterparts as well.

Table 1: Properties of GaAs and InSb. The intrinsic charge carrier density is denoted by  $n_i$ . The masses  $m_e^*$  and  $m_h^*$  for InSb are taken from [44] and [45], respectively. For GaAs,  $m_e^*$  and  $m_{e,cond}^*$  (which depends on the doping level  $N_d$ ) are from [46], and  $m_h^*$  is from [47].  $E_g$  for InSb is taken from [48], and  $\mu_e$  and  $\mu_h$  for GaAs are from [49]. The rest of the data are taken from [50]. Note that for InSb, the conductivity effective mass is assumed to be identical to the density-of-states effective mass.

	GaAs (300 K)	InSb (300 K)	InSb (200 K)
$\epsilon_\infty$	10.9	15.7	15.7
$E_g$ (eV)	1.42	0.17	0.20
$n_i$ (cm $^{-3}$ )	$2.1 \times 10^6$	$1.9 \times 10^{16}$	$8.6 \times 10^{14}$
$\mu_e$ (cm $^2$ V $^{-1}$ s $^{-1}$ )	2900 <sup>a</sup> 1100 <sup>b</sup>	77000	151000
$\mu_h$ (cm $^2$ V $^{-1}$ s $^{-1}$ )	190 <sup>a</sup> 80 <sup>b</sup>	850	1910
$m_e^*/m_0$	0.0636	0.0118	0.0126
$m_h^*/m_0$	0.53	0.48	0.44
$m_{e,cond}^*/m_0$	0.0695 <sup>a</sup> 0.101 <sup>b</sup>	0.0118	0.0126

<sup>a</sup>  $N_d = 10^{18}$  cm $^{-3}$ .

<sup>b</sup>  $N_d = 10^{19}$  cm $^{-3}$ .

Once the  $a_n^r$  and  $b_n^r$  coefficients are known, the extinction cross-section for single particles can be found with [43]

$$\sigma_{ext} = -\frac{2\pi}{k_D^2} \sum_{n=1} (2n+1) \text{Re}(a_n^r + b_n^r). \quad (12)$$

**Results.** – Using eq. (12), the extinction spectra for spherical semiconductor nanoparticles will now be determined. To begin with, we will look at intrinsic InSb with thermally excited charge carriers. The data for InSb at  $T = 300$  K is given in table 1, and using eqs. (2), (4) and (5) we find  $\beta = 1.07 \times 10^6$  m/s,  $\omega_p = 6.94 \times 10^{13}$  s $^{-1}$  and  $\gamma = 1.94 \times 10^{12}$  s $^{-1}$ . From the plasma frequency it is immediately seen that excitation of the plasmon must take place in the infrared domain.

In fig. 1(a), the extinction cross section for an InSb nanoparticle at  $T = 300$  K in vacuum with  $R = 150$  nm is plotted. The dashed line is the local-response approximation obtained by setting  $\Delta_n$  equal to zero in eq. (9b). This curve only has a single visible peak which can be recognized as the classical dipole plasmon peak with a frequency close to  $\omega_{dipole} = \omega_p/(\epsilon_\infty + 2\epsilon_D)^{1/2}$ . Peaks from higher-order poles also exist, but are too faint to see here. The full line in the figure is the hydrodynamic solution, and it differs from the classical local-response result in several ways. The first thing we notice is that the dipole peak is shifted towards higher frequencies, and secondly we see that new peaks above the plasma frequency have appeared. The new peaks and the blueshift are clear signatures of nonlocality, and are well known phenomena in metals [5,6,36,51,52]. There, the peaks are known to be

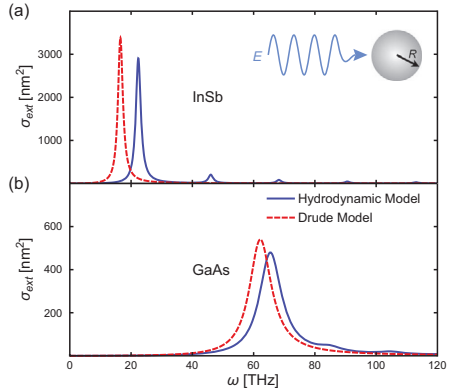


Fig. 1: (Colour online) (a) Extinction spectrum for an InSb nanoparticle in vacuum with  $R = 150$  nm. Charge carriers are thermally excited, and the temperature is 300 K. (b) Extinction spectrum for a GaAs nanoparticle in vacuum with  $R = 50$  nm. The doping level is  $N_d = 10^{18}$  cm $^{-3}$ . The dashed line is the local Drude model, and the full line is the HDM. Material parameters can be found in table 1.

associated with confined bulk plasmons, and the blueshift of the dipole peak is found to increase as the particle gets smaller [5]. The existence of such nonlocal effects in semiconductors has, to our knowledge, not been predicted before. Furthermore, the blueshift in fig. 1(a) is significant, thus facilitating the experimental verification by, for instance, systematically measuring the peak position as a function of particle size.

By using doping, wide-gap semiconductors can also be used as plasmonic materials. To investigate the predictions of the HDM for doped semiconductors, we will consider  $n$ -doped GaAs with a donor (*e.g.* silicon [15]) concentration of  $N_d = 10^{18}$  cm $^{-3}$ . The data for GaAs is shown in table 1, and using eqs. (3), (4) and (5) we find  $\beta = 4.36 \times 10^5$  m/s,  $\omega_p = 2.24 \times 10^{14}$  s $^{-1}$  and  $\gamma = 8.72 \times 10^{12}$  s $^{-1}$ . In fig. 1(b) the extinction spectrum for a doped GaAs nanoparticle with  $R = 50$  nm is plotted. Once again we see oscillations above the plasma frequency and a clear blueshift.

Although the results in fig. 1(a) and 1(b) appear promising, it should be noted that the amplitudes of the signals are about a hundred times weaker than the signal from, for example, a silver particle of the same size. Experimental sensitivity is improving, however, and at least one group has already measured signals of the same magnitude as the ones predicted here [53].

For particles of intrinsic InSb, the temperature will have a significant impact on the optical properties as it affects the charge carrier density and thereby the resonance frequency (as shown experimentally for a planar system

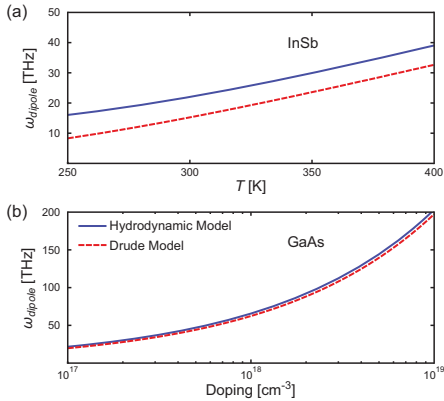


Fig. 2: (Colour online) (a) Dipole resonance frequency as a function of temperature for an InSb nanoparticle in vacuum with  $R = 150$  nm. (b) Dipole resonance frequency as a function of doping level in a GaAs nanoparticle in vacuum with  $R = 50$  nm. The dashed line is the local Drude model, and the full line is the HDM. Material parameters can be found in table 1.

in [54]). To illustrate this, the temperature dependence of the dipole resonance in an InSb nanoparticle is shown in fig. 2(a). This time, to ensure that the results are accurate at the higher temperatures, the Fermi-Dirac distribution is used in the calculations instead of the Boltzmann distribution. As expected, the resonance frequency increases with the temperature for both the local and nonlocal solutions. This effect can be used in new plasmonic experiments where the resonance frequency is controlled within a wide range by varying the temperature.

Such a tunability also exists in doped semiconductors where the resonance frequency instead is controlled by the doping level (as shown experimentally in [23]). In fig. 2(b), the dipole peak position in a GaAs nanoparticle is plotted as a function of the donor concentration, and we see how the resonance frequency goes up as the doping level increases.

The appearance of nonlocal effects in semiconductors is in a sense no surprise, as the model used is identical to the one used for metals (except the expression for  $\beta$ ). What is really noteworthy is the magnitude of the relative blueshift. For metals, this shift is typically in the order of 5–15% for particles of a few nm [55–58], while the blueshift seen in fig. 1(a) is as large as 35% despite a radius of 150 nm. The strong blueshift is primarily explained by the small effective electron mass in InSb, which according to eq. (2) serves to increase  $\beta$ . Interestingly, the relative blueshift is directly related to the non-classical fraction of the energy [59].

To make further comparison with metal nanoparticles, the blueshift relative to the plasma frequency is in fig. 3

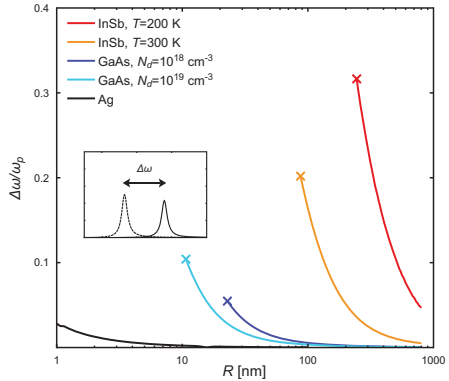


Fig. 3: (Colour online) The nonlocal blueshift  $\Delta\omega$  relative to the plasma frequency  $\omega_p$ , as a function of the nanosphere radius  $R$ . Material parameters can be found in table 1. The lines are cut off with a “x” at the left side where the particles contain fewer than 50 electrons (being a metal, silver is cut off below 1 nm).

shown as a function of particle radius for various materials. The curves were calculated by subtracting the dipole frequency in the local model from the dipole frequency in the HDM and dividing the result by  $\omega_p$ . The red and orange lines show the relative blueshift for InSb at  $T = 200$  K and 300 K, respectively (see the material parameters in table 1). We see that the blueshift increases as the semiconductor particle becomes smaller, quite analogous to what happens for noble metals [5]. But unlike for metals, the curves in fig. 3 also show that a lower temperature gives larger blueshifts for all semiconductor particle sizes. It has to be remembered, though, that the amplitude of the signal also decreases when the temperature is lowered, making detection harder. The “x” at the end of each line indicates the radius where the particle contains 50 electrons (this was the chosen lower limit of the model).

The possibility of observing nonlocal effects in semiconductors was mentioned by Hanham *et al.* in [8] where they studied the optical response of InSb disks with diameters of  $20 \mu\text{m}$ . However, for the simulation of their results they only used the local Drude model. From fig. 3, we now see that this was justified for individual InSb particles at 300 K, as the nonlocal blueshift is negligible for radii larger than  $1 \mu\text{m}$ .

The blue and pale blue lines in fig. 3 show the blueshifts for GaAs particles with doping levels of  $10^{18} \text{ cm}^{-3}$  and  $10^{19} \text{ cm}^{-3}$ , respectively. Although the blueshifts are smaller than for InSb, the tendency is the same.

Finally, the black line in fig. 3 shows the blueshift for silver particles with the parameters  $\beta = 1.08 \times 10^6 \text{ m/s}$ ,  $\omega_p = 1.36 \times 10^{16} \text{ s}^{-1}$  and  $\gamma = 3.80 \times 10^{13} \text{ s}^{-1}$  [6], and

where  $\epsilon_\infty(\omega)$  is found using the method from [38] and data from [60]. We here see that the relative blueshift is smaller than for the semiconductors and occurs for much smaller particles.

The hydrodynamic model is simple both conceptually and computationally, and yet it has showcased an extraordinary predictive power for the optical properties of metals. Semiconductors, however, represent a new group of materials where the HDM has not yet been tested, and the situation might be more complicated. As mentioned in the introduction, semiconductors may support excitons, an effect we have ignored here. Another phenomenon relevant for especially binary and ternary semiconductors is optical phonons which may couple to the plasmon if the resonance frequency is in the same region. This has been investigated for InSb [61,62] and GaAs [18,63], and the mechanism could be included in the dielectric function as an extra term (as is done in [12]).

For InSb there is yet another effect that may have to be taken into account, namely the presence of a *space charge layer*. This charge carrier depleted layer stretching a few hundred angstrom into the material has been discussed in earlier papers [12,64–66]. Such a layer would be significant for the optical properties of the InSb particle, and the question of how it would affect the nonlocal effects is still to be answered.

The size-dependent nonlocal effects which have been investigated here would be relevant when making experimental predictions for semiconductor nanostructures in general. But semiconductors could also be used specifically for research in nonlocal effects, as the required particle sizes are much larger in semiconductors than in metals. This will be an advantage in experimental studies where the extremely small sizes of metal nanoparticles has been a challenge. Another material that also permits observation of nonlocality in larger structures than with metals is graphene. Indeed, blueshifts in arm-chair-terminated graphene nanoflakes could be identified as hydrodynamic nonlocal blueshifts [67]. Very recently, tunable nonlocal response of graphene has been observed in near-field imaging experiments [68]. Both graphene and semiconductors are therefore suited for research in nonlocality, as they allow the experimentalists to explore larger structures and still be able to see deviations from the local response model.

**Conclusions.** – We have shown that size-dependent nonlocal effects are present in semiconductor particles that contain enough charge carriers to be described by the hydrodynamic Drude model. These particles are too big to behave as quantum dots, yet too small for bulk theory to apply. Moreover, we find that the blueshift relative to the plasma frequency is much larger than what is seen in metals and that it occurs in larger particles. This finding makes semiconductors interesting and suitable candidates for further experimental explorations of nonlocal electrodynamic effects: if the required structures can be

upscaled, then the fabrication is correspondingly simplified, and investigations of new, more complex geometries become realistic.

In addition, semiconductors provide the possibility of tuning the optical response by changing the charge carrier density, for instance by temperature control and doping as investigated here. If nanoscale semiconductor structures in the future will be used in new plasmonic experiments and devices, proper modeling of the materials becomes crucial. Based on our results from the hydrodynamic model, we have clarified when nonlocality is not important and the Drude model provides sufficient description, but also when nonlocal effects should be taken into account.

\* \* \*

We gratefully acknowledge support from the Danish Council for Independent Research (FNU 1323-00087) and from Villum Fonden via the VKR Centre of Excellence NATEC-II. The Center for Nanostructured Graphene (CNG) was financed by the Danish National Research Council (DNRF103). NAM is a Villum Investigator supported by Villum Fonden (grant No. 16498).

#### REFERENCES

- [1] GARCÍA DE ABAJO F. J., *J. Phys. Chem. C*, **112** (2008) 17983.
- [2] McMAHON J. M., GRAY S. K. and SCHATZ G. C., *Phys. Rev. Lett.*, **103** (2009) 097403.
- [3] RAZA S., YAN W., STENGER N., WUBS M. and MORTENSEN N. A., *Opt. Express*, **21** (2013) 27344.
- [4] TOSCANO G., STRAUBEL J., KWIAKOWSKI A., ROCKSTUHL C., EVERS F., XU H., MORTENSEN N. A. and WUBS M., *Nat. Commun.*, **6** (2015) 7132.
- [5] CHRISTENSEN T., YAN W., RAZA S., JAUHO A.-P., MORTENSEN N. A. and WUBS M., *ACS Nano*, **8** (2014) 1745.
- [6] RAZA S., BOZHEVOLNYI S. I., WUBS M. and MORTENSEN N. A., *J. Phys.: Condens. Matter*, **27** (2015) 183204.
- [7] FOX M., *Optical Properties of Solids*, 2nd edition (Oxford University Press) 2010.
- [8] HANHAM S. M., FERNÁNDEZ-DOMÍNGUEZ A. I., TENG J. H., ANG S. S., LIM K. P., YOON S. F., NGO C. Y., KLEIN N., PENDRY J. B. and MAIER S. A., *Adv. Mater.*, **24** (2012) OP226.
- [9] HAUG H. and KOCH S. W., *Quantum Theory of the Optical and Electronic Properties of Semiconductors*, 5th edition (World Scientific) 2009.
- [10] KELLY M. J., *Low-dimensional Semiconductors*, 1st edition (Clarendon Press) 1995.
- [11] RITZ A. and LÜTH H., *Phys. Rev. Lett.*, **52** (1984) 1242.
- [12] JONES T. S., SCHWEITZER M. O., RICHARDSON N. V., BELL G. R. and McCONVILLE C. F., *Phys. Rev. B*, **51** (1995) 17675.
- [13] GÓMEZ RIVAS J., KUTTGE M., KURZ H., HARING BOLIVAR P. and SÁNCHEZ-GIL J. A., *Appl. Phys. Lett.*, **88** (1996) 082106.

- [14] NAIK G. V., SHALAEV V. M. and BOLTASSEVA A., *Adv. Mater.*, **25** (2013) 3264.
- [15] MATZ R. and LÜTH H., *Phys. Rev. Lett.*, **46** (1981) 500.
- [16] GRAY-GRYCHOWSKI Z. J., STRADLING R. A., EGDELL R. G., DOBSON P. J., JOYCE B. A. and WOODBRIDGE K., *Solid State Commun.*, **59** (1986) 703.
- [17] BETTI M. G., DEL PENNINO U. and MARIANI C., *Phys. Rev. B*, **39** (1989) 5887.
- [18] CHEN Y., NANNARONE S., SCHAEFER J., HERMANSON J. C. and LAPEYRE G. J., *Phys. Rev. B*, **39** (1989) 7653.
- [19] MENG Y., ANDERSON J. R., HERMANSON J. C. and LAPEYRE G. J., *Phys. Rev. B*, **44** (1991) 4040.
- [20] BIAGI R., MARIANI C. and DEL PENNINO U., *Phys. Rev. B*, **46** (1992) 2467.
- [21] GINN J. C., JARECKI R. L. jr., SHANER E. A. and DAVIDS P. S., *J. Appl. Phys.*, **110** (2011) 043110.
- [22] LUTHER J. M., JAIN P. K., EWERS T. and ALIVISATOS A. P., *Nat. Mater.*, **10** (2011) 361.
- [23] GARCIA G., BUONSANTI R., RUNNERSTROM E. L., MENDELBERG R. J., LLORDES A., ANDERS A., RICHARDSON T. J. and MILLIRON D. J., *Nano Lett.*, **11** (2011) 4415.
- [24] BUONSANTI R., LLORDES A., ALONI S., HELMS B. A. and MILLIRON D. J., *Nano Lett.*, **11** (2011) 4706.
- [25] MANTHIRAM K. and ALIVISATOS A. P., *J. Am. Chem. Soc.*, **134** (2012) 3995.
- [26] SCHIMPF A. M., THAKKAR N., GUNTARDT C. E., MASEILLO D. J. and GAMELIN D. R., *ACS Nano*, **8** (2014) 1065.
- [27] ZHOU S., PI X., NI Z., DING Y., JIANG Y., JIN C., DELERUE C., YANG D. and NOZAKI T., *ACS Nano*, **9** (2015) 378.
- [28] HAPALA P., KUSOVÁ K., PELANT I. and JELÍNEK P., *Phys. Rev. B*, **87** (2013) 195420.
- [29] ZHANG H., KULKARNI V., PRODAN E., NORDLANDER P. and GOVOROV A. O., *J. Phys. Chem. C*, **118** (2014) 16035.
- [30] FAUCHEAUX J. A., STANTON A. L. D. and JAIN P. K., *J. Phys. Chem. Lett.*, **5** (2014) 976.
- [31] MONREAL R. C., ANTOSIEWICZ T. J. and APELL S. P., *J. Phys. Chem. Lett.*, **6** (2015) 1847.
- [32] ZHANG H., ZHANG R., SCHRAMKE K. S., BEDFORD N. M., HUNTER K., KORTSHAGEN U. R. and NORDLANDER P., *ACS Photon.*, **4** (2017) 963.
- [33] WUBS M., *Opt. Expr.*, **23** (2015) 31296.
- [34] RAZA S., CHRISTENSEN T., WUBS M., BOZHEVOLNYI S. I. and MORTENSEN N. A., *Phys. Rev. B*, **88** (2013) 115401.
- [35] SZE S. M., *Physics of Semiconductor Devices*, 1st edition (Wiley) 1969.
- [36] RAZA S., TOSCANO G., JAUHO A.-P., WUBS M. and MORTENSEN N. A., *Phys. Rev. B*, **84** (2011) 121412(R).
- [37] TOSCANO G., RAZA S., JAUHO A.-P., MORTENSEN N. A. and WUBS M., *Opt. Express*, **20** (2012) 4176.
- [38] DAVID C. and GARCÍA DE ABAJO F. J., *J. Phys. Chem. C*, **115** (2011) 19470.
- [39] TOSCANO G., RAZA S., YAN W., JEPPESEN C., XIAO S., WUBS M., JAUHO A.-P., BOZHEVOLNYI S. I. and MORTENSEN N. A., *Nanophotonics*, **2** (2013) 161.
- [40] YAN W., MORTENSEN N. A. and WUBS M., *Phys. Rev. B*, **88** (2013) 155414.
- [41] MIE G., *Ann. Phys. (Leipzig)*, **330** (1908) 377.
- [42] RUPPIN R., *Phys. Rev. Lett.*, **31** (1973) 1434.
- [43] BOHREN C. F. and HUFFMAN D. R., *Absorption and Scattering of Light by Small Particles*, 1st edition (Wiley) 1983.
- [44] STRADLING R. A. and WOOD R. A., *J. Phys. C*, **3** (1970) L94.
- [45] CUNNINGHAM R. W. and GRUBER J. B., *J. Appl. Phys.*, **41** (1970) 1804.
- [46] SZMYD D. M., PORRO P., MAJERFELD A. and LAGOMARSINO S., *J. Appl. Phys.*, **68** (1990) 2367.
- [47] WALTON A. K. and MISHRA U. K., *J. Phys. C*, **1** (1968) 533.
- [48] ROWELL N. L., *Infrared Phys.*, **28** (1988) 37.
- [49] SZE S. M. and IRVIN J. C., *Solid State Electron.*, **11** (1968) 599.
- [50] MADELUNG O., *Semiconductors: Data Handbook*, 3rd edition (Springer-Verlag, Berlin) 2004.
- [51] TIGGESBÄUMKER J., KÖLLER L., MEIWES-BROEK K.-H. and LIEBSCH A., *Phys. Rev. A*, **48** (1993) R1749.
- [52] LINDAU I. and NILSSON P. O., *Phys. Scr.*, **3** (1971) 87.
- [53] BILLAUD P., MARHABA S., GRILLET N., COTTANCIN E., BONNET C., LERMÉ J., VIALLE J.-L., BROYER M. and PELLARIN M., *Rev. Sci. Instrum.*, **81** (2010) 043101.
- [54] HOWELLS S. C. and SCHLIE L. A., *Appl. Phys. Lett.*, **69** (1996) 550.
- [55] CHARLÉ K.-P., KÖNIG L., NEPIJKO S., RABIN I. and SCHULZE W., *Cryst. Res. Technol.*, **33** (1998) 1085.
- [56] RAZA S., STENGER N., KADKHODAZADEH S., FISCHER S. V., KOSTESHA N., JAUHO A.-P., BURROWS A., WUBS M. and MORTENSEN N. A., *Nanophotonics*, **2** (2013) 131.
- [57] RAZA S., KADKHODAZADEH S., CHRISTENSEN T., DI VECE M., WUBS M., MORTENSEN N. A. and STENGER N., *Nat. Commun.*, **6** (2015) 8788.
- [58] SCHOLL J. A., KOH A. L. and DIONNE J. A., *Nature*, **483** (2012) 421.
- [59] YAN W. and MORTENSEN N. A., *Phys. Rev. B*, **93** (2016) 115439.
- [60] WERNER W. S. M., GLANTSCHNIG K. and AMBROSCH-DRAXL C., *J. Phys. Chem. Ref. Data*, **38** (2009) 1013.
- [61] GAUR N. K. S., *Physica B & C*, **82** (1976) 262.
- [62] GU P., TANI M., SAKAI K. and YANG T.-R., *Appl. Phys. Lett.*, **77** (2000) 1798.
- [63] OLSEN C. G. and LYNCH D. W., *Phys. Rev.*, **177** (1969) 1231.
- [64] RITZ A. and LÜTH H., *J. Vac. Sci. Technol. B*, **3** (1985) 1153.
- [65] BELL G. R., JONES T. S. and MCCONVILLE C. F., *Surf. Sci.*, **405** (1998) 280.
- [66] ADOMAVICIUS R., MACUTKEVIC J., SUZANOVICIENE R., ŠIUŠYS A. and KROTKUS A., *Phys. Status Solidi C*, **6** (2009) 2849.
- [67] CHRISTENSEN T., WANG W., JAUHO A.-P., WUBS M. and MORTENSEN N. A., *Phys. Rev. B*, **90** (2014) 241414(R).
- [68] LUNDEBERG M. B., GAO Y., ASGARI R., TAN C., VAN DUPPEN B., AUTORE M., ALONSO-GONZÁLEZ P., WOESSNER A., WATANABE K., TANIGUCHI T., HILLENBRAND R., HONE J., POLINI M. and KOPPENS F. H. L., *Tuning quantum non-local effects in graphene plasmonics*, to be published in *Science* (2017), DOI: 10.1126/science.aan2735.

# Size-dependent nonlocal effects in plasmonic semiconductor particles - Supporting Information

J. R. Maack<sup>1</sup>, N. A. Mortensen<sup>2,3</sup> and M. Wubs<sup>1,3</sup>

<sup>1</sup>Department of Photonics Engineering, Technical University of Denmark, Ørstedss Plads 343, DK-2800 Kongens Lyngby

<sup>2</sup>Center for Nano Optics & Danish Institute for Advanced Study, University of Southern Denmark,

Campusvej 55, DK-5230 Odense M

<sup>3</sup>Center for Nanostructured Graphene, Technical University of Denmark, Ørstedss Plads 343, DK-2800 Kongens Lyngby  
jorom@fotonik.dtu.dk

March 19, 2018

## Longitudinal dielectric function

We present a simple derivation of the longitudinal dielectric function for a semiconductor using the Lindhard approximation. The method is inspired by the one in ref. [1].

The starting point is Fermi's golden rule, from which the following general expression for the longitudinal dielectric function can be found:

$$\epsilon(\mathbf{q}, \omega) = 1 + \frac{2e^2}{\epsilon_0 q^2} \frac{1}{V} \sum_{\alpha\beta} \frac{|\langle \psi_\alpha | e^{i\mathbf{q}\cdot\mathbf{r}} | \psi_\beta \rangle|^2}{E_\beta - E_\alpha - \hbar\omega - i\eta} [f(E_\alpha) - f(E_\beta)], \quad (\text{S1})$$

where  $\mathbf{q}$  is the wavevector,  $\omega$  is the frequency,  $V$  is the volume,  $e$  is the elementary charge and  $E$  is the energy. The functions  $\psi_\alpha$  and  $\psi_\beta$  are the wave functions of the states  $\alpha$  and  $\beta$  between which the excitation takes place. Furthermore,  $f$  is the Fermi-Dirac distribution function and  $\eta$  is a small real number originating from the Kramers-Kronig transformation, and for now it has no physical significance. However, later it will become clear that  $\eta$  is closely related to the phenomenological damping function in the hydrodynamic dielectric function.

Applying the Lindhard approximation, according to which only a single parabolic band is considered and the wavefunctions are assumed to be plane waves, the dielectric function becomes

$$\epsilon(\mathbf{q}, \omega) = 1 + \frac{2e^2}{\epsilon_0 q^2} \frac{1}{V} \sum_{\mathbf{k}} \frac{f(\mathbf{k}) - f(\mathbf{k} + \mathbf{q})}{E(\mathbf{k} + \mathbf{q}) - E(\mathbf{k}) - \hbar\omega - i\eta}, \quad (\text{S2})$$

since the matrix element equals 1. It has also been used that the excitation takes place from wavevector  $\mathbf{k}$  to wavevector  $\mathbf{k} + \mathbf{q}$ . This equation can be rewritten as

$$\epsilon(\mathbf{q}, \omega) = 1 + \frac{4e^2}{\epsilon_0 q^2} \frac{1}{V} \sum_{\mathbf{k}} f(\mathbf{k}) \frac{E(\mathbf{k} + \mathbf{q}) - E(\mathbf{k})}{(E(\mathbf{k} + \mathbf{q}) - E(\mathbf{k}))^2 - (\hbar\omega + i\eta)^2}. \quad (\text{S3})$$

Without loss of generality it is now assumed that  $\mathbf{q}$  is oriented in the  $z$ -direction, and we find that

$$E(\mathbf{k} + \mathbf{q}) - E(\mathbf{k}) = \frac{\hbar^2}{2m_e^*} (2\mathbf{k} \cdot \mathbf{q} + q^2) = \frac{\hbar^2}{2m_e^*} (2k_z q + q^2), \quad (\text{S4})$$

where  $m_e^*$  is the (density-of-states) effective mass of the electron. To proceed, we next make the assumption that  $q$  is small compared to  $\omega$ , which is reasonable when considering electromagnetic radiation. This also means that  $E(\mathbf{k} + \mathbf{q}) - E(\mathbf{k}) \ll \hbar\omega + i\eta$  and the denominator can be expanded as a geometric series

$$\begin{aligned} \epsilon(q, \omega) &= 1 - \frac{4e^2}{\epsilon_0 q^2} \frac{1}{V} \sum_{\mathbf{k}} f(\mathbf{k}) \frac{E(\mathbf{k} + \mathbf{q}) - E(\mathbf{k})}{(\hbar\omega + i\eta)^2} \left( \frac{1}{1 - \frac{(E(\mathbf{k} + \mathbf{q}) - E(\mathbf{k}))^2}{(\hbar\omega + i\eta)^2}} \right) \\ &= 1 - \frac{4e^2}{\epsilon_0 q^2} \frac{1}{V} \sum_{\mathbf{k}} f(\mathbf{k}) \frac{E(\mathbf{k} + \mathbf{q}) - E(\mathbf{k})}{(\hbar\omega + i\eta)^2} \left( 1 + \frac{(E(\mathbf{k} + \mathbf{q}) - E(\mathbf{k}))^2}{(\hbar\omega + i\eta)^2} + \frac{(E(\mathbf{k} + \mathbf{q}) - E(\mathbf{k}))^4}{(\hbar\omega + i\eta)^4} + \dots \right). \end{aligned} \quad (\text{S5})$$

Now the expression in eq. (S4) is used, and it is taken into account that terms containing odd powers of  $k_z$  cancel out:

$$\epsilon(q, \omega) = 1 - \frac{4e^2}{\epsilon_0 q^2} \left( \frac{1}{(\hbar\omega + i\eta)^2} \frac{\hbar^2 q^2}{2m_e^*} \frac{1}{V} \sum_{\mathbf{k}} f(\mathbf{k}) + \frac{1}{(\hbar\omega + i\eta)^4} \frac{3\hbar^6 q^4}{2m_e^{*3}} \frac{1}{V} \sum_{\mathbf{k}} f(\mathbf{k}) k_z^2 + \dots \right). \quad (\text{S6})$$

To continue from here, we have to decide upon the nature of the charge carriers, as this will determine how  $\sum_{\mathbf{k}}$  is evaluated. In the article, we consider both  $n$ -doped semiconductors and thermally excited electrons in intrinsic semiconductors, and we will therefore focus on these two cases. Starting with the case of doped semiconductors, we will make the assumption that the distribution  $f(\mathbf{k})$  is a step-function with the step occurring at the Fermi wavevector  $k_F$ . This is the same as setting the temperature equal zero, and can be justified when the doping is high enough to ignore the temperature spread. The sum in the first term can then be solved by replacing it with an integral

$$\frac{1}{V} \sum_{\mathbf{k}} f(\mathbf{k}) = \frac{1}{VV_k} \int d\mathbf{k} f(\mathbf{k}) = \frac{4\pi}{VV_k} \int_0^{k_F} dk k^2 = \frac{4\pi}{VV_k} \frac{k_F^3}{3} = \frac{n}{2}, \quad (\text{S7})$$

where  $V_k$  is the volume of a single state in  $k$ -space, and  $n$  is the charge carrier density. On the right side we divide by 2 to account for the spin degeneracy. The sum in the second term can be derived with a similar method

$$\frac{1}{V} \sum_{\mathbf{k}} f(\mathbf{k}) k_z^2 = \frac{1}{VV_k} \int_0^{k_F} dk k^4 \int_0^\pi d\theta \sin \theta \cos^2 \theta \int_0^{2\pi} d\phi = \frac{4\pi}{3VV_k} \frac{k_F^5}{5} = \frac{k_F^2}{5} \frac{n}{2}, \quad (\text{S8})$$

and now the dielectric function becomes

$$\epsilon(q, \omega) = 1 - \frac{4e^2}{\epsilon_0 q^2} \left( \frac{1}{(\hbar\omega + i\eta)^2} \frac{\hbar^2 q^2}{2m_e^*} \frac{n}{2} + \frac{1}{(\hbar\omega + i\eta)^4} \frac{3\hbar^6 q^4}{2m_e^{*3}} \frac{k_F^2}{5} \frac{n}{2} + \dots \right). \quad (\text{S9})$$

Assuming that  $(\hbar\omega + i\eta)^2 \approx \hbar^2 \omega^2 + 2i\hbar\omega\eta$  and introducing the damping coefficient  $\gamma = 2\eta/\hbar$  we get

$$\epsilon(q, \omega) = 1 - \frac{\omega_p^2}{\omega^2 + i\gamma\omega} - \frac{\omega_p^2}{(\omega^2 + i\gamma\omega)^2} \frac{3\hbar^2 k_F^2}{5m_e^{*2}} q^2 - \dots, \quad (\text{S10})$$

where

$$\omega_p^2 = \frac{e^2 n}{\epsilon_0 m_e^*} \quad (\text{S11})$$

is the plasma frequency. We will now define the nonlocal parameter for doped semiconductors to be

$$\beta^2 = \frac{3\hbar^2 k_F^2}{5m^2} = \frac{3}{5} v_F^2, \quad (\text{S12})$$

where  $v_F$  is the Fermi velocity. Note, that this definition is identical to the one for metals[2]. With this definition, the dielectric function becomes

$$\epsilon(q, \omega) = 1 - \frac{\omega_p^2}{\omega^2 + i\gamma\omega} - \frac{\omega_p^2}{(\omega^2 + i\gamma\omega)^2} \beta^2 q^2 - \dots. \quad (\text{S13})$$

The final step is to show that the hydrodynamic dielectric function

$$\epsilon(q, \omega) = \epsilon_\infty - \frac{\omega_p^2}{\omega^2 + i\gamma\omega - \beta^2 q^2}, \quad (\text{S14})$$

presented in eq. (1) in the article is in fact a good approximation to eq. (S13). To do this eq. (S14) is expanded in a geometric series

$$\begin{aligned} \epsilon(q, \omega) &= \epsilon_\infty - \frac{\omega_p^2}{\omega^2 + i\gamma\omega} \cdot \frac{1}{1 - \frac{\beta^2 q^2}{\omega^2 + i\gamma\omega}} \\ &= \epsilon_\infty - \frac{\omega_p^2}{\omega^2 + i\gamma\omega} \left( 1 + \frac{\beta^2 q^2}{\omega^2 + i\gamma\omega} + \frac{\beta^4 q^4}{(\omega^2 + i\gamma\omega)^2} + \dots \right) \\ &= \epsilon_\infty - \frac{\omega_p^2}{\omega^2 + i\gamma\omega} - \frac{\omega_p^2}{(\omega^2 + i\gamma\omega)^2} \beta^2 q^2 - \frac{\omega_p^2}{(\omega^2 + i\gamma\omega)^3} \beta^4 q^4 - \dots, \end{aligned} \quad (\text{S15})$$

and we see that this is nearly identical to eq. (S13). Among the differences is  $\epsilon_\infty$  which is absent from eq. (S13). This parameter represents the interband transitions, which are ignored in the derivation, and we simply add it by hand. In the simulation, a constant value found in a data handbook is used for  $\epsilon_\infty$ . Secondly, it should be noted that the hydrodynamic dielectric function only matches up with eq. (S13) to second order in  $q$  and therefore includes nonlocality to the lowest order (whereas the Drude model doesn't include nonlocality at all).

Turning to the thermally excited intrinsic semiconductor, we need to evaluate the  $\sum_{\mathbf{k}}$  sums. For the function  $f(\mathbf{k})$ , the correct choice would be the Fermi-Dirac distribution, but since this would prevent us from finding a simple analytic expression, we will approximate  $f(\mathbf{k})$  by the Boltzmann distribution. This is a good choice as long  $E_c - E_F \gg k_B T$ , where  $E_c$  is the conduction band edge,  $E_F$  is the Fermi energy,  $k_B$  is the Boltzmann constant and  $T$  is the temperature. With this approximation, the first sum becomes

$$\frac{1}{V} \sum_{\mathbf{k}} f(\mathbf{k}) = \frac{4\pi}{VV_k} \int_0^\infty dk k^2 f(k) \approx \frac{4\pi}{VV_k} \left( \frac{2m_e^*}{\hbar^2} \right)^{\frac{3}{2}} \int_{E_c}^\infty dE \sqrt{E - E_c} \exp\left(-\frac{E - E_F}{k_B T}\right), \quad (\text{S16})$$

where it has been used that

$$E = E_c + \frac{\hbar^2 k^2}{2m_e^*}, \quad (\text{S17})$$

and

$$f(E) = \frac{1}{\exp\left(\frac{E - E_F}{k_B T}\right) + 1} \approx \exp\left(-\frac{E - E_F}{k_B T}\right). \quad (\text{S18})$$

We now introduce the variable

$$\rho = \frac{E - E_F}{k_B T}, \quad (\text{S19})$$

which results in the following expression

$$\frac{1}{V} \sum_{\mathbf{k}} f(\mathbf{k}) \approx \frac{4\pi}{VV_k} \left( \frac{2m_e^* k_B T}{\hbar^2} \right)^{\frac{3}{2}} \exp\left(\frac{E_F - E_c}{k_B T}\right) \int_0^\infty d\rho \rho^{\frac{1}{2}} e^{-\rho}. \quad (\text{S20})$$

The integral is found to be

$$\int_0^\infty d\rho \rho^{\frac{1}{2}} e^{-\rho} = \Gamma\left(\frac{3}{2}\right) = \frac{\sqrt{\pi}}{2}, \quad (\text{S21})$$

where  $\Gamma$  is the gamma function. If the Boltzmann distribution does not apply, the integral cannot be reduced to such a simple expression and instead has to be evaluated by numerical methods. The sum therefore becomes

$$\frac{1}{V} \sum_{\mathbf{k}} f(\mathbf{k}) \approx \frac{4\pi}{VV_k} \left( \frac{2m_e^* k_B T}{\hbar^2} \right)^{\frac{3}{2}} \exp\left(\frac{E_F - E_c}{k_B T}\right) \frac{\sqrt{\pi}}{2} = \frac{n}{2}. \quad (\text{S22})$$

Here  $n$  is the density of the electrons alone as the holes are ignored. Using a similar method, the sum in the second term of eq. (S6) is found to be

$$\frac{1}{V} \sum_{\mathbf{k}} f(\mathbf{k}) k_z^2 \approx \frac{4\pi}{VV_k} \left( \frac{2m_e^* k_B T}{\hbar^2} \right)^{\frac{5}{2}} \exp\left(\frac{E_F - E_c}{k_B T}\right) \frac{1}{3} \Gamma\left(\frac{5}{2}\right) = \frac{m_e^* k_B T}{\hbar^2} \frac{n}{2}. \quad (\text{S23})$$

Inserting these expressions for the sums back into eq. (S6) results in a dielectric function similar to eq. (S13), but where  $\beta$  now is given by

$$\beta^2 = \frac{3k_B T}{m_e^*}, \quad (\text{S24})$$

while the plasma frequency is again given by eq. (S11). This concludes the derivation of the longitudinal dielectric function for doped semiconductors and intrinsic semiconductors with thermally excited electrons.

## References

- [1] G. Grosso and G. P. Parravicini. *Solid state physics*. 2nd ed. (Academic Press, 2014).
- [2] T. Christensen, W. Yan, S. Raza, A.-P. Jauho, N. A. Mortensen, and M. Wubs. *Nonlocal response of metallic nanospheres probed by light, electrons, and atoms*. ACS Nano **8**, 1745 (2014).



## **Publication C**

J. R. Maack, N. A. Mortensen & M. Wubs

**Two-fluid hydrodynamic model for semiconductors**

Phys. Rev. B **97**, 115415 (2018)

**Two-fluid hydrodynamic model for semiconductors**Johan R. Maack,<sup>1</sup> N. Asger Mortensen,<sup>2</sup> and Martijn Wubs<sup>1</sup><sup>1</sup>*Department of Photonics Engineering, Technical University of Denmark, Ørstedts Plads 343, DK-2800 Kongens Lyngby, Denmark*<sup>2</sup>*Center for Nano Optics and Danish Institute for Advanced Study, University of Southern Denmark, Campusvej 55, DK-5230 Odense M, Denmark* (Received 3 January 2018; revised manuscript received 23 February 2018; published 13 March 2018)

The hydrodynamic Drude model (HDM) has been successful in describing the optical properties of metallic nanostructures, but for semiconductors where several different kinds of charge carriers are present an extended theory is required. We present a two-fluid hydrodynamic model for semiconductors containing electrons and holes (from thermal or external excitation) or light and heavy holes (in *p*-doped materials). The two-fluid model predicts the existence of two longitudinal modes, an acoustic and an optical, whereas only an optical mode is present in the HDM. By extending nonlocal Mie theory to two plasmas, we are able to simulate the optical properties of two-fluid nanospheres and predict that the acoustic mode gives rise to peaks in the extinction spectra that are absent in the HDM.

DOI: [10.1103/PhysRevB.97.115415](https://doi.org/10.1103/PhysRevB.97.115415)**I. INTRODUCTION**

Plasmonics, the study of collective excitations of electrons, takes place on ever smaller scales as fabrication and characterization techniques continue to improve. While this allows for the design of entirely new devices and materials with promising properties, it also requires improved theoretical tools to properly model the systems.

Metals, by far the most widely used plasmonic materials, are often described very accurately by the Drude model. But when the sizes approach the nanoscale, the model is no longer able to explain experimentally observable phenomena like, for example, the blueshift of the resonance frequency of the localized surface plasmon (LSP) in metallic nanospheres [1]. An improved model that has been successful in describing the optical properties of metals on the nanoscale is the hydrodynamic Drude model (HDM) [2–12]. In this model, the polarization depends *nonlocally* on the electrical field, and the aforementioned blueshift appears as a size-dependent nonlocal effect [7,13,14]. Furthermore, the HDM also predicts the existence of confined bulk plasmons in nanoparticles [5,7], something that also has been found experimentally [15].

While metals are the most commonly used plasmonic materials because of their large density of free electrons, semiconductors are also interesting due to the tunability of the electron density, either statically by doping or dynamically by applying a bias. Furthermore, intrinsic semiconductors may contain plasmas created either thermally or by external excitations (e.g., from a laser), and here the electron density can be controlled dynamically with the temperature or the excitation energy, respectively. Plasmonics has already been shown in several papers for doped semiconductors [16–28], biased semiconductors [29–32], laser excited semiconductors [33], and thermally excited intrinsic semiconductors [34–37].

Among these studies, Refs. [24–30] investigated plasmons in nanostructures of semiconductors, but except for Refs. [27,29] they all used the Drude model to describe their

results. And just as for metals one would expect that the Drude model only is accurate for semiconductor structures down to a certain size. Now, it is well known that semiconductor particles of only a few nanometers behave as quantum dots, but in the intermediate size regime between structures described by the Drude model and quantum dots a different theoretical framework is needed (see, e.g., Refs. [38–40]).

Recently we made a case for applying the HDM to semiconductor structures in the mentioned intermediate size regime [41]. In that paper, we adapted the HDM to nanospheres made of doped semiconductors and intrinsic semiconductors with thermally excited charge carriers. In both cases we found that the nonlocal blueshift was even more pronounced than in metals and occurred in larger particles. In essence, this can be attributed to the increased Fermi wavelength and smaller effective mass in semiconductors, as compared to that in metals. Based on the HDM we also predicted the existence of standing bulk plasmons above the plasma frequency in semiconductors, and very recently these resonances were measured by de Ceglia *et al.* [42] in doped semiconductors. These interesting new developments are no doubt only the beginning of a series of investigations of hydrodynamic behavior in various semiconductor structures.

In the present paper, we propose an extension of the HDM for semiconductors. In Ref. [41] we assumed that only electrons were present as charge carriers (and so did de Ceglia *et al.* [42]), and due to the generally smaller effective mass of the electrons compared to the holes this is a reasonable approximation whenever electrons are present as majority charge carriers. In general, however, semiconductors may contain several different kinds of charge carriers such as electrons, heavy holes, and light holes, and ideally all should be taken into account. Therefore, the aim of this paper is to develop a hydrodynamic model for materials containing more than one kind of charge carrier. We will restrict ourselves to include only two different types of charge carriers, e.g., electrons and holes or heavy and light holes, and call the model

the *hydrodynamic two-fluid model* (as opposed to the HDM which contains only one hydrodynamic fluid). Other models that include multiple charge carriers already exist in the form of transport equations [43,44], and quantum-mechanical and semiclassical theories [45–50]. And while Ref. [47] briefly considers the hydrodynamic model for a two-fluid system, we will here present a more detailed analysis of the optical properties as well as consider finite systems. Our extension of a single fluid (appropriate for majority-carrier systems) to a two-fluid description shows interesting phenomena beyond the independent-fluids approximation that constitute an integral part of the local-response electrodynamics of doped semiconductors, i.e., the mere addition of electron and hole conductivities [44].

In the next section, we will present the theoretical foundation for the two-fluid model, which will then be supported by a microscopic derivation in Sec. III. In Sec. IV we will discuss some of the general properties of the model, while in Sec. V we will focus on systems of spherical geometry and derive extended versions of the Mie coefficients that take two hydrodynamic fluids into account. These coefficients will be used in Sec. VI, where the optical properties of semiconductor nanoparticles will be calculated.

## II. THE MODEL

In the traditional HDM, the electrical field and the current density are determined by a wave equation and a hydrodynamic equation of motion [9]. A natural extension to the HDM is therefore to include multiple hydrodynamic plasmas, each described with a hydrodynamic equation of motion. In the model presented here, we will consider two different kinds of charge carriers (or fluids), such as electrons and holes or light and heavy holes. The governing equations for the two-fluid model are therefore

$$\frac{\beta_a^2}{\omega^2 + i\gamma_a\omega} \nabla(\nabla \cdot \mathbf{J}_a) + \mathbf{J}_a = \frac{i\omega\epsilon_0\omega_a^2}{\omega^2 + i\gamma_a\omega} \mathbf{E}, \quad (1a)$$

$$\frac{\beta_b^2}{\omega^2 + i\gamma_b\omega} \nabla(\nabla \cdot \mathbf{J}_b) + \mathbf{J}_b = \frac{i\omega\epsilon_0\omega_b^2}{\omega^2 + i\gamma_b\omega} \mathbf{E}, \quad (1b)$$

$$-\nabla \times \nabla \times \mathbf{E} + \frac{\omega^2}{c^2} \epsilon_\infty \mathbf{E} = -i\mu_0\omega(\mathbf{J}_a + \mathbf{J}_b), \quad (1c)$$

where Eqs. (1a) and (1b) are the linearized hydrodynamic equations of motion related to the charge carriers  $a$  and  $b$ , respectively, and Eq. (1c) is the wave equation originating from Maxwell's equations. Here  $\omega_a$  and  $\omega_b$  are the plasma frequencies for the two fluids,  $\gamma_a$  and  $\gamma_b$  are the damping constants, and  $\beta_a$  and  $\beta_b$  are the nonlocal parameters. Note that if one of the current densities is set to zero (whereby the corresponding hydrodynamic equation can be removed) the equations reduce to the original equations of the HDM [see Eqs. (15) in Ref. [9]]. Although not considered here, it is also clear that the model easily could be extended to more than two types of charge carriers.

The real-space equations will be the starting point for most practical problems, but it can also be instructive to look in the reciprocal space as well. If the material is assumed to be

infinite, the spacial Fourier transforms of Eqs. (1) are [51]

$$-\frac{\beta_i^2}{\omega^2 + i\gamma_i\omega} \mathbf{q}(\mathbf{q} \cdot \mathbf{J}_i) + \mathbf{J}_i = \frac{i\omega\epsilon_0\omega_i^2}{\omega^2 + i\gamma_i\omega} \mathbf{E}, \quad (2)$$

$$\mathbf{q} \times \mathbf{q} \times \mathbf{E} + \frac{\omega^2}{c^2} \epsilon_\infty \mathbf{E} = -i\mu_0\omega(\mathbf{J}_a + \mathbf{J}_b), \quad (3)$$

where  $\mathbf{q}$  is the wave vector and  $i = a, b$ . Let us now consider the transversal and the longitudinal parts of the field separately. Starting with the transversal, or divergence-free, part of the field, this has the property  $\mathbf{q} \cdot \mathbf{E}^T = 0$  (and similarly for  $\mathbf{J}_a^T$  and  $\mathbf{J}_b^T$ ). This also means that  $\mathbf{q} \times \mathbf{q} \times \mathbf{E}^T = -q^2 \mathbf{E}^T$ , and Eqs. (3) and (2) can be combined to

$$q^2 = \left( \epsilon_\infty - \frac{\omega_a^2}{\omega^2 + i\gamma_a\omega} - \frac{\omega_b^2}{\omega^2 + i\gamma_b\omega} \right) \frac{\omega^2}{c^2}. \quad (4)$$

From the relation  $\epsilon_T \omega^2 / c^2 = q^2$  we now see that the transversal dielectric function is given by

$$\epsilon_T(\omega) = \epsilon_\infty - \frac{\omega_a^2}{\omega^2 + i\gamma_a\omega} - \frac{\omega_b^2}{\omega^2 + i\gamma_b\omega}. \quad (5)$$

The longitudinal, or rotation-free, part of the field has the property  $\mathbf{q} \times \mathbf{E}^L = 0$  (and similarly for  $\mathbf{J}_a^L$  and  $\mathbf{J}_b^L$ ). This means that  $\mathbf{q}(\mathbf{q} \cdot \mathbf{J}_i^L) = q^2 \mathbf{J}_i^L$ , and Eqs. (3) and (2) give us

$$0 = \epsilon_\infty - \frac{\omega_a^2}{\omega^2 + i\gamma_a\omega - \beta_a^2 q^2} - \frac{\omega_b^2}{\omega^2 + i\gamma_b\omega - \beta_b^2 q^2}. \quad (6)$$

From the relation  $\epsilon_L = 0$  we now see that the longitudinal dielectric function is given by

$$\epsilon_L(q, \omega) = \epsilon_\infty - \frac{\omega_a^2}{\omega^2 + i\gamma_a\omega - \beta_a^2 q^2} - \frac{\omega_b^2}{\omega^2 + i\gamma_b\omega - \beta_b^2 q^2}. \quad (7)$$

We here see that  $\epsilon_L$  is nonlocal (i.e., depends on the wave number  $q$ ), while  $\epsilon_T$  is local. This can be compared with the dielectric functions of the single-fluid HDM [51]:

$$\epsilon_T(\omega) = \epsilon_\infty - \frac{\omega_p^2}{\omega^2 + i\gamma\omega}, \quad (8a)$$

$$\epsilon_L(q, \omega) = \epsilon_\infty - \frac{\omega_p^2}{\omega^2 + i\gamma\omega - \beta^2 q^2}, \quad (8b)$$

where  $\epsilon_T$  and  $\epsilon_L$  also are local and nonlocal, respectively.

For the two-fluid model, we notice that if the fluids have the same  $\gamma$ 's and  $\beta$ 's then the plasma frequencies in the nominators of Eqs. (5) and (7) could be combined into a single effective parameter given by

$$\omega_{\text{eff}}^2 = \omega_a^2 + \omega_b^2, \quad (9)$$

whereby the expressions for  $\epsilon_T$  and  $\epsilon_L$  become equal to Eqs. (8a) and (8b), respectively. In other words, a two-fluid system can effectively be described by the single-fluid HDM whenever both  $\gamma_a = \gamma_b$  and  $\beta_a = \beta_b$ .

## III. MICROSCOPIC FOUNDATION

In this section, we will show that the expression for  $\epsilon_L$  in the two-fluid model in fact can be derived from quantum

mechanics by using a slightly modified version of the Lindhard approximation. We will consider a system of fermions described by the Hamiltonian  $H_0$  subject to a perturbation of the form

$$H_1 = U_0 e^{i(\mathbf{q}\cdot\mathbf{r}-\omega t)} + U_0^* e^{-i(\mathbf{q}\cdot\mathbf{r}-\omega t)}, \quad (10)$$

where  $U_0$  is the amplitude of the perturbation. According to Fermi's "golden rule," this results in the following expression for the longitudinal dielectric function [52]:

$$\epsilon_L(\mathbf{q}, \omega) = 1 + \frac{2e^2}{\epsilon_0 q^2} \frac{1}{V} \sum_{\alpha\beta} \frac{|\langle \psi_\beta | e^{i\mathbf{q}\cdot\mathbf{r}} | \psi_\alpha \rangle|^2}{E_\beta - E_\alpha - \hbar\omega - i\eta} \times [f(E_\alpha) - f(E_\beta)], \quad (11)$$

where  $V$  is the volume,  $e$  is the elementary charge, and  $E$  is the energy (the electrical field is not used in this section so there is no risk of confusion). The excitation takes place between the states  $|\psi_\alpha\rangle$  and  $|\psi_\beta\rangle$ , the function  $f$  is the Fermi-Dirac distribution, and  $\eta$  is a small real number originating from the Dirac identity [52].

We will now apply the Lindhard approximation in which the bands are assumed to be isotropic and perfectly parabolic and the wave functions are plane waves. This means that the matrix element in  $\epsilon_L(\mathbf{q}, \omega)$  equals 1 when the excitation is from  $\mathbf{k}$  to  $\mathbf{k} + \mathbf{q}$  and zero otherwise. But different from the typical Lindhard approximation in which only a single band is taken into account, we will here include two bands in the derivation. Excitations between these two bands are neglected, however, which is a reasonable approximation when considering energies smaller than the band gap. The result is

$$\epsilon_L(\mathbf{q}, \omega) = 1 + \chi_a(\mathbf{q}, \omega) + \chi_b(\mathbf{q}, \omega), \quad (12)$$

where the susceptibilities for bands  $a$  and  $b$  are given by

$$\chi_i(\mathbf{q}, \omega) = \frac{2e^2}{\epsilon_0 q^2} \frac{1}{V} \sum_{\mathbf{k}} \frac{f_i(\mathbf{k}) - f_i(\mathbf{k} + \mathbf{q})}{E_i(\mathbf{k} + \mathbf{q}) - E_i(\mathbf{k}) - \hbar\omega - i\eta}. \quad (13)$$

In Appendix A we show that in the  $\mathbf{q} \rightarrow 0$  limit Eq. (13) can be rewritten as

$$\chi_i(q, \omega) = -\frac{\omega_i^2}{\omega^2 + i\gamma\omega} - \frac{\omega_i^2}{(\omega^2 + i\gamma\omega)^2} \beta_i^2 q^2 - \dots, \quad (14)$$

where  $\gamma$  is the damping constant and the plasma frequencies are given by

$$\omega_i^2 = \frac{e^2 n_i}{\epsilon_0 m_i^*}. \quad (15)$$

Here  $n_i$  and  $m_i^*$  are the charge-carrier density and the effective mass, respectively, of band  $i$ . The nonlocal parameter  $\beta_i$  depends on the nature of the charge carriers. In this paper we will consider them to be electrons and holes in an intrinsic semiconductor originating either from thermal excitation or laser excitation across the band gap, or heavy and light holes in a  $p$ -doped semiconductor. As shown in Appendix A, the nonlocal parameter is in these cases given by

$$\begin{array}{l} \text{Thermally excited} \\ \text{charge carriers} \end{array} \quad \beta_i^2 = \frac{3k_B T}{m_i^*}, \quad (16)$$

$$\begin{array}{l} \text{Laser excited charge carriers} \\ \text{Heavy and light holes} \end{array} \quad \beta_i^2 = \frac{3k_{Fi}^2 \hbar^2}{5m_i^{*2}} = \frac{3}{5} v_{Fi}^2, \quad (17)$$

where  $T$  is the temperature,  $k_B$  is Boltzmann's constant, and  $k_{Fi}$  and  $v_{Fi}$  are the Fermi wave number and the Fermi velocity, respectively, of band  $i$ . For thermally excited charge carriers, it has been assumed that the temperature is low enough for the Fermi-Dirac distribution to be approximated by the Boltzmann distribution (see Appendix A). For laser-excited charge carriers and heavy and light holes, the distribution has been approximated with a step function. This also means that a quasiequilibrium is assumed to form in the laser-excited semiconductor. Expressions for  $n_i$  and  $k_{Fi}$  are found in Appendix B.

If we assume that  $\beta_i^2 q^2 \ll \omega^2 + i\gamma\omega$ , then the expression in Eq. (14) can be rewritten by using the fact that it resembles a geometric series to first order. Together with Eq. (12), we then find that the longitudinal dielectric function is given by

$$\epsilon_L(q, \omega) = 1 - \frac{\omega_a^2}{\omega^2 + i\gamma\omega - \beta_a^2 q^2} - \frac{\omega_b^2}{\omega^2 + i\gamma\omega - \beta_b^2 q^2}, \quad (18)$$

which is almost identical to Eq. (7) from previous section. The main difference is the presence of  $\epsilon_\infty$  in Eq. (7) which contains the interband transitions. This parameter is simply added "by hand," and the value can often be found as a constant in data books. The second discrepancy is the damping constant  $\gamma$  which in Eq. (7) is different for the two charge carriers. Since the charge carriers are expected to have different mobilities  $\mu_a$  and  $\mu_b$ , and the damping constants are related to the mobilities by [53]

$$\gamma_i = \frac{e}{m_{i,\text{cond}}^* \mu_i}, \quad (19)$$

we will allow  $\gamma_i$  to assume different values for the two charge carriers. Note that the effective mass entering Eq. (19) is the *conductivity effective mass*, while  $m_i^*$  used in Eqs. (15)–(17) is the *density-of-states effective mass*.

The parameters  $\omega_i$ ,  $\beta_i$ , and  $\gamma_i$  will in general be different for the two fluids, but there are situations where they coincide. An intrinsic semiconductor with identical effective masses and mobilities of electrons and holes would according to Eqs. (15) and (16) have the same plasma frequency,  $\beta$  and  $\gamma$  for the two fluids. A more typical semiconductor where  $m_e^* < m_h^*$  could also be modulated to obtain  $\beta_e = \beta_h$  by *combining*  $p$  doping and laser excitation. A larger density of holes would then be used to compensate for the fact that they are heavier than electrons, and obtaining  $m_h^*/m_e^* = k_{Fh}/k_{Fe}$  would according to Eq. (17) result in identical  $\beta$ 's [note that  $k_{Fi}^3 = 3\pi^2 n_i$  according to Eq. (A6)].

#### IV. BULK AND GENERAL PROPERTIES

In this section, we will analyze some of the general properties of the two-fluid model as well as properties related to the infinite medium. The vector wave equations derived here will also be used in Sec. V.

### A. Normal modes

For the single-fluid HDM, it has been found useful to derive a set of homogeneous equations for the transversal and longitudinal components of the current density [54] as originally introduced by Boardman and Paranjape [55]. We will accordingly derive a set of Boardman equations for the two-fluid model. The first step is to apply either the curl or the divergence to Eqs. (1) whereby a set of equations is obtained for either the transversal or the longitudinal fields, respectively. This is shown in Appendix C using a compact matrix notation. Secondly, we introduce the following linear relations for both transversal ( $T$ ) and longitudinal ( $L$ ) current densities:

$$\mathbf{J}_a^z = a_1^z \mathbf{J}_1^z + a_2^z \mathbf{J}_2^z, \quad (20a)$$

$$\mathbf{J}_b^z = b_1^z \mathbf{J}_1^z + b_2^z \mathbf{J}_2^z, \quad (20b)$$

where  $z = T, L$ . Notice that all current densities share the properties  $\nabla \times \mathbf{J} = \nabla \times \mathbf{J}^T$  and  $\nabla \cdot \mathbf{J} = \nabla \cdot \mathbf{J}^L$ . We now require that  $\mathbf{J}_1$  is independent of  $\mathbf{J}_2$ , which results in eight equations in total: For both curl and divergence we get two for both  $\mathbf{J}_1$  and  $\mathbf{J}_2$ . The four equations for the longitudinal fields

$$\left[ \beta_a^2 \nabla^2 + \omega(\omega + i\gamma_a) - \frac{\omega_a^2}{\epsilon_\infty} \left( 1 + \frac{b_j^L}{a_j^L} \right) \right] \nabla \cdot \mathbf{J}_j = 0, \quad (21a)$$

$$\left[ \beta_b^2 \nabla^2 + \omega(\omega + i\gamma_b) - \frac{\omega_b^2}{\epsilon_\infty} \left( 1 + \frac{a_j^L}{b_j^L} \right) \right] \nabla \cdot \mathbf{J}_j = 0 \quad (21b)$$

with  $j = 1, 2$  are the Boardman equations for the divergence. The four equations for the transversal fields

$$\left[ c^2 \nabla^2 + \omega^2 \epsilon_\infty - \frac{\omega^2 \omega_a^2}{\omega(\omega + i\gamma_a)} \left( 1 + \frac{b_j^T}{a_j^T} \right) \right] \nabla \times \mathbf{J}_j = 0, \quad (22a)$$

$$\left[ c^2 \nabla^2 + \omega^2 \epsilon_\infty - \frac{\omega^2 \omega_b^2}{\omega(\omega + i\gamma_b)} \left( 1 + \frac{a_j^T}{b_j^T} \right) \right] \nabla \times \mathbf{J}_j = 0 \quad (22b)$$

are the Boardman equations for the curl. The Boardman equations are useful tools when finding the current densities and the electrical fields, and below we use the Boardman equations for the divergence to find the dispersion relations for the longitudinal fields.

### B. Vector wave equation

When solving Maxwell's equations for any geometry, such as the spherically symmetric systems considered in Sec. V, a suitable starting point is the vector wave equation. Therefore we will now derive the vector wave equation for both the transversal and the longitudinal electrical fields and simultaneously find the dispersion relations.

Considering purely transversal fields, Eqs. (1) become

$$\mathbf{J}_i^T = \frac{i\omega\epsilon_0\omega_i^2}{\omega^2 + i\gamma_i\omega} \mathbf{E}^T \quad i = a, b, \quad (23)$$

$$\nabla^2 \mathbf{E}^T + \frac{\omega^2}{c^2} \epsilon_\infty \mathbf{E}^T = -i\mu_0\omega(\mathbf{J}_a^T + \mathbf{J}_b^T), \quad (24)$$

which can be combined directly into the vector wave equation for the transversal field

$$\nabla^2 \mathbf{E}^T + k_T^2 \mathbf{E}^T = 0, \quad (25)$$

where the transversal wave number is given by

$$k_T^2 = \frac{\omega^2}{c^2} \left( \epsilon_\infty - \frac{\omega_a^2}{\omega^2 + i\gamma_a\omega} - \frac{\omega_b^2}{\omega^2 + i\gamma_b\omega} \right). \quad (26)$$

Notice that this is consistent with the expression for  $\epsilon_T$  in Sec. II, but differs from that by being valid for any geometry (and not just for the infinite case).

Deriving the vector wave equation for the longitudinal field requires a slightly different procedure. Turning to the Boardman equations (21a) and (21b) with  $j = 1$ , we notice that they both have the form

$$(\nabla^2 + k^2) \nabla \cdot \mathbf{J}_1 = 0. \quad (27)$$

This also means that the variable  $k$  must be the same in both cases

$$\begin{aligned} k^2 &= \frac{\omega(\omega + i\gamma_a)}{\beta_a^2} - \frac{\omega_a^2}{\beta_a^2 \epsilon_\infty} \left( 1 + \frac{b_1^L}{a_1^L} \right) \\ &= \frac{\omega(\omega + i\gamma_b)}{\beta_b^2} - \frac{\omega_b^2}{\beta_b^2 \epsilon_\infty} \left( 1 + \frac{a_1^L}{b_1^L} \right). \end{aligned} \quad (28)$$

From this we find an expression for the ratio  $b_1^L/a_1^L$  which we will call  $\alpha_1^L$ :

$$\begin{aligned} \frac{b_1^L}{a_1^L} &= \alpha_1^L = \frac{\beta_a^2 \epsilon_\infty}{\omega_a^2} \frac{1}{2} \left( k_a^2 - k_b^2 \right. \\ &\quad \left. \mp \sqrt{(k_a^2 - k_b^2)^2 + \frac{4\omega_a^2 \omega_b^2}{\beta_a^2 \beta_b^2 \epsilon_\infty^2}} \right), \\ k_i^2 &= \left( \omega(\omega + i\gamma_i) - \frac{\omega_i^2}{\epsilon_\infty} \right) \frac{1}{\beta_i^2} \quad i = a, b. \end{aligned} \quad (29)$$

Now, the same procedure can be carried out for Eqs. (21a) and (21b) with  $j = 2$ , and this gives us instead  $\alpha_2^L = b_2^L/a_2^L$ . However, the expression for  $\alpha_2^L$  is exactly the same as the one for  $\alpha_1^L$  because the Boardman equations for the divergence of  $\mathbf{J}_1$  and  $\mathbf{J}_2$  are the same. Although this seems strange, it is in fact exactly what we would expect: since we have put no restraints on  $\nabla \cdot \mathbf{J}_1$  and  $\nabla \cdot \mathbf{J}_2$  (or equivalently  $\mathbf{J}_1^L$  and  $\mathbf{J}_2^L$ ), they each have to contain both solutions ["+" and "-" in Eq. (29)]. We can therefore chose  $\alpha_1^L$  as the "-" solution and  $\alpha_2^L$  as the "+" solution (and this will be done henceforth).

We can also obtain an expression for  $k^2$  by inserting either  $\alpha_1^L$  or  $\alpha_2^L$  back into Eq. (28). The result is two different wave numbers belonging to  $\mathbf{J}_1^L$  and  $\mathbf{J}_2^L$ , respectively:

$$k_{L,2}^2 = \frac{1}{2} \left( k_a^2 + k_b^2 \pm \sqrt{(k_a^2 - k_b^2)^2 + \frac{4\omega_a^2 \omega_b^2}{\beta_a^2 \beta_b^2 \epsilon_\infty^2}} \right). \quad (30)$$

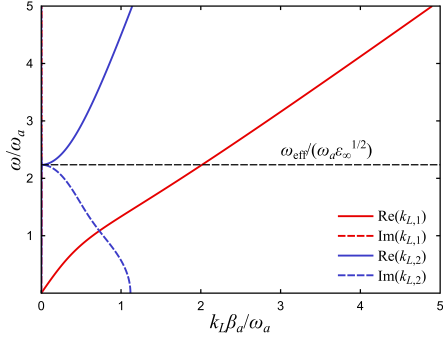


FIG. 1. The dispersion relations of the optical mode (blue lines) and the acoustic mode (red lines). The full and dashed lines show the real and imaginary components, respectively, of  $k_{L,j}$ . The parameters are  $\omega_b/\omega_a = 2$ ,  $\beta_b/\beta_a = 4$ ,  $\gamma_a = \gamma_b = 0.01\omega_a$ , and  $\epsilon_\infty = 1$ . Notice that the optical mode has a finite imaginary component (i.e., is damped) below  $\omega_{\text{eff}}/\epsilon_\infty^{1/2}$ . Due to the small damping constants, the red dashed line lies almost exactly on top of the  $y$  axis.

Here  $k$  has been given the subscript “ $L$ ,” because it turns out that this is in fact the longitudinal wave number. This can be seen by taking the divergence of Ampere’s law and defining the longitudinal fields  $\mathbf{E}_1^L$  and  $\mathbf{E}_2^L$  where  $\mathbf{E}_j^L \propto \mathbf{J}_j^L$ . Introducing this into Eq. (27) we find

$$\nabla^2 \mathbf{E}_j^L + k_{L,j}^2 \mathbf{E}_j^L = 0 \quad j = 1, 2, \quad (31)$$

which is the sought vector wave equation for the longitudinal fields.

### C. Dispersion for an infinite medium

With Eq. (30) we are now in a position to plot the dispersion relations for the longitudinal modes  $k_{L,j}(\omega)$  for an infinite medium. In Fig. 1 we show  $k_{L,j}(\omega)\beta_d/\omega_a$  as a function of  $\omega/\omega_a$ , and we notice that the two modes ( $j = 1, 2$ ) have very different appearances. The mode  $k_{L,1}(\omega)$  follows almost a straight line, while  $k_{L,2}(\omega)$  is real-valued above a line given by  $\omega_{\text{eff}}/\epsilon_\infty^{1/2}$  with  $\omega_{\text{eff}}^2 = \omega_a^2 + \omega_b^2$  and imaginary (damped) below it. Because the  $j = 2$  mode has nonzero  $\omega$  for  $k_{L,2} \approx 0$ , it can be excited by electromagnetic radiation, and for that reason it is denoted the optical mode. The  $j = 1$  mode is denoted the acoustic mode, and unless methods for momentum matching are applied it cannot be excited by electromagnetic radiation. The appearance of an optical and an acoustic branch in systems with two different kinds of charge carriers has been observed before in random-phase-approximation models for infinite media [45,48,49]. Here we have found the formation of an optical and an acoustic mode in a two-fluid hydrodynamic model for an infinite medium, something that was briefly touched upon by Schaefer and von Baltz [47]. In Sec. VI we will analyze both modes in finite systems.

The graphical presentation in Fig. 1 can be supported by making approximations to Eq. (30). By isolating the frequency

such that we obtain  $\omega_j(k)$ , and taking the limit  $k \rightarrow 0$ , we get the following expressions (ignoring loss):

$$\omega_1^2(k) \approx \frac{\omega_b^2 \beta_a^2 + \omega_a^2 \beta_b^2}{\omega_{\text{eff}}^2} k^2, \quad (32a)$$

$$\omega_2^2(k) \approx \frac{\omega_{\text{eff}}^2}{\epsilon_\infty} + \frac{\omega_a^2 \beta_a^2 + \omega_b^2 \beta_b^2}{\omega_{\text{eff}}^2} k^2. \quad (32b)$$

Here it is clear that the acoustic mode ( $\omega_1$ ) has a linear dependence on  $k$ , while the optical mode ( $\omega_2$ ) mainly is imaginary below the line  $\omega_{\text{eff}}/\epsilon_\infty^{1/2}$ .

In Fig. 1 we also see that  $\text{Im}(k_{L,2})$  is cut off at  $\text{Im}(k_{L,2})\beta_d/\omega_a \approx 1.1$  for  $\omega = 0$ . More generally the cutoff value is  $\text{Im}(k_{L,2}) = (\omega_a^2/\beta_a^2 + \omega_b^2/\beta_b^2)^{1/2}/\epsilon_\infty^{1/2}$  as follows from Eq. (30). This is no unique property of the two-fluid model, and the single-fluid HDM has a similar cutoff at  $\omega_p/(\beta \epsilon_\infty^{1/2})$  [see the expression for  $k_L$  below Eq. (37) in Sec. VI].

That the model contains two longitudinal modes follows directly from the fact that it includes two different kinds of charge carriers. It can be compared with the single-fluid HDM that only has one longitudinal mode. This is an optical mode, i.e., damped below a certain frequency, and for this reason no longitudinal excitations are expected in this low-frequency region [54]. The two-fluid model, on the other hand, also has an acoustic mode which in principle could give rise to excitations below  $\omega_{\text{eff}}/\epsilon_\infty^{1/2}$ . In Sec. VI we will consider the optical properties of spherical particles. There we will see that peaks indeed emerge in the spectrum below the dipole LSP as a direct consequence of the acoustic mode. In that section we will also show that at higher frequencies the two fluids will decouple, and the optical response then will resemble that of two independent charge-carrier species.

## V. EXTENDED MIE THEORY

We wish to analyze the two-fluid model for finite systems, and in this paper we will focus on spherically symmetric systems. Maxwell’s equations were originally solved for transversal waves in spherical geometry by Mie [56], and Ruppini later found a solution including longitudinal waves [57] which has been used together with the HDM for spherical metal particles [5,7,58]. The addition of a second longitudinal wave, however, results in a different system of equations, and here we will derive the Mie coefficients for the two-fluid model.

In spherical geometry, the general solutions to the transversal wave equation [Eq. (25)] are  $\mathbf{m}_{\sigma ml}$  and  $\mathbf{n}_{\sigma ml}$ , and the solutions to the longitudinal wave equation [Eq. (31)] are  $\mathbf{l}_{\sigma ml}$  [59]. Here “ $e$ ” and “ $o$ ” are short-hand notation for even and odd, and  $m$  and  $l$  are integers for which  $m \leq l$  holds. We now consider a typical experimental scenario where a plane wave  $\mathbf{E}_i$  is incident on a spherical particle which results in a wave scattered (or reflected) from the particle  $\mathbf{E}_r$ , and a wave transmitted into the particle  $\mathbf{E}_t$ . Because the functions  $\mathbf{m}_{\sigma ml}(k_T, \mathbf{r})$ ,  $\mathbf{n}_{\sigma ml}(k_T, \mathbf{r})$ , and  $\mathbf{l}_{\sigma ml}(k_{L,j}, \mathbf{r})$  form a complete basis, any wave can be written as a linear combination of these. For an  $x$ -polarized plane wave propagating in the  $z$  direction, it can be shown that the linear combination only uses functions of the forms  $\mathbf{m}_{o1l}$ ,  $\mathbf{n}_{e1l}$ , and  $\mathbf{l}_{o1l}$  [59]. Furthermore, we will assume that the exterior medium is purely dielectric, which means that

the incident and reflected fields can be written in terms of  $\mathbf{m}_{o1l}$  and  $\mathbf{n}_{e1l}$  alone. This means that

$$\begin{aligned} \mathbf{E}_i(\mathbf{r}, t) &= E_0 e^{-i\omega t} \sum_{l=1}^{\infty} i^l \frac{2l+1}{l(l+1)} (\mathbf{m}_{o1l}^{(1)}(k_D, \mathbf{r}) - i \mathbf{n}_{e1l}^{(1)}(k_D, \mathbf{r})), \end{aligned} \quad (33)$$

$$\begin{aligned} \mathbf{E}_r(\mathbf{r}, t) &= E_0 e^{-i\omega t} \sum_{l=1}^{\infty} i^l \frac{2l+1}{l(l+1)} (a_l^r \mathbf{m}_{o1l}^{(3)}(k_D, \mathbf{r}) - i b_l^r \mathbf{n}_{e1l}^{(3)}(k_D, \mathbf{r})), \end{aligned} \quad (34)$$

where  $k_D = \epsilon_D^{1/2} \omega / c$  and  $\epsilon_D$  is the permittivity of the surrounding dielectric. The superscripts 1 and 3 indicate that the contained spherical Bessel functions are Bessel functions of the first kind ( $j_l$ ) and Hankel functions of the first kind ( $h_l^{(1)}$ ), respectively. The expansion coefficients  $a_l^r$  and  $b_l^r$  in the reflected field are known as the *Mie coefficients*, and the primary goal in this section is to obtain expressions for these.

The transmitted field (i.e., inside the sphere) contains, in addition to the transversal fields, two different longitudinal fields:

$$\begin{aligned} \mathbf{E}_t(\mathbf{r}, t) &= E_0 e^{-i\omega t} \sum_{l=1}^{\infty} i^l \frac{2l+1}{l(l+1)} (a_l^t \mathbf{m}_{o1l}^{(1)}(k_T, \mathbf{r}) - i b_l^t \mathbf{n}_{e1l}^{(1)}(k_T, \mathbf{r}) \\ &\quad + c_l^t \mathbf{h}_{e1l}^{(1)}(k_{L,1}, \mathbf{r}) + c_{2l}^t \mathbf{h}_{e1l}^{(1)}(k_{L,2}, \mathbf{r})), \end{aligned} \quad (35)$$

where  $k_T$  and  $k_{L,j}$  are given by Eqs. (26) and (30), respectively.

To find the Mie coefficients, a set of suitable boundary conditions (BCs) must be provided. By requiring that the fields satisfy Maxwell's equations and are finite at boundaries, it is found that the parallel components of the electrical and the magnetic fields are continuous, i.e.,  $\Delta \mathbf{E}_{\parallel} = \mathbf{0}$  and  $\Delta \mathbf{B}_{\parallel} = \mathbf{0}$ . While these Maxwell BCs are sufficient in the local-response solution, additional BCs are needed in the two-fluid model. A similar problem was encountered in the HDM where it was found that one additional BC was needed. A physically meaningful BC that is widely used in the HDM is  $\mathbf{J}_{\perp} = \mathbf{0}$ , which implies that the charge carriers cannot leave the surface [9]. The two-fluid model requires *two* additional BCs, and here we will use the conditions  $\mathbf{J}_{b,\perp} = \mathbf{0}$  and  $\mathbf{J}_{a,\perp} = \mathbf{0}$ . (or equivalently  $\mathbf{J}_{1,\perp} = \mathbf{0}$  and  $\mathbf{J}_{2,\perp} = \mathbf{0}$ ).

Given these BCs, we obtain the system of linear equations presented in Appendix D from which  $a_l^{r,t}$ ,  $b_l^{r,t}$ , and  $c_l^{r,t}$  can be found. The  $a_l^r$  and  $b_l^r$  coefficients, which are of primary interest, are given by

$$a_l^r = \frac{-j_l(x_D)[x_T j_l(x_T)]' + j_l(x_T)[x_D j_l(x_D)]'}{h_l^{(1)}(x_D)[x_T j_l(x_T)]' - j_l(x_T)[x_D h_l^{(1)}(x_D)]'}, \quad (36a)$$

$$b_l^r = \frac{-\epsilon_D j_l(x_D)(\Delta_l + [x_T j_l(x_T)]') + \epsilon_T j_l(x_T)[x_D j_l(x_D)]'}{\epsilon_D h_l^{(1)}(x_D)(\Delta_l + [x_T j_l(x_T)]') - \epsilon_T j_l(x_T)[x_D h_l^{(1)}(x_D)]'}, \quad (36b)$$

where  $x_D = Rk_D$  and  $x_T = Rk_T$ . The differentiation (denoted with the prime) is with respect to the argument. The parameter

$\Delta_l$  is given by

$$\Delta_l = \frac{j_l(x_T)l(l+1)}{A} \left( \frac{j_l(x_1)C_2}{x_1 j_l'(x_1)} - \frac{j_l(x_2)C_1}{x_2 j_l'(x_2)} \right), \quad (36c)$$

where  $x_j = Rk_{L,j}$  and

$$C_j = \frac{\omega_a^2 \epsilon_{\infty} k_{L,j}^2}{\beta_a^2 (1 + \frac{\alpha_j^t}{\alpha_j^r})} - \frac{\omega_b^2 \epsilon_{\infty} k_{L,j}^2}{\beta_b^2 (1 + \alpha_j^t)}, \quad (36d)$$

$$A = \frac{(\omega^2 + i\gamma_a \omega)(\omega^2 + i\gamma_b \omega)(\alpha_1^t - \alpha_2^t)}{\beta_a^2 \beta_b^2 (1 + \alpha_1^t)(1 + \alpha_2^t)}, \quad (36e)$$

and  $\alpha_j$  is defined in Eq. (29). The coefficients  $a_l^r$  are related to oscillations of the magnetic type, and the expression is identical to the one found in the classical local derivation [59]. The coefficients  $b_l^r$  are related to oscillations of the electrical type, and the expression is different from the local result *unless* the nonlocal parameter  $\Delta_l$  is set to zero. It should also be mentioned that the formula for  $b_l^r$  is identical to the one found for the single-fluid HDM [57,58], except that there  $\Delta_l$  is given by [58]

$$\Delta_l = \frac{j_l(x_T)j_l(x_L)l(l+1)}{x_L j_l'(x_L)} \left( \frac{\epsilon_T}{\epsilon_{\infty}} - 1 \right), \quad (37)$$

where  $x_T = R\epsilon_T^{1/2} \omega / c$  and  $\epsilon_T$  is given by Eq. (8a). Also defined is the dimensionless parameter  $x_L = Rk_L$  where  $k_L = (\omega^2 + i\gamma\omega - \omega_p^2/\epsilon_{\infty})^{1/2}/\beta$ .

When the expressions for  $a_l^r$  and  $b_l^r$  have been found, the extinction cross section is easily calculated with [59]

$$\sigma_{\text{ext}} = -\frac{2\pi}{k_D^2} \sum_{l=1}^{\infty} (2l+1) \text{Re}(a_l^r + b_l^r). \quad (38)$$

In the next section, Eq. (38) will be used to find the extinction spectra of nanospheres in the two-fluid model.

## VI. NUMERICAL RESULTS

In this section, we will present some numerical simulations of the optical properties of both realistic and artificial materials containing two-fluid systems.

### A. Features in the extinction spectrum

First we will analyze the artificial material "semiconductor A" with the parameters  $\omega_a = 3.6 \times 10^{14} \text{ s}^{-1}$ ,  $\omega_b = 1.8 \times 10^{14} \text{ s}^{-1}$ ,  $\gamma_a = \gamma_b = 1.0 \times 10^{12} \text{ s}^{-1}$ ,  $\beta_a = 4.3 \times 10^5 \text{ m s}^{-1}$ ,  $\beta_b = 1.4 \times 10^5 \text{ m s}^{-1}$ , and  $\epsilon_{\infty} = 5$ . As we will see later, these parameters are comparable to those of a realistic semiconductor with the exception of the damping constants which have been set low to make the characteristic features of the spectrum clear. We will now consider a spherical particle of this material with  $R = 10 \text{ nm}$  surrounded by vacuum ( $\epsilon_D = 1$ ). Equation (38) then gives us the extinction cross section which is shown with the solid line in Fig. 2(a) as a function of the relative frequency  $\omega/\omega_{\text{eff}}$  where  $\omega_{\text{eff}}^2 = \omega_a^2 + \omega_b^2$ . The spectrum has been normalized with  $\sigma_{\text{geom}} = \pi R^2$ .

The large peak situated around  $\omega/\omega_{\text{eff}} = 0.4$  can be recognized as the dipole LSP resonance,  $\omega_{\text{LSP}}$ , which is also present in the classical local result. However, the peak is shifted to higher frequencies in the two-fluid model as can be seen in the

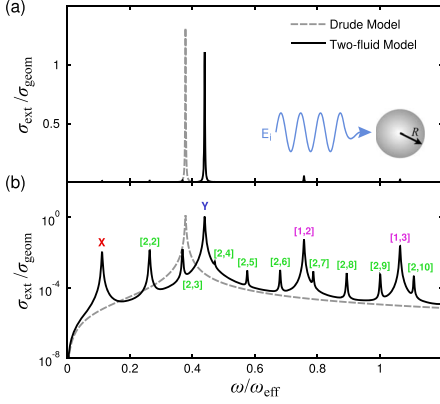


FIG. 2. (a) The extinction spectrum for semiconductor A (see parameters in the main text) with  $R = 10$  nm and  $\epsilon_D = 1$ . The spectrum has been normalized with  $\sigma_{\text{geom}} = \pi R^2$ . The dashed line is the local Drude model, and the full line is the two-fluid model. (b) The same spectrum plotted with the logarithmic y axis. The bulk plasmon peaks are labeled with  $[j, n]$ , while the first acoustic peak and the LSP peak are indicated with “X” and “Y,” respectively.

figure by comparing with the local Drude model shown with a dashed line. The local result was found by setting  $\Delta_l = 0$  in Eq. (36b). This blueshift is a well-known nonlocal effect that is also observed in the single-fluid HDM for both metals [7,13] and semiconductors [41]. There it is found that the blueshift increases as the particle radius is reduced.

In Fig. 2(a) we also see small peaks that appear to be present only in the nonlocal model. To investigate this further, the extinction spectrum is shown again in Fig. 2(b) in a semi-logarithmic plot. Now the peaks have become more visible, and several even smaller peaks have appeared. Apart from the LSP resonance, none of these peaks are present in the local solution and, as we will show later, several are not present in the single-fluid HDM either.

To understand the nature of these resonances, we will consider wavelengths much larger than the particle whereby all the Mie coefficients in Eq. (36b) except  $b_1^{\prime}$  are reduced to zero (see Ref. [59]). Now, when looking for frequencies where the expression diverges, we notice that this occurs whenever  $j_1^{\prime}(x_1)j_1^{\prime}(x_2)$  in the denominator of  $\Delta_1$  vanishes. If we consider the high-frequency region, we can introduce the following large-argument approximation for the spherical Bessel functions [59]:

$$j_l(x_j) \approx \frac{1}{x_j} \cos\left(x_j - \frac{l+1}{2}\pi\right), \quad (39)$$

and we find that the condition  $j_1^{\prime}(x_1)j_1^{\prime}(x_2) = 0$  is approximately fulfilled whenever  $x_j = \pi n$  with  $j = 1, 2$  and  $n = 1, 2, \dots$ . The expression for  $k_{L,j}$  in Eq. (30) can also be simplified at high frequency when  $k_a, k_b \gg 2\omega_a\omega_b/\beta_a\beta_b\epsilon_{\infty}$

(here ignoring loss):

$$k_{L,j}^2 \approx \frac{1}{2} \left[ \left( \omega^2 - \frac{\omega_a^2}{\epsilon_{\infty}} \right) \frac{1}{\beta_a^2} + \left( \omega^2 - \frac{\omega_b^2}{\epsilon_{\infty}} \right) \frac{1}{\beta_b^2} \right. \\ \left. \pm \left( \omega^2 - \frac{\omega_a^2}{\epsilon_{\infty}} \right) \frac{1}{\beta_a^2} - \left( \omega^2 - \frac{\omega_b^2}{\epsilon_{\infty}} \right) \frac{1}{\beta_b^2} \right]. \quad (40)$$

Combining this with the condition for  $x_j$ , we get the following expressions for the resonances:

$$\omega^2 = \begin{cases} \frac{\pi^2 n^2 \beta_a^2}{R^2} - \frac{\omega_a^2}{\epsilon_{\infty}} & (j = 1) \\ \frac{\pi^2 n^2 \beta_b^2}{R^2} - \frac{\omega_b^2}{\epsilon_{\infty}} & (j = 2) \end{cases}. \quad (41)$$

Here we see that the positions of the peaks are given by two arrays that depend on the properties of either the  $a$  fluid or the  $b$  fluid. In other words, the charge carriers behave as two independent fluids for high frequencies. In Fig. 2(b), the large peaks above  $\omega_{\text{LSP}}$  can be identified as resonances of the  $a$  fluid and are found with the  $j = 1$  expression, while the small peaks are resonances of the  $b$  fluid found with the  $j = 2$  expression (notice that the distances between the peaks are determined by  $\beta_a$  and  $\beta_b$ ). The peaks have been labeled with  $[j, n]$ , and we notice that  $n$  does not start at 1 as is natural to expect. It turns out that the  $n = 1$  peak simply does not exist and is an artifact of the approximations leading to Eq. (41).

What is particularly noteworthy in the spectrum is that resonances are found in the region below the LSP peak which is “forbidden” in the HDM. The reason is that the  $a$  and  $b$  fluids hybridize and form both an optical and an acoustic branch, where the acoustic branch is characterized by a primarily real wave number at frequencies below the LSP peak. This gives rise to the peaks below  $\omega_{\text{LSP}}$  for what reason we will call them *acoustic peaks*. The single-fluid HDM, on the other hand, only contains an optical longitudinal branch, which means that no bulk plasmon peaks can exist below the LSP peak [54].

Among the acoustic peaks in Fig. 2, we find two bulk plasmon peaks labeled with [2,2] and [2,3]. However, as a result of the hybridization, these resonances are not purely related to the  $b$  fluid, and their positions are therefore only poorly predicted by Eq. (41). Also found below  $\omega_{\text{LSP}}$  is a resonance marked with “X,” and it turns out that this is quite different from the bulk plasmons. To see this, the charge distribution inside the sphere is shown in Fig. 3 for different frequencies. The contour plots show the distribution in the  $xz$  plane when the incoming wave is moving in the  $z$  direction, and the electrical field is polarized in the  $x$  direction. We here see that the first acoustic peak, marked with “X,” is in fact a surface plasmon characterized by a high charge density near the surface. We will discuss this resonance in detail below. The resonance marked with [2,2], on the other hand, is a bulk plasmon with a high charge density near the center, and its distribution is nearly identical to the one marked with [1,2] which is the bulk plasmon of the  $a$  fluid of the same order. The peaks marked with [2,5] and [1,3] are bulk plasmons of higher orders for the  $b$  fluid and the  $a$  fluid, respectively. The charge distribution for the LSP peak is also shown (marked with “Y”), and we see from the contour plot that although it is indeed a surface plasmon it also displays the pattern of a confined bulk plasmon. The reason is that the LSP resonance hybridizes with the  $b$ -fluid bulk plasmon marked by [2,4], resulting in a charge

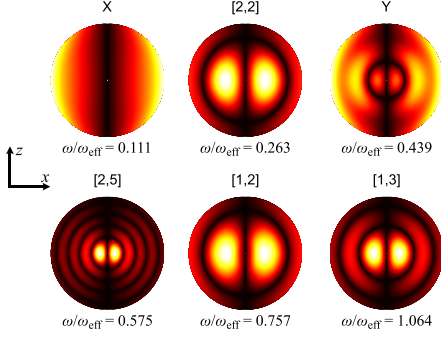


FIG. 3. The charge distribution in the  $xz$  plane for semiconductor A at different frequencies. The damping constants have been set to  $\gamma_a = \gamma_b = 1.0 \times 10^{11} \text{ s}^{-1}$  to make the patterns more clear. The incoming wave is directed in the  $z$  direction with the electrical field polarized in the  $x$  direction.

distribution with features from both surface and bulk plasmons. Such a hybridization would never take place in the HDM where the surface plasmons always are clearly separated in frequency from the bulk plasmons.

Notice that all the charge distributions are dipole modes, i.e., symmetric along the direction of the  $\mathbf{E}$  field, and the same is true for all the visible peaks in Fig. 2(b). A family of higher-order modes in fact does exist for each peak, but they are too faint to be seen in this spectrum (see Ref. [7] for an analysis of multipoles in the HDM).

### B. Comparison to the HDM

It has already been indicated that the two-fluid model is similar to the traditional single-fluid HDM on some points and different on others. To analyze the differences, the extinction spectra for semiconductor A as calculated by the two different models are shown in Fig. 4 for  $R = 10 \text{ nm}$  and  $\epsilon_D = 1$ . The extinction cross section has been calculated for the single-fluid HDM by only including one kind of charge carrier and ignoring the other (this was also done in Ref. [41]). In this case, the single-fluid parameters are given by  $\omega_p = \omega_j$ ,  $\beta = \beta_j$ , and  $\gamma = \gamma_j$ , and the nonlocal parameter  $\Delta_j$  is found with Eq. (37) rather than Eq. (36c).

When the  $a$  fluid is included in the single-fluid HDM, the spectrum with the dashed magenta line is obtained, and we see that it reproduces the  $j = 1$  bulk plasmon peaks found in the two-fluid model very well. This is related to the fact that the bulk plasmon peaks in the two-fluid model mainly are determined by the properties of the charge carriers separately, as was indicated in Eq. (41). Additionally, the LSP peak in the single-fluid model is almost at the same position as the one in the two-fluid model.

The dash-dotted green line in the figure shows the extinction cross section for the single-fluid HDM when only the  $b$  fluid is included, and we see that it matches well with the  $j = 2$  bulk plasmon peaks in the two-fluid model. It also reproduces two

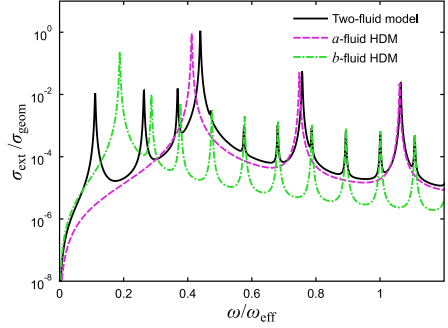


FIG. 4. The spectrum of semiconductor A (parameters given in the main text) as found by the two-fluid model is shown with the solid black line. The dashed magenta line and the dash-dotted green line show the spectra found with the single-fluid HDM when including the  $a$  fluid and  $b$  fluid, respectively.

of the acoustic peaks reasonably well, but is completely off when it comes to the first acoustic peak [marked with “X” in Fig. 2(b)]. This first peak is therefore a feature of the two-fluid model that cannot be reproduced by two independent single-fluid models.

It was mentioned in Sec. II that the two-fluid model reduces to the single-fluid model if  $\beta_a = \beta_b$  and  $\gamma_a = \gamma_b$ . This is shown in Fig. 5 where the extinction spectrum for semiconductor A in the two-fluid model is plotted for increasingly similar  $\beta$  values. The green dashed line in the figure shows the single-fluid HDM with  $\omega_p^2 = \omega_a^2 + \omega_b^2$  and  $\beta = \beta_a$ , and we see that it is exactly on top of the line showing the  $\beta_b = 0.9999\beta_a$  case. Confirming that the two-fluid model reduces to the single-fluid HDM for  $\beta_a = \beta_b$  is also a corroboration of the numerical results. Finally, it is worth mentioning that the local approximation,

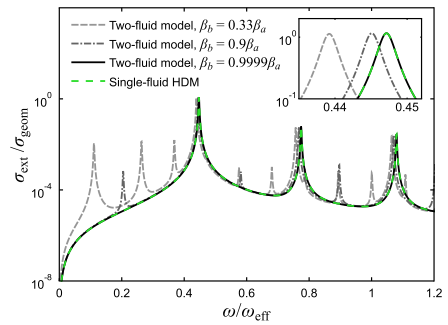


FIG. 5. The spectrum of semiconductor A (parameters given in the main text) as found by the two-fluid model for different values of  $\beta_b$ :  $0.33\beta_a$ ,  $0.9\beta_a$ , and  $0.9999\beta_a$ . When the  $\beta$ 's approach the same value, the spectrum coincides with the one predicted by the single-fluid HDM (shown with the dashed green line).

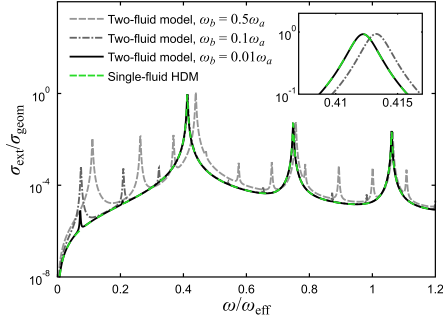


FIG. 6. The spectrum of semiconductor A (parameters given in the main text) as found by the two-fluid model for different values of  $\omega_b$ :  $0.5\omega_a$ ,  $0.1\omega_a$ , and  $0.01\omega_a$ . As  $\omega_b$  diminishes, the spectrum becomes identical to the one obtained by the single-fluid HDM (shown with the dashed green line).

$\beta_a = \beta_b = 0$ , is a special case of identical  $\beta$ 's. This can be understood from the fact that in the Drude model both current densities are directly proportional to the electrical field, which means that they always can be collected into an effective current density (still assuming that  $\gamma_a = \gamma_b$ ).

Apart from the singular situation where the  $\beta$ 's and  $\gamma$ 's are identical, the two-fluid model should ideally always be applied to semiconductors where two kinds of charge carriers are present. But as noted in the Introduction, materials where electrons are present as majority carriers can effectively be considered single-fluid systems. The smaller effective mass and larger density of electrons compared to holes will according to Eq. (15) result in a much larger plasma frequency. And this in turn causes the electrons to determine the optical properties almost completely, which means that it is sufficient to use the single-fluid HDM. In Fig. 6, the spectrum of semiconductor A is shown for various values of  $\omega_b$ . We see that for  $\omega_b = 0.01\omega_a$  almost all unique features of the two-fluid model are gone, and the spectrum coincides with the one predicted by the single-fluid HDM including only charge carrier  $a$ . Ratios of 0.01 between the plasma frequencies are easily obtained in doped semiconductors. If we consider an  $n$ -doped semiconductor with  $n = 10^{18} \text{ cm}^{-3}$  and an intrinsic carrier concentration of  $n_{\text{int}} = 10^{16} \text{ cm}^{-3}$ , the fundamental relation [44]  $n_{\text{int}}^2 = np$  tells us that the hole concentration will be  $p = 10^{14} \text{ cm}^{-3}$ . Accounting for the larger mass of the holes ( $h$ ) compared to the electrons ( $e$ ) we indeed obtain  $\omega_h/\omega_e < 0.01$ . For this reason we propose the two-fluid model for  $p$ -doped systems and systems where  $\omega_h/\omega_e > 0.1$ .

### C. Indium antimonide and gallium arsenide

After analyzing the artificial material semiconductor A, we will now look at more realistic semiconductors. The first material we will consider is intrinsic InSb where the electrons are thermally excited across the band gap. As seen in Table I, InSb has a very narrow band gap which gives rise to relatively high charge-carrier densities even at room

TABLE I. Data for GaAs and InSb. The intrinsic charge-carrier density is denoted by  $n_i$ . The masses  $m_e^*$  and  $m_h^*$  for InSb are taken from Refs. [60,61], respectively. For GaAs,  $m_e^*$  and  $m_{e,\text{cond}}^*$  (which depends on the doping level  $N_a$ ) are from Ref. [62], and  $m_h^*$  and  $m_{hh}^*$  are from Ref. [63].  $E_g$  for InSb is taken from Ref. [64], and  $\mu_e$  and  $\mu_h$  for GaAs are from Ref. [65]. The rest of the data are taken from Ref. [66]. Note that for InSb the value of  $m_{e,\text{cond}}^*$  is assumed to be identical to  $m_e^*$ , and  $m_{hh}^*$  is the 0-K value.

	GaAs (300 K)	InSb (300 K)	InSb (400 K)
$\epsilon_\infty$	10.86	15.68	15.68
$E_g$ (eV)	1.424	0.174	0.146
$n_i$ ( $\text{cm}^{-3}$ )	$2.18 \times 10^6$	$1.34 \times 10^{16}$	$5.73 \times 10^{16}$
$\mu_e$ ( $\text{cm}^2 \text{ V}^{-1} \text{ s}^{-1}$ )	7000 <sup>a</sup>	77000	48000
	1100 <sup>b</sup>		
$\mu_h$ ( $\text{cm}^2 \text{ V}^{-1} \text{ s}^{-1}$ )	400 <sup>a</sup>	850	480
	80 <sup>b</sup>		
$m_e^*/m_0$	0.0636	0.0115	0.0100
$m_{e,\text{cond}}^*/m_0$	0.0636 <sup>a</sup>	0.0115	0.0100
	0.1014 <sup>b</sup>		
$m_{hh}^*/m_0$	0.093	0.016	0.016
$m_{hh}^*/m_0$	0.50	0.37	0.40

<sup>a</sup> $N_a = 0 \text{ cm}^{-3}$ .

<sup>b</sup> $N_a = 10^{19} \text{ cm}^{-3}$ .

temperature. If we choose  $T = 300 \text{ K}$ , electrons ( $e$ ) as the  $a$  fluid, and holes ( $h$ ) as the  $b$  fluid and use the data from Table I, we then find  $\omega_e = 6.09 \times 10^{13} \text{ s}^{-1}$ ,  $\omega_h = 1.07 \times 10^{13} \text{ s}^{-1}$ ,  $\gamma_e = 1.99 \times 10^{12} \text{ s}^{-1}$ ,  $\gamma_h = 6.67 \times 10^{12} \text{ s}^{-1}$ ,  $\beta_e = 1.13 \times 10^6 \text{ m s}^{-1}$ , and  $\beta_h = 1.99 \times 10^5 \text{ m s}^{-1}$ . Here we have used Eqs. (15) and (19), but the values of  $n_i$  and  $\beta_i$  have been found by numerical solution of the sums in Eqs. (A9) and (A10) rather than by using Eqs. (B7) and (16). This allows us to use the Fermi-Dirac distribution instead of the Boltzmann distribution and thus obtain slightly more accurate values.

Considering a very small particle of InSb would give us clearly visible nonlocal effects which are interesting in terms of analyzing the model, but the number of charge carriers, which scale as  $R^{-3}$ , would also be smaller. And at some point there will be too few charge carriers for them to be considered a plasma, which means that a plasma model no longer is suitable. Therefore we will choose the radius of the InSb particle to be 100 nm, which results in the number of electrons and holes being  $N_e = N_h = 56$ . If we then choose the surrounding medium to be vacuum, we find the extinction spectrum shown in Fig. 7(a) with the dashed red line. Here we see the LSP peak at  $\sim 3 \times 10^{13} \text{ s}^{-1}$  followed by several electron bulk plasmon peaks. The hole plasmon peaks are completely invisible, a result of the size of the particle and the low mobility of the holes. However, one of the acoustic peaks is still visible, which could be interesting in terms of verifying the model.

The solid blue line in Fig. 7(a) shows the extinction spectrum of a 40-nm intrinsic GaAs particle in vacuum with electrons excited to the conduction band by a laser pulse. The pulse has an energy density of  $u_{\text{pulse}} = 10^5 \text{ J cm}^{-3}$  which results in a number of electrons and holes of  $N_e = N_h = 114$ . Using the equations from Sec. III and Appendix B we find  $\omega_e = 1.46 \times 10^{14} \text{ s}^{-1}$ ,  $\omega_h = 5.07 \times 10^{13} \text{ s}^{-1}$ ,  $\gamma_e = 3.95 \times 10^{12} \text{ s}^{-1}$ ,  $\gamma_h = 1.16 \times 10^{13} \text{ s}^{-1}$ ,  $\beta_e = 3.29 \times 10^5 \text{ m s}^{-1}$ , and  $\beta_h = 3.95 \times 10^4 \text{ m s}^{-1}$ . We here

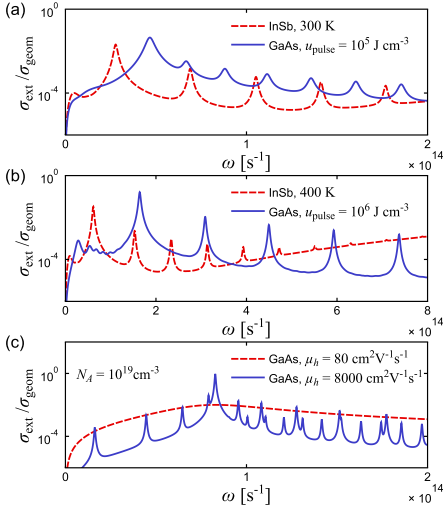


FIG. 7. Extinction spectra for InSb and GaAs. In all cases is  $\epsilon_D = 1$ . (a) The dashed red line and the solid blue line show the spectra for intrinsic InSb at 300 K with  $R = 100$  nm and laser excited GaAs with  $u_{\text{pulse}} = 10^5 \text{ J cm}^{-3}$  and  $R = 40$  nm, respectively. (b) The dashed red line and the solid blue line show the spectra for intrinsic InSb at 400 K with  $R = 60$  nm and laser excited GaAs with  $u_{\text{pulse}} = 10^6 \text{ J cm}^{-3}$  and  $R = 15$  nm, respectively. (c) The spectrum for  $p$ -doped GaAs with  $N_A = 10^{19} \text{ cm}^{-3}$  and  $R = 30$  nm is shown with the dashed red line. For the solid blue line the mobility of the holes is artificially set 100 times higher.

recognize the largest peak as the LSP peak followed by a series of electron bulk plasmon peaks, while the hole bulk plasmon peaks are completely suppressed by damping.

It is also interesting to consider a higher temperature for the InSb particle and a stronger laser pulse for the GaAs particle. The dashed red line in Fig. 7(b) shows an intrinsic InSb particle with  $R = 60$  nm at 400 K which results in  $N_e = N_h = 51$ , and the solid blue line shows an intrinsic GaAs particle with  $R = 15$  nm and  $u_{\text{pulse}} = 10^6 \text{ J cm}^{-3}$  which results in  $N_e = N_h = 57$ . Here the acoustic peaks, one of the interesting features of the spectra, are more visible.

To analyze the two-fluid model for semiconductors with light and heavy holes, we will consider  $p$ -doped GaAs with an acceptor concentration of  $N_A = 10^{19} \text{ cm}^{-3}$ . According to the equations of Sec. III and Appendix B, this results in a concentration of light and heavy holes of  $n_{lh} = 7.43 \times 10^{17} \text{ cm}^{-3}$  and  $n_{hh} = 9.26 \times 10^{18} \text{ cm}^{-3}$  and the parameters  $\omega_{lh} = 1.59 \times 10^{14} \text{ s}^{-1}$ ,  $\omega_{hh} = 2.43 \times 10^{14} \text{ s}^{-1}$ ,  $\gamma_{lh} = \gamma_{hh} = 5.79 \times 10^{13} \text{ s}^{-1}$ ,  $\beta_{lh} = 2.70 \times 10^5 \text{ m s}^{-1}$ , and  $\beta_{hh} = 1.17 \times 10^5 \text{ m s}^{-1}$ . Here it has been assumed that the light and heavy holes have the same damping constant which is found with  $\mu_h$  from Table I and  $m_{h,\text{cond}}$  from Eq. (B8). Choosing  $R = 30$  nm and  $\epsilon_D = 1$  produces the extinction spectrum shown with the

dashed red line in Fig. 7(c). Here the only visible feature is the LSP peak, while the bulk plasmons are completely damped. For the purpose of analyzing the model, the solid blue line shows the spectrum for the same material, but with the mobility of the holes set 100 times larger. Now we see the bulk plasmon peaks for both charge carriers as well as the peaks below  $\omega_{lSP}$ .

Another group of semiconductors that is gaining increasing popularity as plasmonic materials is the transparent conducting oxides (TCO) such as indium tin oxide (ITO), aluminum-doped ZnO (AZO), and indium-doped CdO (In:CdO). ITO was used in Refs. [25,29,30], and In:CdO was used in Refs. [33,42]. Apart from the advantages that TCOs share with other semiconductors (such as tunability), they are particularly suitable for the creation of thin films and often allow for heavy doping [67]. The most commonly used TCOs, including ITO, AZO, and In:CdO, are  $n$ -type semiconductors [68] (ZnO and CdO are even  $n$ -type semiconductors without intentional doping [23,69]) and, as established above, materials with electrons as majority carriers can be modeled with the single-fluid HDM. However, much effort is currently going into the development of  $p$ -type TCOs [70–72], and it is not unlikely that TCOs suitable for investigating the two-fluid model will be discovered.

In our model, we have left out some of the mechanisms found in real semiconductors. As mentioned in Sec. III, interband transitions are ignored, and the effects of them are assumed to be contained in  $\epsilon_\infty$ . This is a reasonable approximation as long as the energies considered are smaller than the band gap. Some semiconductors also contain excitons which are caused by the Coulomb interaction between electrons and holes and give rise to energy levels inside the band gap. However, for doped semiconductors and intrinsic semiconductors with narrow band gaps, the screening from the high density of charge carriers significantly weakens the binding energy of the excitons [73]. It is therefore a decent approximation for these materials to leave out excitons. A third kind of excitation especially found in nonelemental semiconductors is optical phonons. These resonances of the lattice may couple to the plasmons if they are in the same frequency range, and this interaction has been studied for both InSb [74,75] and GaAs [76,77]. It should also be mentioned that for InSb, in particular, a charge-carrier depleted region known as the *space-charge layer* may exist close to the surface which would be relevant for the optical properties. This layer has been investigated in several earlier papers [34,78–80], and the question of how it affects features such as the acoustic peak still remains. Finally, the two-fluid model, just as the single-fluid HDM, does not account for Landau damping whereby the energy of the plasmons dissipates into single-particle excitations. The excitation of single particles depends on the momentum  $q$ , and in that sense Landau damping is a size-dependent nonlocal loss mechanism. Although not considered here, nonlocal damping could be incorporated into the two-fluid model by allowing the  $\beta$ 's to become complex as it is done for the single-fluid HDM in Refs. [9,42,81].

#### D. The acoustic peaks

One of the defining characteristics of the two-fluid model is the presence of resonances below  $\omega_{lSP}$ , and the experimental observation of these could potentially be used to verify the

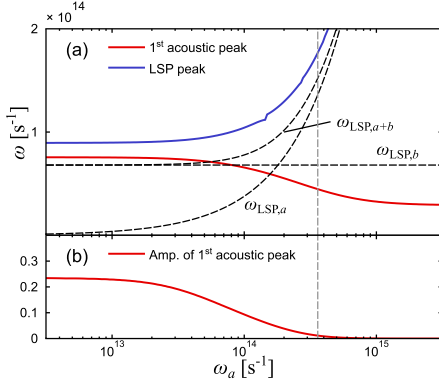


FIG. 8. (a) The spectral position of the first acoustic peak as a function of  $\omega_a$  for semiconductor A is shown with a red line, while the blue line shows the position of the LSP peak. The vertical dashed line shows the value  $\omega_a = 3.6 \times 10^{14} \text{ s}^{-1}$  which was used in previous figures with semiconductor A. The dent in the blue line around  $\omega_a \approx 10^{14} \text{ s}^{-1}$  is not a numerical artifact, but is caused by bulk plasmon resonances that are superimposed on the LSP peak and thereby make the definition of the peak ambiguous. (b) The amplitude of the first acoustic peak normalized with  $\sigma_{\text{geom}}$  as a function of  $\omega_a$ .

model. Therefore this section will be used to analyze these acoustic peaks, and the focus will be on the first acoustic peak [marked with “X” in Fig. 2(b)].

We will start by considering the artificial material semiconductor A, and in Fig. 8(a) the spectral positions of the first acoustic peak and the LSP peak are shown as functions of  $\omega_a$  with a red and blue line, respectively. Here it is interesting to note that while the LSP peak blueshifts as  $\omega_a$  increases, the acoustic peak instead moves to lower frequencies. Also shown in the figure with dashed black lines is the position of the LSP peak in the local response approximation as given by  $\omega_{\text{LSP},a+b} = (\omega_a^2 + \omega_p^2)^{1/2} / (\epsilon_\infty + 2\epsilon_D)^{1/2}$  (including both kinds of charge carriers) and  $\omega_{\text{LSP},i} = \omega_i / (\epsilon_\infty + 2\epsilon_D)^{1/2}$  (including charge carrier  $a$  or  $b$ ). The vertical dashed line marks  $\omega_a = 3.6 \times 10^{14} \text{ s}^{-1}$ , which was used in previous figures with semiconductor A.

Apart from the position of the acoustic peak, the amplitude will also play a role, especially in terms of detecting the resonance. Figure 8(b) shows the amplitude of the first acoustic peak, and we here see that it decreases when  $\omega_a$  goes up.

Turning to intrinsic GaAs, Fig. 9(a) shows the spectral positions of the first acoustic peak and the LSP peak as functions of the radius of the particle. The particle has been excited by a laser pulse of  $u_{\text{pulse}} = 10^6 \text{ J cm}^{-3}$  and is surrounded by vacuum. Here we see that the position of the acoustic peak, shown with a red line, blueshifts when  $R$  is reduced. The LSP peak, shown with a blue line, also blueshifts, which is similar to what is found in the HDM for both metals [5,7] and semiconductors [41].

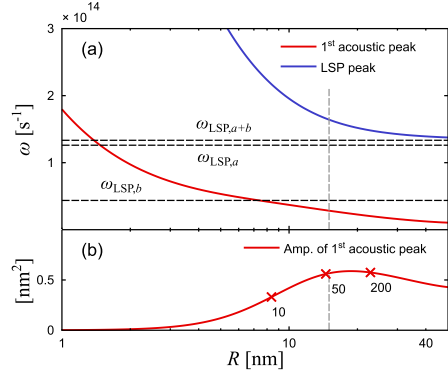


FIG. 9. (a) The spectral positions of the first acoustic peak and the LSP peak as functions of  $R$  for intrinsic GaAs shown with a red and blue line, respectively. GaAs was excited with a laser pulse of  $u_{\text{pulse}} = 10^6 \text{ J cm}^{-3}$ . The vertical dashed line marks the value  $R = 15 \text{ nm}$  which was used in Fig. 7(b). (b) The amplitude of the first acoustic peak as a function of  $R$  (un-normalized). The number of electrons in the particle is indicated for three different sizes.

Figure 9(b) shows the amplitude of the first acoustic peak, and it is interesting to see that the height of the peak reaches a maximum around  $R = 20 \text{ nm}$ . The number of electrons in the particle is also given in the figure for three different particle sizes. Note that the extinction cross section in this figure is the absolute value, since normalization with  $\pi R^2$  would make the interpretation of the results more difficult.

As the first acoustic peak could be used to verify the model, it is relevant to find the scenario where this resonance is easiest to detect. Figure 8 shows the amplitude and position of the peak as functions of  $\omega_a$  for semiconductor A, but for a realistic semiconductor it will not be possible to freely vary this parameter. For laser-excited GaAs, Fig. 9(b) shows, interestingly, that the amplitude of the acoustic peak reaches a maximum for a certain finite radius, and a similar behavior is expected for other materials and geometries.

The materials investigated here are not all equally well suited to test the model. In the case of  $p$ -doped GaAs, it was found that none of the features of the two-fluid model are present due to the low mobility of the holes. However, a  $p$ -doped semiconductor with higher mobility of the holes might still be used to test the two-fluid model. In the case of laser-excited GaAs with  $u_{\text{pulse}} = 10^6 \text{ J cm}^{-3}$ , clear acoustic peaks were found, but it must be remembered that the charge carriers will decay over time, which will create new experimental opportunities and challenges. Finally, intrinsic InSb with thermally excited charge carriers is perhaps the best candidate in terms of testing the model, as the spectrum remains stable over time and is expected to contain the acoustic peaks.

## VII. CONCLUSIONS

The hydrodynamic Drude model, which has successfully described the optical properties of metallic nanostructures, can be adapted to semiconductors by accounting for the fact that several different kinds of charge carriers are present. In this paper, we have presented a two-fluid hydrodynamic model for semiconductors containing electrons and holes or light and heavy holes. We have shown that the two-fluid model is supported by a microscopic theory, and simultaneously we found expressions for the nonlocal parameter  $\beta$  for thermally excited charge carriers, laser excited charge carriers, and  $p$ -doped semiconductors with light and heavy holes.

It was found that the two hydrodynamic fluids hybridize to form an acoustic and an optical branch, both longitudinal, whereas the single-fluid HDM only contains an optical branch. An extended Mie theory was developed to accommodate the two longitudinal waves, and this theory was subsequently applied to semiconductor nanospheres to find the extinction spectra. We found that in addition to the well-known features of the single-fluid HDM the two-fluid model displays at least two additional optical features: (1) a second set of bulk plasmon resonances and (2) acoustic resonances below the dipole LSP

peak, of which the first attains its maximal strength at a finite particle size [Fig. 9(b)]. Although we considered only spherical particles here, it is expected that these features will be present in other geometries as well.

The acoustic resonances are particularly interesting since they are completely absent in the single-fluid HDM, and experimental observation of these peaks could serve as verification of the two-fluid model. To this end we analyzed different materials and different kinds of charge carriers. Here we saw that for the considered  $p$ -doped semiconductors with light and heavy holes the damping was too high to discern any of the features of the two-fluid model. On the other hand, the intrinsic semiconductor particles that we studied, with thermally excited or laser-excited charge carriers, both have acoustic peaks in their spectra.

## ACKNOWLEDGMENTS

We thank C. Ciraci for directing us to Ref. [42]. We acknowledge support from the Danish Council for Independent Research (DFF Grant No. 1323-00087). N.A.M. is a VILLUM Investigator supported by VILLUM FONDEN (Grant No. 16498). Center for Nano Optics is financially supported by the University of Southern Denmark (SDU 2020 funding).

## APPENDIX A: THE SUSCEPTIBILITY

We will show that the susceptibility is given by Eq. (14). Starting from Eq. (13), this can be rewritten in the following way by using the temporary variable  $\mathbf{k}' = -\mathbf{k} - \mathbf{q}$ :

$$\begin{aligned} \chi_i(\mathbf{q}, \omega) &= \frac{2e^2}{\epsilon_0 q^2} \frac{1}{V} \left( \sum_{\mathbf{k}} \frac{f_i(\mathbf{k})}{E_i(\mathbf{k} + \mathbf{q}) - E_i(\mathbf{k}) - \hbar\omega - i\eta} - \sum_{\mathbf{k}'} \frac{f_i(\mathbf{k}')}{E_i(\mathbf{k}') - E_i(\mathbf{k}' + \mathbf{q}) - \hbar\omega - i\eta} \right) \\ &= \frac{4e^2}{\epsilon_0 q^2} \frac{1}{V} \sum_{\mathbf{k}} f_i(\mathbf{k}) \frac{E_i(\mathbf{k} + \mathbf{q}) - E_i(\mathbf{k})}{[E_i(\mathbf{k} + \mathbf{q}) - E_i(\mathbf{k})]^2 - (\hbar\omega + i\eta)^2}. \end{aligned} \quad (\text{A1})$$

For holes the substitutions  $f_i \rightarrow 1 - f_i$  and  $E_i \rightarrow E_v - E_i$  can be made in order to treat the electrons and holes on equal footing ( $E_v$  is the valence-band edge). However, this will leave Eq. (A1) unchanged. The next step is to take the limit  $\mathbf{q} \rightarrow \mathbf{0}$  which allows for the series expansion

$$\chi_i(\mathbf{q}, \omega) = -\frac{4e^2}{\epsilon_0 q^2} \frac{1}{V} \sum_{\mathbf{k}} f_i(\mathbf{k}) \frac{E_i(\mathbf{k} + \mathbf{q}) - E_i(\mathbf{k})}{(\hbar\omega + i\eta)^2} \left( 1 + \frac{[E_i(\mathbf{k} + \mathbf{q}) - E_i(\mathbf{k})]^2}{(\hbar\omega + i\eta)^2} + \dots \right). \quad (\text{A2})$$

Without loss of generality it is assumed that  $\mathbf{q} = q\hat{z}$ , which means that

$$E_i(\mathbf{k} + \mathbf{q}) - E_i(\mathbf{k}) = \frac{\hbar^2}{2m_i^*} (2k_z q + q^2), \quad (\text{A3})$$

and inserting this into  $\chi_i(\mathbf{q}, \omega)$  gives us

$$\chi_i(q, \omega) = -\frac{4e^2}{\epsilon_0 q^2} \left( \frac{1}{(\hbar\omega + i\eta)^2} \frac{\hbar^2 q^2}{2m_i^*} \frac{1}{V} \sum_{\mathbf{k}} f_i(\mathbf{k}) + \frac{1}{(\hbar\omega + i\eta)^4} \frac{3\hbar^6 q^4}{2m_i^{*3}} \frac{1}{V} \sum_{\mathbf{k}} f_i(\mathbf{k}) k_z^2 + \dots \right), \quad (\text{A4})$$

where it has been taken into account that odd powers of  $k_z$  cancel out.

To evaluate the  $\mathbf{k}$  sums in Eq. (A4) for light and heavy holes, we assume that  $T = 0$  K, whereby the distribution becomes a step function. By using that the volume of a single state in  $k$  space is  $V_k = (2\pi)^3/V$ , we find the first sum to be

$$\frac{1}{V} \sum_{\mathbf{k}} f_i(\mathbf{k}) = \frac{1}{V V_k} \int d\mathbf{k} f_i(\mathbf{k}) = \frac{4\pi}{V V_k} \int_0^{k_{Fi}} dk k^2 = \frac{4\pi}{V V_k} \frac{k_{Fi}^3}{3}, \quad (\text{A5})$$

which by definition also is equal to  $n_i/2$ . From this we also find the following simple relation:

$$k_{Fi}^3 = 3\pi^2 n_i. \quad (\text{A6})$$

The second sum is given by

$$\frac{1}{V} \sum_{\mathbf{k}} f_i(\mathbf{k}) k_z^2 = \frac{1}{V V_k} \int_0^{k_{Fi}} dk k^4 \int_0^\pi d\theta \sin \theta \cos^2 \theta \int_0^{2\pi} d\phi = \frac{4\pi}{3V V_k} \frac{k_{Fi}^5}{5} = \frac{k_{Fi}^2 n_i}{5 \cdot 2}. \quad (\text{A7})$$

The same results are obtained for laser-excited charge carriers, except that the Fermi levels  $k_{Fi}$  are for the quasiequilibria that are assumed to be formed.

For the thermally excited intrinsic semiconductor, we will assume that the Fermi-Dirac distribution can be approximated by the Boltzmann distribution

$$f_e(E) = \frac{1}{\exp\left(\frac{E-E_F}{k_B T}\right) + 1} \approx \exp\left(-\frac{E-E_F}{k_B T}\right),$$

which is reasonable for electrons whenever  $E_c - E_F \gg k_B T$  where  $E_c$  is the conduction-band edge (a similar expression exists for holes). For electrons, the first sum becomes

$$\frac{1}{V} \sum_{\mathbf{k}} f_e(\mathbf{k}) = \frac{4\pi}{V V_k} \int_0^\infty dk k^2 f_e(k) \approx \frac{2\pi}{V V_k} \left(\frac{2m_e^*}{\hbar^2}\right)^{\frac{3}{2}} \int_{E_c}^\infty dE \sqrt{E-E_c} \exp\left(-\frac{E-E_F}{k_B T}\right), \quad (\text{A8})$$

where it has been used that

$$E = E_c + \frac{\hbar^2 k^2}{2m_e^*}.$$

We now introduce the variable  $\rho = (E - E_F)/k_B T$ , whereby the integral can be identified as a gamma function. With this, the sum is found to be

$$\frac{1}{V} \sum_{\mathbf{k}} f_e(\mathbf{k}) \approx \frac{2\pi}{V V_k} \left(\frac{2m_e^* k_B T}{\hbar^2}\right)^{\frac{3}{2}} \exp\left(\frac{E_F - E_c}{k_B T}\right) \frac{\sqrt{\pi}}{2}, \quad (\text{A9})$$

which by definition also is equal to  $n_e/2$ . Using a similar method, the second sum is found to be

$$\frac{1}{V} \sum_{\mathbf{k}} f_e(\mathbf{k}) k_z^2 \approx \frac{2\pi}{V V_k} \left(\frac{2m_e^* k_B T}{\hbar^2}\right)^{\frac{5}{2}} \exp\left(\frac{E_F - E_c}{k_B T}\right) \frac{1}{3} \Gamma\left(\frac{5}{2}\right) = \frac{m_e^* k_B T n_e}{\hbar^2 \cdot 2}. \quad (\text{A10})$$

The sums for the holes can be found in the same way.

Inserting the expressions of the sums into Eq. (A4), using  $\eta^2 \approx 0$  and defining  $\gamma = 2\eta/\hbar$  gives us Eq. (14) where  $\beta_i$  is given by either Eq. (16) or (17) depending on the nature of the charge carriers.

## APPENDIX B: CHARGE-CARRIER DENSITIES AND FERMİ WAVE NUMBERS

To find expressions for  $k_{Fih}$  and  $k_{Fhh}$  for light and heavy holes, we will use the fact that the Fermi energy is the same for both kinds of holes:

$$\frac{\hbar^2 k_{Fih}^2}{2m_{lh}^*} = \frac{\hbar^2 k_{Fhh}^2}{2m_{hh}^*}. \quad (\text{B1})$$

If we then use the relation between  $n_i$  and  $k_{Fi}$  from Eq. (A6) and assume complete ionization,  $N_a = n_{lh} + n_{hh}$ , we straight away get

$$k_{Fih} = k_{Fhh} \sqrt{\frac{m_{lh}^*}{m_{hh}^*}} = \left[ \frac{N_a 3\pi^2}{1 + \left(\frac{m_{lh}^*}{m_{hh}^*}\right)^{\frac{3}{2}}} \right]^{\frac{1}{3}}. \quad (\text{B2})$$

For laser-excited charge carriers, the energy density of a laser pulse that excites electrons from the valence band to the conduction band is given by

$$u_{\text{pulse}} = u_e + u_{lh} + u_{hh} + E_g n_e, \quad (\text{B3})$$

where  $u_i$  is the energy density of the charge-carrier type  $i$  with respect to the band edge, and  $e$ ,  $lh$ , and  $hh$  are electrons,

light holes, and heavy holes, respectively. From Eq. (A6) and  $E_i = \hbar^2 k^2 / 2m_i^*$  we have  $n_i = E_{Fi}^{3/2} (2m_i^*)^{3/2} / 3\pi^2 \hbar^3$  and the energy densities are given by

$$u_i = \frac{(2m_i^*)^{\frac{3}{2}}}{2\pi^2 \hbar^3} \int_0^{E_{Fi}} dE_i E_i^{\frac{3}{2}} = \frac{3\hbar^2}{10m_i^*} (3\pi^2)^{\frac{2}{3}} n_i^{\frac{5}{3}}. \quad (\text{B4})$$

Inserting this into Eq. (B3) and using the following definition of the density-of-states hole mass [44],

$$m_h^* = (m_{lh}^{\frac{3}{2}} + m_{hh}^{\frac{3}{2}})^{\frac{2}{3}}, \quad (\text{B5})$$

together with charge conservation  $n_e = n_h = n_{lh} + n_{hh}$  and Eq. (B1) we obtain

$$u_{\text{pulse}} = \frac{3\hbar^2}{10} (3\pi^2)^{\frac{2}{3}} \left( \frac{1}{m_e^*} + \frac{1}{m_h^*} \right) n_e^{\frac{5}{3}} + E_g n_e. \quad (\text{B6})$$

From this expression, the density of electrons can be found using numerical tools, and  $k_{Fi}$  is found using Eq. (A6).

For thermally excited charge carriers in an intrinsic semiconductor, the charge-carrier densities are given by [44]

$$n_e = n_h = 2 \left( \frac{2\pi k_B T}{\hbar^2} \right)^{\frac{3}{2}} m_e^{\frac{3}{2}} m_h^{\frac{3}{2}} \exp\left(\frac{-E_g}{2k_B T}\right), \quad (\text{B7})$$

where  $E_g$  is the band gap. Here it is assumed that the Boltzmann distribution can be used for the electrons.

For both laser-excited and thermally excited charge carriers the density-of-states effective hole mass is given by Eq. (B5),

while the conductivity effective hole mass is given by [82]

$$m_{h,\text{cond}}^* = \frac{m_{hh}^* \frac{3}{2} + m_{hh}^* \frac{3}{2}}{m_{hh}^* \frac{3}{2} + m_{hh}^* \frac{3}{2}}. \quad (\text{B8})$$

### APPENDIX C: MATRIX NOTATION

Here, we rewrite the two-fluid equations (1) in a matrix notation:

$$\hat{\mathcal{L}}\mathbf{E} = -i\omega\mu_0 \begin{pmatrix} 1 \\ 1 \end{pmatrix} \begin{pmatrix} \mathbf{J}_a \\ \mathbf{J}_b \end{pmatrix}, \quad (\text{C1a})$$

$$\underbrace{\begin{pmatrix} \frac{\beta_a^2}{\omega_a^2} & 0 \\ 0 & \frac{\beta_b^2}{\omega_b^2} \end{pmatrix}}_{\equiv \xi^2} \nabla(\nabla \cdot) \begin{pmatrix} \mathbf{J}_a \\ \mathbf{J}_b \end{pmatrix} + k^2 \underbrace{\begin{pmatrix} \frac{c^2}{\omega_a^2} & 0 \\ 0 & \frac{c^2}{\omega_b^2} \end{pmatrix} \mathbf{I} + \begin{pmatrix} \frac{i\gamma_a}{\omega} & 0 \\ 0 & \frac{i\gamma_b}{\omega} \end{pmatrix}}_{\equiv \Lambda^2} \begin{pmatrix} \mathbf{J}_a \\ \mathbf{J}_b \end{pmatrix} = i\omega\epsilon_0 \begin{pmatrix} 1 \\ 1 \end{pmatrix} \mathbf{E}, \quad (\text{C1b})$$

where  $\hat{\mathcal{L}} = -\nabla \times \nabla \times + \epsilon_\infty k^2$  with  $k = \omega/c$ , while  $\mathbf{I}$  is a  $2 \times 2$  identity matrix. Next, we follow a trick developed in Ref. [83], where one acts with  $\hat{\mathcal{L}}$  on the constitutive equation (C1b). At first sight, this generates less appealing fourth-order derivatives, but the curl of any gradient field vanishes, and we are eventually left with only second-order derivatives, i.e.,

$$[\epsilon_\infty \xi^2 \nabla(\nabla \cdot) - \Lambda^2 \nabla \times \nabla \times - \mathbf{M}] \begin{pmatrix} \mathbf{J}_a \\ \mathbf{J}_b \end{pmatrix} = 0, \quad (\text{C2})$$

where  $\mathbf{M} \equiv \hat{\mathbf{I}} - \epsilon_\infty k^2 \Lambda^2$  and  $\hat{\mathbf{I}}$  is a  $2 \times 2$  all-ones matrix. While  $\xi$  and  $\Lambda$  are diagonal matrices,  $\mathbf{M}$  has nonzero off-diagonal elements and the two currents are consequently coupled. The coupling originates from a mutual interaction through common electromagnetic fields (which we have integrated out).

To find the uncoupled homogeneous equations for the normal modes, we take either the curl or the divergence of Eq. (C2) and obtain the following equations:

$$[\Lambda^2 \nabla^2 - \mathbf{M}] \nabla \times \begin{pmatrix} \mathbf{J}_a \\ \mathbf{J}_b \end{pmatrix} = 0, \quad (\text{C3a})$$

$$[\epsilon_\infty \xi^2 \nabla^2 - \mathbf{M}] \nabla \cdot \begin{pmatrix} \mathbf{J}_a \\ \mathbf{J}_b \end{pmatrix} = 0, \quad (\text{C3b})$$

where it is used that  $\nabla^2 = \nabla(\nabla \cdot) - \nabla \times \nabla \times$ . Next, the linear relations between  $\{J_a, J_b\}$  and  $\{J_1, J_2\}$  given in Eqs. (20) are introduced for both the transversal fields (the curl equation) and the longitudinal fields (the divergence equation), which gives us

$$[\Lambda^2 \mathbf{K}_T \nabla^2 - \mathbf{M} \mathbf{K}_T] \nabla \times \begin{pmatrix} \mathbf{J}_1 \\ \mathbf{J}_2 \end{pmatrix} = 0, \quad (\text{C4a})$$

$$[\epsilon_\infty \xi^2 \mathbf{K}_L \nabla^2 - \mathbf{M} \mathbf{K}_L] \nabla \cdot \begin{pmatrix} \mathbf{J}_1 \\ \mathbf{J}_2 \end{pmatrix} = 0, \quad (\text{C4b})$$

where

$$\mathbf{K}_z = \begin{pmatrix} a_1^z & a_2^z \\ b_1^z & b_2^z \end{pmatrix},$$

with  $z = T, L$ . If we then require that  $\mathbf{J}_1$  and  $\mathbf{J}_2$  are uncoupled for both the transversal and the longitudinal fields, the  $2 \times 2$  nondiagonal matrices can be treated as  $4 \times 4$  diagonal matrices. In other words, we obtain eight homogeneous equations in total: for both curl and divergence we get two for both  $\mathbf{J}_1$  and  $\mathbf{J}_2$ . These are the Boardman equations written explicitly in Sec. IV. The fact that there are two equations for every  $\nabla \times \mathbf{J}_j$  and  $\nabla \cdot \mathbf{J}_j$  can be used to find the coefficients  $a_j^z$  and  $b_j^z$  which so far have been undetermined.

### APPENDIX D: LINEAR EQUATIONS

When applying the boundary conditions  $\Delta \mathbf{E}_\parallel = 0$ ,  $\Delta \mathbf{B}_\parallel = 0$ ,  $\mathbf{J}_{a,\perp} = 0$ , and  $\mathbf{J}_{b,\perp} = 0$  to the electrical fields in Eqs. (33)–(35), the following system of linear equations is obtained:

$$-a_1^r h_1^{(1)}(x_D) + a_1^t j_1(x_T) = j_1(x_D), \quad (\text{D1a})$$

$$-a_1^r [x_D h_1^{(1)}(x_D)]' + a_1^t [x_T j_1(x_T)]' = [x_D j_1(x_D)]', \quad (\text{D1b})$$

$$-b_1^r \frac{[x_D h_1^{(1)}(x_D)]'}{k_D} + b_1^t \frac{[x_T j_1(x_T)]'}{k_T} + i c_{11}^t j_1(x_1) + i c_{21}^t j_1(x_2) = \frac{[x_D j_1(x_D)]'}{k_D}, \quad (\text{D1c})$$

$$-b_1^r x_D h_1^{(1)}(x_D) + b_1^t x_T j_1(x_T) = x_D j_1(x_D), \quad (\text{D1d})$$

$$-ib_l' \frac{l(l+1)}{x_T} j_l(x_T) + c_{1l}' j_l'(x_1) k_{L,1} \left( 1 + \frac{\beta_a^2 \epsilon_\infty k_{L,1}^2}{\omega_a^2 (1 + \alpha_1)} \right) + c_{2l}' j_l'(x_2) k_{L,2} \left( 1 + \frac{\beta_a^2 \epsilon_\infty k_{L,2}^2}{\omega_a^2 (1 + \alpha_2)} \right) = 0, \quad (\text{Dle})$$

$$-ib_l' \frac{l(l+1)}{x_T} j_l(x_T) + c_{1l}' j_l'(x_1) k_{L,1} \left( 1 + \frac{\beta_b^2 \epsilon_\infty k_{L,1}^2}{\omega_b^2 (1 + \alpha_1^{-1})} \right) + c_{2l}' j_l'(x_2) k_{L,2} \left( 1 + \frac{\beta_b^2 \epsilon_\infty k_{L,2}^2}{\omega_b^2 (1 + \alpha_2^{-1})} \right) = 0, \quad (\text{Dlf})$$

which directly allows us to find  $a_l'$  and  $b_l'$ .

- 
- [1] J. Tiggesbäumker, L. Köller, K.-H. Meiwes-Broer, and A. Liebsch, *Phys. Rev. A* **48**, R1749(R) (1993).
- [2] J. Vielma and P. T. Leung, *J. Chem. Phys.* **126**, 194704 (2007).
- [3] F. J. García de Abajo, *J. Phys. Chem. C* **112**, 17983 (2008).
- [4] J. M. McMahon, S. K. Gray, and G. C. Schatz, *Phys. Rev. Lett.* **103**, 097403 (2009).
- [5] S. Raza, W. Yan, N. Stenger, M. Wubs, and N. A. Mortensen, *Opt. Express* **21**, 27344 (2013).
- [6] D. de Ceglia, S. Campione, M. A. Vincenti, F. Capolino, and M. Scalora, *Phys. Rev. B* **87**, 155140 (2013).
- [7] T. Christensen, W. Yan, S. Raza, A.-P. Jauho, N. A. Mortensen, and M. Wubs, *ACS Nano* **8**, 1745 (2014).
- [8] M. Scalora, M. A. Vincenti, D. de Ceglia, and J. W. Haus, *Phys. Rev. A* **90**, 013831 (2014).
- [9] S. Raza, S. I. Bozhevolnyi, M. Wubs, and N. A. Mortensen, *J. Phys.: Condens. Matter* **27**, 183204 (2015).
- [10] G. Toscano, J. Straubel, A. Kwiatkowski, C. Rockstuhl, F. Evers, H. Xu, N. A. Mortensen, and M. Wubs, *Nat. Commun.* **6**, 7132 (2015).
- [11] C. Ciraci and F. Della Sala, *Phys. Rev. B* **93**, 205405 (2016).
- [12] J. M. Fitzgerald, P. Narang, R. V. Craster, S. A. Maier, and V. Giannini, *Proc. IEEE* **104**, 2307 (2016).
- [13] S. Raza, N. Stenger, S. Kadkhodazadeh, S. V. Fischer, N. Koste-sha, A.-P. Jauho, A. Burrows, M. Wubs, and N. A. Mortensen, *Nanophotonics* **2**, 131 (2013).
- [14] S. Raza, S. Kadkhodazadeh, T. Christensen, M. Di Vecce, M. Wubs, N. A. Mortensen, and N. Stenger, *Nat. Commun.* **6**, 8788 (2015).
- [15] I. Lindau and P. O. Nilsson, *Phys. Scr.* **3**, 87 (1971).
- [16] W. E. Anderson, R. W. Alexander, Jr., and R. J. Bell, *Phys. Rev. Lett.* **27**, 1057 (1971).
- [17] R. Matz and H. Lüth, *Phys. Rev. Lett.* **46**, 500 (1981).
- [18] Z. J. Gray-Grychowski, R. A. Stradling, R. G. Egdell, P. J. Dobson, B. A. Joyce, and K. Woodbridge, *Solid State Comm.* **59**, 703 (1986).
- [19] M. G. Betti, U. del Pennino, and C. Mariani, *Phys. Rev. B* **39**, 5887 (1989).
- [20] Y. Meng, J. R. Anderson, J. C. Hermanson, and G. J. Lapeyre, *Phys. Rev. B* **44**, 4040 (1991).
- [21] R. Biagi, C. Mariani, and U. del Pennino, *Phys. Rev. B* **46**, 2467 (1992).
- [22] J. C. Ginn, R. L. Jarecki, Jr., E. A. Shaner, and P. S. Davids, *J. Appl. Phys.* **110**, 043110 (2011).
- [23] E. Sachet, C. T. Shelton, J. S. Harris, B. E. Gaddy, D. L. Irving, S. Curtarolo, B. F. Donovan, P. E. Hopkins, P. A. Sharma, A. L. Sharma, J. Ihlefeld, S. Franzen, and J.-P. Maria, *Nat. Mater.* **14**, 414 (2015).
- [24] J. M. Luther, P. K. Jain, T. Ewers, and A. P. Alivisatos, *Nat. Mater.* **10**, 361 (2011).
- [25] G. Garcia, R. Buonsanti, E. L. Runnerstrom, R. J. Mendelsberg, A. Llordes, A. Anders, T. J. Richardson, and D. J. Milliron, *Nano Lett.* **11**, 4415 (2011).
- [26] K. Manthiram and A. P. Alivisatos, *J. Am. Chem. Soc.* **134**, 3995 (2012).
- [27] A. M. Schimpf, N. Thakkar, C. E. Gunthardt, D. J. Masiello, and D. R. Gamelin, *ACS Nano* **8**, 1065 (2014).
- [28] S. Zhou, X. Pi, Z. Ni, Y. Ding, Y. Jiang, C. Jin, C. Delerue, D. Yang, and T. Nozaki, *ACS Nano* **9**, 378 (2015).
- [29] X. Liu, J.-H. Kang, H. Yuan, J. Park, S. J. Kim, Y. Cui, H. Y. Hwang, and M. L. Brongersma, *Nat. Nanotechnol.* **12**, 866 (2017).
- [30] X. Liu, J.-H. Kang, H. Yuan, J. Park, Y. Cui, H. Y. Hwang, and M. L. Brongersma, *ACS Photonics* (2018), doi:10.1021/acsphotonics.7b01517.
- [31] J. A. Dionne, K. Diest, L. A. Sweatlock, and H. A. Atwater, *Nano Lett.* **9**, 897 (2009).
- [32] K. Anglin, T. Ribaudo, D. C. Adams, X. Qian, W. D. Goodhue, S. Dooley, E. A. Shaner, and D. Wasserman, *J. Appl. Phys.* **109**, 123103 (2011).
- [33] Y. Yang, K. Kelly, E. Sachet, S. Campione, T. S. Luk, J.-P. Maria, M. B. Sinclair, and I. Brener, *Nat. Photonics* **11**, 390 (2017).
- [34] G. R. Bell, T. S. Jones, and C. F. McConville, *Surf. Sci.* **405**, 280 (1998).
- [35] J. Gómez Rivas, M. Kuttge, H. Kurz, P. H. Bolivar, and J. A. Sánchez-Gil, *Appl. Phys. Lett.* **88**, 082106 (2006).
- [36] T. H. Isaac, W. L. Barnes, and E. Hendry, *Appl. Phys. Lett.* **93**, 241115 (2008).
- [37] S. M. Hanham, A. I. Fernández-Domínguez, J. H. Teng, S. S. Ang, K. P. Lim, S. F. Yoon, C. Y. Ngo, N. Klein, J. B. Pendry, and S. A. Maier, *Adv. Mater.* **24**, OP226 (2012).
- [38] P. Hapala, K. Kůsová, I. Pelant, and P. Jelínek, *Phys. Rev. B* **87**, 195420 (2013).
- [39] H. Zhang, V. Kulkarni, E. Prodan, P. Nordlander, and A. O. Govorov, *J. Phys. Chem. C* **118**, 16035 (2014).
- [40] R. C. Monreal, T. J. Antosiewicz, and S. P. Apell, *J. Phys. Chem. Lett.* **6**, 1847 (2015).
- [41] J. R. Maack, N. A. Mortensen, and M. Wubs, *EPL* **119**, 17003 (2017).
- [42] D. de Ceglia, M. Scalora, M. A. Vincenti, S. Campione, K. Kelley, E. L. Runnerstrom, J.-P. Maria, G. A. Keeler, and T. S. Luk, *arXiv:1712.03169* (2017).
- [43] A. Jünger, *Transport Equations for Semiconductors*, 1st ed. (Springer, New York, 2009).
- [44] S. M. Sze, *Physics of Semiconductor Devices*, 1st ed. (Wiley, New York, 1969).
- [45] D. Pines, *Can. J. Phys.* **34**, 1379 (1956).
- [46] O. Entin-Wohlman and H. Gutfreund, *J. Phys. C* **17**, 1071 (1984).

- [47] F. C. Schaefer and R. von Baltz, *Z. Phys. B* **69**, 251 (1987).
- [48] D. C. Scott, R. Binder, M. Bonitz, and S. W. Koch, *Phys. Rev. B* **49**, 2174 (1994).
- [49] M. Bonitz, J. F. Lampin, F. X. Camescasse, and A. Alexandrou, *Phys. Rev. B* **62**, 15724 (2000).
- [50] H. Zhang, R. Zhang, K. S. Schramke, N. M. Bedford, K. Hunter, U. R. Kortshagen, and P. Nordlander, *ACS Photonics* **4**, 963 (2017).
- [51] M. Wubs, *Opt. Express* **23**, 31296 (2015).
- [52] G. Grosso and G. P. Parravicini, *Solid State Physics*, 2nd ed. (Academic, New York, 2014).
- [53] H. A. Lyden, *Phys. Rev.* **134**, A1106 (1964).
- [54] S. Raza, G. Toscano, A.-P. Jauho, M. Wubs, and N. A. Mortensen, *Phys. Rev. B* **84**, 121412(R) (2011).
- [55] A. D. Boardman and B. V. Paranjape, *J. Phys. F* **7**, 1935 (1977).
- [56] G. Mie, *Ann. Phys.* **330**, 377 (1908).
- [57] R. Ruppin, *Phys. Rev. Lett.* **31**, 1434 (1973).
- [58] C. David and F. J. García de Abajo, *J. Phys. Chem. C* **115**, 19470 (2011).
- [59] J. A. Stratton, *Electromagnetic Theory*, 1st ed. (McGraw-Hill, New York, 1941).
- [60] R. A. Stradling and R. A. Wood, *J. Phys. C* **3**, L94 (1970).
- [61] M. Oszwaldowski and M. Zimpel, *J. Phys. Chem. Solids* **49**, 1179 (1988).
- [62] D. M. Szymyd, P. Porro, A. Majerfeld, and S. Lagomarsino, *J. Appl. Phys.* **68**, 2367 (1990).
- [63] A. K. Walton and U. K. Mishra, *J. Phys. C* **1**, 533 (1968).
- [64] N. L. Rowell, *Infrared Phys.* **28**, 37 (1988).
- [65] S. M. Sze and J. C. Irvin, *Solid-State Electron.* **11**, 599 (1968).
- [66] O. Madelung, *Semiconductors: Data Handbook*, 3rd ed. (Springer-Verlag, Berlin, 2004).
- [67] G. V. Naik, V. M. Shalaev, and A. Boltasseva, *Adv. Mater.* **25**, 3264 (2013).
- [68] A. Comin and L. Manna, *Chem. Soc. Rev.* **43**, 3957 (2014).
- [69] K. L. Chopra, S. Major, and D. K. Pandya, *Thin Solid films* **102**, 1 (1983).
- [70] D. O. Scanlon and G. W. Watson, *J. Mater. Chem.* **22**, 25236 (2012).
- [71] K. H. L. Zhang, K. Xi, M. G. Blamire, and R. G. Egdell, *J. Phys.: Condens. Matter* **28**, 383002 (2016).
- [72] K. Tang, S.-L. Gu, J.-D. Ye, A.-M. Zhu, R. Zhang, and Y.-D. Zheng, *Chin. Phys. B* **26**, 047702 (2017).
- [73] H. Haug and S. W. Koch, *Quantum Theory of the Optical and Electronic Properties of Semiconductors*, 5th ed. (World Scientific, Singapore, 2009).
- [74] N. K. S. Gaur, *Physica B and C* **82**, 262 (1976).
- [75] P. Gu, M. Tani, K. Sakai, and T.-R. Yang, *Appl. Phys. Lett.* **77**, 1798 (2000).
- [76] C. G. Olson and D. W. Lynch, *Phys. Rev.* **177**, 1231 (1969).
- [77] Y. Chen, S. Nannarone, J. Schaefer, J. C. Hermanson, and G. J. Lapeyre, *Phys. Rev. B* **39**, 7653 (1989).
- [78] A. Ritz and H. Lüth, *J. Vac. Sci. Technol. B* **3**, 1153 (1985).
- [79] T. S. Jones, M. O. Schweitzer, N. V. Richardson, G. R. Bell, and C. F. McConville, *Phys. Rev. B* **51**, 17675 (1995).
- [80] R. Adomavicius, J. Macutkevicius, R. Suzanoviciene, A. Šiušys, and A. Krotkus, *Phys. Status Solidi C* **6**, 2849 (2009).
- [81] N. A. Mortensen, S. Raza, M. Wubs, T. Søndergaard, and S. I. Bozhevolnyi, *Nat. Commun.* **5**, 3809 (2014).
- [82] W. G. Spitzer and H. Y. Fan, *Phys. Rev.* **106**, 882 (1957).
- [83] G. Toscano, S. Raza, W. Yan, C. Jeppesen, S. Xiao, M. Wubs, A.-P. Jauho, S. I. Bozhevolnyi, and N. A. Mortensen, *Nanophotonics* **2**, 161 (2013).



## Bibliography

- [1] L. Tonks and I. Langmuir. *Oscillations in ionized gases*. Phys. Rev. **33**, 195 (1929).
- [2] D. Pines and D. Bohm. *A collective description of electron interactions: II. collective vs individual particle aspects of the interactions*. Phys. Rev. **85**, 338 (1952).
- [3] J. M. Pitarke, V. M. Silkin, E. V. Chulkov and P. M. Echenique. *Theory of surface plasmons and surface-plasmon polaritons*. Rep. Prog. Phys. **70**, 1 (2007).
- [4] J. A. Scholl, A. L. Koh and J. A. Dionne. *Quantum plasmon resonances of individual metallic nanoparticles*. Nature **483**, 421 (2012).
- [5] M. S. Tame, K. R. McEnery, S. K. Özdemir, J. Lee, S. A. Maier and M. S. Kim. *Quantum plasmonics*. Nat. Phys. **9**, 329 (2013).
- [6] J. M. Fitzgerald, P. Narang, R. V. Craster, S. A. Maier and V. Giannini. *Quantum plasmonics*. Proc. IEEE **104**, 2307 (2016).
- [7] I. Lindau and P. O. Nilsson. *Experimental verification of optically excited longitudinal plasmons*. Phys. Scr. **3**, 87 (1971).
- [8] H. Abe, K.-P. Charlé, B. Tesche and W. Schulze. *Surface plasmon absorption of various colloidal metal particles*. Chem. Phys. **68**, 137 (1982).
- [9] U. Ch. Fischer and D. W. Pohl. *Observation of single-particle plasmons by near-field optical microscopy*. Phys. Rev. Lett. **62**, 458 (1989).
- [10] M. Bosman, E. Ye, S. F. Tan, C. A. Nijhuis, J. K. W. Yang, R. Marty, A. Mlayah, A. Arbouet, C. Girard and M.-Y. Han. *Surface plasmon damping quantified with an electron nanoprobe*. Sci. Rep. **3**, 1312 (2013).
- [11] C. Frydendahl, T. Repän, M. Geisler, S. M. Novikov, J. Beermann, A. V. Lavrinenko, S. Xiao, S. I. Bozhevolnyi, N. A. Mortensen and N. Stenger. *Optical reconfiguration and polarization control in semi-continuous gold films close to the percolation threshold*. Nanoscale **9**, 12014 (2017).
- [12] J. Sukham, O. Takayama, A. V. Lavrinenko and R. Malureanu. *High-quality ultrathin gold layers with an APTMS adhesion for optimal performance of surface plasmon polariton-based devices*. ACS Appl. Mater. Inter. **9**, 25049 (2017).

- [13] M. Anderegg, B. Feuerbacher and B. Fitton. *Optically excited longitudinal plasmons in potassium*. Phys. Rev. Lett. **27**, 1565 (1971).
- [14] T. Kloos. *Plasmaschwingungen in Al, Mg, Li, Na und K angeregt durch schnelle elektronen*. Z. Phys. **265**, 225 (1973).
- [15] S. Chen, Z. Fan and D. L. Carroll. *Silver nanodisks: Synthesis, characterization and self-assembly*. J. Phys. Chem. B **106**, 10777 (2002).
- [16] K. L. Kelly, E. Coronado, L. L. Zhao and G. C. Schatz. *The optical properties of metal nanoparticles: The influence of size, shape and dielectric environment*. J. Phys. Chem. B **107**, 668 (2003).
- [17] E. Prodan, C. Radloff, N. J. Halas and P. Nordlander. *A hybridization model for the plasmon response of complex nanostructures*. Science **302**, 419 (2003).
- [18] E. Hao and G. C. Schatz. *Electromagnetic fields around silver nanoparticles and dimers*. J. Chem. Phys. **120**, 357 (2004).
- [19] A. I. Fernández-Domínguez, A. Wiener, F. J. García-Vidal, S. A. Maier and J. B. Pendry. *Transformation-optics description of nonlocal effects in plasmonic nanostructures*. Phys. Rev. Lett. **108**, 106802 (2012).
- [20] A. H. Castro Neto, F. Guinea, N. M. R. Peres, K. S. Novoselov and A. K. Geim. *The electronic properties of graphene*. Rev. Mod. Phys. **81**, 109 (2009).
- [21] T. Low, A. Chaves, J. D. Caldwell, A. Kumar, N. X. Fang, P. Avouris, T. F. Heinz, F. Guinea, L. Martin-Moreno and F. Koppens. *Polaritons in layered two-dimensional materials*. Nat. Mater. **16**, 182 (2017).
- [22] M. Settnes, J. R. M. Saavedra, K. S. Thygesen, A.-P. Jauho, F. J. García de Abajo and N. A. Mortensen. *Strong plasmon-phonon splitting and hybridization in 2D materials revealed through a self-energy approach*. ACS Photonics **4**, 2908 (2017).
- [23] J. Homola, S. S. Yee and G. Gauglitz. *Surface plasmon resonance sensors: review*. Sensor Actuat. B-Chem. **54**, 3 (1999).
- [24] P. K. Jain, X. Huang, I. H. El-Sayed and M. A. El-Sayed. *Noble metals on the nanoscale: Optical and photothermal properties and some applications in imaging, sensing, biology, and medicine*. Accounts Chem. Res. **41**, 1578 (2008).
- [25] J. W. Cleary, G. Medhi, R. E. Peale, W. R. Buchwald, O. Edwards and I. Oladeji. *Infrared surface plasmon resonance biosensor*. Proc. Soc. Photo.-Opt. Ins. **7673**, 767306 (2010).

- [26] T. Y. Jeon, D. J. Kim, S.-G. Park, S.-H. Kim and D.-H. Kim. *Nanostructured plasmonic substrates for use as SERS sensors*. *Nano Converg.* **3**, 18 (2016).
- [27] L. R. Hirsch, R. J. Stafford, J. A. Bankson, S. R. Sershen, B. Rivera, R. E. Price, J. D. Hazle, N. J. Halas and J. L. West. *Nanoshell-mediated near-infrared thermal therapy of tumors under magnetic resonance guidance*. *PNAS* **100**, 13549 (2003).
- [28] L. Tang, S. E. Kocobas, S. Latif, A. K. Okyay, D.-S. Ly-Gagnon, K. C. Saraswat and D. A. B. Miller. *Nanometre-scale germanium photodetector enhanced by a near-infrared dipole antenna*. *Nat. Photonics* **2**, 226 (2008).
- [29] W. Cai, J. S. White and M. L. Brongersma. *Compact, high-speed and power-efficient electrooptic plasmonic modulators*. *Nano Lett.* **9**, 4403 (2009).
- [30] M. Moskovits and D. H. Jeong. *Engineering nanostructures for giant optical fields*. *Chem. Phys. Lett.* **397**, 91 (2004).
- [31] J. Zhang, Y. Fu, M. H. Chowdhury and J. R. Lakowicz. *Metal-enhanced single-molecule fluorescence on silver particle monomer and dimer: Coupling effect between metal particles*. *Nano Lett.* **7**, 2101 (2007).
- [32] F. Le, D. W. Brandl, Y. A. Urzhumov, H. Wang, J. Kundu, N. J. Halas, J. Aizpurua and P. Nordlander. *Metallic nanoparticle arrays: A common substrate for both surface-enhanced Raman scattering and surface-enhanced infrared absorption*. *ACS Nano* **2**, 707 (2008).
- [33] J. A. Schuller, E. S. Barnard, W. Cai, Y. C. Jun, J. S. White and M. L. Brongersma. *Plasmonics for extreme light concentration and manipulation*. *Nat. Mater.* **9**, 193 (2010).
- [34] L. Cao, D. N. Barsic, A. R. Guichard and M. L. Brongersma. *Plasmon-assisted local temperature control to pattern individual semiconductor nanowires and carbon nanotubes*. *Nano Lett.* **7**, 3523 (2007).
- [35] H. A. Atwater and A. Polman. *Plasmonics for improved photovoltaic devices*. *Nat. Mater.* **9**, 205 (2010).
- [36] X. Zhu, C. Vannahme, E. Højlund-Nielsen, N. A. Mortensen and A. Kristensen. *Plasmonic colour laser printing*. *Nat. Nanotechnol.* **11**, 325 (2016).
- [37] M. S. Tame, C. Lee, J. Lee, D. Ballester, M. Paternostro, A. V. Zayats and M. S. Kim. *Single-photon excitation of surface plasmon polaritons*. *Phys. Rev. Lett.* **101**, 190504 (2008).
- [38] S. I. Bozhevolnyi and N. A. Mortensen. *Plasmonics for emerging quantum technologies*. *Nanophotonics* **6**, 1185 (2017).

- [39] J. Henzie, J. Lee, M. H. Lee, W. Hasan and T. W. Odom. *Nanofabrication of plasmonic structures*. *Annu. Rev. Phys. Chem.* **60**, 147 (2009).
- [40] X. Chen, H.-R. Park, M. Pelton, X. Piao, N. C. Lindquist, H. Im, Y. J. Kim, J. S. Ahn, K. J. Ahn, N. Park, D.-S. Kim and S.-H. Oh. *Atomic layer lithography of wafer-scale nanogap arrays for extreme confinement of electromagnetic waves*. *Nat. Commun.* **4**, 2361 (2013).
- [41] G. V. Naik, V. M. Shalaev and A. Boltasseva. *Alternative plasmonic materials: Beyond gold and silver*. *Adv. Mater.* **25**, 3264 (2013).
- [42] A. Comin and L. Manna. *New materials for tunable plasmonic colloidal nanocrystals*. *Chem. Soc. Rev.* **43**, 3957 (2014).
- [43] P. R. Ohodnicki Jr., C. Wang and M. Andio. *Plasmonic transparent conducting metal oxide nanoparticles and nanoparticle films for optical sensing applications*. *Thin Solid Films* **539**, 327 (2013).
- [44] C. M. Hessel, V. P. Pattani, M. Rasch, M. G. Panthani, B. Koo, J. W. Tunnell and B. A. Korgel. *Copper selenide nanocrystals for photothermal therapy*. *Nano Lett.* **11**, 2560 (2011).
- [45] T. Ando. *The electronic properties of graphene and carbon nanotubes*. *NPG Asia Mater.* **1**, 17 (2009).
- [46] A. Lauchner, A. E. Schlather, A. Manjavacas, Y. Cui, M. J. McClain, G. J. Stec, F. J. García de Abajo, P. Nordlander and N. J. Halas. *Molecular plasmonics*. *Nano Lett.* **15**, 6208 (2015).
- [47] J. Moll, S. Daehne, J. R. Durrant and D. A. Wiersma. *Optical dynamics of excitons in J aggregates of a carbocyanine dye*. *J. Chem. Phys.* **102**, 6362 (1995).
- [48] M. J. Gentile, S. A. R. Horsley and W. L. Barnes. *Localized exciton-polariton modes in dye-doped nanospheres: a quantum approach*. *J. Opt.* **18**, 015001 (2016).
- [49] D. J. Griffiths. *Introduction to Electrodynamics*. 3rd ed. (Pearson, 2008).
- [50] J. D. Jackson. *Classical Electrodynamics*. (Wiley, 1962).
- [51] P. Young. *Longitudinal and transverse dynamical response of the electron gas in the random phase approximation (RPA)*. Lecture note (Physics 232), 2006.
- [52] M. Wubs. *Classification of scalar and dyadic nonlocal optical response models*. *Opt. Express* **23**, 31296 (2015).

- [53] L. Novotny and B. Hecht. *Principles of Nano-Optics*. (Cambridge, 2006).
- [54] S. A. Maier. *Plasmonics: Fundamentals and Applications*. (Springer, 2007).
- [55] G. Mie. *Beiträge zur Optik trüber Medien, speziell kolloidaler Metallösungen*. Ann. Phys. **330**, 377 (1908).
- [56] S. Asano and G. Yamamoto. *Light scattering by a spheroidal particle*. Appl. Opt. **14**, 29 (1975).
- [57] R. Ruppin. *Extinction properties of thin metallic nanowires*. Opt. Commun. **190**, 205 (2001).
- [58] M. S. Gockenbach. *Understanding and implementing the finite element method*. (SIAM, 2006).
- [59] R. W. Scharstein. *Mellin transform solution for the static line-source excitation of a dielectric wedge*. IEEE Antenn. Propag. **41**, 1675 (1993).
- [60] A. Otto. *Excitation of nonradiative surface plasma waves in silver by the method of frustrated total reflection*. Z. Phys. **216**, 398 (1968).
- [61] E. Kretschmann and H. Raether. *Radiative decay of non radiative surface plasmons excited by light*. Z. Naturforsch. **23A**, 2135 (1968).
- [62] C. F. Bohren and D. R. Huffman. *Absorption and Scattering of Light by Small Particles*. (Wiley, 1983).
- [63] E. C. Le Ru, W. R. C. Somerville and B. Auguié. *Radiative correction in approximate treatments of electromagnetic scattering by point and body scatterers*. Phys. Rev. A **87**, 012504 (2013).
- [64] E. Betzig and J. K. Trautman. *Near-field optics: microscopy, spectroscopy, and surface modification beyond the diffraction limit*. Science **257**, 189 (1992).
- [65] J.-J. Greffet and R. Carminati. *Image formation in near-field optics*. Prog. Surf. Sci. **56**, 133 (1997).
- [66] A. V. Zayats, I. I. Smolyaninov and A. A. Maradudin. *Nano-optics of surface plasmon polaritons*. Phys. Rep. **408**, 131 (2005).
- [67] R. F. Egerton. *Electron energy-loss spectroscopy in the TEM*. Rep. Prog. Phys. **72**, 016502 (2009).
- [68] F. J. García de Abajo. *Optical excitations in electron microscopy*. Rev. Mod. Phys. **82**, 209 (2010).

- [69] T. Christensen, W. Yan, S. Raza, A.-P. Jauho, N. A. Mortensen and M. Wubs. *Nonlocal response of metallic nanospheres probed by light, electrons, and atoms*. ACS Nano **8**, 1745 (2014).
- [70] K. H. Drexhage. *Influence of a dielectric interface on fluorescence decay time*. J. Lumin. **1–2**, 693 (1970).
- [71] W. P. Halperin. *Quantum size effects in metal particles*. Rev. Mod. Phys. **58**, 533 (1986).
- [72] R. O. Jones. *Density functional theory: Its origins, rise to prominence, and future*. Rev. Mod. Phys. **87**, 897 (2015).
- [73] E. Townsend and G. W. Bryant. *Which resonances in small metallic nanoparticles are plasmonic?* J. Opt. **16**, 114022 (2014).
- [74] P. B. Johnson and R. W. Christy. *Optical constants of the noble metals*. Phys. Rev. B **6**, 4370 (1972).
- [75] F. J. García de Abajo. *Nonlocal effects in the plasmons of strongly interacting nanoparticles, dimers, and waveguides*. J. Phys. Chem. C **112**, 17983 (2008).
- [76] J. Lindhard. *On the properties of a gas of charged particles*. Dan. Mat. Fys. Medd. **28**, 1 (1954).
- [77] G. Grosso and G. P. Parravicini. *Solid State Physics*. 2nd ed. (Academic Press, 2014).
- [78] N. D. Mermin. *Lindhard dielectric function in the relaxation-time approximation*. Phys. Rev. B **1**, 2362 (1970).
- [79] A. Jünger. *Transport Equations for Semiconductors*. (Springer, 2009).
- [80] A. R. Melnyk and M. J. Harrison. *Theory of optical excitation of plasmons in metals*. Phys. Rev. B **2**, 835 (1970).
- [81] F. Sauter. *Der Einfluß von Plasmawellen auf das Reflexionsvermögen von Metallen (I)*. Z. Physik **203**, 488 (1967).
- [82] F. Forstmann and H. Stenschke. *Electrodynamics at metal boundaries with inclusion of plasma waves*. Phys. Rev. Lett. **38**, 1365 (1977).
- [83] P. Jewsbury. *Electrodynamic boundary conditions at metal interfaces*. J. Phys. F: Met. Phys. **11**, 195 (1981).
- [84] A. D. Boardman and R. Rupp. *The boundary conditions between spatially dispersive media*. Surf. Sci. **112**, 153 (1981).

- [85] G. Toscano, J. Straubel, A. Kwiatkowski, C. Rockstuhl, F. Evers, H. Xu, N. A. Mortensen and M. Wubs. *Resonance shifts and spill-out effects in self-consistent hydrodynamic nanoplasmonics*. Nat. Commun. **6**, 7132 (2015).
- [86] C. Ciraci and F. Della Sala. *Quantum hydrodynamic theory for plasmonics: Impact of the electron density tail*. Phys. Rev. B **93**, 205405 (2016).
- [87] A. L. Fetter. *Electrodynamics of a layered electron gas. I. single layer*. Ann. Phys. **81**, 367 (1973).
- [88] P. Halevi. *Hydrodynamic model for the degenerate free-electron gas: Generalization to arbitrary frequencies*. Phys. Rev. B **51**, 7497 (1995).
- [89] N. A. Mortensen, S. Raza, M. Wubs, T. Søndergaard and S. I. Bozhevolnyi. *A generalized non-local optical response theory for plasmonic nanostructures*. Nat. Commun. **5**, 3809 (2014).
- [90] U. Kreibig and L. Genzel. *Optical absorption of small metallic particles*. Surf. Sci. **156**, 678 (1985).
- [91] S. Link and M. A. El-Sayed. *Size and temperature dependence of the plasmon absorption of colloidal gold nanoparticles*. J. Phys. Chem. B **103**, 4212 (1999).
- [92] M. Gaudry, E. Cottancin, M. Pellarin, J. Lermé, L. Arnaud, J. R. Huntzinger, J. L. Vialle, M. Broyer, J. L. Rousset, M. Treilleux and P. Mélinon. *Size and composition dependence in the optical properties of mixed (transition metal/noble metal) embedded clusters*. Phys. Rev. B **67**, 155409 (2003).
- [93] U. Kreibig and C. V. Fragstein. *The limitation of electron mean free path in small silver particles*. Z. Physik **224**, 307 (1969).
- [94] S. Raza, S. I. Bozhevolnyi, M. Wubs and N. A. Mortensen. *Nonlocal optical response in metallic nanostructures*. J. Phys.: Condens. Matter **27**, 183204 (2015).
- [95] Å. Ljungbert and P. Apell. *The role of electron-hole pair excitations in the optical absorption of metals, particularly metal spheres*. Solid State Commun. **46**, 47 (1983).
- [96] P. Apell and D. R. Penn. *Optical properties of small metal spheres: Surface effects*. Phys. Rev. Lett. **50**, 1316 (1983).
- [97] J. A. Stratton. *Electromagnetic Theory*. (McGraw-Hill, 1941).
- [98] R. Ruppin. *Optical properties of a plasma sphere*. Phys. Rev. Lett. **31**, 1434 (1973).

- [99] R. Ruppin. *Optical properties of small metal spheres*. Phys. Rev. B **11**, 2871 (1975).
- [100] C. David and F. J. García de Abajo. *Spatial nonlocality in the optical response of metal nanoparticles*. J. Phys. Chem. C **115**, 19470 (2011).
- [101] S. Raza, W. Yan, N. Stenger, M. Wubs and N. A. Mortensen. *Blueshift of the surface plasmon resonance in silver nanoparticles: substrate effects*. Opt. Express **21**, 27344 (2013).
- [102] S. Raza, N. Stenger, S. Kadkhodazadeh, S. V. Fischer, N. Kostesha, A.-P. Jauho, A. Burrows, M. Wubs and N. A. Mortensen. *Blueshift of the surface plasmon resonance in silver nanoparticles studied with EELS*. Nanophotonics **2**, 131 (2013).
- [103] R. Fuchs and F. Claro. *Multipolar response of small metallic spheres: Nonlocal theory*. Phys. Rev B **35**, 3722 (1987).
- [104] J. Tiggesbäumker, L. Köller, K.-H. Meiwes-Broer and A. Liebsch. *Blue shift of the Mie plasma frequency in Ag clusters and particles*. Phys. Rev. A **48**, R1749 (1993).
- [105] K.-P. Charlé, L. König, S. Nepijko, I. Rabin and W. Schulze. *The surface plasmon resonance of free and embedded Ag-clusters in the size range  $1.5 \text{ nm} < D < 30 \text{ nm}$* . Cryst. Res. Technol. **33**, 1085 (1998).
- [106] C. Ciraci, R. T. Hill, J. J. Mock, Y. Urzhumov, A. I. Fernández-Domínguez, S. A. Maier, J. B. Pendry, A. Chilkoti and D. R. Smith. *Probing the ultimate limits of plasmonic enhancement*. Science **337**, 1072 (2012).
- [107] S. Raza, M. Wubs, S. I. Bozhevolnyi and N. A. Mortensen. *Nonlocal study of ultimate plasmon hybridization*. Opt. Lett. **40**, 839 (2015).
- [108] S. Raza, G. Toscano, A.-P. Jauho, M. Wubs and N. A. Mortensen. *Unusual resonances in nanoplasmonic structures due to nonlocal response*. Phys. Rev. B **84**, 121412(R) (2011).
- [109] C. H. Chen. *Plasmon dispersion in single-crystal magnesium*. J. Phys. C: Solid State Phys. **9**, L321 (1976).
- [110] F. Abeles, Y. Borensztein, M. de Crescenzi and T. Lopez-Rios. *Optical evidence for longitudinal waves in very thin Ag layers*. Surf. Sci. **101**, 123 (1980).
- [111] M. M. Özer, E. J. Moon, A. G. Eguiluz and H. H. Weitering. *Plasmon response of a quantum-confined electron gas probed by core-level photoemission*. Phys. Rev. Lett. **106**, 197601 (2011).

- [112] M. Pelton and G. W. Bryant. *Introduction to Metal-Nanoparticle Plasmonics*. (Wiley, 2013).
- [113] J. Doak, R. K. Gupta, K. Manivannan, K. Ghosh and P. K. Kahol. *Effect of particle size distributions on absorbance spectra of gold nanoparticles*. *Physica E* **42**, 1605 (2010).
- [114] J. A. Fauchaux, A. L. D. Stanton and P. K. Jain. *Plasmon resonances of semiconductor nanocrystals: Physical principles and new opportunities*. *J. Phys. Chem. Lett.* **5**, 976 (2014).
- [115] P. H. Siegel. *Terahertz technology in biology and medicine*. *IEEE Trans. Microw. Theory. Tech.* **52**, 2438 (2004).
- [116] S. M. Hanham, A. I. Fernández-Domínguez, J. H. Teng, S. S. Ang, K. P. Lim, S. F. Yoon, C. Y. Ngo, N. Klein, J. B. Pendry and S. A. Maier. *Broad-band terahertz plasmonic response of touching InSb disks*. *Adv. Mater.* **24**, OP226 (2012).
- [117] S. C. Howells and L. A. Schlie. *Transient terahertz reflection spectroscopy of undoped InSb from 0.1 THz to 1.1 THz*. *Appl. Phys. Lett.* **69**, 550 (1996).
- [118] J. Gómez Rivas, M. Kuttge, H. Kurz, P. H. Bolivar and J. A. Sánchez-Gil. *Low-frequency active surface plasmon optics on semiconductors*. *Appl. Phys. Lett.* **88**, 082106 (2006).
- [119] K. Anglin, T. Ribaudó, D. C. Adams, X. Qian, W. D. Goodhue, S. Dooley, E. A. Shaner and D. Wasserman. *Voltage-controlled active mid-infrared plasmonic devices*. *J. Appl. Phys.* **109**, 123103 (2011).
- [120] X. Liu, J.-H. Kang, H. Yuan, J. Park, S. J. Kim, Y. Cui, H. Y. Hwang and M. L. Brongersma. *Electrical tuning of a quantum plasmonic resonance*. *Nat. Nanotechnol.* **12**, 866 (2017).
- [121] X. Liu, J.-H. Kang, H. Yuan, J. Park, Y. Cui, H. Y. Hwang and M. L. Brongersma. *Tuning of plasmons in transparent conductive oxides by carrier accumulation*. *ACS photonics* **5**, 1493 (2018).
- [122] Y. Yang, K. Kelly, E. Sacht, S. Campione, T. S. Luk, J.-P. Maria, M. B. Sinclair and I. Brener. *Femtosecond optical polarization switching using a cadmium oxide-based perfect absorber*. *Nat. Photonics* **11**, 390 (2017).
- [123] S. M. Sze. *Physics of Semiconductor Devices*. (Wiley, 1969).
- [124] K. Seeger. *Semiconductor Physics*. 9th ed. (Springer, 2004).

- [125] D. A. Neamen. *Semiconductor Physics and Devices*. 3rd ed. (McGraw-Hill, 2003).
- [126] J. R. Chelikowsky and M. L. Cohen. *Nonlocal pseudopotential calculations for the electronic structure of eleven diamond and zinc-blende semiconductors*. Phys. Rev. B **14**, 556 (1976).
- [127] W. G. Spitzer and H. Y. Fan. *Determination of optical constants and carrier effective mass of semiconductors*. Phys. Rev. **106**, 882 (1957).
- [128] E. O. Kane. *Band structure of indium antimonide*. J. Phys. Chem. Solids **1**, 249 (1957).
- [129] E. M. Conwell. *Properties of silicon and germanium: II*. Proc. IRE **46**, 1281 (1958).
- [130] G. M. Martin, J. P. Farges, G. Jacob and J. P. Hallais. *Compensation mechanisms in GaAs*. J. Appl. Phys. **51**, 2840 (1980).
- [131] F. A. Trumbore. *Solid solubilities of impurity elements in germanium and silicon*. Bell Syst. Tech. J. **39**, 205 (1960).
- [132] H. A. Lyden. *Measurement of the conductivity effective mass in semiconductors using infrared reflection*. Phys. Rev. **134**, A1106 (1964).
- [133] S. M. Sze and J. C. Irvin. *Resistivity, mobility and impurity levels in GaAs, Ge, and Si at 300K*. Solid-State Electron. **11**, 599 (1968).
- [134] A. Raymond, J. L. Robert and C. Bernard. *The electron effective mass in heavily doped GaAs*. J. Phys. C: Solid State Phys. **12**, 2289 (1979).
- [135] D. M. Szmyd, P. Porro, A. Majerfeld and S. Lagomarsino. *Heavily doped GaAs:Se. I. Photoluminescence determination of the electron effective mass*. J. Appl. Phys. **68**, 2367 (1990).
- [136] R. A. Stradling and R. A. Wood. *The temperature dependence of the band-edge effective masses of InSb, InAs and GaAs as deduced from magnetophonon magnetoresistance measurements*. J. Phys. C: Solid State Phys. **3**, L94 (1970).
- [137] H. Haug and S. W. Koch. *Quantum Theory of the Optical and Electronic Properties of Semiconductors*. 5th ed. (World Scientific, 2009).
- [138] P. Giannozzi, S. de Gironcoli, P. Pavone and S. Baroni. *Ab initio calculations of phonon dispersions in semiconductors*. Phys. Rev. B **43**, 7231 (1991).
- [139] C. G. Olson and D. W. Lynch. *Longitudinal-optical-phonon-plasmon coupling in GaAs*. Phys. Rev. **177**, 1231 (1969).

- [140] N. K. S. Gaur. *Longitudinal optical phonon-plasmon coupling in InSb and InAs*. Physica B & C **82**, 262 (1976).
- [141] Y. Chen, S. Nannarone, J. Schaefer, J. C. Hermanson and G. J. Lapeyre. *Coupled plasmon and phonon excitations in the space-charge layer on GaAs(110) surfaces*. Phys. Rev. B **39**, 7653 (1989).
- [142] P. Gu, M. Tani, K. Sakai and T.-R. Yang. *Detection of terahertz radiation from longitudinal optical phonon-plasmon coupling modes in InSb film using an ultrabroadband photoconductive antenna*. Appl. Phys. Lett. **77**, 1798 (2000).
- [143] C. Sikorski and U. Merkt. *Spectroscopy of electronic states in InSb quantum dots*. Phys. Rev. Lett. **62**, 2164 (1989).
- [144] H. D. Barber. *Effective mass and intrinsic concentration in silicon*. Solid State Electron. **10**, 1039 (1967).
- [145] M. Oszwaldowski and M. Zimpel. *Temperature dependence of intrinsic carrier concentration and density of states effective mass of heavy holes in InSb*. J. Phys. Chem. Solids **49**, 1179 (1988).
- [146] A. K. Walton and U. K. Mishra. *Light and heavy hole masses in GaAs and GaSb*. J. Phys. C: Solid State Phys. **1**, 533 (1968).
- [147] N. L. Rowell. *Infrared photoluminescence of intrinsic InSb*. Infrared Phys. **28**, 37 (1988).
- [148] O. Madelung. *Semiconductors: Data Handbook*. 3rd ed. (Springer-Verlag, Berlin, 2004).
- [149] E. Kooi. *Formation and composition of surface layers and solubility limits of phosphorus during diffusion in silicon*. J. Electrochem. Soc. **111**, 1383 (1964).
- [150] R. Soref, R. E. Peale and W. Buchwald. *Longwave plasmonics on doped silicon and silicides*. Opt. Express **16**, 6507 (2008).
- [151] J. A. Dionne, K. Diest, L. A. Sweatlock and H. A. Atwater. *PlasMOSter: A metal-oxide-Si field effect plasmonic modulator*. Nano Lett. **9**, 897 (2009).
- [152] J. C. Ginn, R. L. Jarecki Jr., E. A. Shaner and P. S. Davids. *Infrared plasmons on heavily-doped silicon*. J. Appl. Phys. **110**, 043110 (2011).
- [153] S. Zhou, X. Pi, Z. Ni, Y. Ding, Y. Jiang, C. Jin, C. Delerue, D. Yang and T. Nozaki. *Comparative study on the localized surface plasmon resonance of boron- and phosphorus-doped silicon nanocrystals*. ACS Nano **9**, 378 (2015).

- [154] N. J. Kramer, K. S. Schramke and U. R. Kortshagen. *Plasmonic properties of silicon nanocrystals doped with boron and phosphorus*. Nano Lett. **15**, 5597 (2015).
- [155] A. V. Krasavin and A. V. Zayats. *Silicon-based plasmonic waveguides*. Opt. Express **18**, 11791 (2010).
- [156] W. Walukiewicz. *Intrinsic limitations to the doping of wide-gap semiconductors*. Physica B **302–303**, 123 (2001).
- [157] M. Konagai, T. Yamada, T. Akatsuka, K. Saito, E. Tokumitsu and K. Takahashi. *Metallic p-type GaAs and GaAlAs grown by metalorganic molecular beam epitaxy*. J. Cryst. Growth **98**, 167 (1989).
- [158] R. Matz and H. Lüth. *Conduction-band surface plasmons in the electron-energy-loss spectrum of GaAs(110)*. Phys. Rev. Lett. **46**, 500 (1981).
- [159] Z. J. Gray-Grychowski, R. A. Stradling, R. G. Egdell, P. J. Dobson, B. A. Joyce and K. Woodbridge. *Observation of interfacial plasmons on MBE-grown GaAs by high-resolution electron-energy-loss spectroscopy*. Solid State Commun. **59**, 703 (1986).
- [160] M. G. Betti, U. del Pennino and C. Mariani. *Collective and vibrational excitations on the n-doped GaAs(110) surface*. Phys. Rev. B **39**, 5887 (1989).
- [161] Y. Meng, J. R. Anderson, J. C. Hermanson and G. J. Lapeyre. *Hole-plasmon excitations on a p-type GaAs(110) surface*. Phys. Rev. B **44**, 4040(R) (1991).
- [162] R. Biagi, C. Mariani and U. del Pennino. *Hole-plasmon damping on heavily doped p-type GaAs(110)*. Phys. Rev. B **46**, 2467 (1992).
- [163] W. E. Anderson, R. W. Alexander Jr. and R. J. Bell. *Surface plasmons and the reflectivity of n-type InSb*. Phys. Rev. Lett. **27**, 1057 (1971).
- [164] A. J. Hoffman, L. Alekseyev, S. S. Howard, K. J. Franz, D. Wasserman, V. A. Podolskiy, E. E. Narimanov, D. L. Sivco and C. Gmachl. *Negative refraction in semiconductor metamaterials*. Nat. Mater. **6**, 946 (2007).
- [165] S. Law, D. C. Adams, A. M. Taylor and D. Wasserman. *Mid-infrared designer metals*. Opt. Express **20**, 12155 (2012).
- [166] S. H. Brewer and S. Franzen. *Calculation of the electronic and optical properties of indium tin oxide by density functional theory*. Chem. Phys. **300**, 285 (2004).

- [167] C. Rhodes, S. Franzen, J.-P. Maria, M. Losego, D. N. Leonard, B. Laughlin, G. Duscher and S. Weibel. *Surface plasmon resonance in conducting metal oxides*. J. Appl. Phys. **100**, 054905 (2006).
- [168] C. Rhodes, M. Cerruti, A. Efremenko, M. Losego, D. E. Aspnes, J.-P. Maria and S. Franzen. *Dependence of plasmon polaritons on the thickness of indium tin oxide thin films*. J. Appl. Phys. **103**, 093108 (2008).
- [169] M. Y. C. Xu, M. Z. Alam, A. J. Zilkie, K. Zeaiter and J. S. Aitchison. *Surface plasmon polaritons mediated by ITO at near infrared wavelength*. In: Proceedings of the Conference on Lasers and Electro-Optics/Quantum Electronics and Laser Science Conference. San Jose, CA, USA, 2008, IEEE, pp. 2135–2136.
- [170] G. Garcia, R. Buonsanti, E. L. Runnerstrom, R. J. Mendelsberg, A. Llordes, A. Anders, T. J. Richardson and D. J. Milliron. *Dynamically modulating the surface plasmon resonance of doped semiconductor nanocrystals*. Nano Lett. **11**, 4415 (2011).
- [171] R. Buonsanti, A. Llordes, S. Aloni, B. A. Helms and D. J. Milliron. *Tunable infrared absorption and visible transparency of colloidal aluminum-doped zinc oxide nanocrystals*. Nano Lett. **11**, 4706 (2011).
- [172] J. Kim, G. V. Naik, N. K. Emani, U. Guler and A. Boltasseva. *Plasmonic resonances in nanostructured transparent conducting oxide films*. IEEE J. Sel. Top. Quant. **19**, 4601907 (2013).
- [173] J. R. Hendrickson, S. Vangala, N. Nader, K. Leedy, J. Guo and J. W. Cleary. *Plasmon resonance and perfect light absorption in subwavelength trench arrays etched in gallium-doped zinc oxide film*. Appl. Phys. Lett. **107**, 191906 (2015).
- [174] D. de Ceglia, M. Scalora, M. A. Vincenti, S. Campione, K. Kelley, E. L. Runnerstrom, J.-P. Maria, G. A. Keeler and T. S. Luk. *Viscoelastic optical nonlocality of low-loss epsilon-near-zero nanofilms*. Sci. Rep. **8**, 9335 (2018).
- [175] K. Santiago, R. Mundle, C. B. Samantaray, M. Bahoura and A. K. Pradhan. *Nanopatterning of atomic layer deposited Al:ZnO films using electron beam lithography for waveguide applications in the NIR region*. Opt. Mater. Express **2**, 1743 (2012).
- [176] K. Manthiram and A. P. Alivisatos. *Tunable localized surface plasmon resonances in tungsten oxide nanocrystals*. J. Am. Chem. Soc. **134**, 3995 (2012).
- [177] J. A. Faucheaux and P. K. Jain. *Plasmons in photocharged ZnO nanocrystals revealing the nature of charge dynamics*. J. Phys. Chem. Lett. **4**, 3024 (2013).

- [178] A. M. Schimpf, N. Thakkar, C. E. Gunthardt, D. J. Masiello and D. R. Gamelin. *Charge-tunable quantum plasmons in colloidal semiconductor nanocrystals*. ACS Nano **8**, 1065 (2014).
- [179] Y. E. Kesim, E. Battal and A. K. Okyay. *Plasmonic materials based on ZnO films and their potential for developing broadband middle-infrared absorbers*. AIP adv. **4**, 077106 (2014).
- [180] E. Sachet, C. T. Shelton, J. S. Harris, B. E. Gaddy, D. L. Irving, S. Curtarolo, B. F. Donovan, P. E. Hopkins, P. A. Sharma, A. L. Sharma, J. Ihlefeld, S. Franzen and J.-P. Maria. *Dysprosium-doped cadmium oxide as a gateway material for mid-infrared plasmonics*. Nat. Mater. **14**, 414 (2015).
- [181] J. M. Luther, P. K. Jain, T. Ewers and A. P. Alivisatos. *Localized surface plasmon resonances arising from free carriers in doped quantum dots*. Nat. Mater. **10**, 361 (2011).
- [182] Y. Xie, L. Carbone, C. Nobile, V. Grillo, S. D'Agostino, F. Della Sala, C. Giannini, A. Altamura, C. Oelsner, C. Kryschy and P. D. Cozzoli. *Metallic-like stoichiometric copper sulfide nanocrystals: Phase- and shape-selective synthesis, near-infrared surface plasmon resonance properties, and their modeling*. ACS Nano **7**, 7352 (2013).
- [183] I. Kriegel, C. Jiang, J. Rodríguez-Fernández, R. D. Schaller, D. V. Talapin, E. da Como and J. Feldmann. *Tuning the excitonic and plasmonic properties of copper chalcogenide nanocrystals*. J. Am. Chem. Soc. **134**, 1583 (2012).
- [184] F. Scotognella, G. Della Valle, A. R. S. Kandada, D. Dorfs, M. Zavelani-Rossi, M. Conforti, K. Miszta, A. Comin, K. Korobchevskaya, G. Lanzani, L. Manna and F. Tassone. *Plasmon dynamics in colloidal Cu<sub>2-x</sub>Se nanocrystals*. Nano Lett. **11**, 4711 (2011).
- [185] G. R. Bell, T. S. Jones and C. F. McConville. *Spatial variation of plasmon damping near the polar surfaces of InAs and InSb*. Surf. Sci. **405**, 280 (1998).
- [186] J. G. Rivas, C. Janke, P. H. Bolivar and H. Kurz. *Transmission of THz radiation through InSb gratings of subwavelength apertures*. Opt. Express **13**, 847 (2005).
- [187] T. H. Isaac, W. L. Barnes and E. Hendry. *Determining the terahertz optical properties of subwavelength films using semiconductor surface plasmons*. Appl. Phys. Lett. **93**, 241115 (2008).
- [188] P. Shewmon. *Diffusion in Solids*. 2nd ed. (Wiley, 1991).
- [189] Y. Takamura, S. H. Jain, P. B. Griffin and J. D. Plummer. *Thermal stability of dopants in laser annealed silicon*. J. Appl. Phys. **92**, 230 (2002).

- [190] J. H. Neave, P. J. Dobson, J. J. Harris, P. Dawson and B. A. Joyce. *Silicon doping of MBE-grown GaAs films*. Appl. Phys. A **32**, 195 (1983).
- [191] K. L. Chopra, S. Major and D. K. Pandya. *Transparent conductors - a status review*. Thin Solid films **102**, 1 (1983).
- [192] H. D. Jang, C. M. Seong, H. K. Chang and H. C. Kim. *Synthesis and characterization of indium-tin oxide (ITO) nanoparticles*. Curr. Appl. Phys. **6**, 1044 (2006).
- [193] Y. Zhao, H. Pan, Y. Lou, X. Qiu, J. Zhu and C. Burda. *Plasmonic Cu<sub>2-x</sub>S nanocrystals: Optical and structural properties of copper-deficient copper(I) sulfides*. J. Am. Chem. Soc. **131**, 4253 (2009).
- [194] W. Liu, A. Y. Chang, R. D. Schaller and D. V. Talapin. *Colloidal InSb nanocrystals*. J. Am. Chem. Soc. **134**, 20258 (2012).
- [195] T. Salminen, J. Dahl, M. Tuominen, P. Laukkanen, E. Arola and T. Niemi. *Single-step fabrication of luminescent GaAs nanocrystals by pulsed laser ablation in liquids*. Opt. Mater. Express **2**, 799 (2012).
- [196] R. Intartaglia, K. Bagga, M. Scotto, A. Diaspro and F. Brandi. *Luminescent silicon nanoparticles prepared by ultra short pulsed laser ablation in liquid for imaging applications*. Opt. Mater. Express **2**, 510 (2012).
- [197] A. Pinczuk, J. Shah and P. A. Wolff. *Collective modes of photoexcited electron-hole plasmas in GaAs*. Phys. Rev. Lett. **47**, 1487 (1981).
- [198] D. Pines. *Electron interaction in solids*. Can. J. Phys. **34**, 1379 (1956).
- [199] D. Pines and J. R. Schrieffer. *Collective behavior in solid-state plasmas*. Phys. Rev. **124**, 1387 (1961).
- [200] J. Ruvalds. *Are there acoustic plasmons?* Adv. Phys. **30**, 677 (1981).
- [201] O. Entin-Wohlman and H. Gutfreund. *Acoustic plasmons and superconductivity: I. The role of exchange*. J. Phys. C: Solid State Phys. **17**, 1071 (1984).
- [202] F. C. Schaefer and R. von Baltz. *Acoustic plasmons in a two-component Fermi system*. Z. Phys. B **69**, 251 (1987).
- [203] D. C. Scott, R. Binder, M. Bonitz and S. W. Koch. *Multiple undamped acoustic plasmons in three-dimensional two-component nonequilibrium plasmas*. Phys. Rev. B **49**, 2174 (1994).

- [204] M. Bonitz, J. F. Lampin, F. X. Camescasse and A. Alexandrou. *Nonequilibrium plasmons in optically excited semiconductors*. Phys. Rev. B **62**, 15724 (2000).
- [205] K. El Sayed, R. Binder, D. C. Scott and S. W. Koch. *Undamping of acoustic plasmons in nonequilibrium plasmas*. Phys. Rev. B **47**, 10210 (1993).
- [206] L. E. Ballentine. *Quantum Mechanics: A Modern Development*. (World Scientific, 1998).
- [207] L. D. Landau and E. M. Lifshitz. *Statistical Physics*. 2nd ed. (Pergamon, 1969).

Johan Rosenkrantz Maack received a BSc in nanotechnology (2010) and a MSc in optics and electronics (2013) from Aarhus University in Denmark. Following graduation, he worked as an electrical engineer before commencing his PhD studies at the Technical University of Denmark in May 2015. The PhD studies were conducted in the Structured Electromagnetic Materials group under the supervision of Assoc. Prof. Martijn Wubs and Prof. N. Asger Mortensen. The PhD thesis was defended August 2018, and the evaluation committee consisted of Dr. Antonio I. Fernández-Domínguez, Prof. Marcello Ferrera and Assoc. Prof. Andrei Lavrinenko.

---

Technical University of Denmark

Department of Photonics Engineering  
Ørsteds Plads, building 343  
DK-2800, Kgs. Lyngby

<http://www.fotonik.dtu.dk/>